Characterization of multi-wall carbon nanotubes and their applications

Katsounaros, Anestis

Characterization of Multi-Wall Carbon Nanotubes and their Applications

Anestis Katsounaros

A Thesis Submitted to the faculty of the University of London
in partial fulfilment of the requirements for the degree of

Doctor of Philosophy

School of Electronic Engineering and Computer Science,
Queen Mary, University of London
London E1 4NS, United Kingdom

September 2011

Abstract

Carbon nanotubes (CNT) and their applications is a field which has attract a lot of interest in the past two decades. Since the first invention of CNTs in 1991, and in view of utilising nanoantennas, the focus in many laboratories around the world has shifted to trying to lengthen nanotubes longer from nanometers to few centimeters. Eventually this could lead to CNTs' use in sub-millimeter, millimiter wave and microwave antenna applications.

In this thesis, fundamental properties of carbon nanotube films are investigated, and some applications such as the use of CNTs as absorbers or CNT doped liquid crystals are considered. The concept of frequency tunable patch antennas is also presented. Simulation and measurement results of the liquid crystal based antenna show that frequency tuning is possible, through the use of a liquid crystal cell as a substrate. Additionally, greater tuning can be achieved using liquid crystals with higher dielectric anisotropy at microwave frequencies. This can be achieved by using CNT doped liquid crystals.

As mentioned, microwave and terahertz measurements of vertically aligned carbon nanotube arrays placed on the top surface of a rectangular silicon substrate are presented. The S-parameters are calculated allowing the extraction of the complex permittivity, permeability and conductivity of the samples. Theoretical models are being introduced delineating the behaviour of the multi-walled nanotube (MWNT) samples. The material properties of this film provide useful data for potential microwave and terahertz applications such as absorbers.

Finally, finite-difference time-domain (FDTD) modelling of CNTs is introduced, verifying the measurements that have been performed, confirming that CNT arrays can be highly absorptive. A novel estimation of the permittivity and permeability of an individual carbon nanotube is presented and a periodic structure is simulated, under periodic boundary conditions, consisting of solid anisotropic cylinders. In addition, the optical properties of vertically aligned carbon nanotube (VACNT) arrays, when the periodicity is both within the sub-wavelength and wavelength

regime are calculated. The effect of geometrical parameters of the tube such as length, diameter and inter-tube distance between two consecutive tubes are also examined.

Acknowledgements

First and foremost I would like to express my gratitude to my supervisor, Prof. Yang Hao for his supervision, advice and guidance throughout this research project. His encouragement and support has enabled me to grow as a student as well as a researcher. Without his constant help and motivation this thesis would not have been possible.

Additionally, I would like to thank to Prof. Clive Parini and the School of Electronic Engineering and Computer Science for giving me the opportunity to complete my Ph.D. studies in the antenna research group in Queen Mary, University of London, as well as the financial support during these years.

I would also like to thank Prof. William Milne, Prof. William Crossland, Dr. Neil Collings, Dr. Mark Mann and Dr. Oksana Trushkevych from the University of Cambridge, for their input from a very early stage of this project as well as for the sample preparation, which has been a vital part of this work.

It is of great importance to recognize the people that have played an important role in my first steps towards the fields of Physics and Electromagnetics. Dr Aikaterini Siakavara, Prof. John Sahalos and Dr Alexandros Feresidis, have inspired me to address the possibility to progress in academia.

Throughout my Ph.D. studies, I have been surrounded by, not only colleagues, but also valuable friends: Mr. Max Munoz, Dr. Christos Argyropoulos, Dr. Themos Kallos, Dr. Andrea Sani, Dr. Khalid Rajab, Dr. Pavel Belov, Dr. Angela Demetriadou, Dr. Yan Zhao, Mr. George Palikaras, Mr. Jiefu Zhang, Mr. Yifeng Fan. My deepest gratitude to you all for making our office a comfortable place to work!

Furthermore, I would like to thank Mr. Costas Mistrellides, Miss Ayfer Kahraman, Mr Costas Mandilaras, Miss Alma Daskalaki, for the very special moments we

passed together. These will remain unforgettable. I would also like to thank Mr. Costas Mistrellides for the time he spent proof-reading this thesis.

Above all, I would like to thank my family, and especially my parents, Marios and Angela, for all their love, encouragement and spiritual support. It is maybe the best place to say thank you for all that they have given up for me to be and study in the United Kingdom.

Table of Contents

Abstract ii

Acknowledgements iv

Table of Contents vi

List of Figures x

List of Tables xviii

Publication List xix

Chapter 1: Introduction 1

Chapter 2: Introduction to Carbon Nanotubes 7

2.1 Introduction 7

2.2 History 9

2.3 Structure 10

2.4 Electrical Properties 14

2.5 Carbon nanotubes on antenna applications 21

2.6 Solving the Hallen's type integral equation for a CNT dipole antenna 22

2.6.1 Conductivity 22

2.6.2 Input Impedance 23

2.6.3 Final form of the Hallen's type integral equation 27

2.7 Further Discussion 28

2.7.1 Resonance frequency of carbon nanotube antennas 28

2.7.2 The relaxation frequency damping effect 30

2.8 Summary 32

Chapter 3: Characterization of Vertically-Aligned Carbon Nanotube Films 33

3.1 Introduction 33

3.2 Carbon nanotube film geometry and fabrication process 34

3.3 X-band measurement 35
3.3.1 Experimental setup and method of extraction 36
3.3.2 Parameter extraction 39
3.4 Ku-band measurement 47
3.5 Terahertz time-domain spectroscopy technique 57
3.5.1 Experimental Setup 58
3.5.2 Data Analysis 59
3.6 Drude model versus measurement results 69
3.7 DC resistance of the vertically-aligned CNT array film 73
3.8 Summary 77
Chapter 4: Modeling Techniques of Carbon Nanotubes 79
4.1 Introduction 79
4.2 Circuit model for spinless electrons in a one-channel quantum wire 81
4.2.1 Magnetic Inductance 82
4.2.2 Kinetic Inductance 83
4.2.3 Electrostatic Capacitance 84
4.2.4 Quantum Capacitance 84
4.2.5 Wave Velocity 85
4.2.6 Characteristic Impedance 86
4.3 Circuit Model for metallic single-wall carbon nanotube 88
4.3.1 Spin - charge separation at DC 88
4.3.2 Non-interacting circuit model for metallic single-wall Carbon Nanotube 88
4.3.3 Interacting circuit model for metallic single-wall Carbon Nanotube 89
4.3.4 Spin - charge separation at AC 90
4.4 Maxwell Equations 91
4.5 Fundamentals of the Finite-Difference Time-Domain Method 93
4.6 Summary 100

Chapter 5: Further Investigation of Carbon Nanotube Properties 101

5.1 Introduction..... 101

5.2 General permittivity and permeability functions in X-band and Ku-band..... 102

5.3 Permittivity and permeability function for an individual carbon nanotube.... 111

5.4 Carbon nanotube for a dipole nano-antenna..... 119

5.5 Geometrical effect of vertically aligned carbon nanotube arrays at optical frequencies 121

5.5.1 Volume fraction..... 123

5.5.2 Length effect..... 125

5.5.3 Radius and periodicity 127

5.6 Summary..... 129

Chapter 6: Optically Transparent and Liquid Crystal Substrate Based Antennas ... 131

6.1 Introduction..... 131

6.2 Optically transparent Ultra Wide-Band antenna..... 132

6.2.1 Introduction to Ultra Wide-Band Technology..... 133

6.2.2 Optically transparent and conductive films 135

6.2.3 Proposed Antenna..... 136

6.3 Liquid Crystals..... 142

6.4 Carbon Nanotube doped liquid crystal 144

6.5 Frequency tunable antennas..... 148

6.5.1 Proposed Antenna..... 148

6.5.2 Antenna Design 149

6.5.3 Simulated Results 150

6.5.4 CNT-doped liquid crystal antenna..... 153

6.5.5 Simulated Results 154

6.5.6 Measurement Results..... 157

6.6 Summary..... 161

Chapter 7: Conclusion and future work 162

7.1 Conclusions 162

7.2 Future work..... 166

References 170

List of Figures

Figure 1: Carbon allotropes. a) graphite and b) diamond [2]..... 7
Figure 2: Carbon allotropes. a) C-60 buckyball and b) Carbon nanotube [2]..... 8
Figure 3: Single-Walled Nanotubes (SWNTs) can be viewed as seamless cylinders rolled up from a graphene sheet [56]. 11
Figure 4: a) a Single-Walled Carbon Nanotube (SWNT) and b) a Multi-Walled Carbon Nanotube (MWNT). The pictures were taken by an Atomic Force Microscope (AFM) and a Transmission Electron Microscope (TEM) respectively [58]. 11
Figure 5: A graphene sheet. A coordinate system, lattice basis vectors and position vector are also presented. The small circles denote the position of carbon atoms and the lines represent carbon - carbon bonds [61]. 12
Figure 6: Hybridization at the Carbon atom. Vectors represent the electrons and two different directions of the vectors correspond to the spins, according to Pauli exclusion principle [62]. 13
Figure 7: The three different possible structures of a Carbon Nanotube. Zigzag, armchair and chiral respectively [63]. 15
Figure 8: a) The real space unit vectors and the hexagonal lattice unit cell. Distance between two carbon atoms is $a_{C-C} = 0.1421nm$. b) The corresponding reciprocal space, showing the reciprocal lattice vectors [66]. 16
Figure 9: Electronic structure of graphene according to equation (2.4). This is calculated within a tight-binding model [69]..... 18
Figure 10: a) band structure of a (5,5) armchair nanotube. b) Band structure of a (9,0) zigzag nanotube. c) Band structure of the semi-conducting zigzag tube (8,0) [66]..... 19
Figure 11: Band structure and Density of States for the (10,10) armchair nanotube. At Fermi level the DOS is finite [66]..... 20
Figure 12: Band structure and Density of States (DOS) for the (10,0) zigzag nanotube. At Fermi level the DOS is equal to zero [66]..... 20

Figure 13: Carbon Nanotube geometry. 22
Figure 14: Conductivity σ_{cn} as a function for carbon nanotubes, for various $m = n$ values. Solid and dashed lines represent $\mathrm{Re}(\sigma)$ and $\mathrm{Im}(\sigma)$ respectively [13]. 25
Figure 15: Conductivity σ_{cn} as a function of frequency for carbon nanotubes with $m = 40$ and $a = 2.712nm$, and σ_{2d} for an infinitely thin two-dimensional bulk approximation (TDBA) copper tube having the same radius. Solid lines are $\mathrm{Re}(\sigma)$ and dashed lines are $\mathrm{Im}(\sigma)$ [13]. 27
Figure 16: Input impedance for a carbon nanotube dipole antenna ($m = 40$) and for TDBA copper tube dipole having the same radius and length, $L = 10\mu m$. Solid lines are $\mathrm{Re}(Z_{in}/R_o)$ and dashed lines are $\mathrm{Im}(Z_{in}/R_o)$. Square boxes denote resonance frequencies and R_o is the channel resistance (quantum resistance, ≅12.9 kΩ) [13]. 29
Figure 17: Input impedance for a carbon nanotube dipole antenna ($m = 40$) and for TDBA copper tube dipole having the same radius and length, $L = 1\mu m$. Solid lines are $\mathrm{Re}(Z_{in}/R_o)$ and dashed lines are $\mathrm{Im}(Z_{in}/R_o)$ [13]. 30
Figure 18: Input impedance versus frequency, for three different carbon nanotube dipole antennas. The effect of relaxation frequency damping on antenna resonances is clearly presented [13]. 31
Figure 19: Current distribution on a carbon nanotube antenna with $m = 40$, radius $= 2.712nm$ and $L = 10\mu m$. Frequencies are shown on the graphs [13]. 32
Figure 20: SEM image from the vertically aligned CNT film [89]. 36
Figure 21: Measurement using Transmission/Reflection method with a waveguide [63]. 37
Figure 22: Effective medium extracted parameters of the VACNT film. a-b) 30 μm c-d) 95 μm e-f) 252 μm. 40
Figure 23: Effective medium extracted relative permittivity of all the VACNT films. 42

Figure 24: Effective medium extracted relative permeability of all the VACNT films. 42
Figure 25: Effective medium extracted conductivity of all the VACNT films. 44
Figure 26: Simulated and measured reflection and transmission coefficients of the VACNT films. a-b) 30 μm c-d) 95 μm e-f) 252 μm. 45
Figure 27: Measured absorption of the VACNT films. 46
Figure 28: Effective medium extracted parameters of the VACNT film. a-b) 30 μm c-d) 70 μm e-f) 95 μm g-h) 252 μm..... 49
Figure 29: Effective medium extracted permittivity of all the VACNT films..... 51
Figure 30: Effective medium extracted real permeability of all the VACNT films. 51
Figure 31: Effective medium extracted imaginary permeability of all the VACNT films. 52
Figure 32: Effective medium extracted conductivity of all the VACNT films. 53
Figure 33: Simulated and measured reflection and transmission coefficients of the VACNT films. a-b) 30 μm c-d) 70 μm e-f) 95 μm g-h) 252 μm. 54
Figure 34: Measured absorption of the VACNT films. 55
Figure 35: Extracted permittivity and permeability of the samples across the whole measured frequency band. a-b) 30 μm c-d) 95 μm e-f) 252 μm. 56
Figure 36: Measured absorption of the three samples across the X- and Ku-frequency bands. 57
Figure 37: Schematic Diagram of terahertz time-domain spectroscopy (THz-TDS) transmission characterization setup [101]..... 58
Figure 38: Reference and sample time-domain signal. 59
Figure 39: Reference and sample frequency-domain signal. 60
Figure 40: a) vertically aligned carbon nanotubes grown on doped-silicon substrate b) CNTs attached on a sticky tape. 61
Figure 41: Retrieved real and imaginary permittivity for 3 of the samples. 62
Figure 42: Extracted conductivity of the three nanotube films. 64
Figure 43: Fitting curves of the complex permittivity of the three samples, fitted with the combination of Drude-localized Lorentzian absorption..... 65

Figure 44: Fitting curves of the complex permittivity of the three samples, fitted with the improved Drude model that is expressed with (3.23). 67
Figure 45: Extracted complex permittivity, for all the six samples that have been measured with THz-TDS. Fitted curves are also present. 68
Figure 46: Plasma frequency versus thickness for VACNT films. 69
Figure 47: Fitting curves of the complex permittivity of the a-b) 30 μm and c-d) 252 μm samples fitted with the improved Drude model. 70
Figure 48: Comparison of measured absorption with the one extracted from improved Drude model. a) 30 μm b) 252 μm. 71
Figure 49: Absorption versus thickness of VACNT films for different frequencies. 72
Figure 50: a) Diffusive and b) Ballistic transport of electrons in 1-D wires..... 74
Figure 51: a) SEM image of the vertically aligned CNT array and b) simplified model showing the entaglements of the nanotubes [105]. 75
Figure 52: Equivalent circuit model of the vertically aligned CNT array [105]..... 75
Figure 53: Measured DC resistance of the vertically-aligned CNT array showing the length effect. 76
Figure 54: Measured DC resistance of the vertically aligned CNT array showing the thickness effect. 77
Figure 55: Circuit diagram for 1-D system of spinless electrons [116, 117]. 82
Figure 56: A Carbon Nanotube placed over a ground plane [116, 117]. 82
Figure 57: Circuit model for non-interacting electrons in a single-wall carbon nanotube. Two propagating channels, each one with spin up and spin down channel. There is no relation between these four channels [116]. 89
Figure 58: Circuit model for interacting electrons in a single-wall carbon nanotube. We can clearly visualize that the channels are not independent now [116]. 89
Figure 59: FDTD computation domain of the effective medium VACNT films for the case of plane wave excitation. 103
Figure 60: Comparison of FDTD results and measurements of the VACNT films (X-band). a) 30 μm b) 95 μm c) 252 μm. 104

Figure 61: Comparison of FDTD results and measurements of the VACNT films (Ku-band). a) 30 μm b) 95 μm c) 252 μm. 105
Figure 62: Comparison of numerical simulations (FDTD), full-wave simulations (CST) and measurements of the VACNT films. Magnitude of S-parameters and absorption are plotted. a-b) 30 μm c-d) 95 μm e-f) 252 μm. 106
Figure 63: Relative permittivity of the three VACNT films. The general permittivity function (GEF) is calculated by taking the mean value on each frequency point. 107
Figure 64: Relative permeability of the three VACNT films. The general permeability function (GMF) is calculated. 108
Figure 65: General permittivity function. 109
Figure 66: General permeability function 109
Figure 67: Measured and simulated magnitude and phase S-parameters. The simulations have been performed using the general permittivity (GEF) and permeability function (GMF). a-b) 30 μm c-d) 95 μm e-f) 252 μm. 110
Figure 68: a) Multi-walled carbon nanotubes with dielectric constant ε_m b) effective medium. 112
Figure 69: a) cross-section of the unit cell b) 3D-view. 112
Figure 70: Vertical component of the permittivity, $\varepsilon_\perp$, of a single CNT. The results were fitted with the conventional lossy medium. 114
Figure 71: Parallel component of the permittivity, $\varepsilon_\parallel$, of a single CNT. The results were fitted with the conventional lossy medium. 115
Figure 72: Vertical component of the permeability, $\mu_\perp$, of a single CNT. The results were fitted with the Lorentz model. 116
Figure 73: Vertical component of the permeability, $\mu_\parallel$, of a single CNT. The results were fitted with the Lorentz model. 117
Figure 74: Comparison of the magnitude of S-parameters of the effective medium presented in section 5.2 and the periodic structure of CNTs. 118
Figure 75: Comparison of the phase of S-parameters of the effective medium presented in section 5.2 and the periodic structure of CNTs. 119

Figure 76: A sketch of a CNT with the two permittivity components and single layer graphite with the anisotropic dielectric tensor. 122
Figure 77: Effective permittivity function of an individual CNT at optical frequencies [129]. 123
Figure 78: Transmission and reflection of the CNT array from HFSS simulations for different volume fractions..... 124
Figure 79: Absorption of the CNT array from HFSS simulations for different volume fractions. 124
Figure 80: Transmission and reflection of the CNT array from HFSS simulations for different lengths. 126
Figure 81: Absorption of the CNT array from HFSS simulations for different lengths. 126
Figure 82: Transmission of the CNT array for different sets of radius - periodicity, obtained by HFSS simulations. 128
Figure 83: Reflection of the CNT array for different sets of radius - periodicity, obtained by HFSS simulations..... 128
Figure 84: Absorption of the CNT array for different sets of radius - periodicity obtained by HFSS simulations..... 129
Figure 85: Optically transparent antenna for automobile applications. 132
Figure 86: Potential applications for UWB radio communications: the first three scenarios (HDR-WPAN, WBAN, IWAN) assume a network of UWB devices deployed in a residential or office environment, mainly to enable wireless video/audio distribution for entertainment, control signals or high-rate data transfers. The fourth scenario (OPPN) presents a deployment in outdoor peer-to-peer situations, while the fifth (WBAN) takes industry and commercial environments into account [166]. 134
Figure 87: Transmission and reflection response of the optically transparent conductive AgHT film in the visible and infrared spectrum [169]..... 136
Figure 88: UWB transparent antenna. The University logo is placed underneath the antenna to show the transparency. A penny is placed on the left down corner, for scale purposes [170, 171]. 137
Figure 89: Schematic Diagram of the proposed antenna. 138

Figure 90: Measurement and simulated return loss of the transparent UWB antenna. 138
Figure 91: Gain sweep for the optically transparent UWB antenna using both coaxial cable and optical fibre. 139
Figure 92: Gain sweep for the aluminum UWB antenna using both coaxial cable and optical fibre. 140
Figure 93: Antenna gain comparison between optically transparent antenna and aluminum antenna using the OEFS system. We can easily realize that the optically transparent antenna has 5dB less gain, constantly in all frequency. 140
Figure 94: Measured radiation patterns at 1GHz, 2GHz, 3GHz and 6GHz of the optically transparent and aluminum antenna. H-plane co-polarization and cross-polarization are shown. 141
Figure 95: Measured radiation patterns at 1GHz, 2GHz, 3GHz and 6GHz of the optically transparent and aluminum antenna. E-plane co-polarization and cross-polarization are shown. 142
Figure 96: Schematic of molecule alignment in a nematic phase [63]. 143
Figure 97: Liquid crystal cell. Orientation of the liquid crystal occurs above a threshold voltage. 143
Figure 98: Schematic of molecules alignment in smectic A phase and smectic C phase, respectively [63]. 144
Figure 99: Alignment of the CNT-doped liquid crystal when a field is applied..... 145
Figure 100: Comparison of Δε in 1-4 GHz range, switching with 0.5V/μm for pure and CNT doped E7 liquid crystal [190]. 146
Figure 101: Δε of pure and CNT doped E7 liquid crystal, at 30 GHz, against temperature [190]. 147
Figure 102: Sweeping from $\varepsilon_{\perp}$ to $\varepsilon_{\parallel}$ and from $\tan\delta_{\perp}$ to $\tan\delta_{\parallel}$, at 3 GHz for both pure and CNT doped E7 liquid crystal [190]. 147
Figure 103: Schematic diagram of the proposed microstrip patch antenna. Top view and side view respectively. 150
Figure 104: Reflection parameter changing the relative permittivity of the liquid crystal substrate. The values of permittivity correspond to a change of bias voltage from 0V up to 20V. 151

Figure 105: a) 3D radiation pattern of the tunable patch antenna, when the voltage is set at 0V $(\varepsilon = 2.41)$. E-plane cuts for b) 0V, c) 2V, d) 4V, e) 10V and f) 20V . All figures are at 3 GHz. 152
Figure 106: Reflection parameter changing the relative permittivity of the CNT-doped liquid crystal substrate. The values of permittivity correspond to a change of bias voltage from 0V up to 20V. 155
Figure 107: a) 3D radiation pattern of the new tunable patch antenna, when the voltage is set at 0V $(\varepsilon = 2.51)$. E-plane cuts for b) 0V, c) 2V, d) 4V, e) 10V and f) 20V . All figures are at 3 GHz. 156
Figure 108: Schematic diagram of the fabricated microstrip patch antenna operating at 11 GHz. Top view and side view respectively. 158
Figure 109: Frequency tuning of the fabricated microstrip patch antenna applying DC bias voltage. 159
Figure 110: Comparison between simulation and measurement of the tunable microstrip patch antenna. 160

List of Tables

Table 1: Input impedance and efficiency for a solid cylindrical metal wire (0.47λ) for different radius values [13]. 26
Table 2: VNA uncertainties. 41
Table 3: Average systematic errors of material parameters. 41
Table 4: VNA uncertainties. 49
Table 5: Average systematic errors of material parameters. 50
Table 6: Fitting parameters for the measurements presented in Figure 41. 63
Table 7: Fitting parameters for the Drude - Lorentzian model. 66
Table 8: Fitting parameters for the improved Drude model. 68
Table 9: Fitting parameters of the two samples that measurements have been performed across the 8 GHz - 2.5 THz frequency band. 70
Table 10: Absorption level of VACNT films for different frequencies and thickness. 72
Table 11: Fitting parameters of the relative permittivity of a single CNT. 114
Table 12: Fitting parameters of the relative permeability of a single CNT. 116
Table 13: Normalized input impedance and efficiency of a carbon nanotube dipole antenna for several frequencies [13]. 120
Table 14: Efficiency comparison between [13] and model proposed by (5.5) and (5.6). 121
Table 15: Properties of AgHT and ITO optically transparent conductive films. 136
Table 16: Real and imaginary dielectric permittivity with losses of the E7 liquid crystal at 3GHz [190]. 149
Table 17: Resonance frequencies versus directivity and efficiency for the different states. 153
Table 18: Real and imaginary dielectric permittivity with losses of the E7+0.01%wt CNT liquid crystal at 3 GHz [190]. 154
Table 19: Resonance frequencies versus directivity and efficiency for the different states. 157
Table 20: Antenna performance over the tuning range from no-field to 25 V. 159
Table 21: Permittivity values of E7-liquid crystal at 11 GHz [177]. 159

Publication List

Journals:

- A. Katsounaros, Y. Hao, N. Collings, and W.A. Crossland, "Optically Transparent Ultra Wide-Band Antenna", Electronic Letters, vol. 45, no. 14, pp. 722-723.
- A. Katsounaros, K. Z. Rajab, Y. Hao, M. Mann, W. I. Milne, "Microwave Characterization of Vertically Aligned Multi-Walled Carbon Nanotube Arrays", Applied Physics Letters, vol. 98, 203105. Published also in Virtual Journal of Nanoscale Science & Technology, May 30, (2011).
- A. Katsounaros, M. Mann, M. Naftaly, K. Z. Rajab, Y. Hao, W. I. Milne, "Terahertz time-domain spectroscopy characterisation of vertically aligned carbon nanotube films", Carbon, vol. 50, no. 3, pp. 939-942.

Conferences:

- A. Katsounaros, Y. Hao, N. Collings, and W.A. Crossland, "Optically Transparent Antenna for Ultra Wide-Band Applications", EUCAP 2009, Berlin, Germany, 23-27 March 2009.
- A. Katsounaros, K. Z. Rajab, K. Hou, M. Mann, M. Naftaly, N. Collings, W.A. Crossland, and Y. Hao, "Refractive Index Evaluation of Multi-Walled Carbon Nanotube Arrays", EUCAP 2010, Barcelona, Spain, 12-16 April 2010.
- A. Katsounaros, K. Z. Rajab, Y. Hao, M. Mann, W. I. Milne, "X-Band Characterization of Multi-Walled Carbon Nanotube Films", ICEAA 2011, Torino, Italy, 12-17 September 2011.
- A. Katsounaros, K. Z. Rajab, Y. Hao, M. Mann, W. I. Milne, "Microwave Characterization of Multi-Walled Carbon Nanotube Arrays", EuMW 2011, Manchester, UK, 11-13 October 2011.

Chapter 1: Introduction

Carbon nanostructures -such as fullerenes [1] and nanotubes [2]- and their applications is a field which has attracted a lot of interest in the past two decades due to their excellent mechanical properties [3], low mass density [4], high electron mobility [5], large current-carrying capability [6], high thermal conductivity [7], and large aspect ratio. These exceptional mechanical and electrical properties and particularly those of carbon nanotubes (CNTs) are the subject of intensive studies [8, 9]. Interest in their physical and chemical properties has also borne the study of several promising applications including field emission displays [10], hydrogen-powered vehicles, artificial muscles, fuel cells and batteries [2, 11, 12]. Additionally microwave applications including nanosized antennas and nano-interconnects [13, 14] have been suggested. Since the first invention of CNTs in 1991, and in view of utilising nanoantennas, the focus in many laboratories around the world has shifted to trying to lengthen nanotubes longer from nanometers to few centimeters. Eventually this could lead to CNTs' use in sub-millimeter, millimiter and centimeter wave antenna applications.

Single-wall carbon nanotubes owe their remarkable electrical properties to the unconventional electronic structure of graphene. Graphene's structure consists of a two-dimensional adjoining honeycomb cells consisting of carbon atoms. Electronic states close to Fermi energy, which is the energy of the highest occupied electronic state at zero temperature, determine the conducting properties of graphene. Due to this graphene partly resembles semiconductors and metals in band structure, depending on the direction of electron movement in this 2-D structure, thus graphene can be seen as a semimetal.

Carbon nanotubes can be either single-wall (SWNT) or multi-wall (MWNT). In its simplest form, single - walled nanotubes (SWNTs) can be viewed as seamless cylinders rolled from a graphene sheet. The manner in which this graphene layer is rolled, leads to a metal or semi-conducting carbon nanotube. That has been theoretically explained and experimentally applied, using scanning tunnelling microscopy from Dekker [15] and Lieber [9]. On the other hand, multi-walled carbon nanotubes, consist of multiple concentric tubes, creating a Russian doll-like model. In general, SWNTs can either be metallic or semiconducting, whereas MWNTs are always metallic (zero band-gap structure).

Since the first aligned CNT array was reported by Thess [16] in 1996, a variety of techniques have been investigated to grow high-quality and super-aligned CNTs [17]. Vertically aligned carbon nanotubes (VACNTs) are CNTs with high aspect ratio [18] and uniform tube length [19] that are aligned perpendicular to a substrate [20]. Both SWNT and MWNT can be grown individually, in bundles or forming an array. VACNT films are grown on different substrates, such as mesoporous silica [21], planar silicon substrates [22] and quartz glass plate [23] and each CNT is able to grow, placing a nano-particle of a catalyst -usually Fe, Co or Ni- on the substrate facilitating the growth of a long and highly pure nanotube [24]. Aligned CNTs can be potentially used in a large number of applications because of their large surface area and high electrical conductivity, such as DNA biosensor [25], glucose [26], pH [27] and NO_2 [28] sensors.

In this study fundamental properties of carbon nanotube films are investigated, and some applications such as the use of CNTs as absorbers or CNT doped liquid crystals are considered. The concept of frequency tunable patch antennas is also presented. Simulation and measurement results of the liquid crystal based antenna show that frequency tuning is possible, through the use of a liquid crystal cell as a substrate. Additionally, greater tuning can be achieved using liquid crystals with higher dielectric anisotropy at microwave frequencies. This can be achieved by using CNT doped liquid crystals.

As mentioned, microwave and terahertz measurements of vertically aligned carbon nanotube arrays placed on the top surface of a rectangular silicon substrate are

presented. The S-parameters are calculated allowing the extraction of the complex permittivity, permeability and conductivity of the samples. Theoretical models are being introduced delineating the behaviour of the MWNT samples. The material properties of this film provide useful data for potential microwave and terahertz applications such as absorbers.

Finally, finite-difference time-domain (FDTD) modelling of CNTs is introduced, verifying the measurements that have been performed, confirming that CNT arrays can be highly absorptive. A novel estimation of the permittivity and permeability of an individual carbon nanotube is presented and a periodic structure is simulated, under periodic boundary conditions, consisting of solid anisotropic cylinders. In addition, the optical properties of VACNT arrays, when the periodicity is both within the sub-wavelength and wavelength regime are calculated. The effect of geometrical parameters of the tube such as length, diameter and inter-tube distance between two consecutive tubes are also examined.

The structure of this thesis is shown as follows:

Chapter 2 provides an overview of the history, the basic concepts and fundamental properties of carbon nanotubes, therein exploring the structural and electrical properties of CNTs. A concept extensively studied in this chapter is that of the transmitting dipole, made by carbon nanotube antenna via a Hallen's-type integral equation. Interesting properties such as that of input impedance, current distribution, and radiation pattern are discussed. The prototype CNT antenna is compared to the conventional dipole antenna made of copper with the same dimensions and the different properties are discussed. Finally, the limitation of using nanotube antennas in antenna applications is discussed.

Chapter 3 presents the characterization of vertically aligned multi-walled carbon nanotube (VACNT) films from microwave to terahertz. The samples are placed on the top surface of a rectangular silicon substrate allowing the extraction of the effective complex permittivity and permeability of the VACNT films in the microwave region. All extracted parameters are verified by full wave simulations and good agreement is obtained. Systematic error analysis is also presented as well as the

errors calculated. Finally, theoretical models are introduced to quantify material properties, which are essential for them to be used for microwave and terahertz applications such as absorbers. In both X- and Ku- bands, the proposed VACNT films exhibit 90% reduction in size compared to conventional materials without losing in absorption.

In Chapter 4, the dynamic properties of single-walled carbon nanotubes are considered from a circuit point of view and an effective RF equivalent circuit is presented. An introduction to modelling techniques, such as the FDTD algorithm, is also given, based on solving the Maxwell's equations for VACNTs. Simulation results are compared with measurement data to validate the model.

Chapter 5 presents a new effective medium model characterized by the general permittivity (GEF) and general permeability functions (GMF). This allows the prediction of the microwave properties of any similarly dense VACNT film, independent of its thickness. A novel estimation of the permittivity and permeability of an individual carbon nanotube is presented. The complex permittivity and permeability of both vertical and parallel components are calculated and fitted using the lossy medium approach for the effective permittivity, and the Lorentz-model for the effective permeability. In addition, the optical properties of VACNT arrays, which the periodicity is both within the sub-wavelength and wavelength regime are calculated. The effect of geometrical parameters of the tube such as length, diameter and inter-tube distance between two consecutive tubes are also examined. Results from the aforementioned simulations show that VACNT films are highly absorptive in optical range.

In Chapter 6, a potential application of MWNTs in antennas is presented. CNT-doped liquid crystals are characterized for the design of an optically transparent and tunable antenna. A planar circular disc monopole antenna for ultra-wideband applications is designed based on the AgHT-4 transparent film. Radiation patterns of the proposed UWB antenna are omni-directional and monopole-like at low frequencies in H-plane and E-plane respectively, and they are compared to those of an identical aluminium UWB antenna. In addition, fundamental ideas on frequency tunable rectangular printed patch antennas using liquid crystal are presented. Simulation and

measurement results show that frequency tuning is possible, using liquid crystal as a substrate. Additionally, it is ascertained that greater tuning can be achieved using liquid crystals with higher dielectric anisotropy at microwave frequencies whilst doping them with carbon nanotubes. Frequency tunable antennas, using carbon nanotubes doped liquid crystals, are simulated. Radiation patterns, directivity and efficiency are presented. The tuning performance using the above technique, is almost two times better, than a patch antenna utilising pure E7-liquid crystal as a substrate.

Finally, in Chapter 7 a summary of the main conclusions and discussion points for further research are presented.

The major contributions presented during this work can be summarised as follows:

- Vertically aligned multi-walled carbon nanotube (VACNT) films are being characterized for the first time up to 2.5 THz. In addition, all the S-parameters (amplitude and phase) were measured, thus allowing both permittivity and permeability to be extracted when treating VACNT films as an effective medium.

- Transmission THz-TDS technique and theoretical models are applied to the VACNT films showing that plasma frequency varies exponentially with the thickness of the sample.

- Theoretical models, such as the Drude model, are expanded over an entire frequency spectrum of interest (8 GHz to 2.5 THz) with the assumption that VACNT films have no magnetic properties ($\mu = 1$). Using that effective medium model, the theoretical absorption is calculated thus confirming the measurements obtained.

- Characterization of the anisotropic permittivity and permeability of an individual carbon nanotube is presented, for the first time, based on measurement results. Both vertical and parallel components of the complex permittivity and complex permeability are calculated and fitted with the lossy

medium approach and the Lorentz-model respectively. This model achieved good agreement when compared with theoretical models from literature.

- An optically transparent antenna for ultra-wideband applications is proposed. Radiation patterns of the proposed UWB antenna are omni-directional and monopole-like in low frequencies in H-plane and E-plane respectively, and they are compared to those of an identical aluminium UWB antenna.

- A tunable patch antenna using liquid crystal as a substrate is demonstrated. It is known that greater tuning can be achieved using doped liquid crystals with carbon nanotubes thus obtaining higher dielectric anisotropy. Simulation results show that almost two times better frequency tuning of a patch antenna is attained.

Chapter 2:

Introduction to Carbon Nanotubes

2.1 Introduction

Carbon is a versatile element able to form a variety of chemical compounds, many of which are fundamental compounds found in nature. Carbon atoms can form single, double and triple bonds, as well as chains, branched chains, and rings when connected to other carbon atoms, giving rise to allotropes. The best known allotropes of carbon are graphite (Figure 1a) and diamond (Figure 1b). Both allotropes have very distinct optical and electrical properties, because of the different geometry of the carbon atoms themselves within the crystal lattice. In diamond, the carbon atoms are bonded together in a tetrahedral lattice arrangement, where in graphite the carbon atoms are bonded together in sheets of a hexagonal lattice. In terms of differing properties, diamond is highly transparent and physically hard, while graphite is opaque and soft. Moreover, diamond has very low electrical conductivity, while graphite is a good conductor.

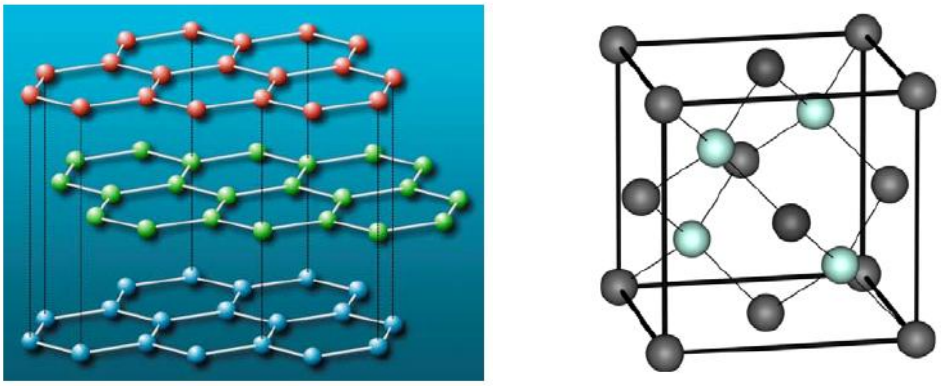

(a) (b)

Figure 1: Carbon allotropes. a) graphite and b) diamond [2].

With the development of microscopes in later years, it has been possible to probe nanometer scale structures, thus more interesting allotropes of carbon have been discovered. In 1985 for the first time, the C-60 buckyball (Figure 2) has been prepared by Harold Kroto [1] at Rice University. In 1996, Kroto shared the Nobel Prize in Chemistry with Robert Curl and Richard Smalley for their roles in the discovery of buckyball and the related class of molecules; fullerenes. This discovery was followed by that of the carbon nanotubes (CNTs) - Figure 2 in 1991.

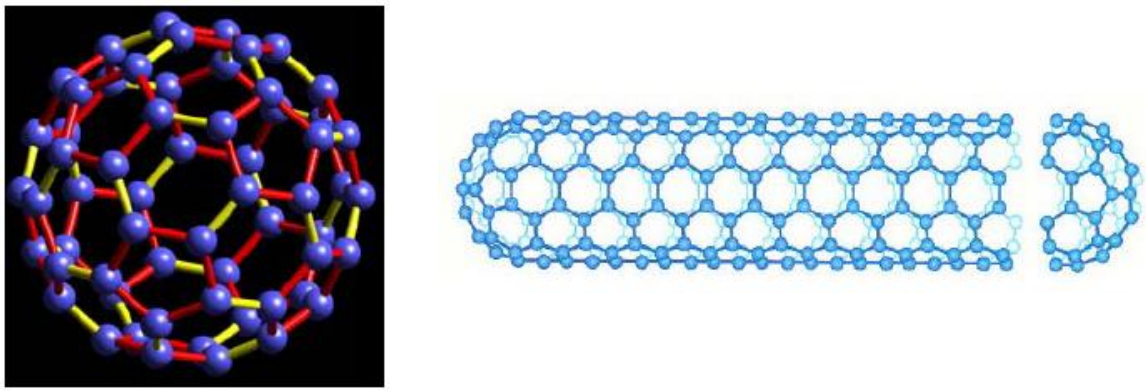

(a) (b)

Figure 2: Carbon allotropes. a) C-60 buckyball and b) Carbon nanotube [2].

These structures, combine a unique set of characteristic properties of carbon allotropes with lower dimensionality. Both zero dimensional buckyballs and one-dimensional carbon nanotubes have emerged as a revolutionary and fast growing science. It is believed that carbon nanotubes may be the key component of future carbon based nano-electronic devices such as nano-scale field-effect transistors [29, 30] and field emission flat-panel displays [31-33]. They can also help to realize many fascinating applications such as hydrogen-powered vehicles [34], artificial muscles [35] and scanning probe microscopy with stronger and thinner cables [36, 37]. Many scientists believe that CNT technology will spearhead the boundaries of radio/wireless communications in the next two decades. One possible and promising application uses the unique electrical properties of carbon nanotubes to make them work as nano-sized antennas. If a CNT could be electromagnetically excited, then it may possibly radiate as a small dipole antenna according to its resonant length (few microns) at frequencies in the terahertz and in the optical range.

2.2 History

Carbon fibers can be regarded the macroscopic analogue of carbon nanotubes. At the beginning of the 19th century, the need for materials with special properties led to the development of carbon fibers. Many scientists at that period were trying to provide a filament for an early model of an electric light bulb. The first ever carbon fiber was produced by Thomas A. Edison using high quality natural fibers, such as bast, jute, manila and hemp, amongst others. After a simple procedure using carbonizable liquids (such as sugar), he managed to produce a high resistance homogeneous filament [38], a structure which could be regarded as a very early model of a modern light bulb filament. After that initial work, many other researchers tried to build upon Edison's work using some more efficient and sturdy filaments, such as those composed of tungsten [39].

Another application using carbon fibers came in the 1950s, in an effort to cover the needs of the space and aircraft industry. In the search of a material with extraordinary mechanical properties which could be used for fabricating lightweight composite materials, carbon fibers emerged as the ideal because of its strength, stiffness and lightweight. This technique, in the following 10 years, became very popular and many laboratories worldwide developed that material further into other important structures [40, 41].

In the next decade, scientists explored various parameters of carbon fiber's applications. One of these was to improve the quality of the products that the existing technology could generate, by reducing the defects of the carbon fiber. Improving carbon fiber structure, following its generation presented a problem to which a solution was the employment of a distinct fabrication technique, using more easily controlled conditions. This led to the catalytic Chemical Vapor Deposition (CVD) process [42-44].

As a result of the expansion in research on CVD technology, the production of very thin filaments have been reported [45, 46]. Endo [45] reports the growth of the thinnest filament yet, with a diameter of less than 10 nm, a result which has attracted much attention in the field. In addition to the discovery of fullerenes, by Kroto and

Smalley [1], research on carbon filaments of very small diameters became more systematic.

In December 1990 at a carbon-carbon composite workshop, Smalley gave an update for his research on fullerenes [47]. Following that, two more important papers were presented, one from Huffman [48] discussing about a new efficient method for fullerene production, and one from M. S. Dresselhaus [49] reviewing carbon fiber research. This workshop, was the inception of Smalley's concept of carbon nanotubes with dimensions comparable to those of C-60. In August 1991, at a fullerene workshop in Philadelphia, M. S. Dresselhaus [50] gave an oral presentation on the symmetry proposed for carbon nanotubes capped at either end by fullerene hemispheres. However, a breakthrough in carbon nanotube research came with Iijima's report [2] in work which received the highest acclaim of other nanotube findings [51] of the same period. Iijima reported nanotubes with length in the order of 1 μm compared to the 10-30 nm [51]. An experimental observation of carbon nanotubes using high-resolution transmission electron microscopy (HRTEM) was given by Iijima's work to investigate these new allotropes of carbon. That work was the one which verified all the previous theoretical works by others [52]. Shortly after Iijima's findings, in July 1992, Ebbesen and Ajayan reported a new method for producing gram quantities of carbon nanotubes [53]. A new era for the Carbon Nanotube research had started.

2.3 Structure

The structure of CNTs originates from that of graphite. One can imagine taking the structure of graphite and removing one of the two-dimensional graphene sheets as depicted in Figure 3. In its simplest form, single - walled nanotubes (SWNTs) can be viewed as seamless cylinders rolled from a piece of graphene sheet. Usually, these structures have a diameter of about $0.7nm - 2nm$ and length reaching up to 1mm [54]. Calculations have shown that collapsing the single wall tube into a flattened two-layer ribbon is energetically more favourable than maintaining the tubular morphology beyond a diameter value of about $2.5nm$ [55].

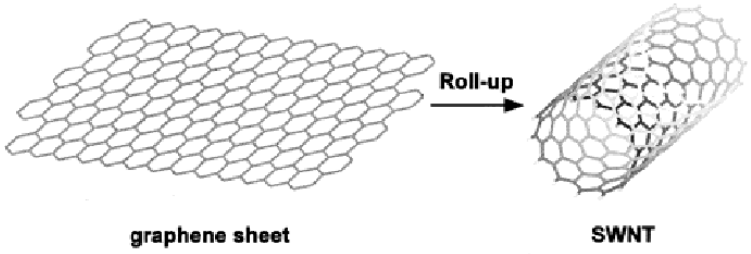

Figure 3: Single-Walled Nanotubes (SWNTs) can be viewed as seamless cylinders rolled up from a graphene sheet [56].

If we neglect the two hemispherical ends of a CNT, which are usually called caps, the large aspect ratio (length/diameter) of the cylinder is found to be between $10^4 - 10^7$. These nanotubes can be considered as one-dimensional nanostructures. Each cap contains six pentagons and an appropriate number and placement of hexagons that are selected to fit perfectly to the long cylindrical section.

Another very similar structure to the above, multi - walled nanotubes (MWNTs), is composed of concentric single-walled nanotubes. It is very easy to distinguish SWNTs from MWNTs using Transmission Electron Microscope (TEM) images. In Figure 4 we can see a MWNT which is several times larger than SWNT. The interlayer spacing in a MWNT is $0.34nm$ as confirmed by HRTEM [2] and STM [57]. Typically, MWNTs have diameters on the order of $10nm$ - $20nm$. In this chapter we will only discuss the structural properties of SWNTs.

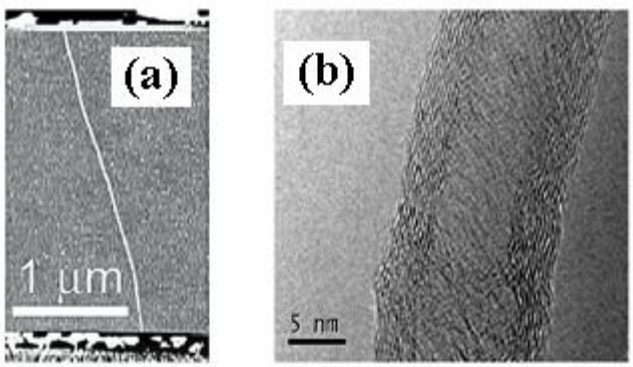

Figure 4: a) a Single-Walled Carbon Nanotube (SWNT) and b) a Multi-Walled Carbon Nanotube (MWNT). The pictures were taken by an Atomic Force Microscope (AFM) and a Transmission Electron Microscope (TEM) respectively [58].

SWNTs can be produced either by a physical process (arc discharge [2] and laser ablation [59]) or by a chemical reaction (chemical vapor deposition [60]). As a quantum system can be fully described by a set of quantum numbers, an individual carbon nanotube can be characterized using only three quantities: diameter, chirality and number of walls. The meaning of these quantities will be explained below. During the growth process it is very hard to control the geometry of individual carbon nanotubes, due to the infinite ways a SWNT can be formed. This gives rise to discrepancies between SWNTs, as well as defects and impurities. MWNTs may be produced without using catalytic particles, thus rendering them, in general, purer than SWNTs.

Figure 5 shows a graphene sheet with a coordinate system, lattice basis vectors and position vector. In this representation, small circles denote the location of carbon atoms and the lines depict carbon - carbon bonds [58]. Due to hybridization carbon atoms will form three bonds instead of four, as depicted in Figure 5.

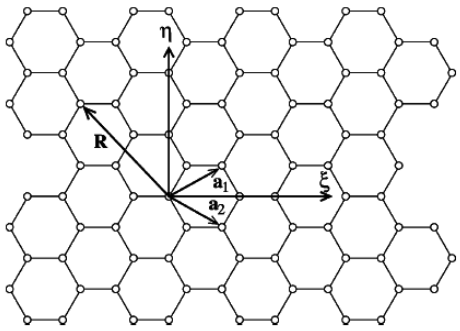

Figure 5: A graphene sheet. A coordinate system, lattice basis vectors and position vector are also presented. The small circles denote the position of carbon atoms and the lines represent carbon - carbon bonds [61].

In quantum mechanics, the so called quantum numbers are a set of four numbers that can describe each electron completely. Therefore, the properties of an atom's electron configuration is described by these four quantities n, l, m and s which are called: energy quantum number, angular quantum number, magnetic quantum number and spin quantum number, respectively. Two of these electrons, can create an orbital. Depending on the value of the quantum number l, the orbitals have different shape and name: s-orbital, p-orbital, d-orbital and f-orbital for $l = 0,1,2$ and 3, respectively.

These names are given due to the characteristics of their spectroscopic lines: sharp, principal, diffuse and fundamental.

Because of the Pauli exclusion principle, the ground state configuration for carbon is $1s^2 2s^2 2p_x^1 2p_y^1$. The first stage in hybridization is the excitation of an electron from the $2s$ orbital to the empty $2p_z$ orbital. Then, the excited carbon, symbolized by C* attains an electron configuration of $1s^2 2s^1 2p_x^1 2p_y^1 2p_z^1$. The one electron in the $2s$ orbital combines together with the two of the $2p$ orbitals (which have different directions) to form three new orbitals called sp^2. Note that one $2p$ orbital is left without any combination with other orbitals.

$$C \quad \frac{\uparrow\downarrow}{1s} \; \frac{\uparrow\downarrow}{2s} \; \frac{\uparrow}{2p_x} \; \frac{\uparrow}{2p_y} \; \frac{}{2p_z}$$

(a)

$$C^* \quad \frac{\uparrow\downarrow}{1s} \; \frac{\uparrow}{2s} \; \frac{\uparrow}{2p_x} \; \frac{\uparrow}{2p_y} \; \frac{\uparrow}{2p_z}$$

(b)

$$C^* \quad \frac{\uparrow\downarrow}{1s} \; \frac{\uparrow}{sp^2} \; \frac{\uparrow}{sp^2} \; \frac{\uparrow}{sp^2} \; \frac{\uparrow}{p}$$

(c)

Figure 6: Hybridization at the Carbon atom. Vectors represent the electrons and two different directions of the vectors correspond to the spins, according to Pauli exclusion principle [62].

It is also worth noting, that the three sp^2 orbitals form bonds with the three nearest neighbouring carbons, giving rise to the so called σ bond, in a manner similar to graphene. The fourth electron belongs to a π orbital which is perpendicular with the cylindrical surface of the CNT. This orbital is the one which helps several layers of graphene to assemble and produce the graphite structure, and for similar reason to assemble MWNTs.

If we go back to Figure 5 we can assign lattice basis vector as $\vec{\alpha}_1$ and $\vec{\alpha}_2$. The relative position vector is $\vec{R} = m\vec{\alpha}_1 + n\vec{\alpha}_2$, where m, n are integers. This vector $\vec{R}$ is called a chiral vector. As explained before, a SWNT can only be viewed by wrapping a graphene sheet into a seamless cylinder. This of course is a simplification in order to understand the structure of CNTs. In reality, rolling a graphene sheet to a cylinder is unattainable.

This cylinder can be formed by rolling the graphene sheet along different directions. If rolled about ξ axis (Figure 5) the tube formed is called a zigzag CNT. If the η axis is used for the cylinder axis, the tube is called an armchair CNT. If the cylinder axis is neither the ξ nor the η axis, the resulting nanotube is called a chiral CNT. Another parameter used to describe nanotubes is the dual index (m, n). This dual index is $(m, 0)$ for zigzag CNTs, (m, m) for armchair CNTs and (m, n) for chiral CNTs. These different CNTs are shown in Figure 7. The cross sectional radius r for a CNT is given by the following equation [13, 58]:

$$r = \frac{\sqrt{3}}{2\pi} b \sqrt{m^2 + mn + n^2} \tag{2.1}$$

where $b = 0.142nm$ is the distance between atoms in graphene.

2.4 Electrical Properties

SWNTs can be either metallic or semiconducting. This depends on the geometry of the specific nanotube. In general, a CNT is metallic when $m - n$ is a multiple of 3. In all other situations, the CNT is characterized as semiconducting. For example, all armchair CNTs are metallic, because as we explained before $m = n$. Zigzag CNTs with $m = 3q$, where q is an integer are also metallic. The rest of the zigzag CNTs and all chiral CNTs are semiconducting. It has been shown that the bandgap of semiconducting nanotubes decreases inversely with an increase in diameter [64, 65]. In contrast with SWNTs, Multi-Walled Nanotubes (MWNTs) are always metallic.

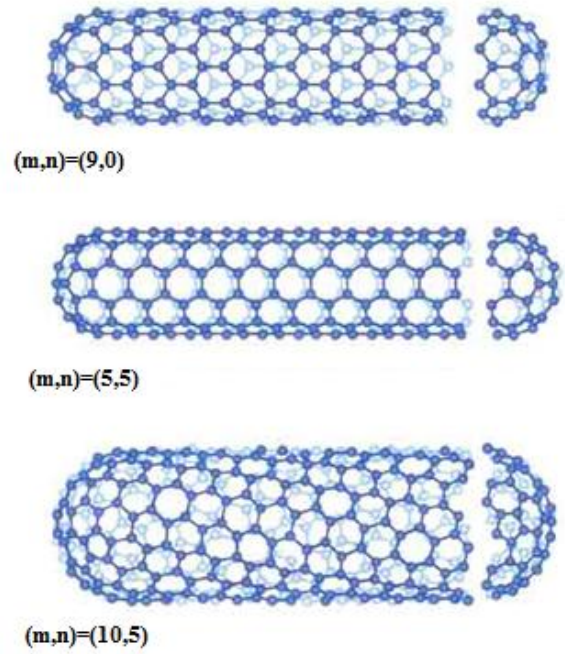

Figure 7: The three different possible structures of a Carbon Nanotube. Zigzag, armchair and chiral respectively [63].

The electronic band structure of a CNT was briefly explained above. We have seen that after hybridization, three sp^2 electrons form a bond with three carbons to produce a graphene sheet. One p orbital left unconnected which is perpendicular to that planar sheet and thus the nanotube surface. This p orbital is responsible for the electronic properties of a CNT because that forms a delocalized π-network across the nanotube.

A useful starting point to understanding the electronic structure and properties of a nanotube, is to assume two carbon atom hexagonal unit cell of graphite. Using the real space coordinate system of Figure 5 and defining the reciprocal lattice vectors in terms of the real space vectors as, $\vec{\alpha}_1 \cdot \vec{\alpha}_1' = 2\pi$ and $\vec{b}_1 \cdot \vec{b}_1' = 2\pi$, we arrive at the Brillouin zone in reciprocal space shown in Figure 8.

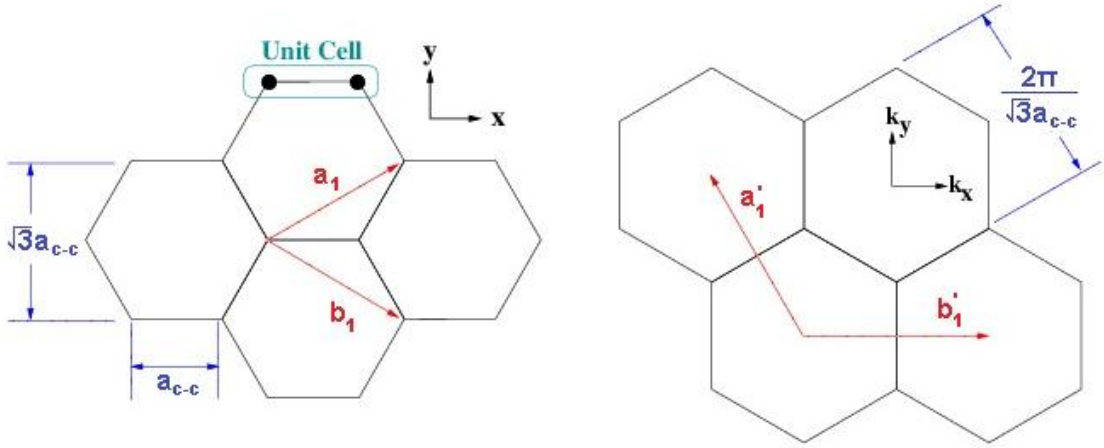

(a) (b)

Figure 8: a) The real space unit vectors and the hexagonal lattice unit cell. Distance between two carbon atoms is $a_{C-C} = 0.1421nm$. b) The corresponding reciprocal space, showing the reciprocal lattice vectors [66].

Considering only one orbital per atom and neglecting overlap, we find the graphite dispersion relation by solving the eigenvalue equation [66]:

$$\mathrm{E}\begin{pmatrix}\varphi_1\\ \varphi_2\end{pmatrix} = \begin{pmatrix}0 & h_o\left(\vec{k}\right)\\ h_o^*\left(\vec{k}\right) & 0\end{pmatrix}\cdot\begin{pmatrix}\varphi_1\\ \varphi_2\end{pmatrix} \tag{2.2}$$

where

$$h_o\left(\vec{k}\right) = \gamma_o\left(1 + e^{i\vec{k}\cdot\vec{a}} + e^{i\vec{k}\cdot\vec{b}}\right). \tag{2.3}$$

The general dispersion relation is derived through the tight-binding approximation for two dimensional graphite [67, 68]:

$$E\left(k_x, k_y\right) = \pm\gamma_o\sqrt{1 + 4\cos\left(\frac{\sqrt{3}}{2}k_x a\right)\cdot\cos\left(\frac{1}{2}k_y a\right) + 4\cdot\cos^2\left(\frac{1}{2}k_y a\right)} \tag{2.4}$$

where $\gamma_o = 2.9eV$ is the value of the overlap integral and $\alpha = \sqrt{3}\cdot\alpha_{C-C}$. This is an approximation, the Slater-Koster scheme, and it is used as a simple approximation for the structure of graphene.

Figure 9 shows the bandstructure for graphene, according to the solution above as a function of k_x and k_y. Graphene has the peculiar property of the valence and

conduction band only meeting each other in six points. These points are in the corner of Brillouin zone: $\left[\left(\pm\frac{4\pi}{3\sqrt{3}a},0\right);\left(\pm\frac{2\pi}{3\sqrt{3}a},\pm\frac{2\pi}{3a}\right)\right]$. Such behaviour, makes graphene a so called semi-metal. The band structure of the single wall carbon nanotubes is found by imposing the following periodic boundary condition in the circumference of the tube:

$$\vec{k}\cdot\vec{R}=2\pi\cdot N \tag{2.5}$$

where $N=0,1,2,...$

For a zigzag nanotube, the boundary condition (2.5) reduces to a condition on k_y,

$$\vec{k}\cdot\vec{R}_{zig}=nak_y=2\pi\cdot N \tag{2.6}$$

where where $N=0,1,2,...n.$

Thus, from (2.4), we find the zigzag energy dispersion relation,

$$E_{n,N}^{zig}\left(k_x\right)=\pm\gamma_o\sqrt{1+4\cos\left(\frac{\sqrt{3}}{2}k_xa\right)\cdot\cos\left(\frac{\pi N}{n}\right)+4\cdot\cos^2\left(\frac{\pi N}{n}\right)} \tag{2.7}$$

For an armchair nanotube, the boundary condition (2.5) becomes:

$$\vec{k}\cdot\vec{R}_{arm}=n\sqrt{3}ak_x=2\pi\cdot N \tag{2.8}$$

where where $N=0,1,2,...n.$

Replacing that into (2.4), it gives the armchair dispersion relation for a nanotube,

$$E_{n,N}^{arm}\left(k_y\right)=\pm\gamma_o\sqrt{1+4\cdot\cos\left(\frac{\pi N}{n}\right)\cdot\cos\left(\frac{1}{2}k_ya\right)+4\cdot\cos^2\left(\frac{1}{2}k_ya\right)} \tag{2.9}$$

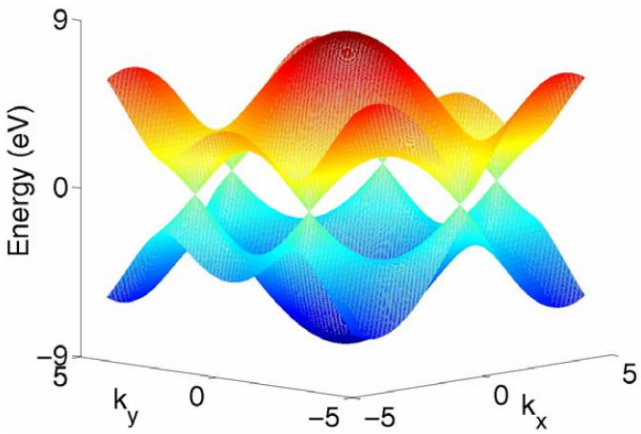

Figure 9: Electronic structure of graphene according to equation (2.4). This is calculated within a tight-binding model [69].

In Figure 10a, one can find the band structure of a $(5,5)$ armchair nanotube. This nanotube, as every armchair nanotube, is metallic and has two bands crossing at the energy of the highest occupied electronic state at zero temperature, which is called Fermi energy. The corners of the hexagons in the reciprocal lattice are the so-called K-points and this is where the conduction and the valence band of graphene touch each other. If one of the quantization lines pass through two K-points, then the nanotube is considered to be metallic. On the other hand, Figure 10b shows the bandstructure of a $(9,0)$ armchair zigzag nanotube. This tube, as has been explained earlier and can also be seen in the graph, is considered to be metallic, due to the band crossing the Fermi level. Figure 10c shows the bandstructure of a $(8,0)$ armchair zigzag nanotube. For this structure the quantization lines do not cross the K-points, therefore the nanotube is considered to be semiconducting with a bandgap of the order of $1eV$ [11]. As aforementioned, a zigzag nanotube is either metallic or semiconducting, depending on its chirality. Only when $m = 3q$ and q is an integer, the nanotube is metallic, whereas all other combinations result in a semiconducting tube.

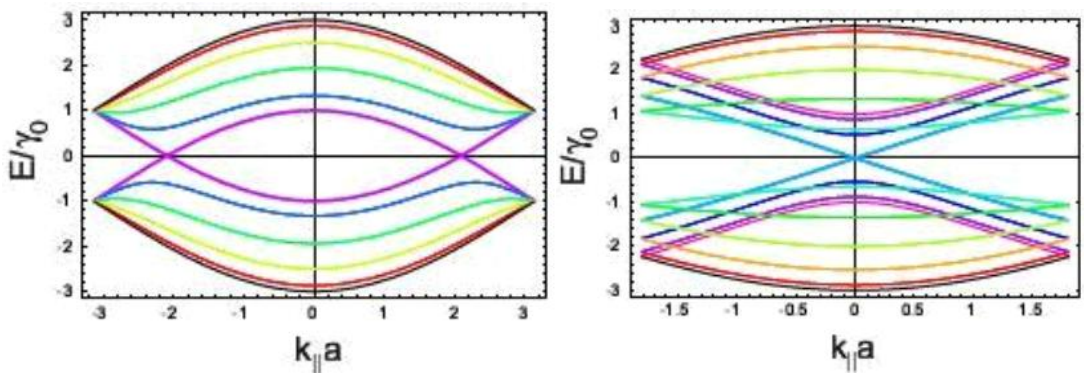

(a) (b)

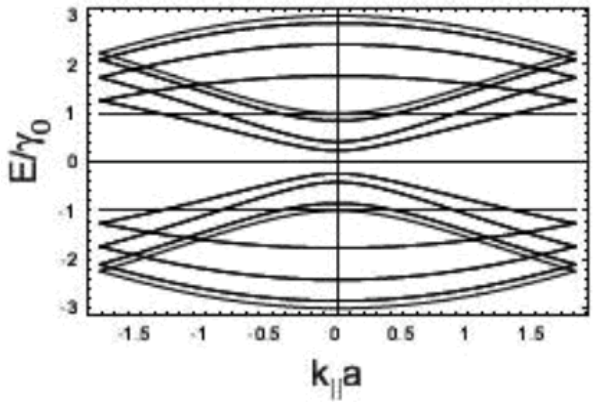

(c)

Figure 10: a) band structure of a (5,5) armchair nanotube. b) Band structure of a (9,0) zigzag nanotube. c) Band structure of the semi-conducting zigzag tube (8,0) [66].

Tight-binding model is also useful to understand the Density of States (DOS) of CNTs. The electronic DOS for an one dimensional material is:

$$n(E) = \frac{1}{\pi\hbar\upsilon(E)}, \qquad \upsilon(E) = \frac{1}{\hbar}\frac{dE}{dk} \tag{2.10}$$

where $\upsilon(E)$ is the group velocity for electrons moving in the $+x$ direction. The DOS of a $(10,10)$ armchair nanotube and a $(10,0)$ zigzag one are shown in Figure 11 and Figure 12, respectively. The metallic nanotube, has a finite DOS at the Fermi energy $E_F = 0$, and the semiconducting tube has zero DOS at E_F.

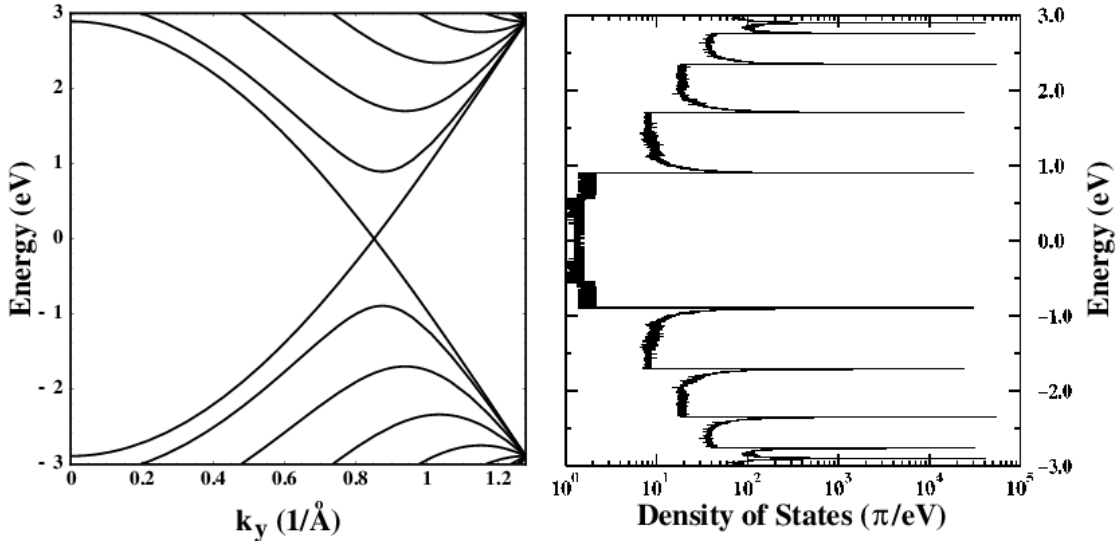

Figure 11: Band structure and Density of States for the (10,10) armchair nanotube. At Fermi level the DOS is finite [66].

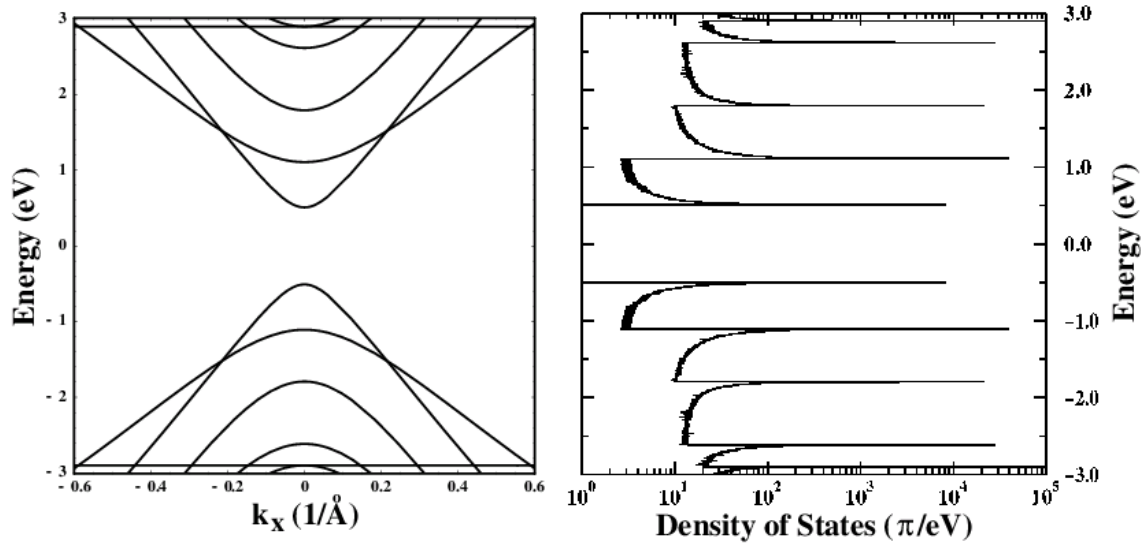

Figure 12: Band structure and Density of States (DOS) for the (10,0) zigzag nanotube. At Fermi level the DOS is equal to zero [66].

As noted above, all the metallic nanotubes have energy bands crossing the Fermi energy. An ideal nanotube contacted by two contact pads would have quasi-Fermi levels of μ_1 and $\mu_2 = \mu_1 - eV_{app}$. With this applied bias, the current only flows through one level between μ_1 and μ_2 which are the bands crossing the Fermi energy of the nanotube. A prediction that has been reported in literature [70, 71] for carbon nanotubes is that transport in the metallic bands may be ballistic. During ballistic transport, there is no electron scattering over the length of the medium and electrons

remain in local equilibrium as they enter and exit from the contact pads. This phenomenon literally takes place when the phase breaking length, l_φ, of the electron states in the nanotube is larger than the momentum relaxation length, l_m, which is much greater than the length of the nanotube, L. Thus the condition for ballistic conduction is $L < l_m < l_\varphi$. Further restrictions apply, where the diameter, D, of the nanotube is comparable to the electron wavelength at the Fermi energy λ_F and D is much less than L.

2.5 Carbon nanotubes on antenna applications

Previous sections dealt with investigating the electronic properties of carbon nanotubes. The major difference between carbon nanotubes and conventional nanoscale wires, is that CNTs can exhibit ballistic transport over at least nanometer lengths [58]. During ballistic transport in a four-channel system, such as CNT, the resistance of the tube is independent of length and is, theoretically, around $6.45k\Omega$ (two parallel propagation channels, $12.9k\Omega$ each).

In [14], we realized that CNT-transmission lines act differently from ordinary metallic transmission lines. Kinetic inductance dominates, over the usual magnetic one, and both electrostatic and quantum capacitance must be taken into account. The result is that wave velocity on a CNT-transmission line is on the order of the Fermi velocity rather than the speed of light. Considering $u_p \approx 6.2u_F \approx 0.02c$, wavelengths are much shorter on a carbon nanotube, compared to a typical macroscopic metallic tube.

In this section, fundamental properties of finite-length dipole CNT antennas are investigated using a Hallen's-type integral equation. Input impedance, current profile and efficiency are presented and compared to ordinary metallic antennas of the same size and shape.

2.6 Solving the Hallen's type integral equation for a CNT dipole antenna

We will consider a CNT similar in structure to that depicted in Figure 13. The cylinder is placed along the z direction, the radius of the cylinder is a and it is said to be infinitely thin.

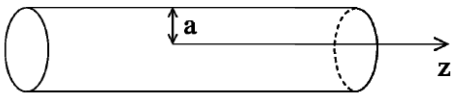

Figure 13: Carbon Nanotube geometry.

2.6.1 Conductivity

The conductivity of the CNT derived starting with Boltzmann's equation [72]. We should note here that the relaxation-time approximation is given by equation (2.11) where it is restricted in the case of a z-directed electric field E_z, where current flows only in z direction:

$$\frac{\partial f}{\partial t} + eE_z \frac{\partial f}{\partial p_z} + u_z \frac{\partial f}{\partial z} = v\left[f_o(p) - f(p,z,t) \right] \tag{2.11}$$

where f is the electron's distribution function, u_z is the electron's velocity, e is the electron's charge, v is the relaxation frequency, p is the two-dimensional electron momentum and f_o is the Fermi-Dirac distribution which is described by the equation (2.12):

$$f_o(p) = \left(1 + e^{\frac{E(p) - E_F}{k_B T}} \right)^{-1} \tag{2.12}$$

where E_F is the Fermi energy, $E(p)$ is the electron's energy, k_B is the Boltzmann's constant and T is the temperature.

Following the derivation as Maksimenko [73, 74] suggested, we find that the conductivity is given by the general equation:

$$\sigma_{zz} = j \frac{2e^2}{(2\pi\hbar)^2} \iint \frac{\partial f_o}{\partial p_z} \frac{u_z}{\omega - jv} d^2 p \tag{2.13}$$

For generally small radius CNTs (where $m < 50$), equation (2.13) can be approximated as

$$\sigma_{cn}(\omega) = \sigma_{zz}(\omega) \simeq -j\frac{2e^2 u_F}{\pi^2 \hbar a(\omega - j\nu)} \tag{2.14}$$

where u_F is the Fermi velocity for CNTs. The units for conductivity in equation (2.14) are S (Siemens), rather than S/m (Siemens per meter) as the carbon nanotube is modelled as an infinitely thin tube, thus supporting a not surface current density.

At this point, it is interesting to compare the conductivity of a CNT which is given by equation (2.14) with the conductivity of a two-dimensional (infinitely thin) metal cylinder, using the Fermi-gas model [75]:

$$\sigma_{2d}(\omega) = \sigma_{zz}(\omega) = -j\frac{e^2 E_F}{\pi\hbar^2(\omega - j\nu)} \tag{2.15}$$

where σ_{2d} denotes the two-dimensional conductivity for a Fermi-gas metal such as copper. By replacing the Fermi energy in equation (2.15) with $E_F = \frac{N_e^{2d}\pi\hbar^2}{m_e}$ [75] we have:

$$\sigma_{2d}(\omega) = -j\frac{e^2 N_e^{2d}}{m_e(\omega - j\nu)} \tag{2.16}$$

where N_e^{2d} is the number of electrons per square meter and m_e is the mass of an electron. For a three dimensional conductor, the equation (2.16) leads to:

$$\sigma_{3d}(\omega) = -j\frac{e^2 N_e^{3d}}{m_e(\omega - j\nu)} \tag{2.17}$$

2.6.2 Input Impedance

The integral equation for current density can be obtained from Ohm's law:

$$J_z(z,\omega) = \sigma(\omega)E_z(z,\omega) \tag{2.18}$$

where for all z along the tube, σ denotes either the carbon nanotube conductivity (2.14) or the conductivity for the metal tube (2.16).

Following the standard antenna analysis, starting with [76]:

$$E(r) = \frac{1}{j\omega\varepsilon}\left(k^2 + \nabla\nabla\right)\int_V g(r,r')J(r')dV' \tag{2.19}$$

where $g(r,r') = \frac{e^{-jkR}}{4\pi R}$ and $R = |r - r'|$.

Taking $J(r) = \hat{z}J_z(z)\delta(\rho - a)$, we obtain:

$$E_z = \frac{1}{j4\pi\omega\varepsilon}\left(k^2 + \frac{\partial^2}{\partial z^2}\right)\int_{-L}^{L} K(z-z')I(z')dz' \tag{2.20}$$

where L is the half-length of the antenna and the standard thin-wire kernel, which is appropriate for a radius in nanometer scale [77]:

$$K(z-z') = \frac{e^{-jk\sqrt{(z-z')^2+a^2}}}{\sqrt{(z-z')^2 + a^2}} \tag{2.21}$$

Considering $I(z) = J_z(z)2\pi\alpha$ Ohm's Law from equation (2.18) becomes:

$$\frac{I(z)}{2\pi\alpha} = \sigma\left(E_z^s(z) + E_z^i(z)\right) \tag{2.22}$$

where $E_z^i(z)$ is the incident field and $E_z^s(z)$ is the scattered field. Writing the scattered field as (2.20) we have the Pocklington integral equation:

$$\left(k^2 + \frac{\partial^2}{\partial z^2}\right)\int_{-L}^{L} K(z-z')I(z')dz' = j4\pi\omega\varepsilon\left(z_i I(z) - E_z^i(z)\right) \tag{2.23}$$

where

$$z_i = \frac{1}{2\pi\alpha\sigma} \tag{2.24}$$

is the antenna impedance per unit length. Moreover, we can define the antenna impedance for the infinitely thin tube, if the metal tube's wall thickness is d :

$$z_i = \frac{1}{2\pi\alpha\left(\sigma_{3d}d\right)} \tag{2.25}$$

if d is small compared to the skin depth, $\delta_s = \sqrt{\frac{2}{\omega\mu\sigma_{3d}}}$. Now if d is much bigger than the skin depth, then:

$$z_i = \frac{1+j}{2\pi\alpha\left(\sigma_{3d}\delta_s\right)} \tag{2.26}$$

We can now plot the conductivity σ_{cn} (for armchair tubes) as a function of frequency for various m (Figure 14). For a carbon nanotube the relaxation frequency is taken as $v = \tau^{-1} = \left(3\cdot 10^{-12}\right)^{-1}$ [73] and here we use $u_F \simeq 9.71\cdot 10^5 m/\sec$.

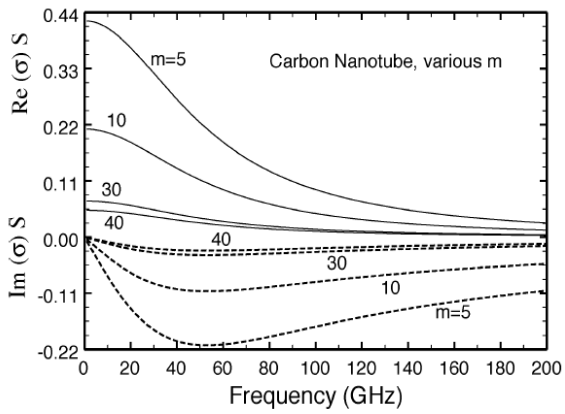

Figure 14: Conductivity σ_{cn} as a function for carbon nanotubes, for various $m = n$ values. Solid and dashed lines represent $\mathrm{Re}(\sigma)$ and $\mathrm{Im}(\sigma)$ respectively [13].

We now compare the CNT results with the metal dipole of the same size and shape. In contrary to the case of a macroscopic metal dipole, the value of conductivity plays an important role for nanometer radius antennas. Considering σ_{3d} is in the order of 10^7, it is clear from (2.25) and (2.26) that if a becomes very small, $|z_i|$ will be relatively large, significantly changing the antenna's properties from the perfectly conducting case, where $|z_i| = 0$.

At this point, we consider a solid copper dipole antenna working at $160GHz$ with a length of 0.47λ. We can calculate the input impedance assuming a perfect conductor, Z_{in}^{pc}, and the input impedance assuming bulk copper, Z_{in}^{σ}, in the following table.

Table 1: Input impedance and efficiency for a solid cylindrical metal wire (0.47λ) for different radius values [13].

Radius µm	**Input Impedance (ohms)**	$e_r = P_r / P_{in}$
3.75	$Z_{in}^{pc} = 69.84 - j7.36$	1.00
	$Z_{in}^{\sigma} = 72.24 - j5.76$	0.97
20x10^{-3}	$Z_{in}^{pc} = 62.78 - j76.96$	1.00
	$Z_{in}^{\sigma} = 1960.13 - j1917.14$	$5.53 \cdot 10^{-3}$
2x10^{-3}	$Z_{in}^{pc} = 62.08 - j106.85$	1.00
	$Z_{in}^{\sigma} = 19788.96 - j19539.85$	$4.82 \cdot 10^{-6}$

We propose that for very small radius values, $|z_i|$ becomes very large, such that Z_{in}^{pc} and Z_{in}^{σ} have very different values. The efficiency is also shown in the above table, where P_r is the radiated power and P_{in} is the input power:

$$P_{in} = \frac{1}{2} \mathrm{Re}\left(Z_{in}\right) I_o^2 \tag{2.27}$$

where I_o is the current at the feed point.

In Figure 15 the conductivity is plotted as a function of frequency for armchair tubes with $m = n = 40$ and for an infinitely thin two-dimensional bulk approximation (TDBA) copper tube with the same radius.

At $10GHz$, we found that $\sigma_{cn} = 0.0512 - j0.00964\ S$ and $\sigma_{2d} = 0.0134 - j0.000021\ S$, where the material described by σ_{2d} has the same parameters as the defined TBDA copper. At this frequency, the real part of the carbon nanotube conductivity, is in the same order of magnitude as the TBDA copper sheet conductivity, although σ_{cn} is quite dispersive compared to σ_{2d}.

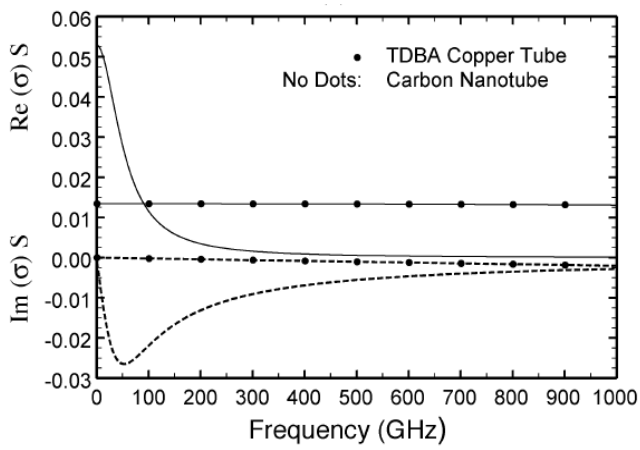

Figure 15: Conductivity σ_{cn} as a function of frequency for carbon nanotubes with $m = 40$ and $a = 2.712nm$, and σ_{2d} for an infinitely thin two-dimensional bulk approximation (TDBA) copper tube having the same radius. Solid lines are $\mathrm{Re}(\sigma)$ and dashed lines are $\mathrm{Im}(\sigma)$ [13].

2.6.3 Final form of the Hallen's type integral equation

Converting the Pocklington equation (2.23) into a Hallen's integral equation [78]:

$$\left(k^2 + \frac{\partial^2}{\partial z^2}\right)\int_{-L}^{L}\left(K(z-z') + q(z-z')\right)I(z')\,dz' = j4\pi\omega\varepsilon E_z^i(z) \qquad (2.28)$$

leads to the function q as

$$q(z-z') = \frac{\omega\varepsilon}{\alpha\sigma}\frac{e^{-jk|z-z'|}}{k} \qquad (2.29)$$

Assuming a slice-gap source of unit voltage at z_o, the final integral equation to solve is

$$\int_{-L}^{L}\left(K(z-z') + q(z-z')\right)I(z')\,dz' = c_1\sin(kz) + c_2\cos(kz) - j\frac{4\pi\omega\varepsilon}{2k}\sin\left(k|z-z_o|\right) \qquad (2.30)$$

where c_1 and c_2 are constants to be determined from $I(z \pm L) = 0$.

2.7 Further Discussion

In this section, the resonance frequency of a carbon nanotube dipole antenna will be investigated and the relationship with the TDBA copper dipole, which proposed above. At the end, the relaxation frequency damping effect will be discussed.

2.7.1 Resonance frequency of carbon nanotube antennas

Assuming a Carbon Nanotube dipole antenna with half-length of $L = 10\mu m$, Figure 16 shows the input impedance of this antenna ($m = 40$, so $a = \text{radius} = 2.712nm$). That antenna resonates at $150GHz$ as the square box shows. On this graph the input impedance of a TDBA copper tube (of the same dimensions) is shown. As expected, the copper dipole will not resonate at those frequencies but resonates at $f = \frac{c}{\lambda} = \frac{3 \cdot 10^8}{40 \cdot 10^{-6}} = 7.5THz$. We can easily find the ratio between the resonance frequency of the CNT and the resonance frequency of an identical, in size, metallic tube. This is given by:

$$r = \frac{f_{CNT}}{f_{TDBA}} = 0.02 \tag{2.31}$$

This means carbon nanotubes exhibit relatively sharp resonances according to the velocity factor:

$$u_p \sim 0.02c \tag{2.32}$$

Carbon nanotube dipole resonances, can be associated with plasmons by the transmission line model developed in [14]. The transmission line model, predicts that $u_p \simeq u_F \simeq 0.01c$. Therefore the wavelength of the antenna should be approximately $\lambda_p \simeq 0.01\lambda_o$, where λ_p is called the plasmon wavelength and λ_o is the free space wavelength.

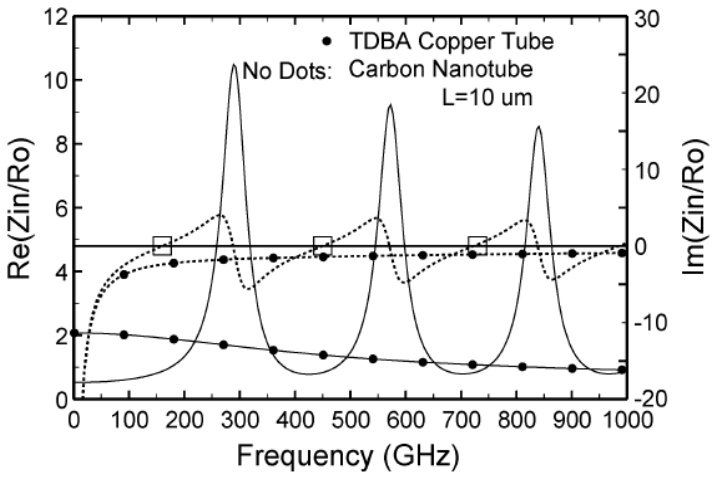

Figure 16: Input impedance for a carbon nanotube dipole antenna ($m = 40$) and for TDBA copper tube dipole having the same radius and length, $L = 10\mu m$. Solid lines are $\mathrm{Re}(Z_{in}/R_o)$ and dashed lines are $\mathrm{Im}(Z_{in}/R_o)$. Square boxes denote resonance frequencies and R_o is the channel resistance (quantum resistance, ≅12.9 kΩ) [13].

The difference between the velocity reduction obtained here $u_p \simeq 0.02c$ and the transmission line prediction $u_p \simeq 0.01c$ is most likely due to the approximate nature of the transmission line method, since the L and C values of the two-wire transmission line will only approximately hold for the corresponding dipole antenna. Furthermore, the transmission line model does not account for radiation, and does not fully account for tube resistance. Thus, the transmission-line model is expected to give valuable yet fairly approximate the actual antenna performance.

For the validation of the above statements, the same procedure has been followed for a carbon nanotube antenna with half-length of $L = 1\mu m$. Figure 17 shows the input impedance of the above antenna, comparing again with a similar one, using the TDBA copper tube with the same radius and length.

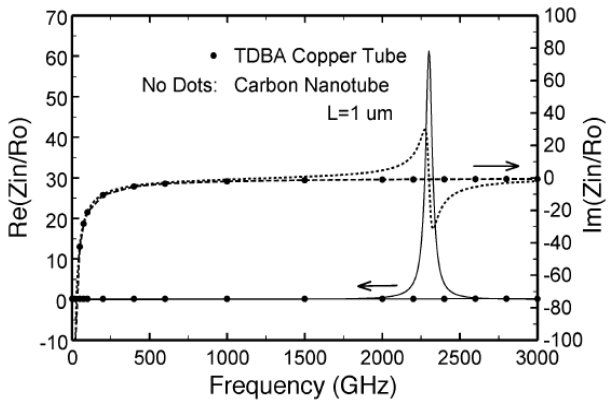

Figure 17: Input impedance for a carbon nanotube dipole antenna ($m = 40$) and for TDBA copper tube dipole having the same radius and length, $L = 1\mu m$. Solid lines are $\mathrm{Re}\left(Z_{in}/R_o\right)$ and dashed lines are $\mathrm{Im}\left(Z_{in}/R_o\right)$ [13].

As can be seen in the above figure, the resonance frequency for that carbon nanotube dipole antenna is around $2300GHz$. The expected resonance for the TDBA is $75THz$ so the ratio is $r = 0.03$.

2.7.2 The relaxation frequency damping effect

In general, resonances occur approximately in the frequency range of

$$\frac{v}{2\pi} \le f \le \frac{u_f}{2\pi\alpha} \tag{2.33}$$

which corresponds to $0.053 \le f \le 56THz$ when $v^{-1} = 3ps$ and $a = 2.712nm$. Outside of this frequency range, current is fully attenuated.

In Figure 18 the input impedance as a function of frequency for different lengths is shown. The effect of relaxation frequency damping on antenna resonances is also shown. We can observe that for an antenna which has half-length $L = 10\mu m$ it resonates around $150GHz$. For a $L = 20\mu m$ antenna, it resonates at around $85GHz$, which is approximately the predicted value $\left(u_p \simeq 0.02c\right)$. The $L = 40\mu m$ antenna is expected to resonate at around $40GHz$, but as figure 18 shows, that doesn't occur until a much higher frequency, which is $140GHz$. This is a result of all the

resonances below the relaxation frequency being suppressed due to relaxation frequency damping.

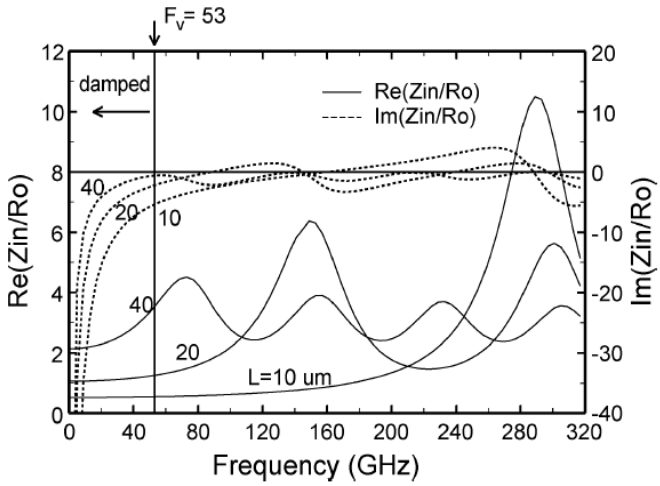

Figure 18: Input impedance versus frequency, for three different carbon nanotube dipole antennas. The effect of relaxation frequency damping on antenna resonances is clearly presented [13].

The following Figure 19, shows the current distribution on the $L = 10\mu m$ carbon nanotube dipole antenna at various frequencies. At very low frequencies, away from the resonance, the current distribution is approximately triangular, as for an ordinary short dipole. For frequencies close to the first resonance (160 GHz), it can be seen that the current is approximately half sinusoid. The current distribution is also shown at frequencies close to the first and second anti-resonance frequencies (292 GHz and 578 GHz).

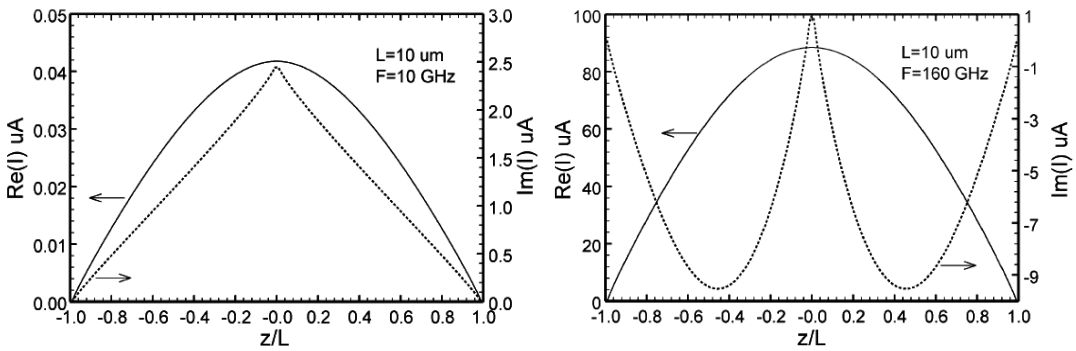

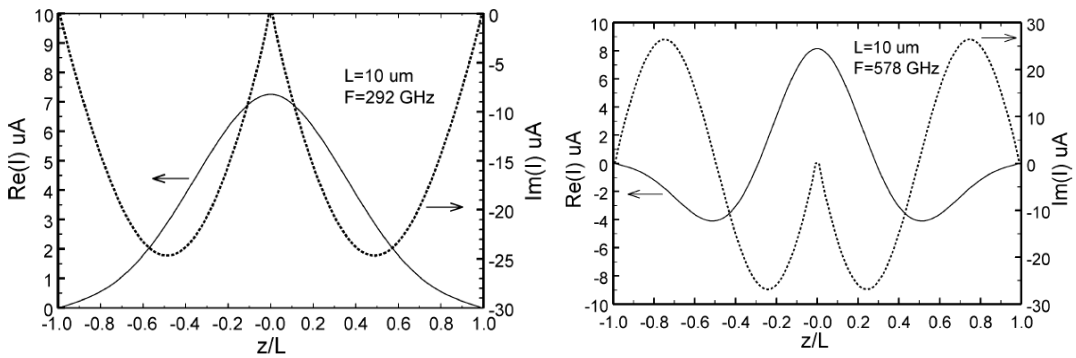

Figure 19: Current distribution on a carbon nanotube antenna with $m = 40$, radius $= 2.712nm$ and $L = 10\mu m$. Frequencies are shown on the graphs [13].

2.8 Summary

The fundamental properties of dipole transmitting antennas formed by carbon nanotubes have been investigated via a Hallén's-type integral equation. The equation is based on semiclassical conductivity, equivalent to a more rigorous quantum mechanical conductivity at the frequencies of interest. Input impedance and current distribution have been discussed, and comparisons have been made to a copper antenna of the same dimensions. It was shown that, due to the properties of the carbon nanotube conductivity function and its relationship to plasmon effects, some properties of the carbon nanotube antennas are quite different from the case of an infinitely thin copper antenna of the same size and shape. Important conclusions are that carbon nanotube antennas exhibit plasmon resonances above a sufficient frequency, with high input impedances which is probably beneficial for connecting to nanoelectronic circuits and very low efficiencies.

Chapter 3: Characterization of Vertically-Aligned Carbon Nanotube Films

3.1 Introduction

At the moment, two are the main available approaches that result to perfectly aligned carbon nanotubes: (a) the application of several post-synthesis techniques such as dispersing CNTs in solutions, followed by aligning them using spin-coating, Langmuir–Blodgett assembly, or blown bubble films technique, and then fixed the aligned CNT structures/patterns by solvent evaporation or resin solidification [79]; and (b) the in-situ growth approaches by growing aligned CNTs by controlled chemical vapor deposition (CVD) and arc discharge techniques [79].

The first work that initiated the further investigation of the in-situ growth of aligned CNTs was the fabrication of a very dense, forest-like aligned MWCNT array [80]. Since then several studies have been reported the growth of both SWCNT and MWCNT forests [81-87]. The most important innovation on this type of growth technique, was the water-assisted CVD growth which led to a very dense vertically aligned carbon nanotube (VACNT) forest [82]. Up to date, researchers tried to make very long CNT forests reaching eventually SWNT forest as long as 1 cm tall [82]. Other groups focused on the enlargement of the area that nanotubes occupying, obtaining SWNT forest with area up to A4 size (210 × 297 mm) [88].

In this study, vertically aligned multiwalled carbon nanotube (VACNT) films have been grown and characterized by rectangular waveguide measurements in X-band, Ku-band and low terahertz frequencies performing transmission terahertz time-domain spectroscopy technique (THz - TDS) [89, 90]. The complex scattering parameters (S-parameters) were measured in all frequency bands, via a vector network analyzer at X-band and Ku-band. The effective complex permittivity of the VACNT films have been extracted from 8 GHz to 2.5 THz and the effective complex permeability was extracted only in the microwave region as the reflection measurement was unable to be performed with the THz-TDS. The extracted parameters were verified by full wave simulations and very good agreement was obtained.

In the microwave region, the results of the systematic error analysis were presented and the errors were within the acceptable range. The performance of VACNT films as an absorber was examined, and comparison with the conventional carbon loaded materials showed a 90% size reduction is possible whilst maintaining the same absorption level.

Moreover, in the THz-TDS, six films with different CNT lengths were prepared and measured thus a time domain signal was obtained. The thickness of the samples varied, ranging from 21 μm to 252 μm. To find the frequency dependent complex permittivity of the above films, an FFT was performed on each signal thus the frequency dependent magnitudes and phases of the received signal were obtained. These transmission spectra were used to investigate the frequency dependent complex permittivity and conductivity, on the assumption that permeability $\mu=1$, of several samples. Finally, it was shown that the samples measured demonstrated Drude behaviour for lossy metals.

3.2 Carbon nanotube film geometry and fabrication process

Plasma Enhanced Chemical Vapor Deposition (PECVD) is an excellent alternative for depositing a variety of thin films at lower temperatures compared to those of CVD reactors. For example, high quality silicon dioxide films can be deposited at 300°C to

$350^{o}C$ compared to CVD which requires temperatures in the range of 650 to 850 degrees centigrade to produce similar quality films.

All the samples of the vertically aligned multi-walled carbon nanotube films were fabricated at the Center for Advance Photonics and Electronics at Cambridge University (CAPE). They are based on an n-type doped single crystal silicon wafer, with dimensions of 42mm x 50mm. Fe catalyst and Al diffusion barrier thin films were deposited onto silicon substrates by sputter coating, to prevent the formation of $FeSi_x$. The thickness of the silicon wafer is 510μm and the resistivity is expected to be 0.015-0.025 $Ohm \cdot cm$. Upon annealing with H_2 for 3mins, the Fe thin film breaks up into nanoparticles which seed the further growth of the nanotubes.

PECVD uses electrical energy to generate plasma to which the energy is transferred into a gas mixture. This transforms the gas mixture into reactive radicals, ions, neutral atoms and molecules, and other highly excited species. These atomic and molecular fragments interact with the silicon substrate and depending on the nature of these interactions, two processes, either etching or deposition processes, occur at the substrate. Since the formation of the reactive and energetic species in the gas phase occurs by collision, the substrate can be maintained at a low temperature. Hence, film formation can occur on substrates at a lower temperature than that possible in the conventional CVD process. This is a major advantage of PECVD.

The nanotubes were grown in a bell jar vacuum chamber with a residual pressure of 10 mbar. Growth was initiated immediately by introducing C_2H_2 into the chamber and applying direct current (DC) glow discharge. By applying different growth times 20s, 40s, 60s, 90s, 2mins and 5mins, six different nanotube samples with lengths of 21μm, 30μm, 35μm, 70μm, 121μm and 252μm respectively, were obtained.

3.3 X-band measurement

As mentioned previously, the scientific applications involving the use of CNTs, in theory, provide a range of solutions to existing problems. Examples are field emission displays, hydrogen-powered vehicles, artificial muscles, fuel cells and batteries [2,

11, 12]. Recently, many microwave applications have been suggested, including nano-sized antennas and nano-interconnects [13, 14].

Although extensive studies have been conducted on CNTs at DC and low frequencies, the electrical properties of CNTs, particularly of MWNTs have yet to be the subject of a comprehensive study at microwave frequencies. In this current study, vertically aligned MWNT films (VACNT) were characterized at X-band by rectangular waveguide measurements [89]. This method enables the accurate extraction of the effective material parameters from the measured S-parameters. The main difference of the current study versus previous studies is the use of highly vertically aligned nanotubes to the substrate (Figure 20). In addition, all the S-parameters (amplitude and phase) were measured, thus allowing both permittivity and permeability to be extracted. It was also shown that VACNT films are superior absorbers in the X-band frequency range, compared to conventional materials.

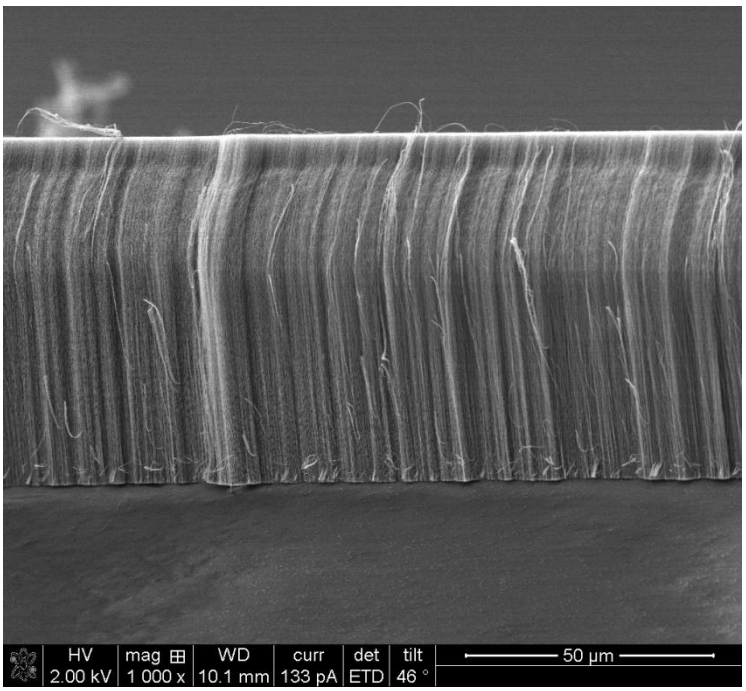

Figure 20: SEM image from the vertically aligned CNT film [89].

3.3.1 Experimental setup and method of extraction

The transmission/reflection line technique was used to obtain the properties of the VACNT films (Figure 21). The samples, which were treated as an effective medium with a known thickness, were placed in a section of a waveguide following

calibration. The VNA was used to measure both complex S-parameters, thus allowing both ε and μ to be solved in terms of the S-parameters.

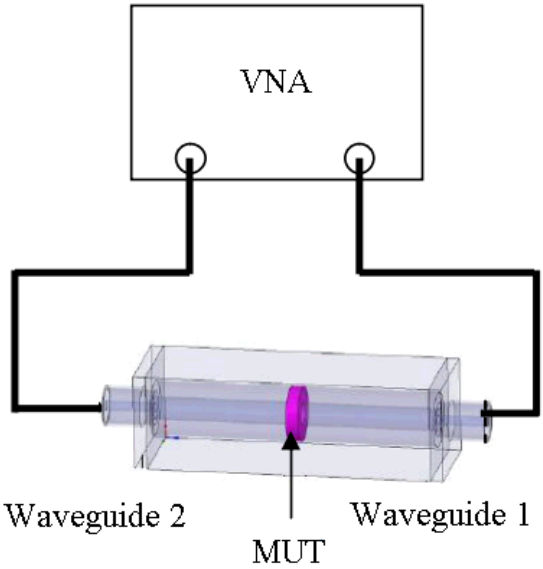

Figure 21: Measurement using Transmission/Reflection method with a waveguide [63].

The samples that have been measured were varying in thickness from 30 μm to 252 μm. The three samples have been measured several times to demonstrate good repeatability. To extract the effective complex permittivity and permeability of the VACNT films, the Nicolson–Ross–Weir approach [91-93] was applied to the measured S-parameters for a given thickness. An algorithm was developed based on that approach.

For a VACNT film with a thickness d, the transmission and reflection coefficients at the air-film interfaces can be obtained from the S-parameters. The S-parameters through the material, referenced to the air-film interfaces, are described by [94]

$$S_{21} = \frac{\left(1-\Gamma^2\right)z}{1-\Gamma^2 z^2} \tag{3.1}$$

$$S_{11} = \frac{\left(1-z^2\right)\Gamma}{1-\Gamma^2 z^2} \tag{3.2}$$

where z and Γ are the transmission and reflection coefficients at the interface, respectively. According to the theory, the transmission coefficient inside the slab is given by

$$z = e^{-\gamma d} \tag{3.3}$$

and the reflection coefficient

$$\Gamma = \frac{\mu\gamma_o - \gamma}{\mu\gamma_o + \gamma} \tag{3.4}$$

where $\gamma_o = \sqrt{k_c^2 - k_o^2}$ and $\gamma = \sqrt{k_c^2 - \mu\varepsilon k_o^2}$ are the propagation constants in the two waveguides filled with free space and the sample respectively. The cut off wave number is given by $k_c = \pi/\alpha$ where $\alpha = 22.86mm$ is the longer dimension of the rectangular waveguide cross-section at X-band.

There is an ambiguity that needs to be clarified once the propagation constant γ is solved in terms of the transmission coefficient, caused by the function $\ln(1/z)$ which has infinite number of solutions when z is complex. The propagation constant can be written as [94]

$$\gamma = \frac{\ln\left|\frac{1}{z}\right| + j\left[\arg\left(\frac{1}{z}\right) + 2m\pi\right]}{d} \tag{3.5}$$

where m is any integer. Equation (3.5) is a continuous function, thus a different value of the branch index m may be required. Once γ is derived, then (3.4) gives the permeability of the VACNT sample

$$\mu = \frac{\gamma(\Gamma + 1)}{\gamma_o(1 - \Gamma)} \tag{3.6}$$

and substituting that into the propagation constant, the permittivity of the sample is calculated

$$\varepsilon = \frac{k_c^2 - \gamma^2}{\mu k_o^2} \tag{3.7}$$

3.3.2 Parameter extraction

The extracted material parameters for all the VACNT films are presented below. To verify the algorithm that has been implemented based on the NRW approach, a CST model was set up comprising of a slab with the thickness of each sample and the complex parameters were extracted from the above material. The slab is placed between two waveguides. A systematic error analysis was also performed. Finally, the absorbing performance of VACNT films were examined and compared to conventional materials.

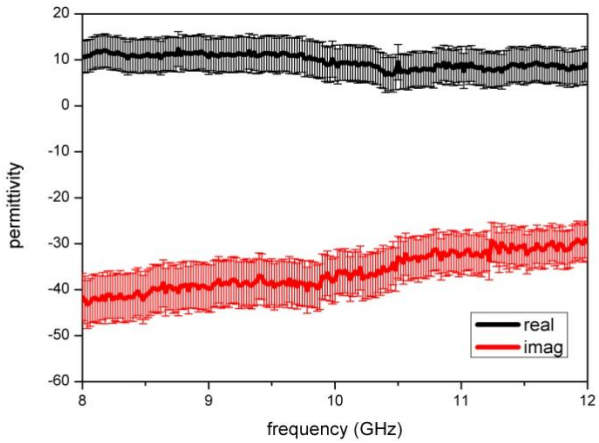

(a)

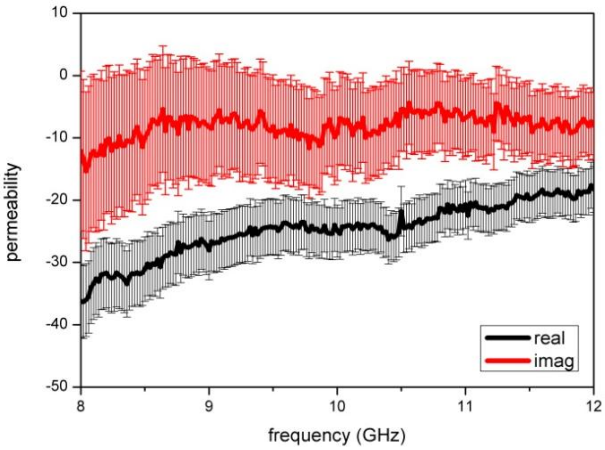

(b)

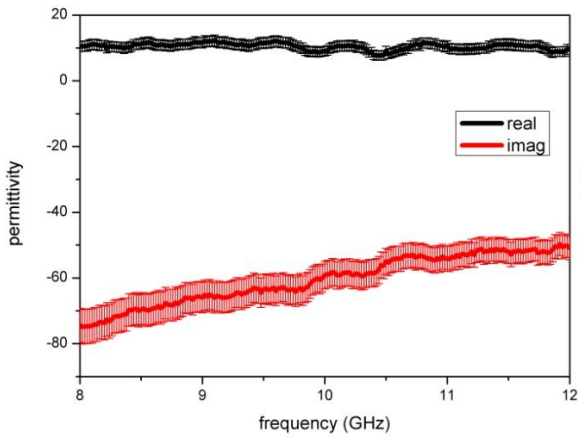

(c)

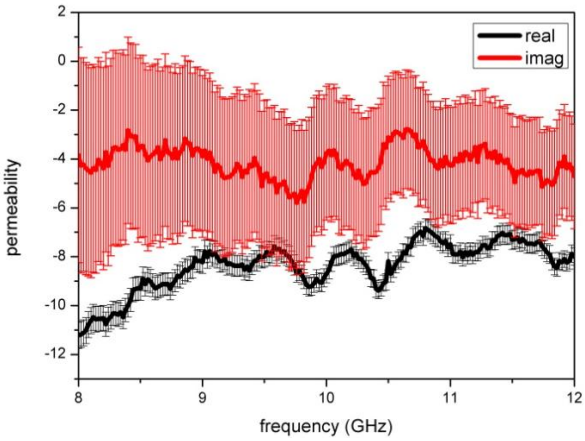

(d)

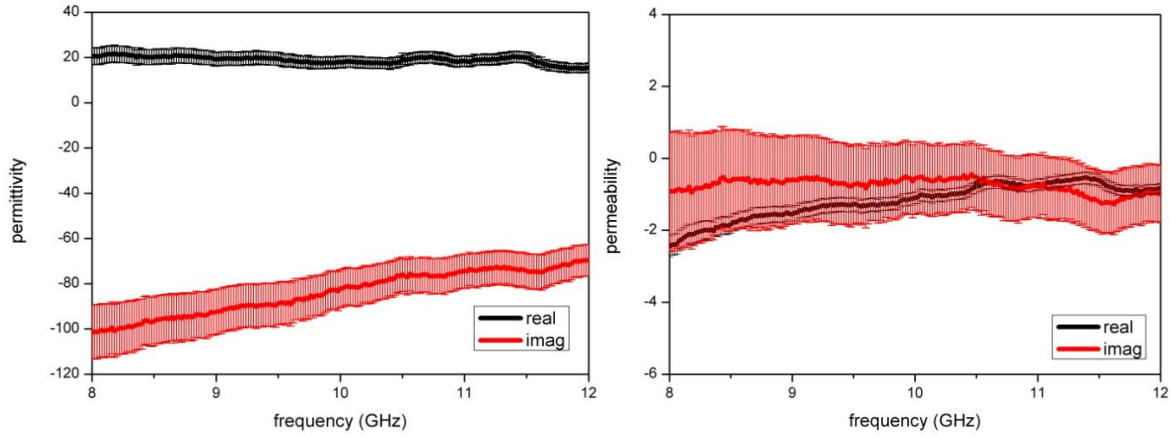

(e) (f)

Figure 22: Effective medium extracted parameters of the VACNT film. a-b) 30 μm c-d) 95 μm e-f) 252 μm.

The extracted complex permittivity $\left(\varepsilon = \varepsilon' - j\varepsilon''\right)$ and permeability $\left(\mu = \mu' - j\mu''\right)$ of each sample are plotted in Figure 22.

A rigorous error analysis [95] based on the uncertainties that have been introduced by the VNA is performed. The uncertainties of the magnitudes and phases of both S_{11} and S_{21} are presented in Table 2. The systematic errors of ε' are calculated by:

$$\Delta\varepsilon' = \sqrt{\left(g_1 \Delta S_{11}^{mag}\right)^2 + \left(g_2 \Delta S_{11}^{ang}\right)^2 + \left(g_3 \Delta S_{21}^{mag}\right)^2 + \left(g_4 \Delta S_{21}^{ang}\right)^2} \tag{3.8}$$

where g_1, g_2, g_3, g_4 are the partial derivatives calculated numerically by:

$$g_1 = \frac{\partial\varepsilon'}{\partial S_{11}^{mag}} = \frac{\varepsilon'\left(S_{11}^{mag} + \delta\right) - \varepsilon'\left(S_{11}^{mag}\right)}{\delta} \tag{3.9}$$

$$g_2 = \frac{\partial\varepsilon'}{\partial S_{11}^{ang}} = \frac{\varepsilon'\left(S_{11}^{ang} + \delta\right) - \varepsilon'\left(S_{11}^{ang}\right)}{\delta} \tag{3.10}$$

$$g_3 = \frac{\partial\varepsilon'}{\partial S_{21}^{mag}} = \frac{\varepsilon'\left(S_{21}^{mag} + \delta\right) - \varepsilon'\left(S_{21}^{mag}\right)}{\delta} \tag{3.11}$$

$$g_4 = \frac{\partial\varepsilon'}{\partial S_{21}^{ang}} = \frac{\varepsilon'\left(S_{21}^{ang} + \delta\right) - \varepsilon'\left(S_{21}^{ang}\right)}{\delta} \tag{3.12}$$

where δ represents a very small change in S_{11}^{mag}, here chosen to be 0.0001. Similarly, the above procedure is repeated for the calculation of $\Delta\varepsilon''$, $\Delta\mu'$ and $\Delta\mu''$ after appropriate re-writing (3.8)-(3.12).

Table 2: VNA uncertainties.

Thickness µm	S_{11}^{mag}	S_{11}^{ang} **deg**	S_{21}^{mag}	S_{21}^{ang} **deg**
30	0.037	0.49	0.012	0.08
95	0.035	0.45	0.015	0.09
252	0.026	0.29	0.028	0.14

Table 3, shows the mean values of the errors for the four material parameters.

Table 3: Average systematic errors of material parameters.

Thickness µm	ε'	ε''	μ'	μ''
30	3.8	4.76	4.36	7.95
95	1.55	4.26	0.41	2.9
252	2.73	8.88	0.18	1.08

The calculated error for the ε', ε'' and μ' is in the region of 15%, 10% and 15% respectively. The error introduced in the μ'' is relatively high and it is due to the sensitivity of the phase measurement. The uncertainties introduced by the VNA (Table 2) are well above the safe margin, thus the average systematic error is the maximum possible.

The extracted parameters plotted in Figure 22 are summarised in the figure below.

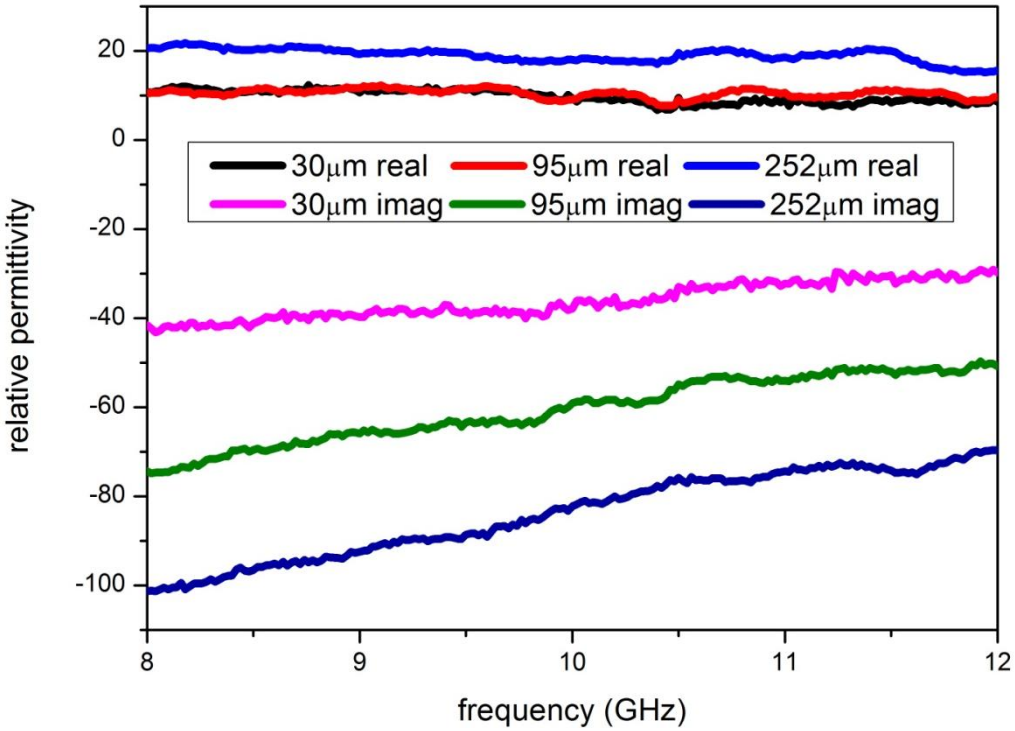

Figure 23: Effective medium extracted relative permittivity of all the VACNT films.

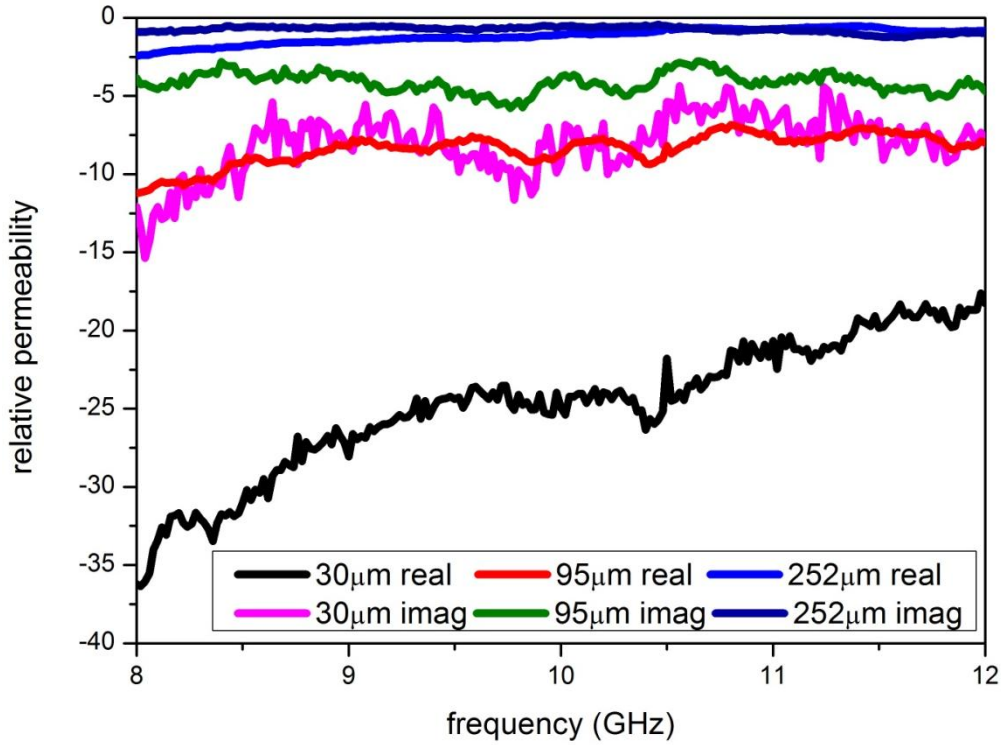

Figure 24: Effective medium extracted relative permeability of all the VACNT films.

It is expected that the corresponding permittivity and permeability of any homogeneous medium, such as the VACNT films, is independent of the thickness.

The three different samples of VACNT films have been grown in a similar fashion but they are not identical to each other. It appears that they exhibit discrepancies arising from non-controlled, geometrical uncertainties in parameters such as air-gaps with neighboring nanotubes, concentrations of CNTs and concentrations of the Fe catalyst, resulting in moderately distinct effective media in all three samples. It is also understood that lengthening nanotubes, create entanglements with adjacent ones, directly proportional to the resulting length. The aforementioned in addition to the measurement uncertainties of the S-parameters and thickness, lead to a much different value of effective permittivity and permeability in each sample as demonstrated in Figure 23 and Figure 24.

Moreover, the real part of permeability function, in all the three cases, takes negative values. The samples that have been measured with the method explained in Figure 21 are very thin in respect to the wavelength. Therefore, the phase measurement of the scattering parameters becomes very sensitive and only the amplitude is considered to be accurate. That appears to affect the real part of the permeability function, resulting in negative values. The average systematic error shown in Table 3 is relatively large, implying the conclusion given above.

The conductivity has been calculated from the imaginary part of the permittivity using the equation $\sigma = \varepsilon'' \varepsilon_o \omega$ and it is plotted in Figure 25.

To verify the algorithm implemented based on the NRW approach, a CST-Microwave Studio model was set up comprising of a slab with the corresponding thickness of the sample and the complex parameters extracted from the above material. The slab was placed between two waveguides. The simulation results are plotted alongside the experimental in Figure 26.

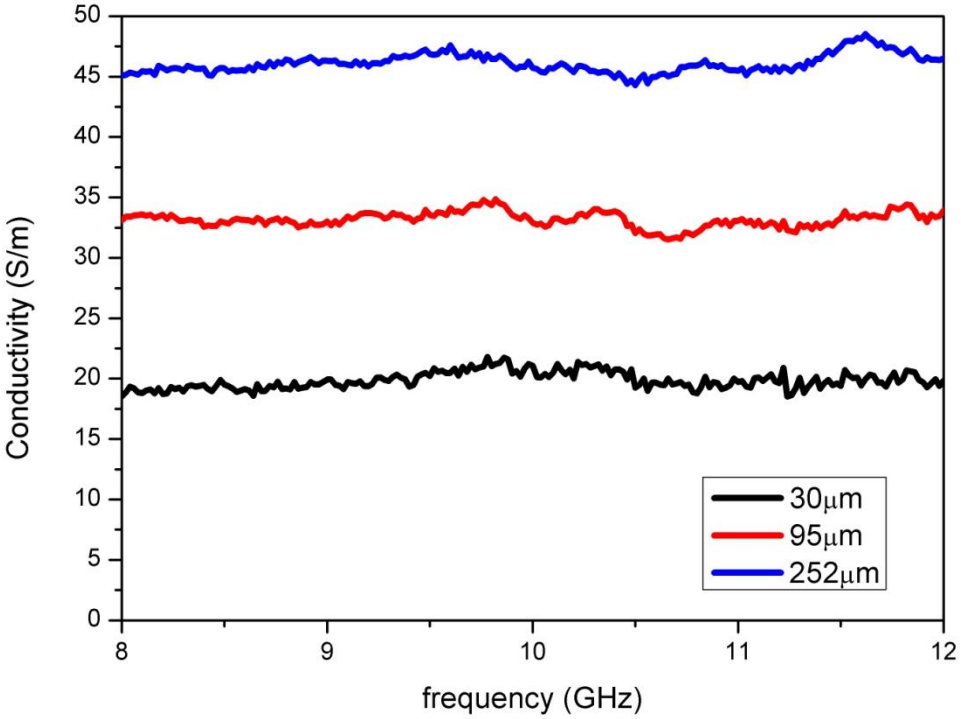

Figure 25: Effective medium extracted conductivity of all the VACNT films.

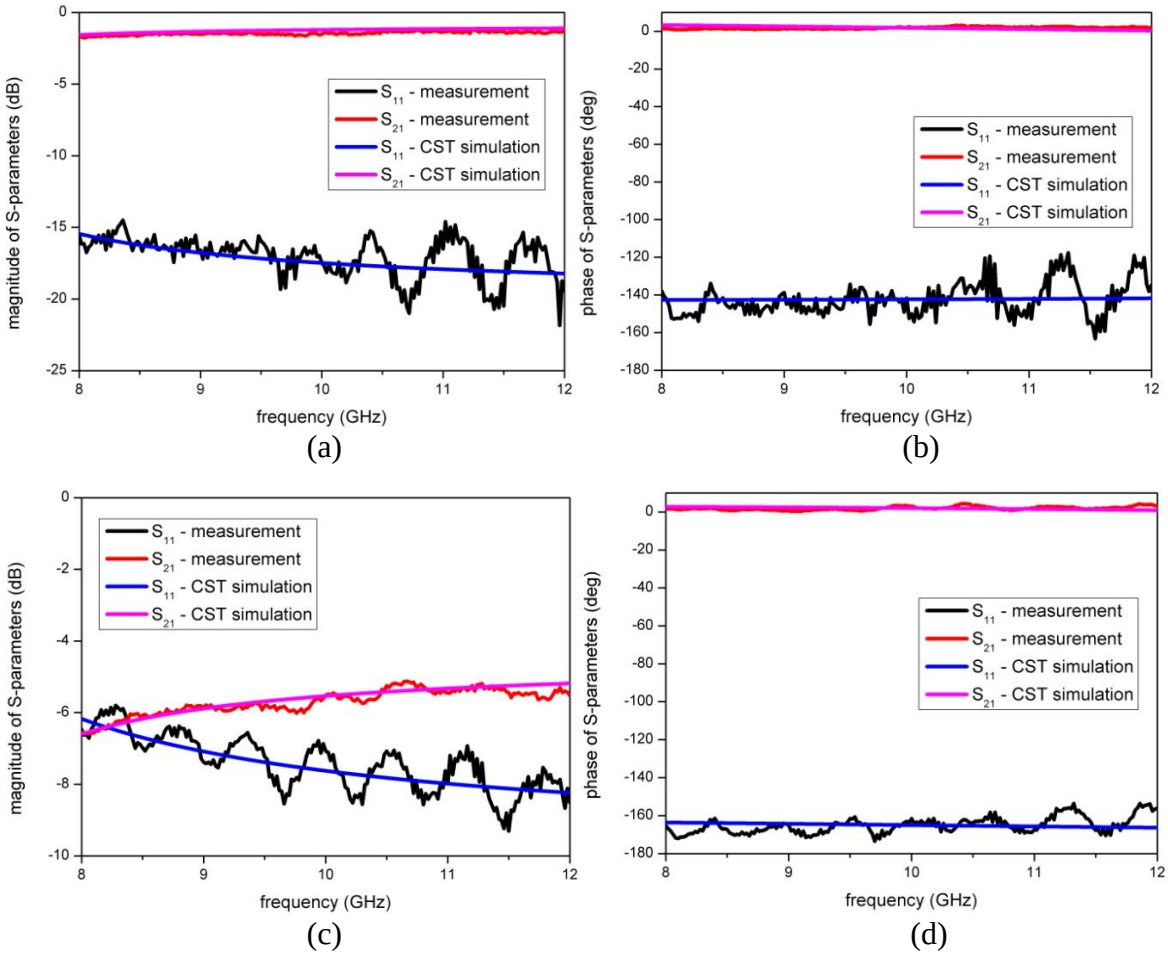

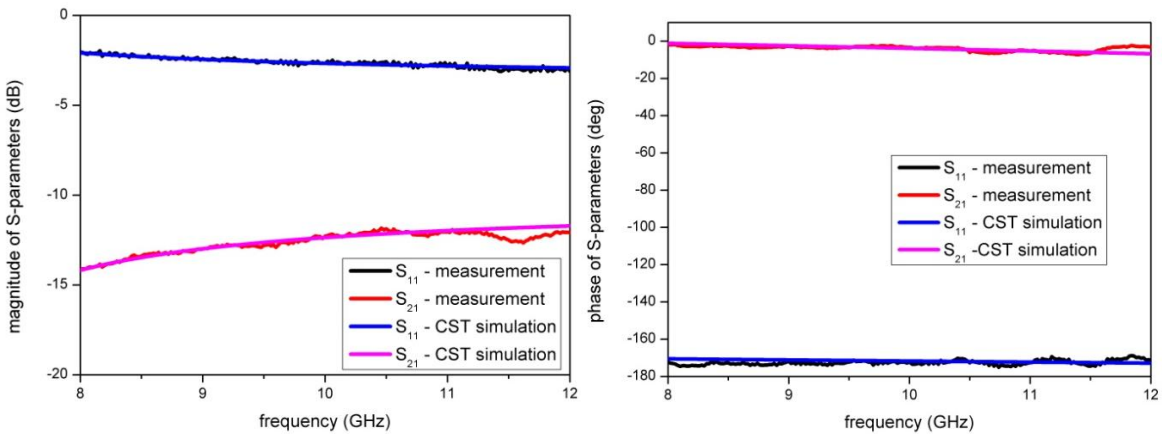

(e) (f)

Figure 26: Simulated and measured reflection and transmission coefficients of the VACNT films. a-b) 30 μm c-d) 95 μm e-f) 252 μm.

Recently it has been reported that CNT films can be highly absorbent of visible light [96] and apart from visible range, enhanced absorption can be observed over a broadband frequency [97]. The absorbing performance of the VACNT films in X-band is examined below. Figure 27 shows the absorption coefficient across the frequency band. The absorption of the VACNT films does not increase as the thickness increases, instead it appears to be a maximum of absorption at 95 μm. The number of samples presented here is not sufficient to identify the optimum thickness of the VACNT film where maximum absorption can be achieved, but they reveal the trend of the absorption curve against the thickness. Rozanov [98] has shown that if a metal-backed absorber is illuminated under normal incident, the thickness of that absorber in X-band frequencies has to be:

$$d \geq \frac{\left| \int_0^{\infty} \ln\left|R(\lambda)\right| d\lambda \right|}{2\pi^2} \tag{3.13}$$

where $R(\lambda)$ is the distribution of the reflection coefficient.

Equation (3.13) provides a very useful dependence of the minimum thickness of a conventional non-magnetic absorber with the frequency response (or wavelength). An approximation, similar to the Bode plots used in filter theory, of that frequency response, is considered to be correct and can be applied here, with the only difference

that frequency is not in logarithmic scale. Therefore, the reflection coefficient, can be expressed as a function of frequency (or wavelength) as:

$$R(f)=\begin{cases} -R_o\left(\dfrac{f-f_1}{f_2-f_1}\right) & f_1 \le f \le f_2 \\ -R_o & f_2 \le f \le f_3 \\ R_o\left(\dfrac{f-f_4}{f_4-f_3}\right) & f_3 \le f \le f_4 \\ 0 & otherwise \end{cases} \tag{3.14}$$

where for X-band the frequencies are set as: $f_1 = 6GHz$, $f_2 = 8GHz$, $f_3 = 12GHz$ and $f_4 = 16GHz$.

Solving equation (3.13) for the frequencies over which the measurement has been performed and for the sample that maximum absorption has been measured, 95 μm, the minimum possible thickness of a conventional absorber is $d = 1.1mm$. Therefore, a 90% reduction in size has been achieved compared to conventional absorbers, maintaining the absorption shown in Figure 27.

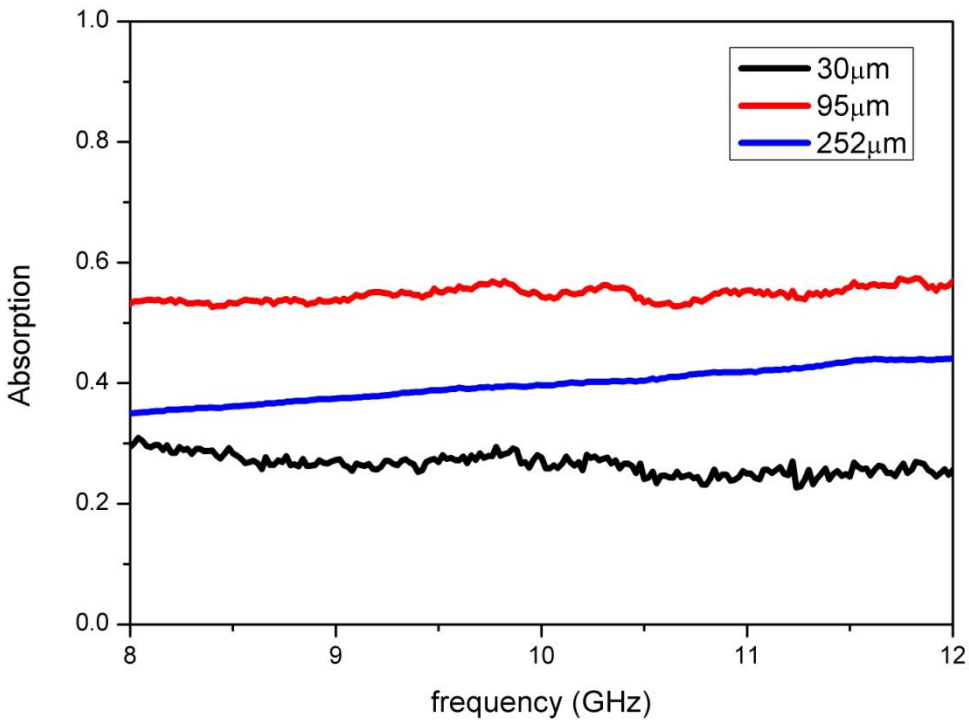

Figure 27: Measured absorption of the VACNT films.

3.4 Ku-band measurement

As it was mentioned before, the electrical properties of CNTs, particularly of MWNTs have yet to be the subject of a comprehensive study at microwave frequencies. In this section, the measurement results of the Ku-band (12.4 GHz - 18 GHz) of the vertically aligned multiwalled carbon nanotube films are presented and the samples are characterized over the whole band.

The method used in this instance, is the same as the one used for the X-band extraction. It enables the accurate extraction of the effective material parameters from the measured S-parameters. Again, all the S-parameters (amplitude and phase) were measured, thus allowing both permittivity and permeability to be extracted. It was also shown that VACNT films are superior absorbers in the Ku-band frequency range, as well as X-band, compared to conventional materials.

The samples were treated as an effective medium with a known thickness and placed in a section of a waveguide following calibration. The VNA was used to measure both complex S-parameters, thus allowing both permittivity ε and permeability μ to be solved in terms of the S-parameters.

The samples measured in this frequency band varied in thickness from 30 μm to 252 μm. Four different samples with CNT length of 30 μm, 70 μm, 95 μm and 252 μm, and they were all measured several times to demonstrate good repeatability. To extract the effective complex permittivity and permeability of the VACNT films, the Nicolson–Ross–Weir approach [91-93] was applied to the measured S-parameters for a given thickness. The algorithm used previously incorporating equations (3.1)-(3.7), has now been modified enabling the accurate extraction of the parameters in that frequency band. Specifically, the change made to the procedure described above, was in equation (3.4) involving the propagation constants in the two waveguides, filled with free space and the sample, given by $\gamma_o = \sqrt{k_c^2 - k_o^2}$ and $\gamma = \sqrt{k_c^2 - \mu\varepsilon k_o^2}$ respectively. The cut off wave number is given by $k_c = \pi/\alpha$ where α is now equal with $\alpha = 15.8mm$ which is the longest dimension of the rectangular waveguide cross-section at Ku-band.

The extracted material parameters are presented below for all the four different VACNT films. To verify the algorithm implemented based on the NRW approach, a similar CST model with the X-band case has set up, which comprises of a slab with the thickness of each sample and the complex parameters extracted from the above material. The slab was placed between two waveguides. A systematic error analysis was also performed. Finally, the absorbing performance of VACNT films was examined and compared to conventional materials.

The extracted complex permittivity $(\varepsilon = \varepsilon' - j\varepsilon'')$ and permeability $(\mu = \mu' - j\mu'')$ of each sample are plotted in Figure 28.

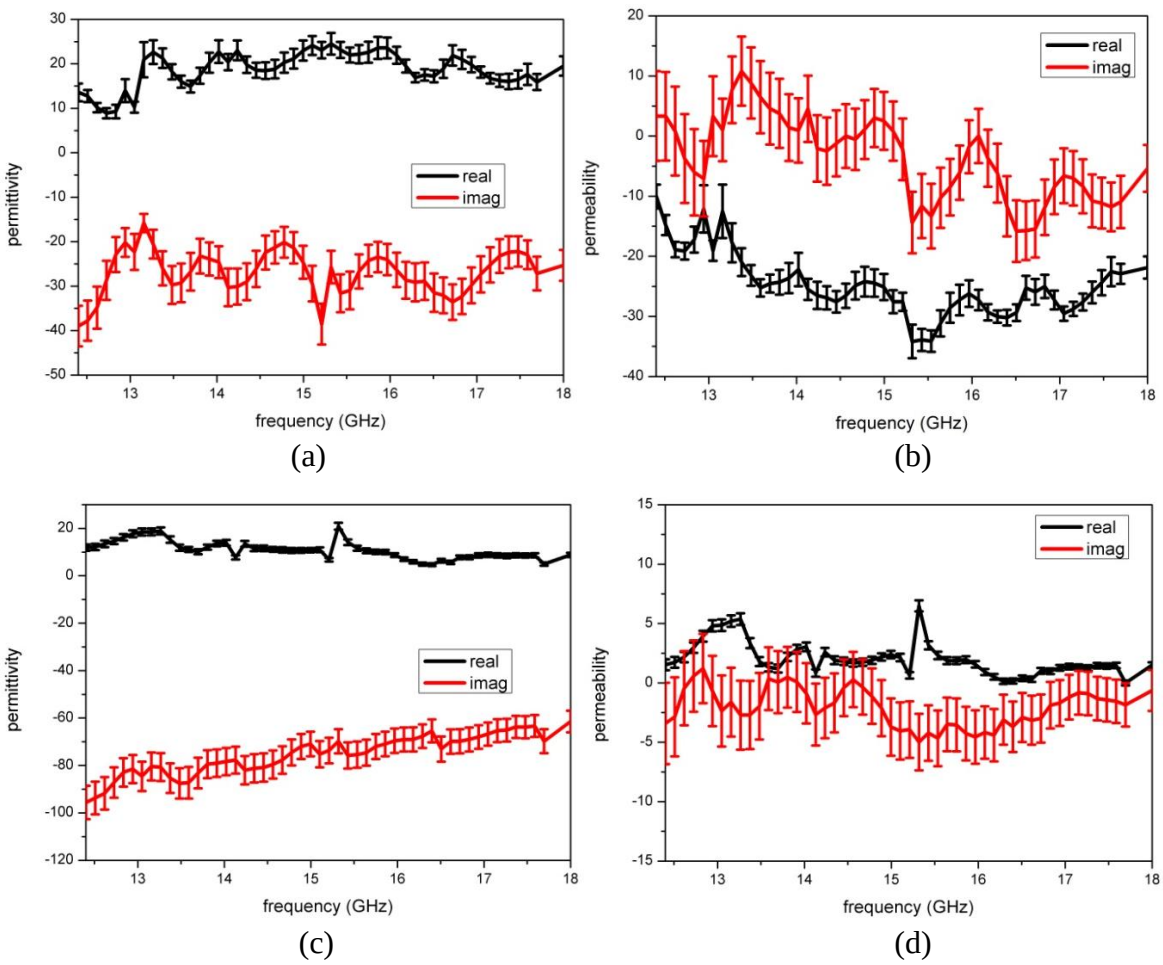

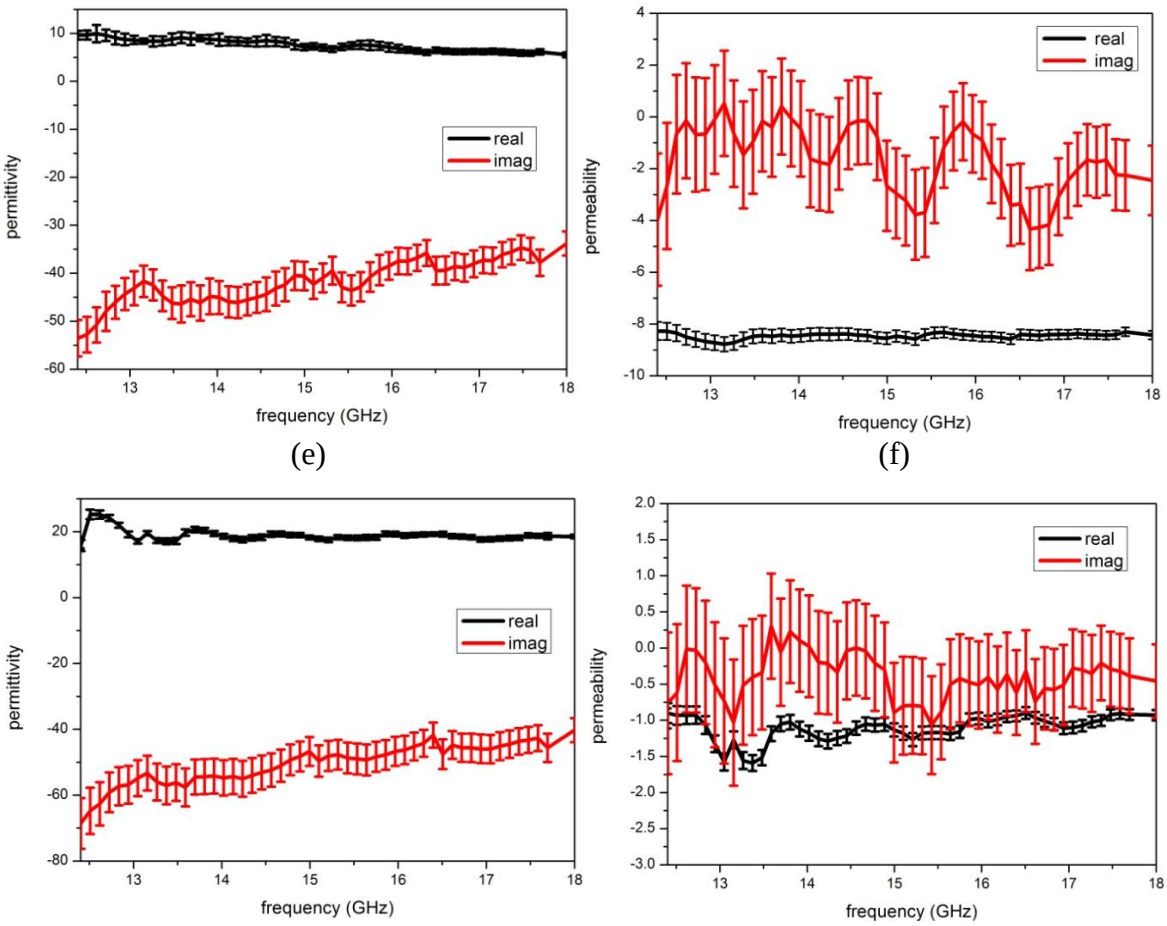

(e) (f)

(g) (h)

Figure 28: Effective medium extracted parameters of the VACNT film. a-b) 30 µm c-d) 70 µm e-f) 95 µm g-h) 252 µm.

A rigorous error analysis based on the uncertainties that have been introduced by the VNA [95] has performed as explained in equations (3.8)-(3.12). The uncertainties of the magnitudes and phases of both S_{11} and S_{21} are presented in Table 4.

Table 4: VNA uncertainties.

Thickness µm	S_{11}^{mag}	S_{11}^{ang} **deg**	S_{21}^{mag}	S_{21}^{ang} **deg**
30	0.035	0.47	0.018	0.06
70	0.033	0.46	0.019	0.08
95	0.033	0.42	0.018	0.12
252	0.027	0.29	0.027	0.14

Table 5, shows the mean values of the errors for the four material parameters.

Table 5: Average systematic errors of material parameters.

Thickness µm	ε'	ε''	μ'	μ''
30	1.91	3.9	2	5.33
70	1.05	5.58	0.32	2.42
95	0.82	3.15	0.23	1.76
252	0.79	4.96	0.09	0.68

The calculated error for the ε', ε'' and μ' is approximately 12%, 9% and 14% respectively. The error introduced in the μ'' is relatively high and it is also attributed to the sensitivity of the phase measurement. The real part of the permeability, μ', in most of the cases, takes negative values. That happens, for the same reason as explained in the previous section, in the X-band case, where the very thin size of the samples, affect the phase measurement of the S-parameters and therefore the permeability function. The uncertainties introduced by the VNA (Table 4) are well above the safe margin, thus the average systematic error is the maximum possible.

The extracted parameters plotted in Figure 28 are summarized in the figure below. For reasons of clarity, real and imaginary part of the permeability are plotted separately.

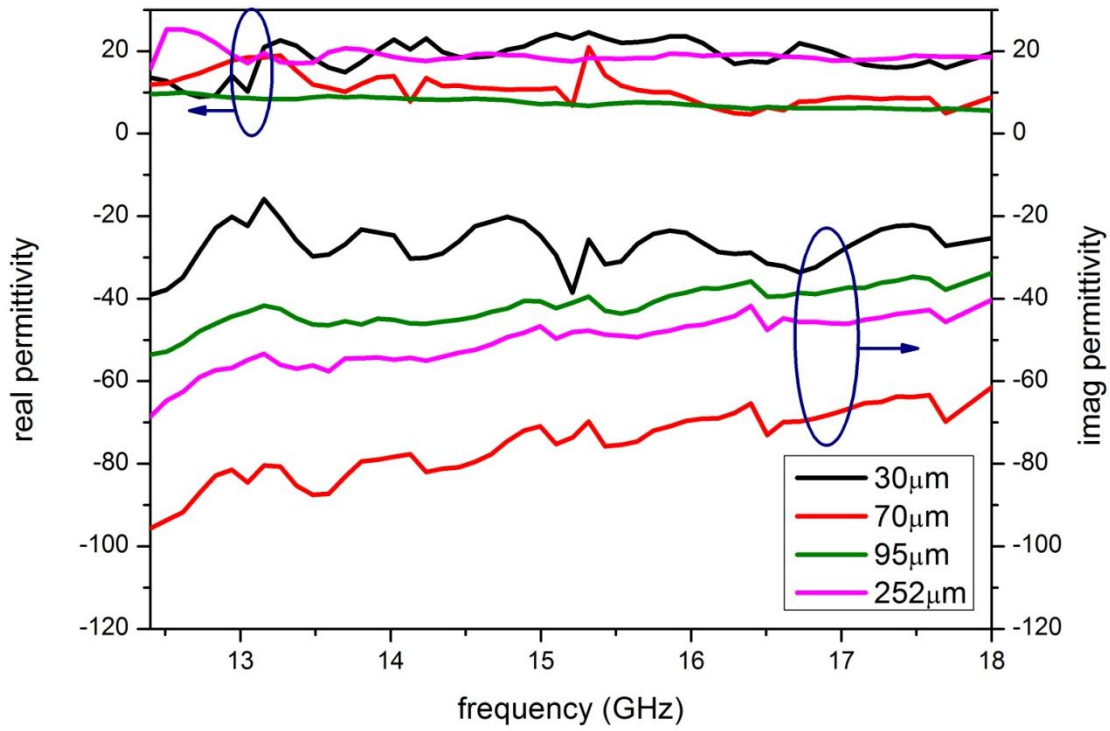

Figure 29: Effective medium extracted permittivity of all the VACNT films.

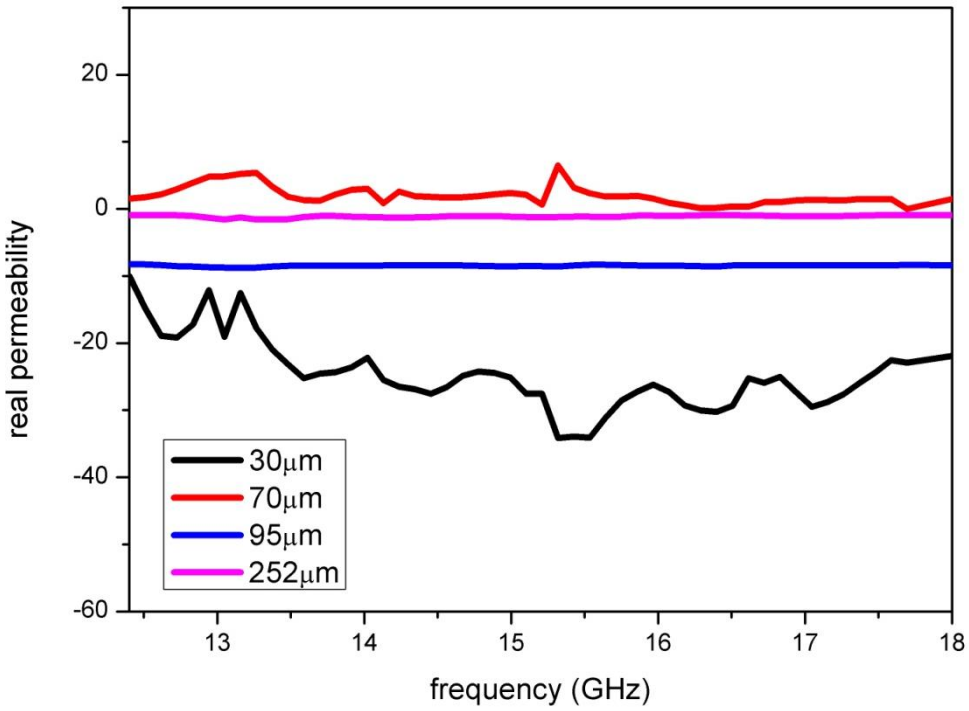

Figure 30: Effective medium extracted real permeability of all the VACNT films.

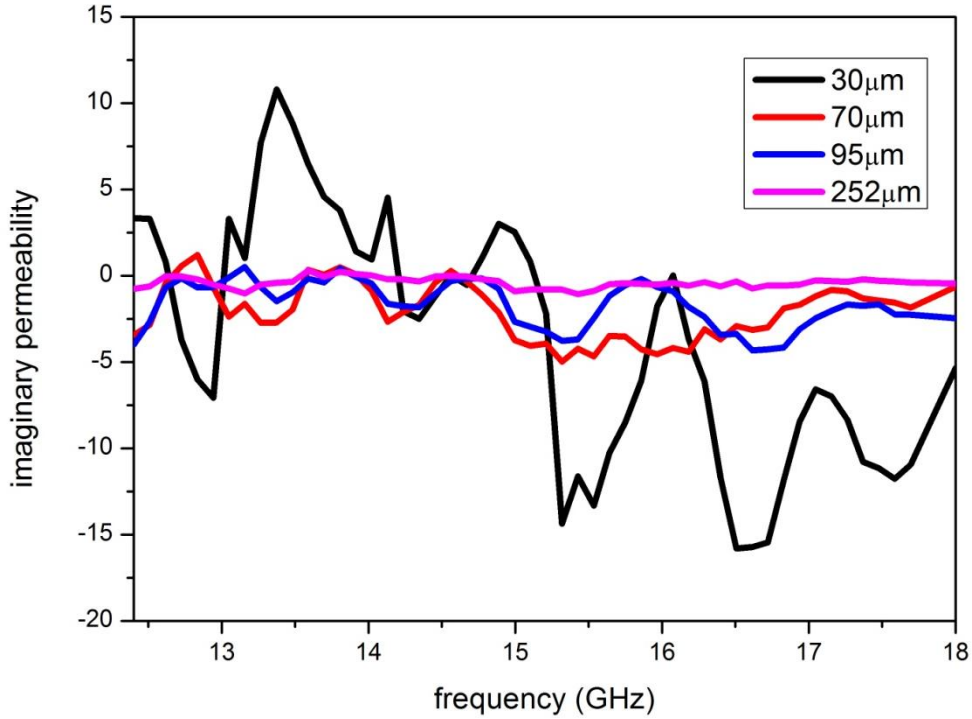

Figure 31: Effective medium extracted imaginary permeability of all the VACNT films.

The conductivity was calculated from the imaginary part of the permittivity using the equation $\sigma = \varepsilon'' \varepsilon_o \omega$, plotted in Figure 32. As it is explained before, although the samples have been grown in a similar way, they are not identical to each other. Some parameters, such as the density of the CNT forest, is not possible to be controlled, therefore, the 70μm thick sample, may have smaller inter-tube distance and exhibit higher conductivity.

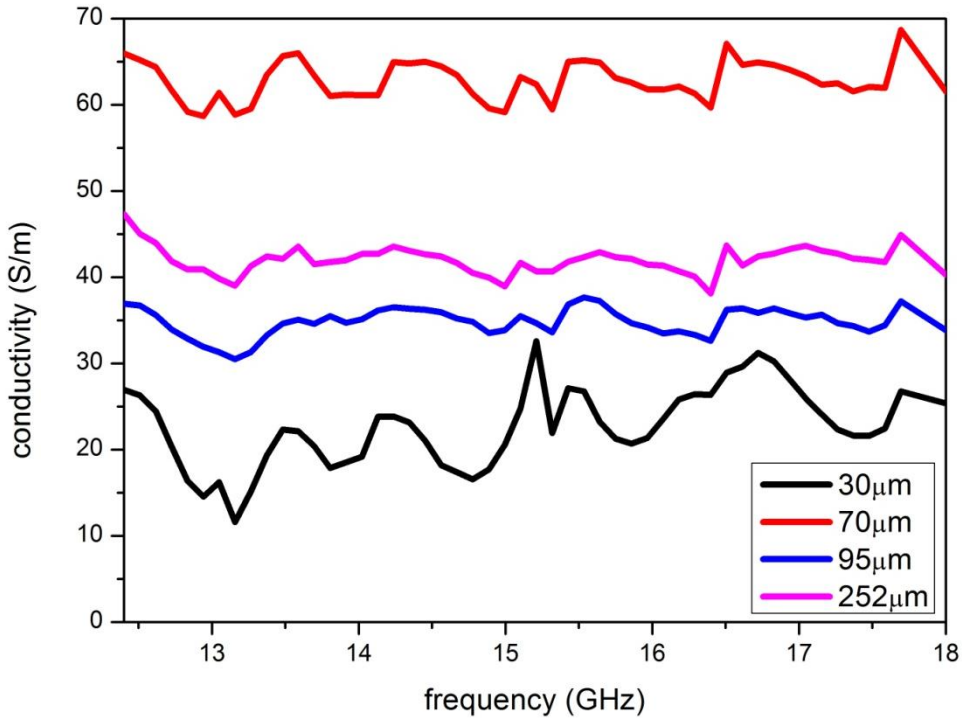

Figure 32: Effective medium extracted conductivity of all the VACNT films.

To verify the algorithm implemented based on the NRW approach, a CST-Microwave Studio model was set up similarly to the one for X-band frequencies. The model was made up of a slab with the thickness of the sample and the complex parameters extracted from the above material. The slab was placed between two waveguides. The simulation results are plotted together with the experimental ones Figure 33.

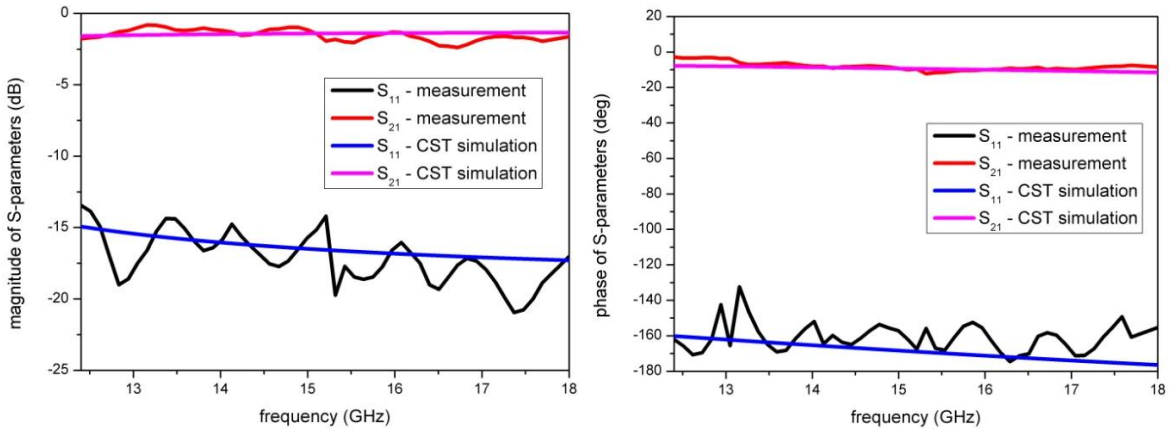

(a) (b)

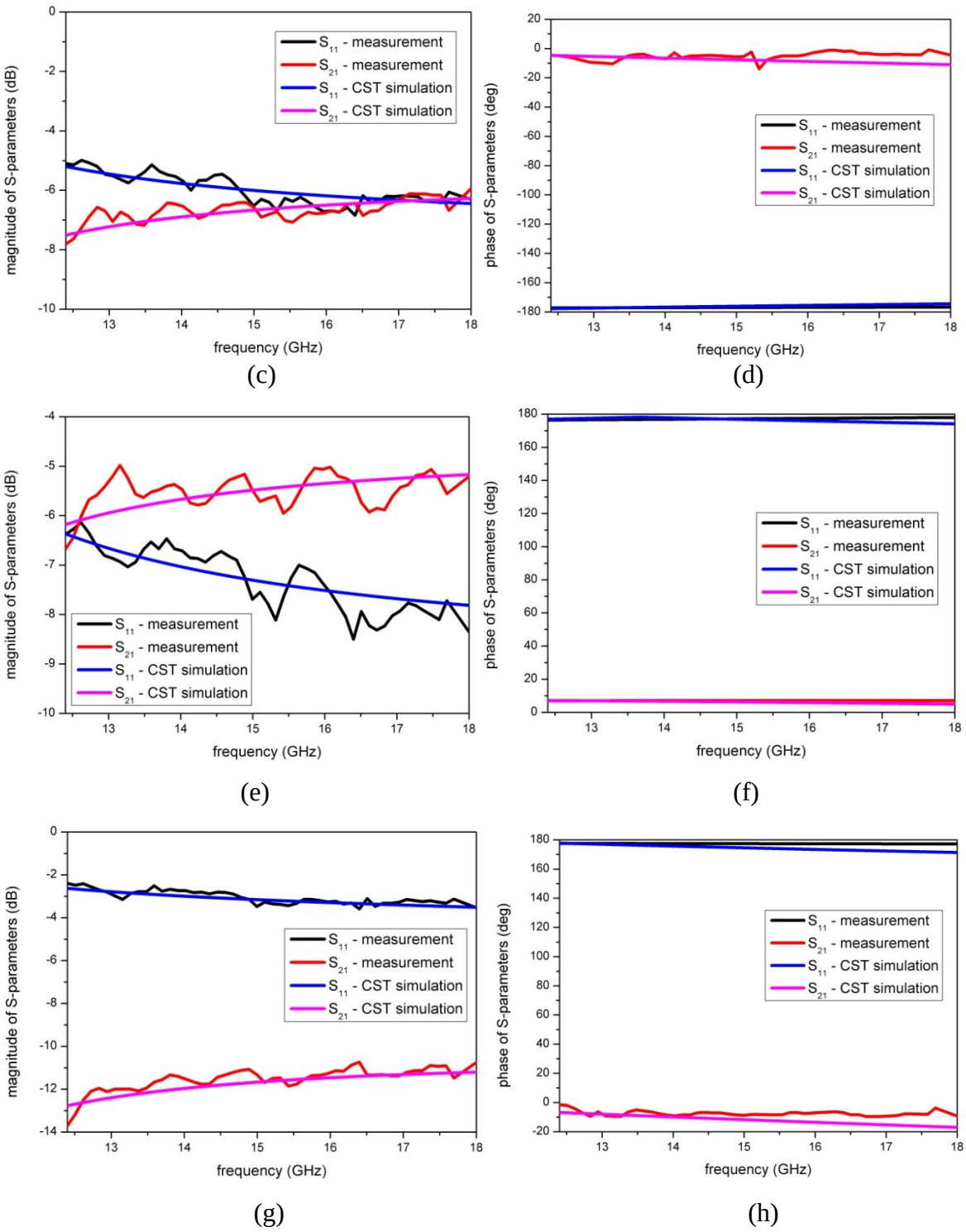

Figure 33: Simulated and measured reflection and transmission coefficients of the VACNT films. a-b) 30 µm c-d) 70 µm e-f) 95 µm g-h) 252 µm.

Again it appears that the absorption of the VACNT films does not increase as the thickness increases, instead, it appears to have a maximum of absorption at 70 µm. The number of samples presented here is not sufficient to identify the optimum

thickness needed for the VACNT film to achieve maximum absorption but the trend of the absorption curve is revealed against the thickness. From Rozanov's equation [98], (3.15), a metal-backed absorber when illuminated under normal incident, has to have a thickness in Ku-band frequencies of

$$d \geq \frac{\left| \int_0^\infty \ln\left|R(\lambda)\right| d\lambda \right|}{2\pi^2} \tag{3.15}$$

where $R(\lambda)$ is the distribution of the reflection coefficient.

Solving (3.15) for the frequencies over which the measurement was performed and for the maximum absorption achieved, the minimum possible thickness of a conventional absorber is $d = 640\mu m$. However, using the VACNT film, 70 μm can absorb exactly the same amount of electromagnetic waves. Therefore, again a 90% reduction in size was achieved compared to conventional absorbers, maintaining the absorption shown in Figure 34.

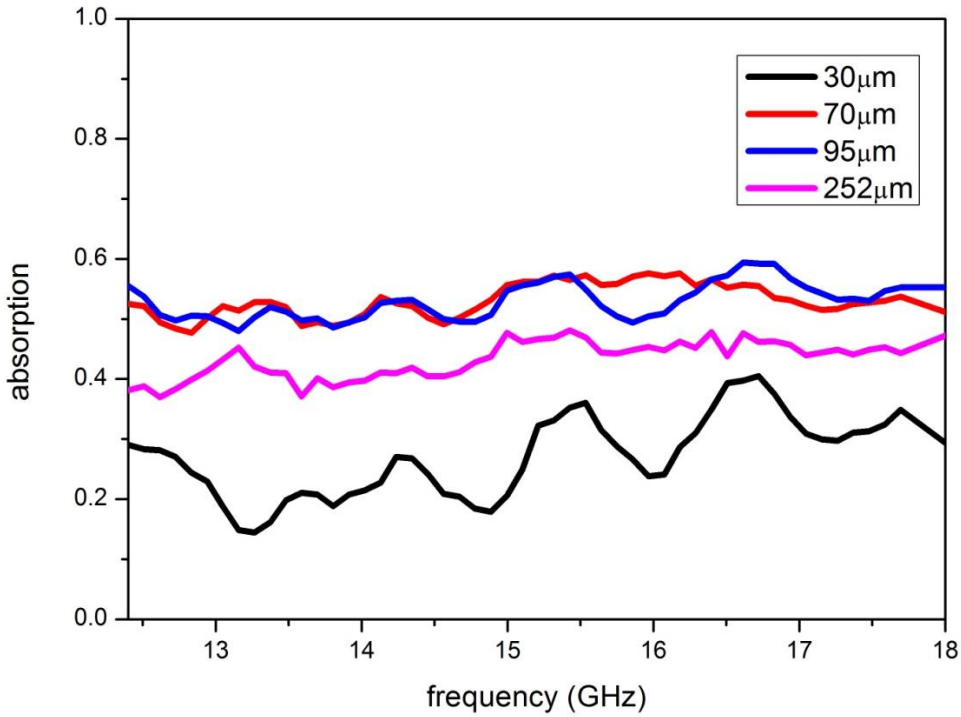

Figure 34: Measured absorption of the VACNT films.

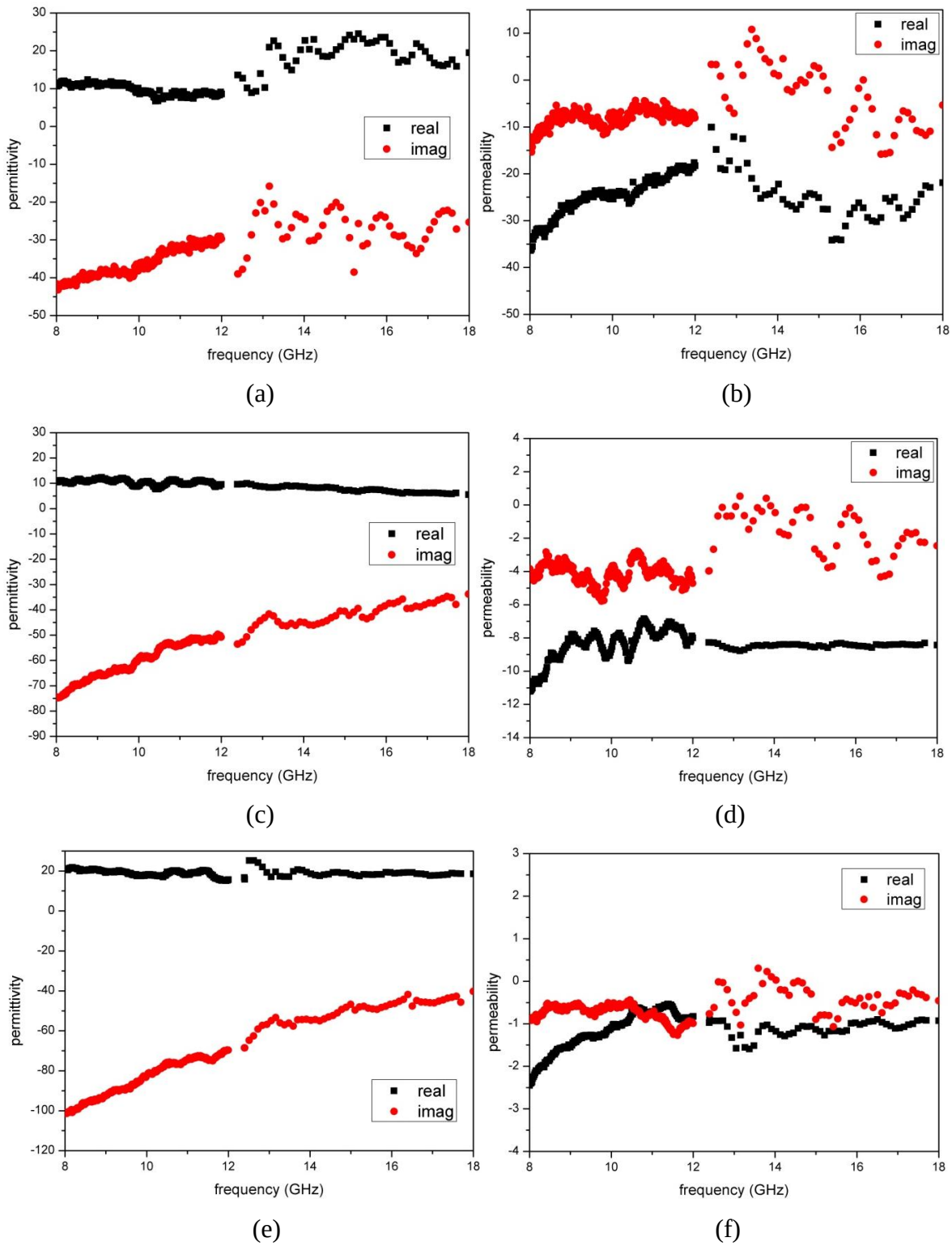

Figure 35: Extracted permittivity and permeability of the samples across the whole measured frequency band. a-b) 30 µm c-d) 95 µm e-f) 252 µm.

The results presented in Figure 22 and Figure 28 appear to have very good continuity. The final extracted dielectric parameters across the whole frequency bands, from 8 GHz to 18 GHz are presented in the figures above.

Similarly, the absorption is plotted across the combined X- and Ku- frequency band.

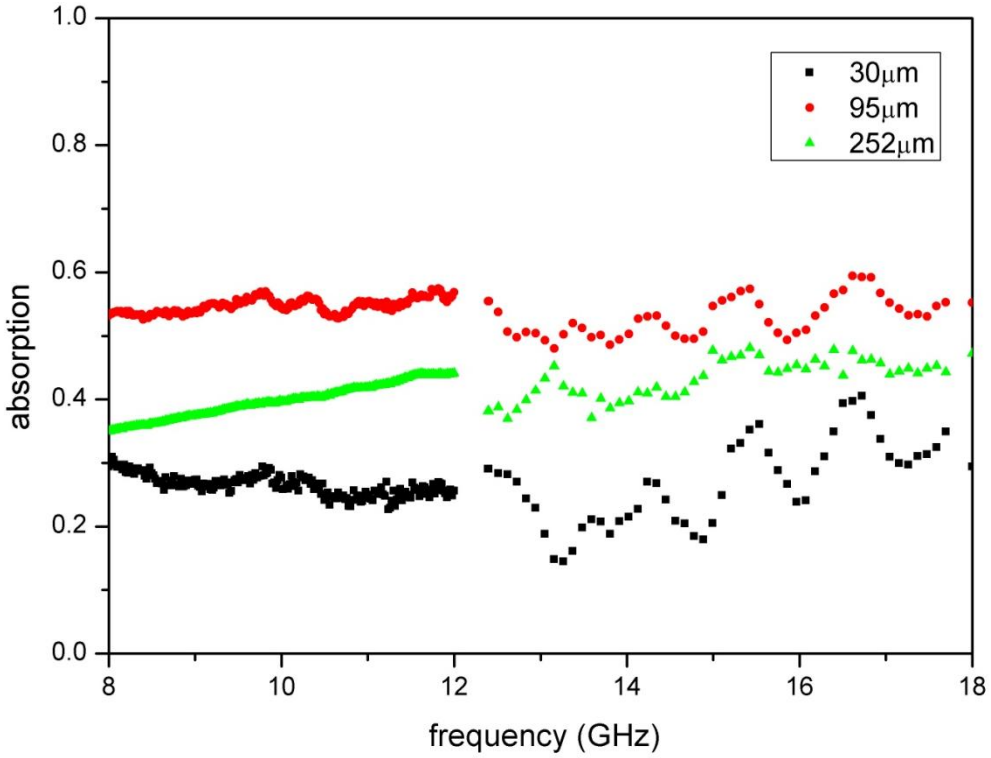

Figure 36: Measured absorption of the three samples across the X- and Ku- frequency bands.

3.5 Terahertz time-domain spectroscopy technique

In this section transmission terahertz time-domain spectroscopy measurements of carbon nanotube arrays is presented. A number of samples with vertically aligned multi - walled carbon nanotube (VACNT) films were prepared and measured using the relatively new technique of THz - Time Domain Spectroscopy (THz - TDS) [99]. The thickness of the samples varied, ranging from 21 μm to 252 μm.

From this measurement, a time domain signal was obtained. To find the frequency dependent complex permittivity of the above films, an FFT was performed on each signal thus obtaining the frequency dependent magnitudes and phases of the received

signal. These transmission spectra were used to investigate the dielectric properties of the samples (on the assumption that permeability μ=1).

Experimental results were obtained from 80GHz to 2.5THz for the VACNT samples plus a reference. Conductivity of CNTs was calculated from the imaginary part of the extracted permittivity.

3.5.1 Experimental Setup

THz - time domain spectroscopy technique (THz-TDS) is one of the best for material characterization in THz regime, and especially for MWNT films, because of the high signal to noise ratio at that frequency range [100]. There are two kinds of possible configurations: Transmission THz-TDS and Reflection THz-TDS.

For transmission measurements, there is a limit on the thickness of the sample. Samples which consist of low resistivity semiconducting materials, should be extremely thin (few μm thicknesses) in order to detect the output signal. These materials strongly absorb THz radiation, when thickness is relatively big, rendering transmission measurements impossible. However, reflection THz-TDS has no such limitations and it is suitable for thick samples or extremely low resistivity materials.

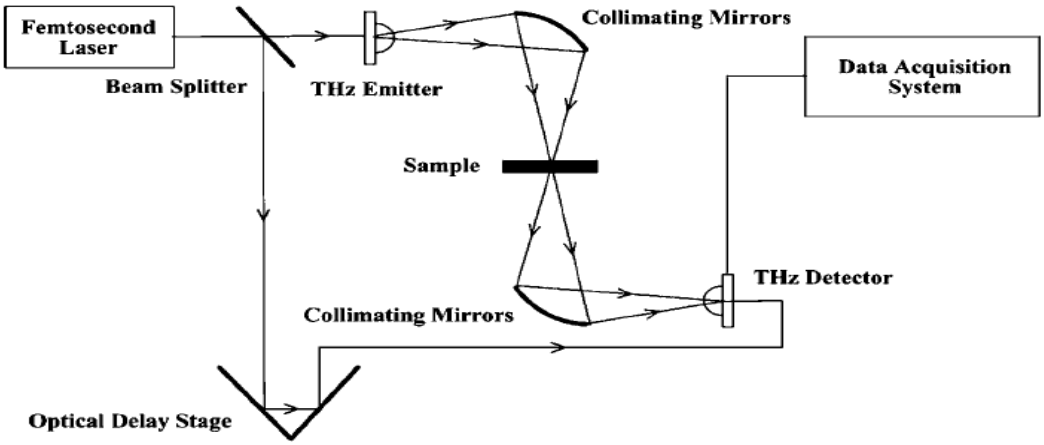

Figure 37: Schematic Diagram of terahertz time-domain spectroscopy (THz-TDS) transmission characterization setup [101].

The experimental setup is described to provide an overview of the system (Figure 37). A very short pulse of terahertz radiation was generated by excitation with a femtosecond laser. The most common method for THz wave generation involves using a biased photoconducting gallium arsenide (GaAS) [102]. The pulsed laser beam was split into two parts, in the ratio 1:4. The main beam was used to generate a THz pulse from the GaAs emitter, which was then passed through the material, either by transmission or reflection, and on to the detector. The secondary laser beam was the probe, which was passed through an optical delay line interacting with the THz beam in the detector. The length of the delay line was scanned so that the probe pulse swept the much longer THz pulse, yielding its amplitude and phase at all points. The time domain data obtained were transformed to frequency domain by applying the Fourier Transform.

3.5.2 Data Analysis

The data recorded from the setup, as described above, are in time-domain containing the reference pulse and the pulse transmitted through the sample (Figure 38).

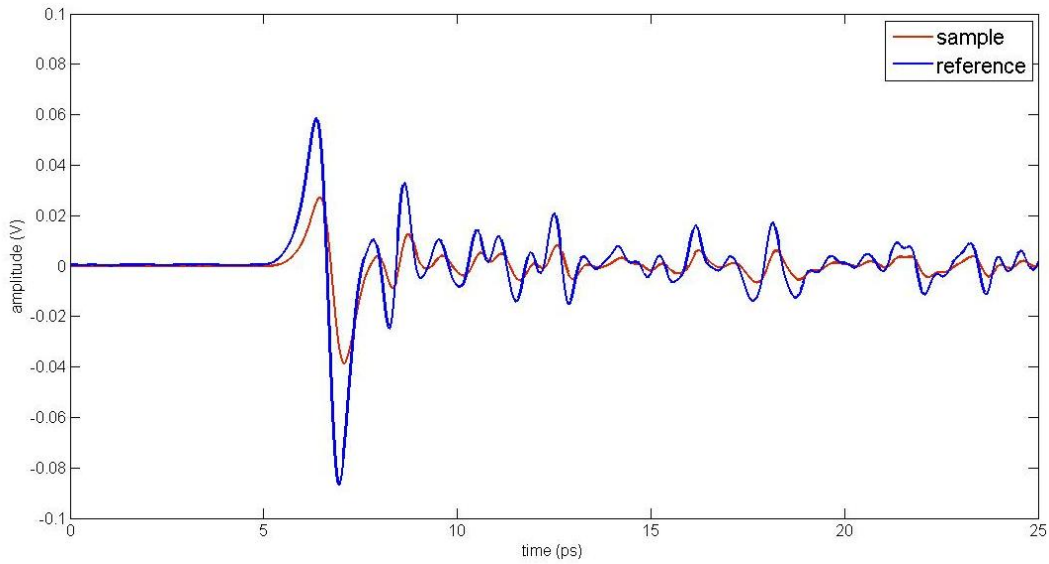

Figure 38: Reference and sample time-domain signal.

A total of $N = 2660$ data points were recorded using $\Delta t = 0.025 ps$ time steps resulting in a 66.5ps trace. The frequency spectrum was obtained with a Fast Fourier Transform (FFT) of the two signals $E_{ref}(t)$ and $E_{sample}(t)$:

$$E_{ref}(\omega) = A_{ref}(\omega) \cdot \exp\left[i \cdot \varphi_{ref}(\omega) \right] \tag{3.16}$$

$$E_{sample}(\omega) = A_{sample}(\omega) \cdot \exp\left[i \cdot \varphi_{sample}(\omega)\right] \tag{3.17}$$

The amplitudes $A_{ref}(\omega)$ and $A_{sample}(\omega)$ and the unwrapped phases $\varphi_{ref}(\omega)$ and $\varphi_{sample}(\omega)$ of an exemplary sample and reference spectra are displayed in Figure 39. Note, that in the engineering community the imaginary unit is usually defined as j, whereas in physics is kept as i. That happens because i is commonly used to denote electric current. Therefore, in the current study, we define $i = -j$.

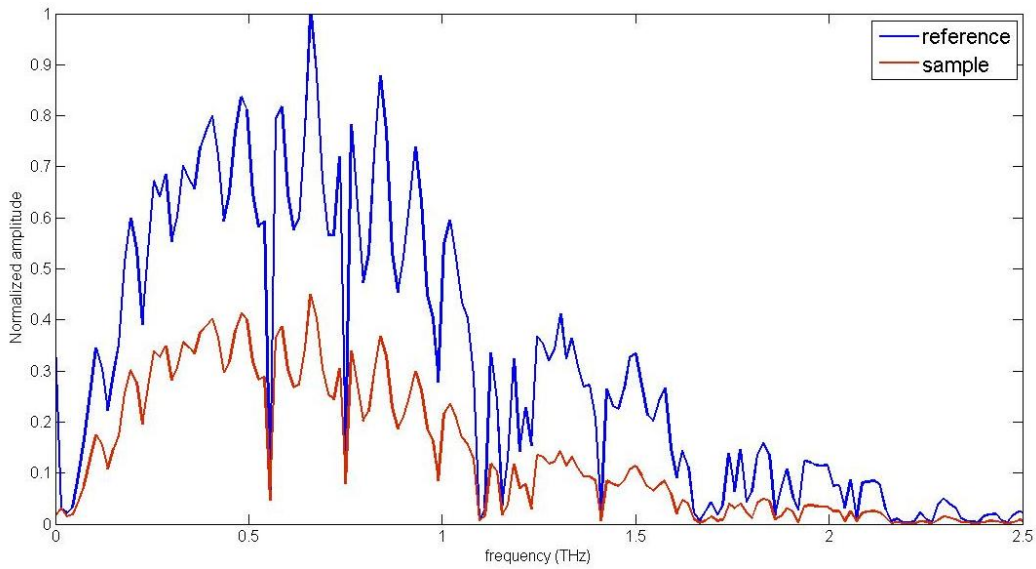

Figure 39: Reference and sample frequency-domain signal.

The amplitude $A(\omega)$ and phase $\varphi(\omega)$ of the ratio of the two spectra, $E_{sample}(\omega)/E_{ref}(\omega)$, were calculated and analyzed to obtain the frequency dependent absorption coefficient $\alpha(\omega)$ and refraction index $n(\omega)$:

$$n(\omega) = 1 - \frac{c}{\omega \cdot d}\varphi(\omega) \tag{3.18}$$

$$a(\omega) = -\frac{2}{d}\ln\left\{\mathrm{A}(\omega)\frac{\left[n(\omega)+1\right]^2}{4n(\omega)}\right\} \tag{3.19}$$

As explained above, the carbon nanotubes are vertically aligned on an n-type doped single crystal silicon wafer, with a resistivity of $0.015 - 0.025\ Ohm \cdot cm.$ Transmission measurement in that case is not possible as the beam cannot pass through the low

resistive substrate and it completely reflects the beam. To enable transmission measurement, a sticky tape has been used to lift and attach the carbon nanotubes on the tape (Figure 40). The reference spectrum was obtained by placing a bare sticky tape at the position shown in Figure 37. The sample spectrum was then placed at the same position and was normalized with respect to the referenced, thus collecting all the information needed for the parameter extraction of the CNT film.

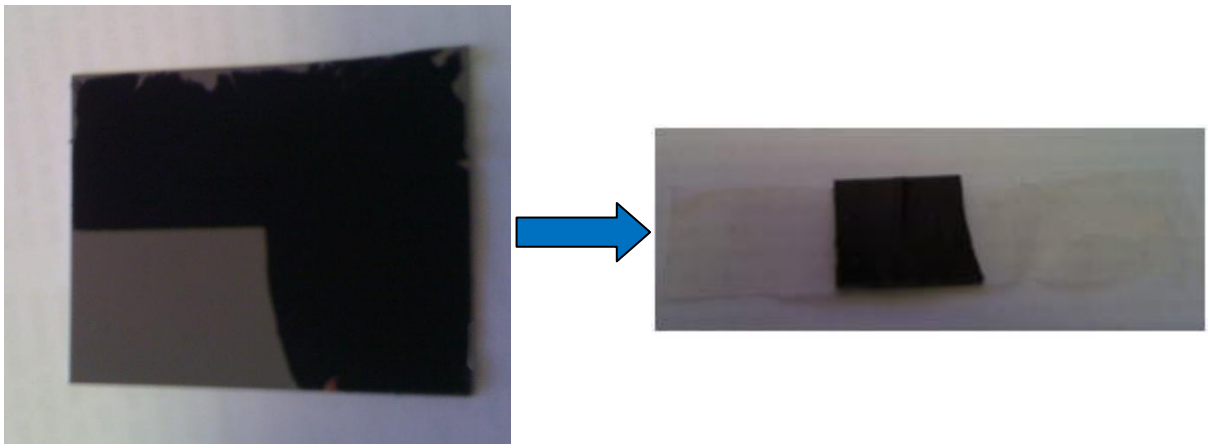

(a) (b)

Figure 40: a) vertically aligned carbon nanotubes grown on doped-silicon substrate b) CNTs attached on a sticky tape.

The refractive index and power absorption were determined using (3.18) and (3.19). The frequency dependent complex dielectric constant ε is equal to the square of the complex refractive index $\tilde{n} = n_r + i \cdot n_i$. The imaginary part of the refractive index was determined from the power absorption coefficient $n_i = \frac{\alpha \cdot \lambda}{4\pi}$. The dielectric constant for the CNT film is described by the following relation:

$$\varepsilon = \varepsilon_{CNT} + i \frac{\sigma}{\omega \cdot \varepsilon_o} \tag{3.20}$$

where ε_{CNT} is the dielectric constant of CNTs, σ is the complex conductivity and ε_o is the free-space permittivity $\left(\varepsilon_o = 8.854 \cdot 10^{-12}\ F/m\right)$.

The measured complex permittivity, power absorption and conductivity of the CNT film, were obtained by the procedure described above. As expected, different samples of the same material, gave exactly the same permittivity values in high frequencies

and slightly different for microwave frequencies, where THz-TDS is not advantageous. Another reason for this variance in lower frequencies is the small thickness of the CNT film, such that a small error in the measured phase, causes significant difference in the extracted complex permittivity. The extracted real and imaginary parts of the permittivity of the CNT film sample are plotted from 80 GHz to 2.5THz in Figure 41 for three of the samples (21 μm - 121 μm and 252 μm).

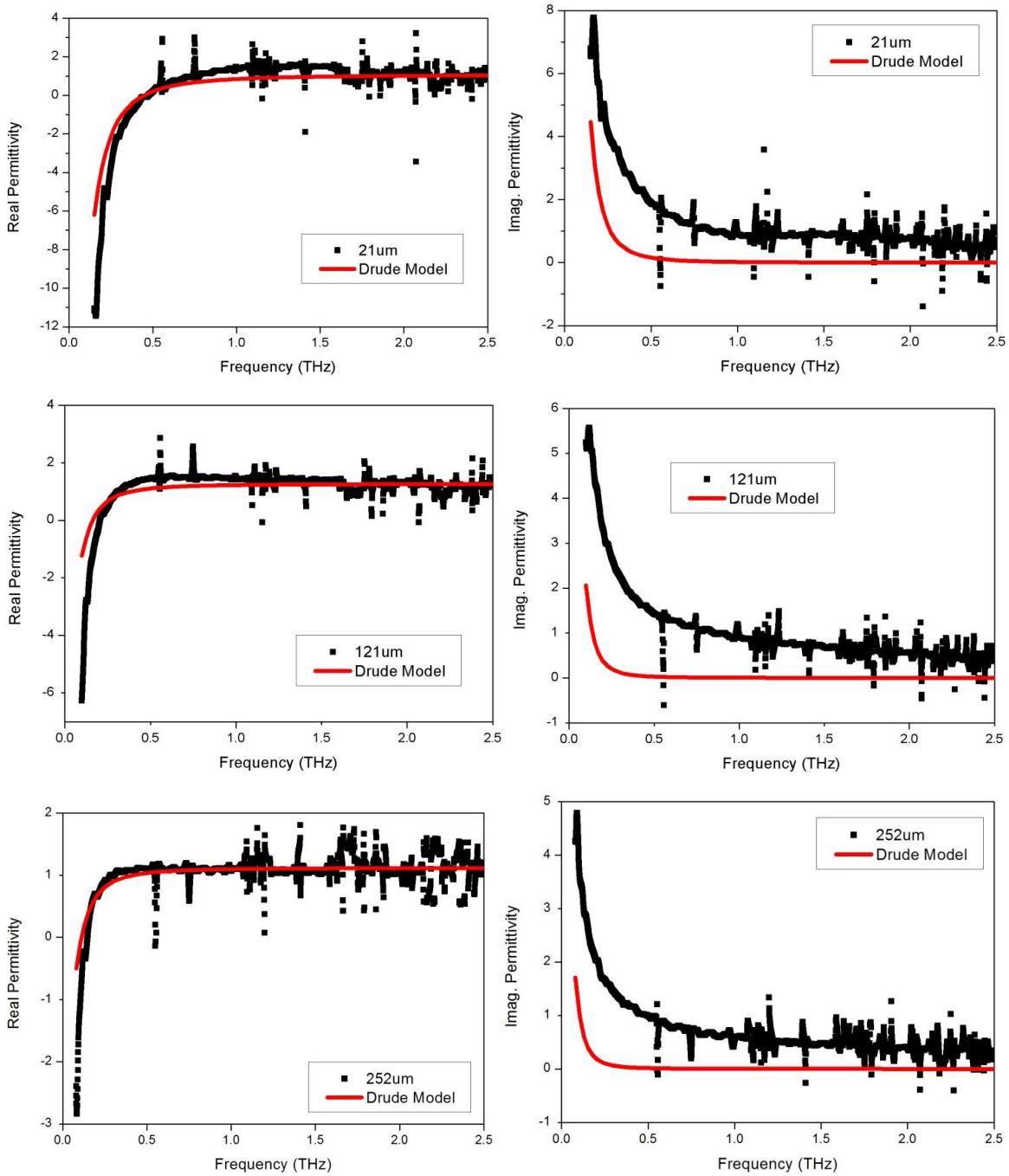

Figure 41: Retrieved real and imaginary permittivity for 3 of the samples.

The Drude model was introduced to fit both real and imaginary part of the permittivity:

$$\varepsilon_m(\omega) = \varepsilon_{MWNT}^{\infty} - \frac{\omega_p^2}{\omega^2 + i\Gamma\omega} \tag{3.21}$$

where $\varepsilon_{MWNT}^{\infty}$ is the permittivity of the MWNT network, ω_p is the plasma frequency and Γ is the electron relaxation rate. The unknown parameters for the fitting were $\varepsilon_{MWNT}^{\infty}$ and Γ. The plasma frequency ω_p was calculated for each sample from the real part. The fitting parameters are given in the following table:

Table 6: Fitting parameters for the measurements presented in Figure 41.

Thickness µm	$\omega_p/2\pi$ **THz**	ε^{∞}	$\Gamma/2\pi$ **THz**
21	0.475	0.657	8.33
121	0.205	1.3488	2.39
252	0.148	1.1874	1.99

Figure 42 shows the extracted values of conductivity for the same 3 samples.

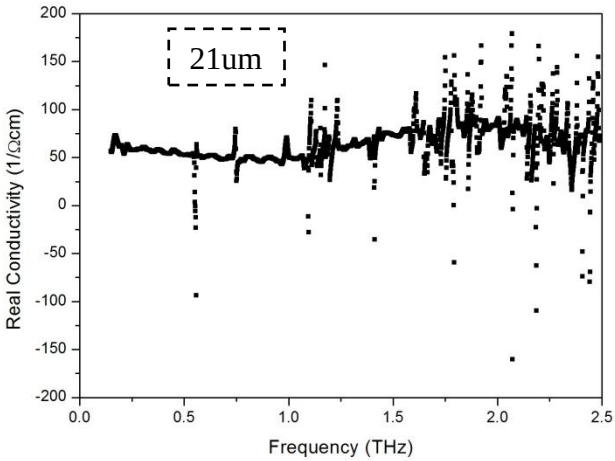

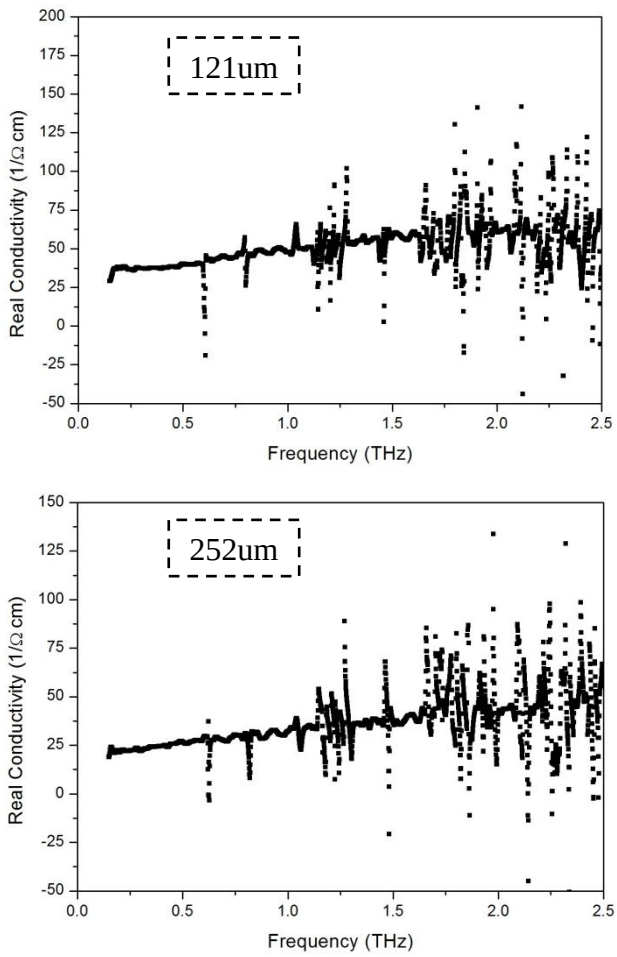

Figure 42: Extracted conductivity of the three nanotube films.

Using the Drude model for fitting of the imaginary part of the permittivity did not produce a suitable result as shown in Figure 41. That is because the carbon nanotube film is not highly conductive (Figure 42) thus another model was introduced to compensate for that effect. A combination of the Drude term with the localized Lorentzian absorption is given by:

$$\varepsilon_m(\omega) = \varepsilon_{MWNT}^{\infty} - \frac{\omega_p^2}{\omega^2 + i\Gamma\omega} + \sum_j \frac{\omega_{pj}^2}{\left(\omega_j^2 - \omega^2\right) - i\Gamma_j\omega} \tag{3.22}$$

where $\varepsilon_{MWNT}^{\infty}$ is the permittivity of the MWNT network, ω_p is the plasma frequency, Γ is the electron relaxation rate, ω_j is the phonon frequency, Γ_j is the spectral width and ω_{pj} is the oscillator strength of the Lorentz oscillators. Similar figure with Figure 41 is presented below, taking into account the combination of the Drude term with the localized Lorentzial absorption.

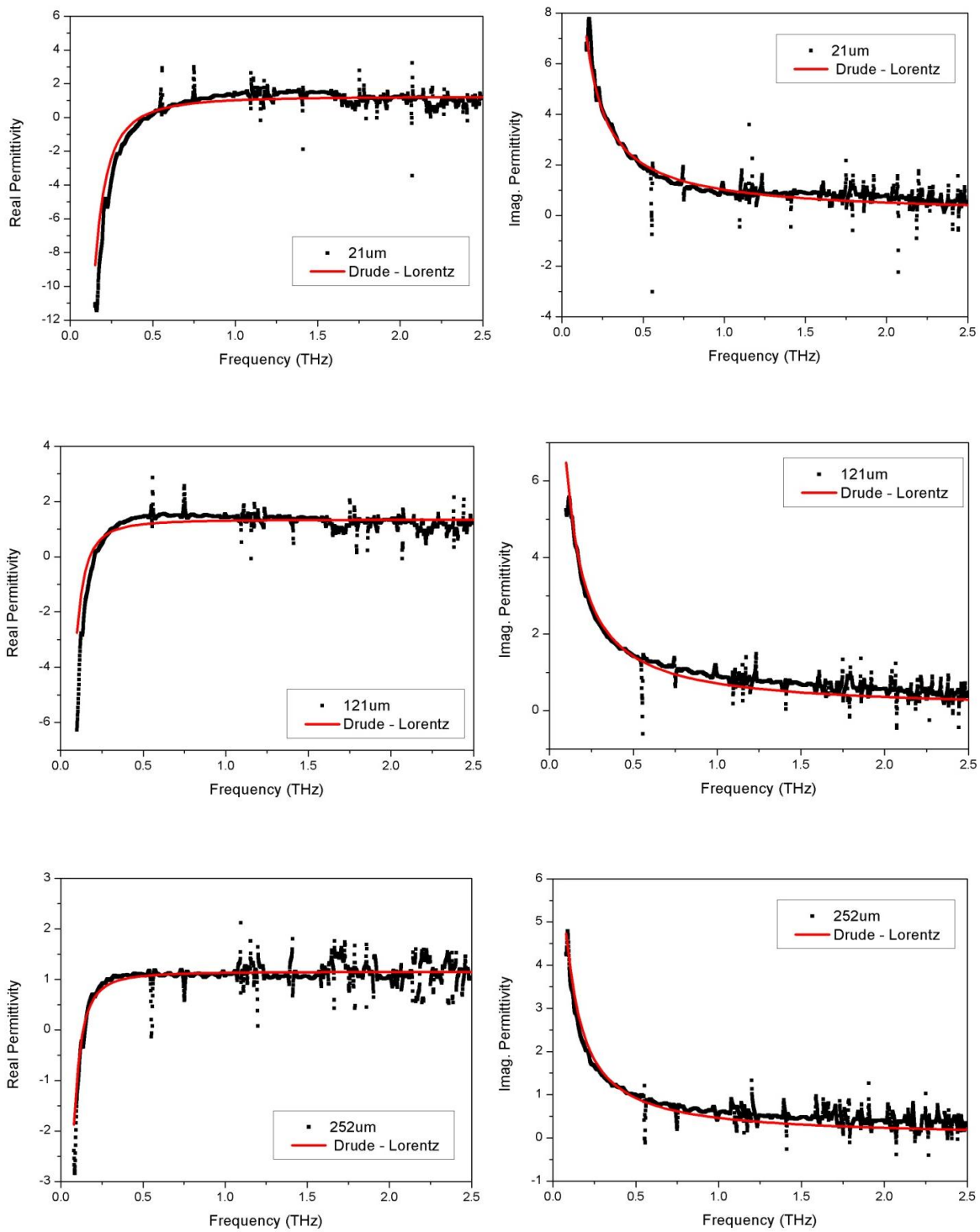

Figure 43: Fitting curves of the complex permittivity of the three samples, fitted with the combination of Drude-localized Lorentzian absorption.

The fitting parameters are given in the following table:

Table 7: Fitting parameters for the Drude - Lorentzian model.

Thickness µm	$\omega_p/2\pi$ THz	ε^{∞}	$\Gamma/2\pi$ THz	$\omega_{pj}/2\pi$ THz	$\omega_j/2\pi$ THz	$\Gamma_j/2\pi$ THz
21	0.658	1.31	0.046	56.06	22.546	3016
121	0.364	1.313	0.034	99.87	42.122	11775
252	0.239	1.11	0.033	69.61	33.06	9362

The combined Drude - Lorentz model, gives accurate fitting curves but physically meaningless parameters. An improved Drude model was introduced, adding an imaginary term equal to the conductance. This model is described by:

$$\varepsilon_m(\omega) = \varepsilon_{MWNT}^{\infty} - \frac{\omega_p^2}{\omega^2 + i\Gamma\omega} + \frac{i\cdot\sigma}{\omega\cdot\varepsilon_o} \tag{3.23}$$

where $\varepsilon_{MWNT}^{\infty}$ is the permittivity of the MWNT network, ω_p is the plasma frequency, Γ is the electron relaxation rate, σ is the conductivity and ε_o is the permittivity of free space. Figure 46 shows both measured data and the fitting from the theoretical model given by 5.8.

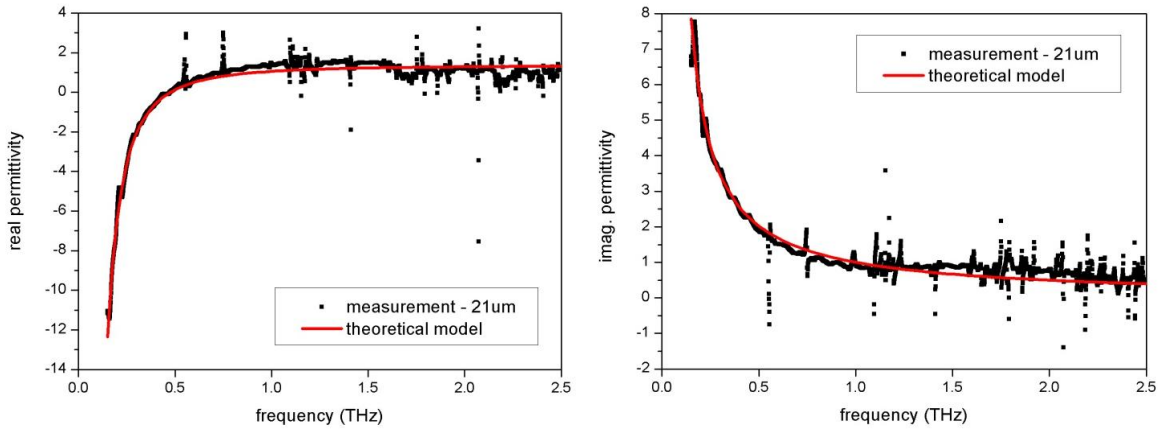

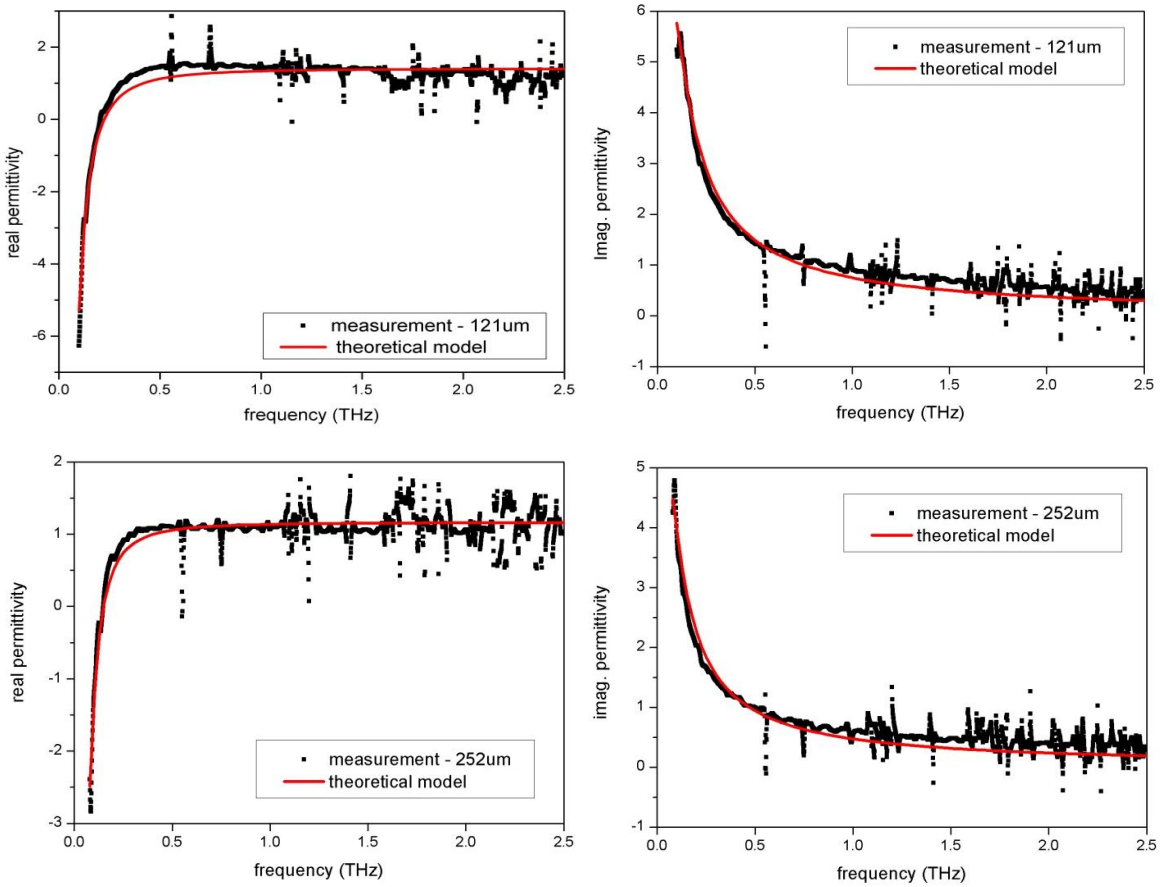

Figure 44: Fitting curves of the complex permittivity of the three samples, fitted with the improved Drude model that is expressed with (3.23).

The extracted real and imaginary permittivity for all the samples fitted with the Drude model introduced in (3.23) are plotted below.

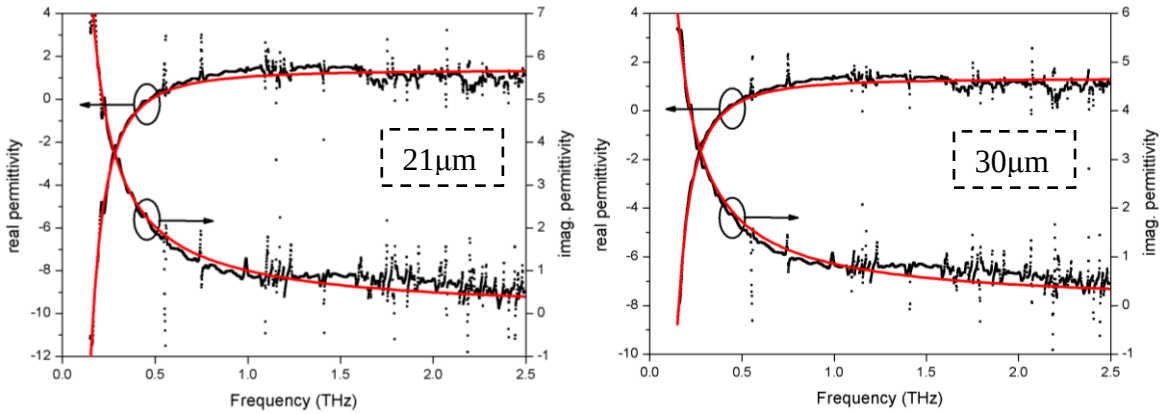

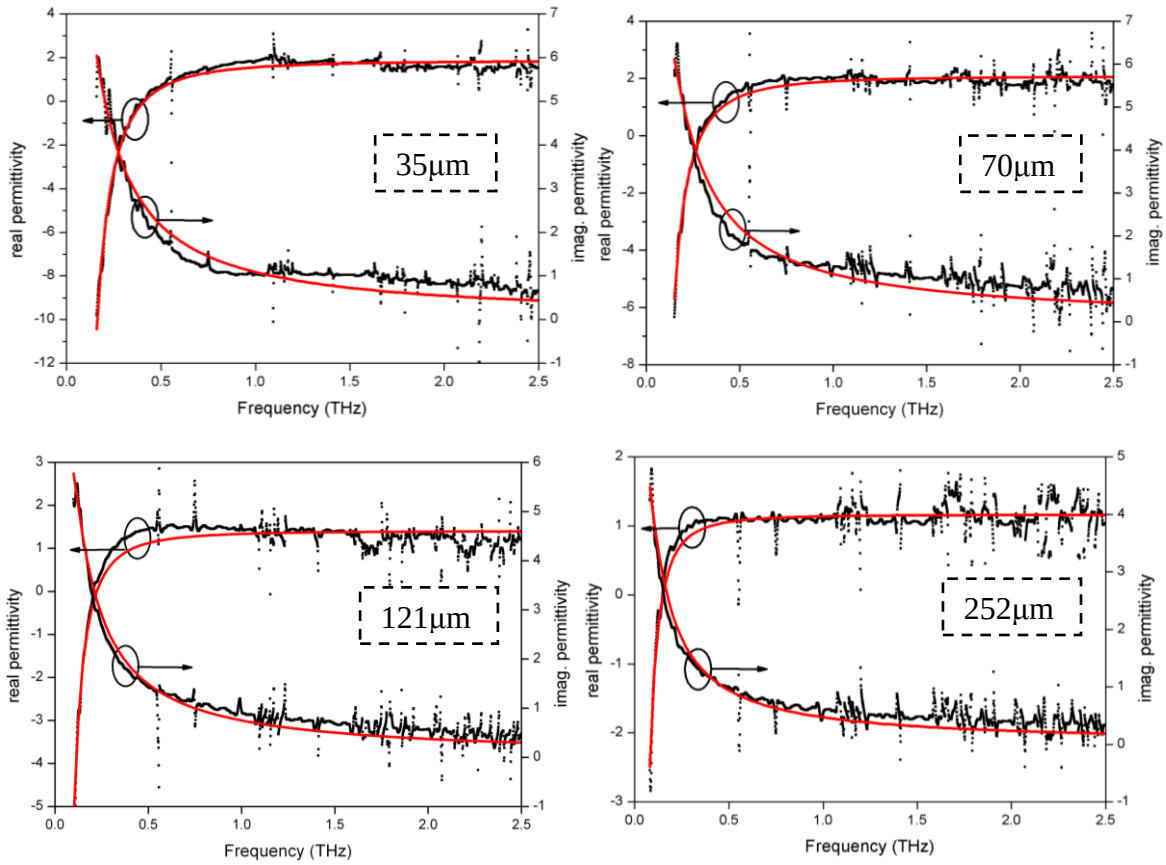

Figure 45: Extracted complex permittivity, for all the six samples that have been measured with THz-TDS. Fitted curves are also present.

The fitting parameters for all the samples are given in the following table:

Table 8: Fitting parameters for the improved Drude model.

Thickness μm	$\omega_p/2\pi$ **THz**	ε^{∞}	$\Gamma/2\pi$ **THz**	σ
21	0.48	1.36	0.013	55.47
30	0.41	1.32	0.005	47.69
35	0.4	1.87	0.01	60.72
70	0.29	2.08	0.026	62.32
121	0.23	1.41	0.026	41.87
252	0.16	1.16	0.032	26.34

The plasma frequency varies exponentially with the thickness of the sample (Figure 46), although one may have expected that it would be constant, since different slab thicknesses of the same material are being measured. However, considering the retrieval of the permittivity, the dependence of the transmission coefficient with exp(ikd) was neglected. Therefore, this exponential dependence appears as a small variation to the values of the plasma frequency.

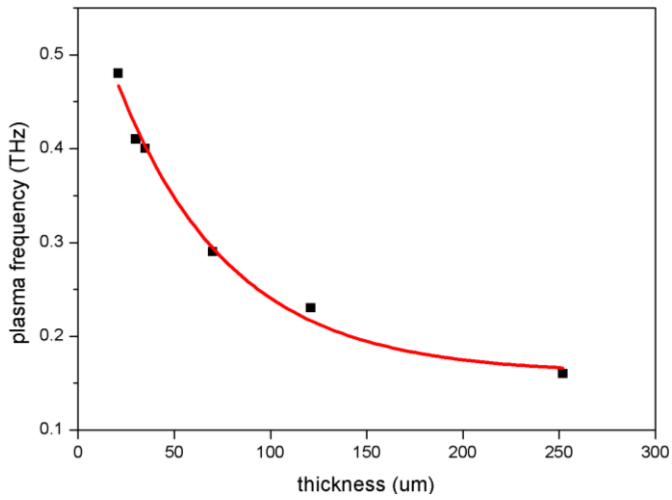

Figure 46: Plasma frequency versus thickness for VACNT films.

3.6 Drude model versus measurement results

In this section, the improved Drude model presented earlier, will be expanded over the entire frequency spectrum measured. In the whole procedure, it was assumed that the VACNT films have no magnetic properties and therefore $\mu = 1$. Measurements were performed in X- and Ku- bands and thus have to be recalculated taking into consideration. THz-TDS results were kept the same. Finally, the effective medium absorption was calculated using the Drude model and compared with the measurements.

The samples presented here are those of the 30 μm and 252 μm films. These two samples were the only ones for which measurements were performed across the entire frequency band, from 8 GHz to 2.5 THz. In Figure 47 we observe the real and imaginary permittivity as well as the fitting of the model presented in (3.23).

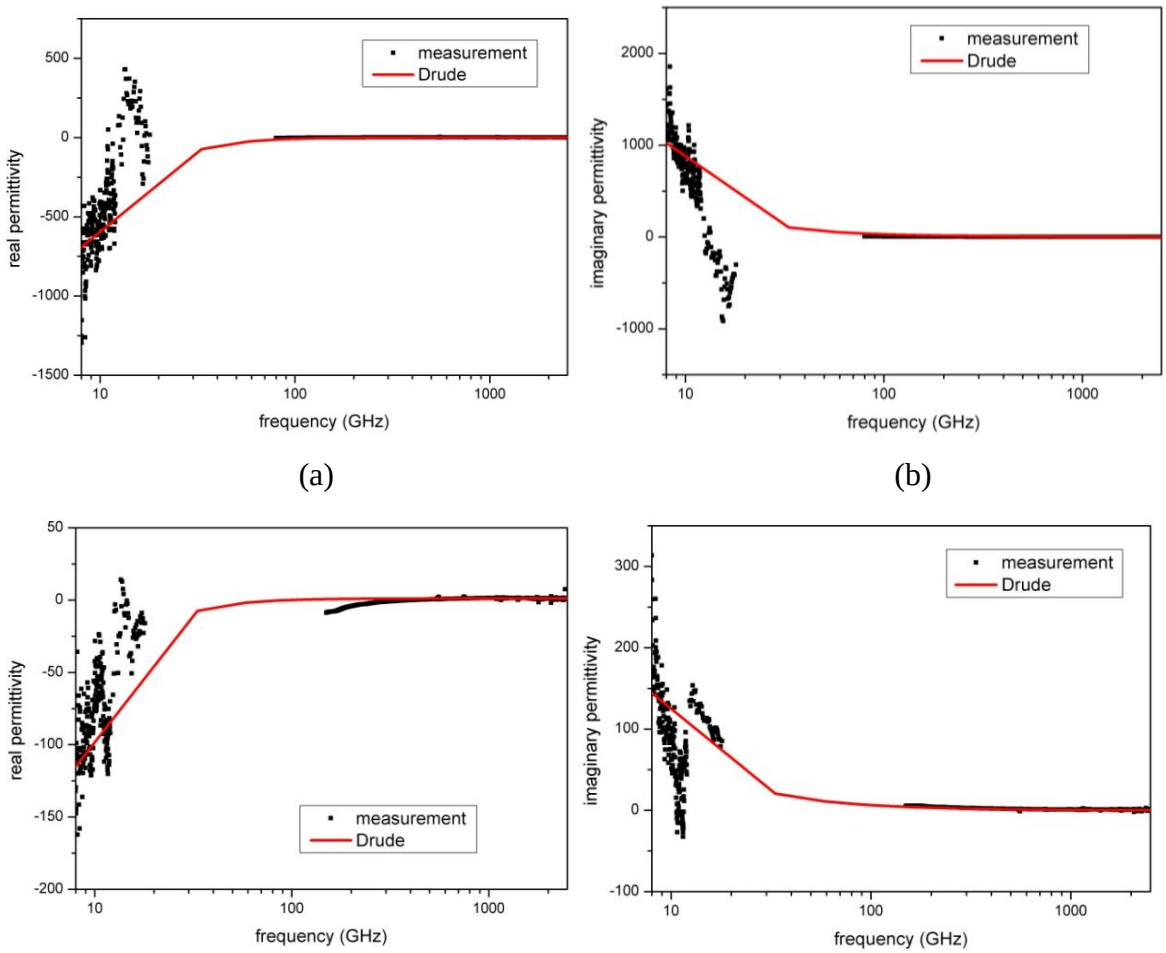

Figure 47: Fitting curves of the complex permittivity of the a-b) 30 μm and c-d) 252 μm samples fitted with the improved Drude model.

The fitting parameters are given in the following table:

Table 9: Fitting parameters of the two samples that measurements have been performed across the 8 GHz - 2.5 THz frequency band.

Thickness μm	$\omega_p/2\pi$ **THz**	ε^{∞}	$\Gamma/2\pi$ **THz**	σ
30	0.291	1.32	0.007	161.29
252	0.098	1.16	0.004	35.78

Figure 47 has been plotted in logarithmic scale for reasons of clarity. The improved Drude model has been fitted to the measurements, keeping the ε^{∞} parameter fixed at the value that has been reported in Table 8. The remaining parameters have been adjusted, however plasma frequency, ω_p, relaxation frequency, Γ, and conductivity σ, are in good agreement with the previously reported values in Table 8.

The improved Drude model, presented above, was constrained in the low microwave band, 8-18 GHz, where the absorption information of the VACNT films is available. Figure 48 shows that the absorption calculated using the Drude model, is relatively close to the measured results that have been presented in Figure 36.

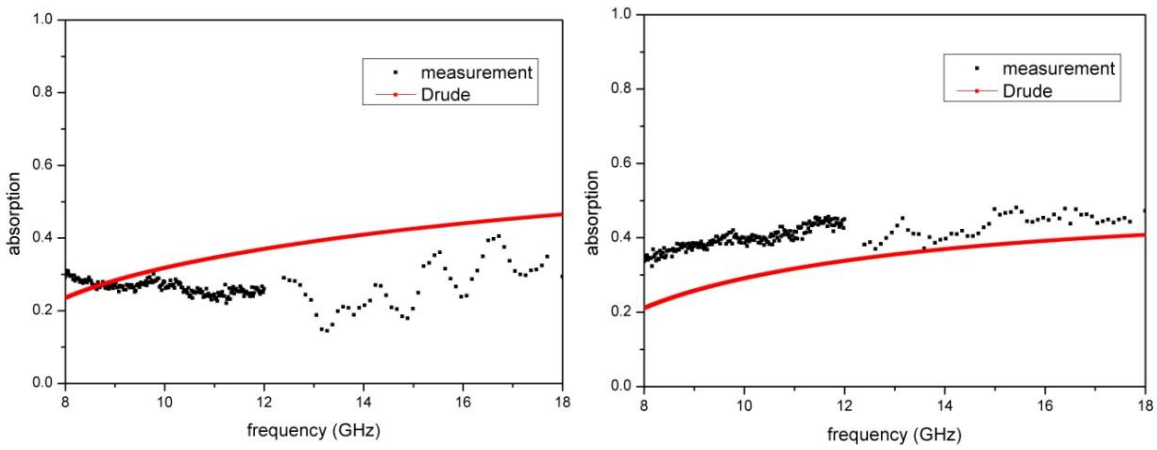

(a) (b)

Figure 48: Comparison of measured absorption with the one extracted from improved Drude model. a) 30 μm b) 252 μm.

Using the effective medium Drude model, the theoretical absorption for each frequency point was calculated. Considering that this theoretical model is not very accurate in low frequencies compared to higher ones, the following table was extracted, where the absorption is calculated in different single frequencies, for all the available VACNT samples.

Table 10: Absorption level of VACNT films for different frequencies and thickness.

Thickness µm	Frequency (GHz)						
	10	**20**	**50**	**100**	**200**	**500**	**1000**
21	0.26	0.32	0.68	0.68	0.49	0.33	0.3
30	0.3	0.41	0.34	0.34	0.34	0.34	0.36
35	0.24	0.33	0.53	0.57	0.68	0.42	0.48
70	0.41	0.35	0.43	0.53	0.53	0.58	0.88
121	0.25	0.33	0.45	0.52	0.54	0.7	0.92
252	0.28	0.39	0.44	0.52	0.67	0.94	0.94

Therefore, Figure 49 can be developed

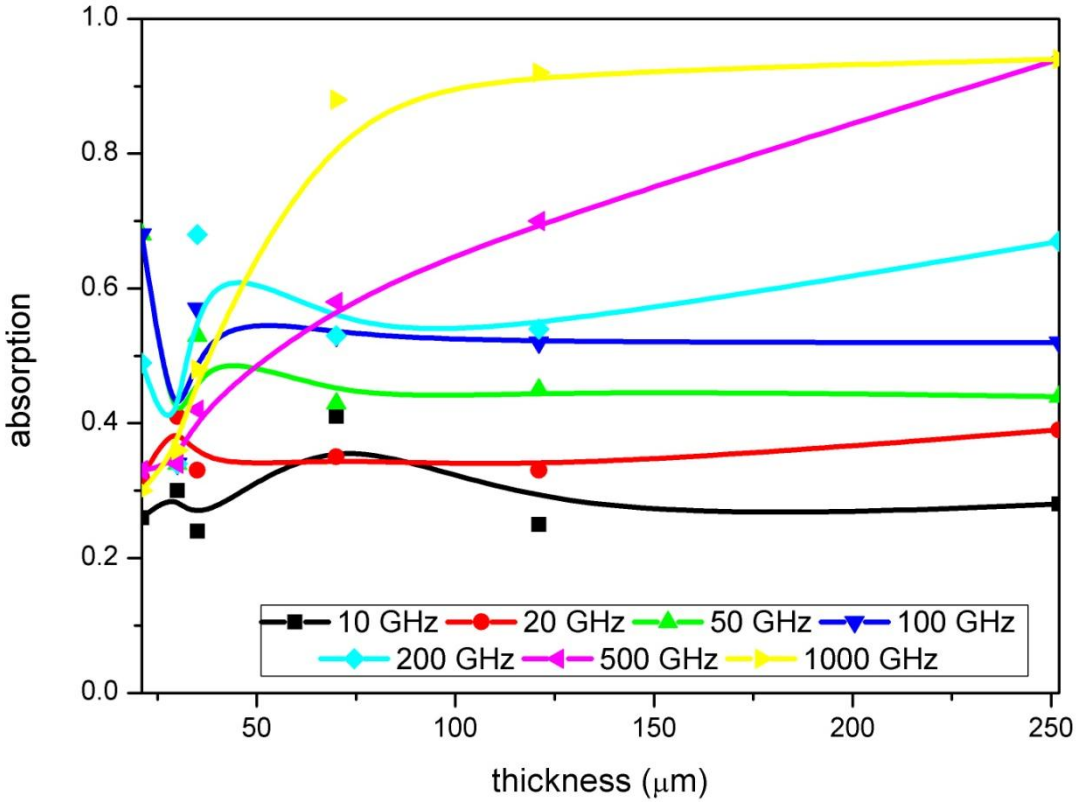

Figure 49: Absorption versus thickness of VACNT films for different frequencies.

For the majority of the frequencies, the absorption of the VACNT films does not increase as the thickness increases, instead it appears to have a maximum of absorption in different positions for each frequency. One can also observe that as the frequency increases, i.e. 10 GHz - 100 GHz - 200 GHz, the maximum absorption is

achieved in lower thicknesses, 70μm ($\lambda/430$) - 50μm ($\lambda/60$) - 40μm ($\lambda/38$). These maxima are not a constant fraction of the wavelength and they are not related to the frequency. As previously explained, all the samples of VACNT films were grown similarly but are not identical to each other. They exhibit discrepancies arising from geometrical uncertainties and most importantly concentrations of the Fe catalyst. This resulted in moderately distinct effective media in all three samples.

Moreover, the absorbing behaviour of the VACNT films in X-band frequency was verified. In Figure 27, it appears that between the three samples measured, 30 μm, 95 μm and 252 μm, the maximum absorption is achieved at 95 μm thickness. Similar behaviour is presented by Figure 49, in the center frequency of the X-band, at 10 GHz.

3.7 DC resistance of the vertically-aligned CNT array film

In this section, certain circuit models of the vertically aligned CNT array were studied. The effective circuit models indicated which parameters affected the conductivity of the CNT film. The sheet resistivity for each of the samples was also measured.

A single CNT dipole exhibits significantly slow wave velocities, around 2% compared with the speed of light ($u_p = 0.02c$ [14], where c is the speed of light) above the relaxation frequency of around 53 GHz [13, 14]. Reported antennas [13, 14] have very low radiation efficiencies due to large resistance along the single CNT, which is in the order of $6.45 k\Omega/\mu m$.

Following Ohm's Law, the resistance of a wire should be proportional to the length of the wire. However, in this case, the electron transport mechanism changes from diffusive to ballistic [103, 104], as the length of the wire is reduced to the mean free path of electrons, as shown in Figure 50. Moreover, when the width of the wire is reduced to the Fermi wavelength scale (around 0.74 nm), the resistance is quantized

in steps of $\frac{h}{2e^2} = 12.9k\Omega$, where $h = 6.626 \cdot 10^{-34} J \cdot s$ is the Planck constant and $e = 1.602 \cdot 10^{-19} C$ is the elementary charge.

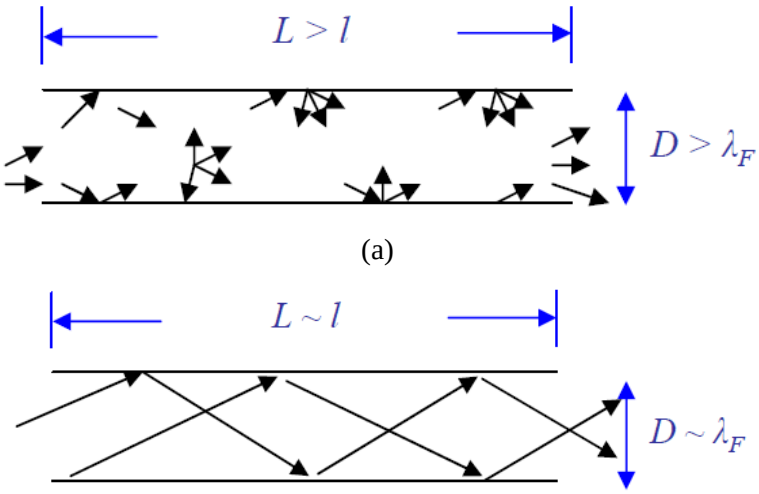

Figure 50: a) Diffusive and b) Ballistic transport of electrons in 1-D wires.

Therefore, a single carbon nanotube has large resistance along the CNT as the diameter is close to Fermi wavelength. The resistance is independent on the length of the CNT. Instead, the resistance can be theoretically calculated by the Landauer formula [103, 104]:

$$R = \frac{h/(2e^2)}{\sum T_j} \tag{3.24}$$

where T_j is the electron transmission probability for the j-th conductance channel. Since $T_j = 1$ for ballistic transport, the resistance of a single CNT is therefore:

$$R = \frac{h/(2e^2)}{N} = \frac{12.9k\Omega}{2} = 6.45k\Omega \tag{3.25}$$

where $N = 2$ is the number of conduction channels of a single CNT. Although this resistance appears to be very high, the conductivity of a single metallic CNT is extremely high considering its small diameter. As shown in [14], given the typical CNT length of 1 μm and diameter of 1.5 nm, the effective conductivity calculated according to Ohm's Law is:

$$\sigma = \frac{1}{R \cdot \pi D^2/4} = \frac{10^{-6}}{6.45 \cdot 10^3 \pi \cdot \left(1.5 \cdot 10^{-9}\right)^2/4} = 8.78 \cdot 10^7\ S/m \qquad (3.26)$$

which is even higher than the conductivity of copper which is $5.96 \cdot 10^7\ S/m$.

Since electrons are transported along the nanotube ballistically, the electric current can flow perpendicular to the nanotube stems only when there are entanglements among CNTs as shown in Figure 51. This entanglement, is the key to high conductivity of the vertically-aligned CNT sheet [105].

The equivalent circuit model of the vertically-aligned CNT array is shown in Figure 52, where N_L, N_W and N_t are the number of touching per unit length along the length, width and thickness direction of the CNT array, respectively. R_1 and R_C are the per-unit-length resistance of single CNT and the contact resistance between two touching CNTs, respectively [105].

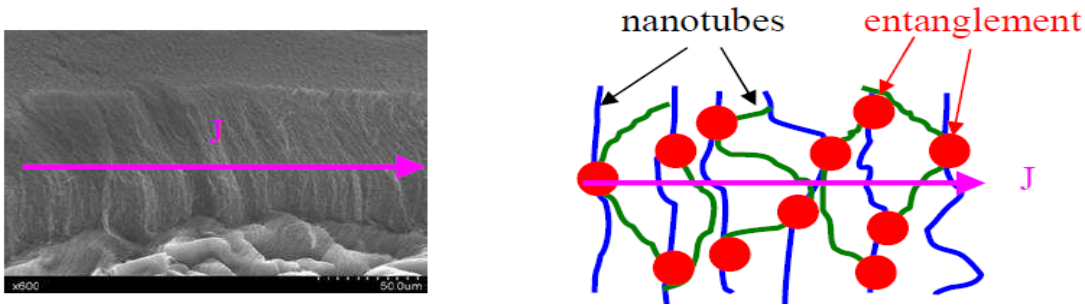

(a) (b)

Figure 51: a) SEM image of the vertically aligned CNT array and b) simplified model showing the entaglements of the nanotubes [105].

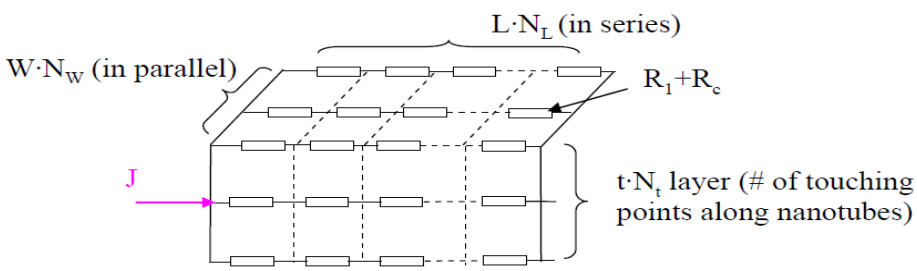

Figure 52: Equivalent circuit model of the vertically aligned CNT array [105].

According to this model the vertically-aligned CNT array has a resistance given by the following equation:

$$R = \left(R_1 + R_C\right)\frac{L \cdot N_L}{W \cdot N_W \cdot t \cdot N_t} \tag{3.27}$$

The above equation has been validated, with regards to the length (L) and the thickness (t) of the CNT lines, measuring the DC resistance of different samples. Figure 53 and Figure 54 show the two sets of measurements taken. The lines are the curves fit into the measurement points. As expected, the DC resistance is proportional to the CNT line length (L) and inversely proportional to the CNT thickness (t).

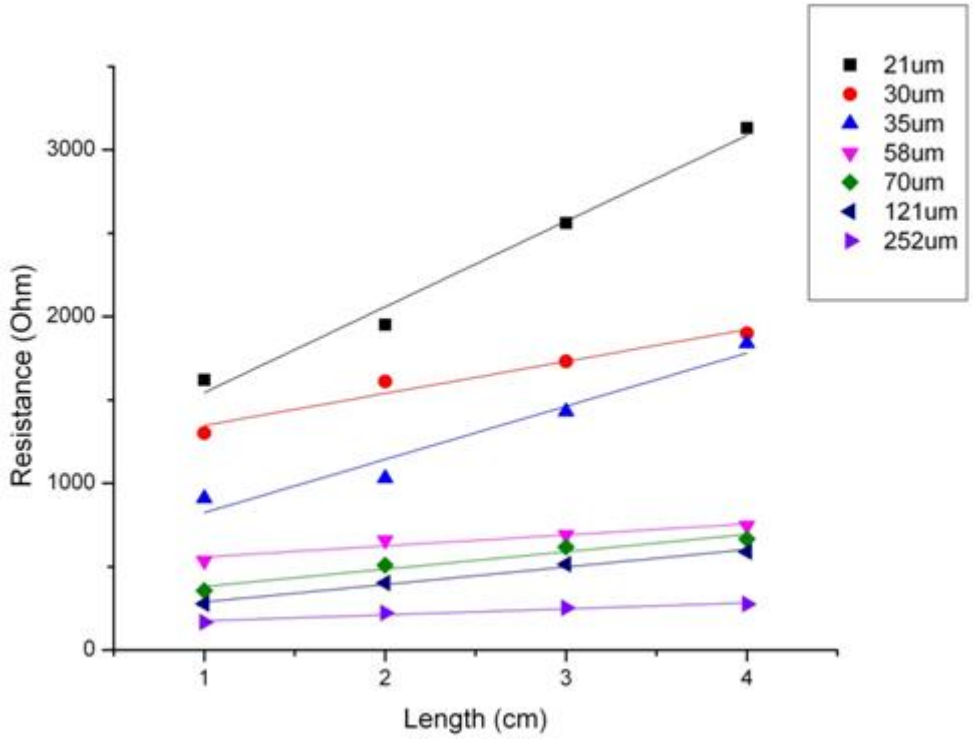

Figure 53: Measured DC resistance of the vertically-aligned CNT array showing the length effect.

The resistance of the CNT sheet can be written in terms of the sheet resistance by:

$$R = R_s \frac{L}{W} \tag{3.28}$$

From equations (3.27) and (3.28) we can obtain the sheet resistance of the vertically-aligned CNT array in Ω / sq:

$$R_s = \frac{R_1 + R_C}{tN_t} \tag{3.29}$$

This equation shows that in order to decrease the sheet resistance of the CNT array, keeping the same thickness of the film, we must increase the number of entanglements along the thickness direction (N_t). That means, the density of the CNTs must be increased or the spacing between them in the array must be reduced.

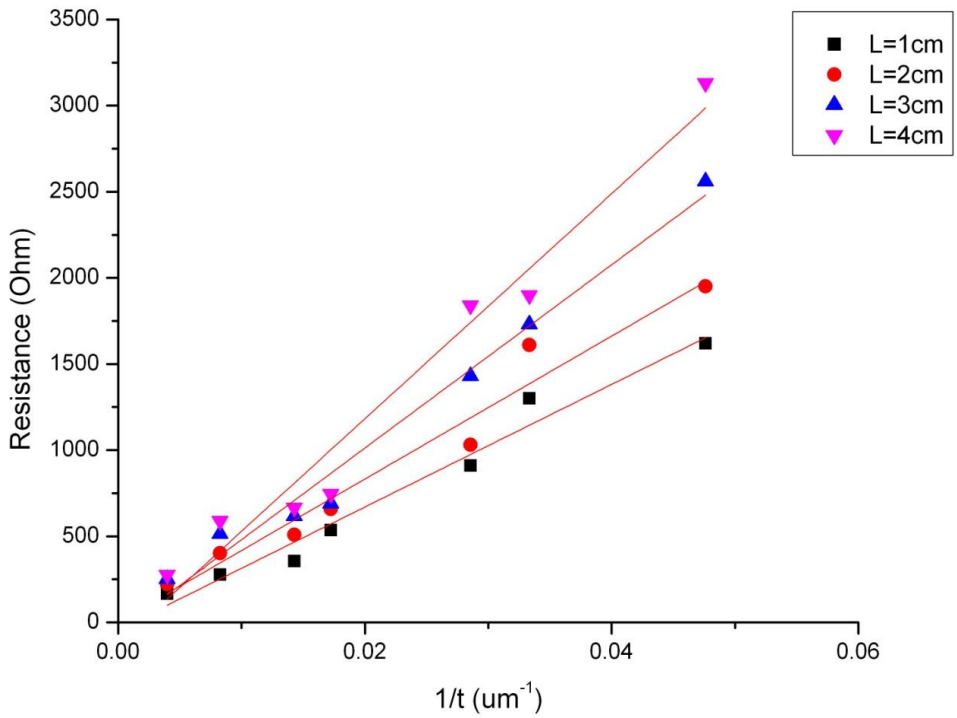

Figure 54: Measured DC resistance of the vertically aligned CNT array showing the thickness effect.

3.8 Summary

In this chapter, several samples with vertically aligned multi - walled carbon nanotube films were fabricated and measured in several frequency bands. Firstly, VACNT films were characterized at X-band frequencies. The relative permittivity and permeability of the VACNT films were extracted from 8 GHz to 12 GHz using the Nicolson–Ross–Weir approach and good agreement with full wave simulations (CST-Microwave Studio) was obtained. A systematic error analysis was presented and the errors calculated were within the acceptable range of errors. The absorbing

performance of VACNT films were examined and compared to conventional materials.

Additionally, Ku-band measurements were performed. The complex relative permittivity and permeability were extracted from the waveguide measurement, similar to the one performed in X-band. Systematic error analysis was applied and the errors were within the acceptable range. The absorbing performance of the VACNT films was examined, and a 90% size reduction was achieved compared to the conventional carbon loaded materials.

Finally, THz-TDS measurements of carbon nanotube arrays placed on the top surface of a rectangular silicon substrate were presented. Several samples with vertically aligned multi - walled carbon nanotube films were fabricated and characterized. From this measurement, a time domain signal was obtained. The frequency dependent complex permittivity was found, applying an FFT on each signal. These transmission spectra were used to investigate the complex permittivity of the films versus the frequency (on the assumption that permeability $\mu=1$), and conductivity of the samples. By introducing the Drude model for lossy metals the behaviour of the VACNT samples was delineated by fitting to the measured complex permittivity. The material properties of this film provide useful information for potential microwave and terahertz applications.

Chapter 4:

Modeling Techniques of Carbon Nanotubes

4.1 Introduction

Two unsolved questions in condensed matter physics are that of the nature of low-lying excitations and that of the ground state of interacting electrons. The most successful theoretical approach to answering the problem of interaction, is given by Landau's theory and the model of Fermi liquids. In Fermi liquids, low-lying excitations are considered to be non-interacting quasi-particles instead of electrons. The inverse quantum lifetime of a quasi-particle is generally less than its energy. This concept, of an independent quasi-particle, is well defined allowing quasi-particles to be treated as non-interacting. Although Landau's Fermi liquid theory describes two and three dimensional systems well, the theory breaks down for one dimensional systems such as Carbon Nanotubes [106].

Tomonaga [107] and Luttinger [108] attempted to establish a model for interacting electrons in one dimension. Gogolin [109] introduced a new method called "bosonization" which will be later used by Luttinger to describe his model. The boson variables describe collective excitations in the electron gas, 1-D plasmons. Haldane [110] claimed that the bosonization description was valid for the low energy excitations of 1-D systems of interacting electrons, thus introducing the term "Luttinger Liquid".

Recent work on 2-D plasmons [111, 112] proposed a transmission line effective circuit model to relate electrical impedance measurement to the properties of the 2-D collective excitation, by measuring the kinetic inductance of a 2-D electron gas and its distributed electrostatic capacitance. Similar techniques will be performed here where 1-D plasmons will be directly excited by setting up standing-wave resonances in finite length SWNTs.

In the first part of this chapter, the kinetic inductance, electrostatic capacitance, quantum capacitance and characteristic impedance for a spinless 1-D quantum wire [113] will be calculated. Following the parameters mentioned above, will be discussed again, in the context of the associated spin of the electrons. Four coupled equations for the voltages on each of the four quantum channels, in a SWNT [114] will be calculated.

In the second part of this chapter, another method for CNT modelling will be presented. Numerical simulation techniques have become the most useful part of mathematical modeling of many natural systems in sciences such as physics and engineering. Additionally computational models, have helped achieve an in-depth understanding of electromagnetic phenomena. In 1873, the now well known Maxwell's equations, described precisely the electromagnetic theory. Subsequently, K. S. Yee [115], in 1966, introduced the first numerical time-domain method to describe Maxwell's equations that has been established almost a century ago.

The rapid development of computer processing power and the simplicity of the implementation of the available method, helped FDTD to quickly become the main simulation technique for electromagnetic problems and general engineering applications, e.g. antenna and communication problems. FDTD is able to accurately compute all the electromagnetic interactions such as propagation, reflection, scattering, diffraction and many more. As it is also a time-domain method, it produces results in the time domain, thus a Fast Fourier Transform (FFT) is needed to transform these results in frequency domain. The main benefit of the time domain techniques, is that they can obtain the whole frequency spectrum of an electromagnetic signal in a single simulation.

Other well known simulation methods are the Finite Element Method (FEM) and the Method of Moments (MoM). They are both frequency domain methods, allowing the computation of the signal for one frequency in one simulation.

4.2 Circuit model for spinless electrons in a one-channel quantum wire

As we have seen in chapter 2, CNTs can be either metallic or semiconducting depending on their geometry. SWNTs are 1D systems and DC conductance can be calculated from Landauer - Buttiker formalism: $G = N\frac{e^2}{h}T$, where N is the number of channels in parallel, e is the electron charge, h the Planck's constant and T the transmission coefficient. For a SWNT there are two propagation channels in a quantum wire, which can also be derived from their band structure. Because of the two possible directions of spin; up and down, 4 parallel propagation channels in total are considered. For now, we will assume that the electron has no spin, so only 1 channel is present and then, $N = 1$.

If the contact is perfect ($T = 1$), and the CNT is scatter-free, the charge carriers travel through the nanotube ballistically. The conductance then is $G = \frac{e^2}{h}$ hence, $R = R_{\min} = \frac{h}{e^2} = 25.8k\Omega$. Usually, $R \geq R_{\min}$ because $T < 1$ (due to reflections at the imperfect metal/CNT interface).

For ac, the equivalent model is theoretically thought to be similar to a transmission line with a distributed quantum capacitance and kinetic inductance per unit length. It is also believed that the electron-electron interactions can be included in the transmission line circuit analogy as an electrostatic capacitance alongside a magnetic inductance. This circuit model described in Figure 55, has yet to be established experimentally.

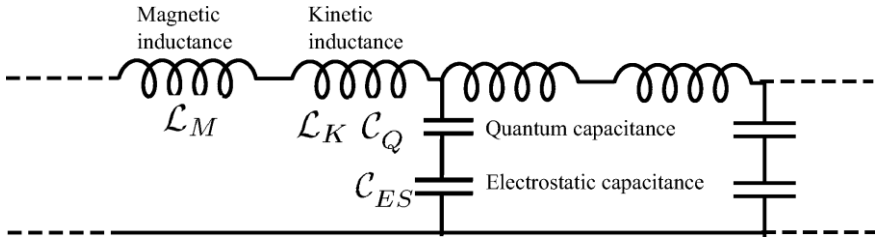

Figure 55: Circuit diagram for 1-D system of spinless electrons [116, 117].

In the following paragraphs all the four parameters, magnetic and kinetic inductance, and electrostatic and quantum capacitance, that appear in Figure 55 will be discussed. This model is based on a CNT over a ground plane (Figure 56). This distance appears in the functions as h. If no ground is present then, this h has to be replaced with the length of the nanotube.

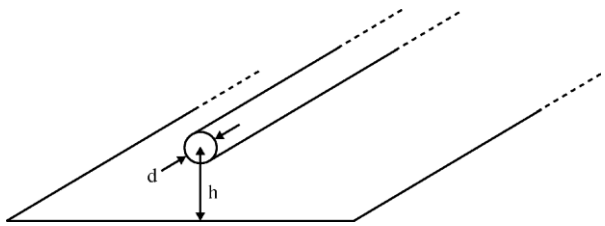

Figure 56: A Carbon Nanotube placed over a ground plane [116, 117].

4.2.1 Magnetic Inductance

When a ground plane is present underneath the 1-D wire (in this situation is a CNT), the magnetic inductance is described by [116]:

$$L_M = \frac{\mu}{2\pi}\cosh^{-1}\left(\frac{2h}{d}\right) \approx \frac{\mu}{2\pi}\ln\left(\frac{h}{d}\right) \tag{4.1}$$

where d is the diameter of the nanotube and h the distance from the ground plane; Figure 56. This equation was derived by setting the inductive energy equal to the stored magnetic energy [116]:

$$\frac{1}{2}LI^2 = \frac{1}{2\mu}\int B(x)^2\, d^3x \tag{4.2}$$

Depending on the geometry of interest, we can use the relation between I and B, to find the final equation. For example, where a nanotube is placed over a ground plane, we use the relation of a wire on top of a ground plane.

For nanotubes the magnetic inductance is logarithmically sensitive to the ratio h/d and for average numbers the numerical value is $L_M \approx 1pH/\mu m$ [116]. That value is given in microns instead of nanometres because modern growing techniques can produce nanotubes with micrometer lengths expanding to some millimetres, in some cases.

4.2.2 Kinetic Inductance

In order to calculate the kinetic inductance per unit length, we first need to calculate the kinetic energy per unit length. That is described, for a 1-D wire, as the sum of the kinetic energies of the left movers and right movers. Generally, if there are i.e. more left movers than right movers, we have a net current which flows through the wire. If the Fermi level of the left movers is raised by $e\Delta\mu/2$ and the Fermi level of the right movers is decreased by $e\Delta\mu/2$, then the current in the 1-D wire is $I = \frac{e^2}{h\Delta\mu}$ [116]. The net increase in energy of the system is the excess number of electrons, $N = \frac{e\Delta\mu}{2\delta}$ in the left against right moving states, multiplied by the energy added per electron $e\Delta\mu/2$, where δ is the single particle energy level spacing, related to the Fermi velocity, $\delta = \frac{\hbar u_F 2\pi}{L}$ [116]. Thus, the excess kinetic energy is given as $\frac{hI^2}{4u_F e^2}$ [116]. If we equate this kinetic energy with the energy of the kinetic inductance: $\frac{1}{2}LI^2$, we derive the following expression for the kinetic inductance per unit length [116]:

$$L_K = \frac{h}{2e^2 u_F} \tag{4.3}$$

where u_F is the Fermi velocity which is taken as $u_F = 8 \cdot 10^5 m/\sec$, so the numerical value for kinetic inductance is $L_K = 16nH/\mu m$ [116].

We can now compare the magnitude of the magnetic inductance to the kinetic inductance for the nanotube. That is [118]:

$$\frac{L_M}{L_K} = a\frac{2}{\pi}\frac{u_F}{c}\ln\left(\frac{h}{d}\right) \tag{4.4}$$

which is approximately 10^{-4}. In equation (4.4), a stands for the fine structure constant and it is $a \approx \frac{1}{137}$. Thus, in 1-D systems the kinetic inductance will always dominate over the magnetic. This is an important point for nanoelectronics as it allows approximation of the difference between macroscopic circuits with long thin wires, between the cases where they are considered to have large magnetic inductance, and the case of nanowires where the kinetic inductance dominates.

4.2.3 Electrostatic Capacitance

For the system depicted in figure 10, the electrostatic capacitance is given by [118]:

$$C_E = \frac{2\pi\varepsilon}{\cosh^{-1}\left(\frac{2h}{d}\right)} \approx \frac{2\pi\varepsilon}{\ln\left(\frac{h}{d}\right)} \tag{4.5}$$

Equation (4.5) can be numerically approximated as $C_E \approx 50aF/\mu m$ [116]. This has been calculated in a similar way to the magnetic inductance, setting the capacitive energy equal to the stored electrostatic energy [117]:

$$\frac{1}{2}\frac{Q^2}{C} = \frac{\varepsilon}{2}\int E(x)^2 \, d^3x \tag{4.6}$$

Again, depending on the geometry of interest, we can use the relation between E and Q, to find the final equation.

4.2.4 Quantum Capacitance

In a classical electron gas, where it can either be 1-D, 2-D or 3-D, there is no energy cost to add an extra electron. This means that we can add an electron with any arbitrary energy to the system. In a quantum electron gas, due to the Pauli exclusion principle, it is only possible to add an electron with energy more than the Fermi energy, and that energy corresponds to an available quantum state.

For nanotubes, which are 1-D systems with length L, the distance between quantum states is described as:

$$\delta E = \frac{dE}{dk}\delta k = \hbar u_F \frac{2\pi}{L} \tag{4.7}$$

By equating this energy cost with an effective quantum capacitance [119, 120] with energy given by:

$$\frac{e^2}{C_Q} = \delta E \tag{4.8}$$

we can derive the quantum capacitance per unit length:

$$C_Q = \frac{2e^2}{hu_F} \tag{4.9}$$

which numerically gives $C_Q = 100aF / \mu m$ [116, 117].

If we compare, similarly with inductances, the electrostatic capacitance with the quantum capacitance we can realize that [116]:

$$\frac{C_{ES}}{C_Q} = \frac{2\pi h}{e^2 \mu u_F} \ln\left(\frac{h}{d}\right) = \frac{1}{a}\frac{2}{\pi}\frac{u_F}{c}\ln\left(\frac{h}{d}\right) \sim 1 \tag{4.10}$$

Thus, both electrostatic and quantum capacitance must be considered when investigating the capacitance behaviour of nano-electronic circuit elements.

4.2.5 Wave Velocity

The wave velocity for any transmission line with distributed inductance and capacitance is given by:

$$u = \frac{1}{\sqrt{LC}} \tag{4.11}$$

It is interesting to note here that if we assume that the magnetic inductance dominates over the kinetic inductance and the electrostatic capacitance dominates over the quantum capacitance, then the wave velocity will be equal to the speed of light, as to a conventional metallic wire [116]:

$$u_{wire} = \sqrt{\frac{1}{L_M C_{ES}}} = \sqrt{\frac{1}{\mu\varepsilon}} = c \tag{4.12}$$

In contrast to the previous calculation, a full solution to the collective mode of a carbon nanotube should include both kinetic and magnetic inductance. The summation of these two is given by:

$$L_{total} = L_K + L_M \tag{4.13}$$

As it was mentioned before, we can approximate the equation: $L_{total} = L_K$.

The same happens for the capacitance, where both electrostatic and quantum capacitance must be considered, resulting in total capacitance of:

$$\frac{1}{C_{total}} = \frac{1}{C_Q} + \frac{1}{C_{ES}} \tag{4.14}$$

If we now neglect the Coulomb interaction, thus neglect the electrostatic capacitance we can calculate the wave velocity for non-interacting tubes, which is [116]:

$$u_{\text{non-interacting}} \approx \sqrt{\frac{1}{L_K C_Q}} = u_F \tag{4.15}$$

Including in our calculation the electrostatic capacitance, would give a different value for the wave velocity, described as [116]:

$$u_{\text{interacting}} \approx \sqrt{\frac{1}{L_K C_{total}}} = \sqrt{\frac{1}{L_K C_Q} + \frac{1}{L_K C_{ES}}} > u_F \tag{4.16}$$

Obviously, this results in a larger value than Fermi velocity.

The ratio of these two wave velocities, which have been calculated in (4.15) and (4.16), gives the 'g' parameter which is very significant in the theory of Luttinger liquids [116]:

$$g = \frac{u_F}{u_{\text{interacting}}} = \frac{1}{\sqrt{1 + \frac{C_Q}{C_{ES}}}} = \frac{1}{\left(1 + a\frac{\pi}{2}\frac{c}{u_F}\frac{1}{\ln(h/d)}\right)^2} \tag{4.17}$$

4.2.6 Characteristic Impedance

The characteristic impedance of the transmission line is defined as the ratio of the ACvoltage to ACcurrent. In the circuit model presented above, the characteristic impedance is independent of position and is given by:

$$Z = \sqrt{\frac{L}{C}} \tag{4.18}$$

As we did for the wave velocity, if we only consider the magnetic inductance and the electrostatic capacitance, the equation (4.18) gives the characteristic impedance of free space:

$$Z_{\text{free-space}} = \sqrt{\frac{L_M}{C_{ES}}} = \sqrt{\frac{\mu}{\varepsilon}} \equiv Z_o = 377\Omega \tag{4.19}$$

If we now consider the quantum capacitance and neglect the electrostatic capacitance, and at the same time replace magnetic inductance with the kinetic inductance (as kinetic inductance dominates in 1-D wires), the equation (4.18) gives the quantum resistance [116, 117]:

$$Z_{\text{non-interacting}} = \sqrt{\frac{L_K}{C_Q}} = \frac{h}{2e^2} = 12.5k\Omega \tag{4.20}$$

With both capacitances considered, the equation (4.18) gives [116]:

$$Z_{\text{interacting}} = \sqrt{\frac{L_K}{C_{total}}} = \sqrt{\frac{L_K}{C_{ES}} + \frac{L_K}{C_Q}} = \sqrt{\frac{L_K}{C_Q}\left(1 + a\frac{\pi}{2}\frac{c}{u_F}\frac{1}{\ln\left(\frac{h}{d}\right)}\right)} = g^{-1}\frac{h}{2e^2} \tag{4.21}$$

To be complete, we must include the magnetic inductance as well, finding the full solution for the characteristic impedance [116]:

$$\begin{aligned} Z_{\text{interacting}} &= \sqrt{\frac{L_{total}}{C_{total}}} = \sqrt{\left(L_K + L_M\right)\left(\frac{1}{C_{ES}} + \frac{1}{C_Q}\right)} = \\ &= \frac{h}{2e^2}\sqrt{\left(1 + a\frac{\pi}{2}\frac{c}{u_F}\frac{1}{\ln\left(\frac{h}{d}\right)}\right)\left(1 + a\frac{2}{\pi}\frac{u_F}{c}\ln\left(\frac{h}{d}\right)\right)} = \\ &= \frac{h}{2e^2}\sqrt{1 + a\left(\frac{\pi}{2}\frac{c}{u_F}\frac{1}{\ln\left(\frac{h}{d}\right)} + \frac{2}{\pi}\frac{u_F}{c}\ln\left(\frac{h}{d}\right)\right) + a^2} \end{aligned} \tag{4.22}$$

4.3 Circuit Model for metallic single-wall carbon nanotube

As previously explained, a carbon nanotube has two propagating channels because of its band structure. In each channel, the electrons can have spin up or spin down, hence, there are four propagating channels in the Landauer - Buttiker formalism. In the rest of this section, we will discuss an effective circuit model which includes the contributions of all four channels.

4.3.1 Spin - charge separation at DC

It is well known that current is carried by electrons with spin up or spin down through a propagating channel. If we try to measure the conductance of such a wire, the electrical contacts are simultaneously found on both spin up and spin down channel in either end of the wire. This means that only two quantum channels are found in parallel. If we could inject current to the one channel, i.e. the spin up channel and at the same time extract current from the spin down channel, then the net charge current would be zero, but not the spin current. This illustrates the separation between spin and charge current in a 1-D wire at DC.

In the following sections we will generalize the above concept to the AC case where two modes for each channel will be considered, exactly as it occurs in a carbon nanotube. We will also neglect the magnetic inductance, as it is negligible compared to the kinetic inductance.

4.3.2 Non-interacting circuit model for metallic single-wall Carbon Nanotube

For the following model, we will assume that there is no electrostatic capacitance in our model, meaning that there is no electron-electron interaction. The ACequivalent circuit model for a carbon nanotube, can be represented simply with four channels in parallel each with its own kinetic inductance and quantum capacitance. Of course, the numerical value of these four kinetic inductances for each channel will be exactly the same. The same happens to the quantum capacitance. All the derivation for these parameters were done in the same manner, written separately for each of the four channels. The equivalent circuit is depicted in Figure 57.

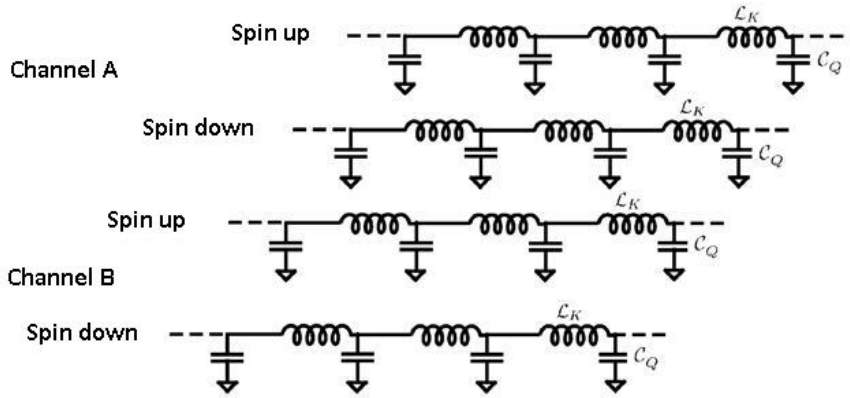

Figure 57: Circuit model for non-interacting electrons in a single-wall carbon nanotube. Two propagating channels, each one with spin up and spin down channel. There is no relation between these four channels [116].

4.3.3 Interacting circuit model for metallic single-wall Carbon Nanotube

At this point the electrostatic capacitance is introduced to present the equivalent circuit model for a carbon nanotube (Figure 58).

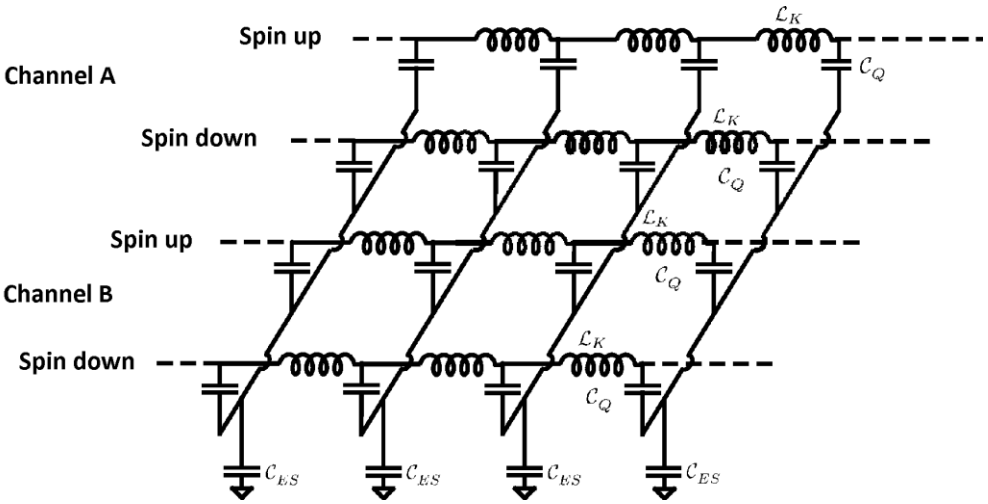

Figure 58: Circuit model for interacting electrons in a single-wall carbon nanotube. We can clearly visualize that the channels are not independent now [116].

Similarly to the DC case, if AC voltage applies to the nanotube, all four channels can be simultaneously excited. At one end of the nanotube, the grounded end, all four channels have zero voltage. At the other end, of the nanotube, called the hot end, all four channels have exactly the same voltage. The voltage along the nanotube will also be the same for all four channels. In that case, all the channels are excited equally and this mode is called normal mode. However, there is no spin current, despite the three normal modes which do not carry net charge current, thus called neutral modes. These however do carry spin currents.

In summary, a carbon nanotube when excited with AC voltage (Figure 58), has three spin modes (differential modes) and one current mode (common mode). We can also note here that the wave velocity for the charge mode is given by [116]:

$$u_{\text{common}} = \sqrt{\frac{1}{L_K}\left(\frac{1}{C_Q} + \frac{4}{C_{ES}}\right)} = u_F\sqrt{1 + \frac{4C_Q}{C_{ES}}} = \frac{u_F}{g} \tag{4.23}$$

and the wave velocity for the three spin modes [116]:

$$u_{\text{differential}} = u_F \tag{4.24}$$

Thus, the charge and spin modes have different velocities.

4.3.4 Spin - charge separation at AC

As discussed previously, the charge mode corresponds to AC currents which flow simultaneously through spin up and spin down channels in the same direction. This means that we will have a local charging-discharging of the nanotube and both quantum and electrostatic capacitance to the ground plane are involved. If we consider the kinetic inductance as well, assuming magnetic inductance is equal to zero, we can calculate the wave velocity. The result is given by (4.23).

The spin mode corresponds to AC currents with spin up electrons flowing in one direction and spin down electrons flowing in the opposite direction. Since these currents are always equal in magnitude to each other, there is never a net (spin) charge at any position along the nanotube. Therefore, the electrostatic capacitance is totally independent from the spin mode, rendering the wave velocity different from the charge mode. The distributed capacitance per unit length for the charge mode

consists of both the quantum and electrostatic capacitance, whereas for the spin mode it consists of only the quantum capacitance. The spin mode velocity is equal to Fermi velocity (4.24), in contrast with the charge mode velocity which is g^{-1} multiplied by the Fermi velocity.

4.4 Maxwell Equations

Maxwell's equations are a set of four equations which can explain every electromagnetic behaviour throughout all media at all times. The equations are based on previous theoretical and practical work by Ampere, Faraday and Gauss. The electromagnetic waves, that are fully characterized by Maxwell's equations, are supposed to propagate in continuous space and time. On the other hand the electromagnetic fields can be maintained when the source is absent, can be in the form of electric or magnetic charges or currents, and can be either static or dynamic.

In an isotropic, homogeneous, linear medium the electric and magnetic fields, $\boldsymbol{E}$ and $\boldsymbol{H}$ respectively, are related to the electric and magnetic flux densities, $\boldsymbol{D}$ and $\boldsymbol{B}$, and the electric and magnetic current densities $\boldsymbol{J}$ and $\boldsymbol{M}$ as described below:

$$\nabla \times \boldsymbol{E} = -\frac{\partial \boldsymbol{B}}{\partial t} - \boldsymbol{M} \tag{4.25}$$

$$\nabla \times \boldsymbol{H} = \frac{\partial \boldsymbol{D}}{\partial t} + \boldsymbol{J} \tag{4.26}$$

$$\nabla \cdot \boldsymbol{D} = \rho \tag{4.27}$$

$$\nabla \cdot \boldsymbol{B} = 0 \tag{4.28}$$

where:

$\boldsymbol{E}$ (V/m) is the electric field

$\boldsymbol{H}$ (A/m) is the magnetic field

$\boldsymbol{D}$ (C/m^2) is the electric flux density

$\boldsymbol{B}$ (Wb/m^2) is the magnetic flux density

$\boldsymbol{M}$ $\left(V/m^2\right)$ is the fictitious magnetic current density

$\boldsymbol{J}$ $\left(A/m^2\right)$ is the conduction electric current density

ρ $\left(C/m^3\right)$ is the electric charge density

The constitutive equations which relate the fields to the properties of the medium are given by:

$$\boldsymbol{D} = \varepsilon_0 \varepsilon_r \boldsymbol{E} \tag{4.29}$$

$$\boldsymbol{B} = \mu_0 \mu_r \boldsymbol{H} \tag{4.30}$$

$$\boldsymbol{J} = \sigma \boldsymbol{E} \tag{4.31}$$

$$\boldsymbol{M} = \sigma^* \boldsymbol{H} \tag{4.32}$$

where:

ε_r is the relative electric permittivity

μ_r is the relative magnetic permeability

ε_0 $\left(F/m\right)$ is the free-space permittivity = 8.854×10^{-12}

μ_0 $\left(H/m\right)$ is the free-space permeability = $4\pi \times 10^{-7}$

σ $\left(S/m\right)$ is the electric conductivity

σ^* $\left(\Omega/m\right)$ is the electric conductivity

The electric permittivity measures the medium's ability to transmit and store electromagnetic waves whereas the magnetic permeability expresses how easily a medium can be magnetised, when a magnetic field is applied. Finally, the conductivity measures the material's strength to conduct electric current.

In general, materials can either be good conductors or dielectrics. The relative permittivity of conventional materials is derived from equations (4.26), (4.29) and (4.31):

$$\nabla \times \boldsymbol{H} = \frac{\partial \boldsymbol{D}}{\partial t} + \boldsymbol{J} = \frac{\partial \varepsilon_r \varepsilon_0 \boldsymbol{E}}{\partial t} + \sigma \boldsymbol{E} = \left(\varepsilon_r \varepsilon_0 \frac{\partial}{\partial t} + \sigma \right) \boldsymbol{E} = \left(\sigma + j\omega \varepsilon_r \varepsilon_0 \right) \boldsymbol{E} =$$
$$= j\omega \varepsilon_0 \left(\varepsilon_r + \frac{\sigma}{j\omega \varepsilon_r} \right) \boldsymbol{E} = j\omega \varepsilon' \boldsymbol{E} = \frac{\partial \varepsilon' \boldsymbol{E}}{\partial t} = \frac{\partial \boldsymbol{D}}{\partial t} \tag{4.33}$$

In the above equation, a harmonic dependence of the source $\exp(j\omega t)$ is assumed hence the phasor form of the partial time derivative is used $\frac{\partial}{\partial t} = j\omega$.

From (4.33) one can derive the complex relative permittivity:

$$\varepsilon_r' = \varepsilon_r + \frac{\sigma}{j\omega \varepsilon_0} = \varepsilon_r - j\frac{\sigma}{\omega \varepsilon_0} \tag{4.34}$$

All conductive material found in nature, have losses. Therefore, it is impossible to have a perfect electric conductor (PEC), due to the imaginary part of the relative permittivity in equation (4.34). The loss, according to (4.34), is strongly dependent on the frequency $\omega = 2\pi f$ and is higher in lower frequencies. The ratio of the imaginary to real part of relative permittivity, is the loss tangent $\tan\delta = \frac{\sigma}{\omega \varepsilon_0 \varepsilon_r}$, which represents the loss rate of the medium.

4.5 Fundamentals of the Finite-Difference Time-Domain Method

In 1910s, L. E. Richardson [121, 122] used the finite difference method (FDM) to solve differential equations for weather forecasting. Ten years later, in 1920s, A. Thom [123] has also used FDM to solve nonlinear hydrodynamic equations. All finite difference techniques, such as FDM and FDTD, substitute differential equations with finite difference approximations. Space and time dimensions are discretised, and they finite difference approximations are calculated in every discrete point. The value of each point is related to the values from some neighboring points, where computational power is needed.

Considering a domain which is lossless and source-free, and every single field vector in Maxwell's equations (4.26)-(4.28) are functions of space and time (x, y, z) and t respectively, then these equations can be transformed to (4.35)-(4.38):

$$\nabla \times \boldsymbol{E} = -\frac{\partial \boldsymbol{B}}{\partial t} \tag{4.35}$$

$$\nabla \times \boldsymbol{H} = \frac{\partial \boldsymbol{D}}{\partial t} \tag{4.36}$$

$$\nabla \cdot \boldsymbol{D} = 0 \tag{4.37}$$

$$\nabla \cdot \boldsymbol{B} = 0 \tag{4.38}$$

We can re-write (4.35) into its vectorial form

$$\begin{aligned} \nabla \times \boldsymbol{E} &= \left(\frac{\partial E_z}{\partial y} - \frac{\partial E_y}{\partial z} \right) \vec{e}_x + \left(\frac{\partial E_x}{\partial z} - \frac{\partial E_z}{\partial x} \right) \vec{e}_y + \left(\frac{\partial E_y}{\partial x} - \frac{\partial E_x}{\partial y} \right) \vec{e}_z = -\frac{\partial \boldsymbol{B}}{\partial t} = \\ &= -\left(\frac{\partial B_x}{\partial t} \vec{e}_x + \frac{\partial B_y}{\partial t} \vec{e}_y + \frac{\partial B_z}{\partial t} \vec{e}_z \right) \end{aligned} \tag{4.39}$$

and from (4.39) we can deduce the following equations:

$$\frac{\partial E_z}{\partial y} - \frac{\partial E_y}{\partial z} = -\frac{\partial B_x}{\partial t} \tag{4.40}$$

$$\frac{\partial E_x}{\partial z} - \frac{\partial E_z}{\partial x} = -\frac{\partial B_y}{\partial t} \tag{4.41}$$

$$\frac{\partial E_y}{\partial x} - \frac{\partial E_x}{\partial y} = -\frac{\partial B_z}{\partial t} \tag{4.42}$$

In the same manner, the (4.36) can be written in the vectorial form

$$\begin{aligned} \nabla \times \boldsymbol{H} &= \left(\frac{\partial H_z}{\partial y} - \frac{\partial H_y}{\partial z} \right) \vec{e}_x + \left(\frac{\partial H_x}{\partial z} - \frac{\partial H_z}{\partial x} \right) \vec{e}_y + \left(\frac{\partial H_y}{\partial x} - \frac{\partial H_x}{\partial y} \right) \vec{e}_z = \frac{\partial \boldsymbol{D}}{\partial t} = \\ &= \left(\frac{\partial D_x}{\partial t} \vec{e}_x + \frac{\partial D_y}{\partial t} \vec{e}_y + \frac{\partial D_z}{\partial t} \vec{e}_z \right) \end{aligned} \tag{4.43}$$

and from (4.39) we can write the following equations:

$$\frac{\partial H_z}{\partial y} - \frac{\partial H_y}{\partial z} = \frac{\partial D_x}{\partial t} \tag{4.44}$$

$$\frac{\partial H_x}{\partial z} - \frac{\partial H_z}{\partial x} = \frac{\partial D_y}{\partial t} \tag{4.45}$$

$$\frac{\partial H_y}{\partial x} - \frac{\partial H_x}{\partial y} = \frac{\partial D_z}{\partial t} \tag{4.46}$$

The discretised (in space and time) equations (4.40)-(4.42) and (4.44)-(4.46) with the constitutive equations (4.29)-(4.30) are the core of the finite difference concept [115]:

$$\begin{aligned} H_x^{n+1}(i,j,k) &= H_x^n(i,j,k) + \frac{\Delta t}{\mu_0 \mu(i,j,k)\Delta z}\left[E_y^n(i,j,k) - E_y^n(i,j,k-1)\right] - \\ &- \frac{\Delta t}{\mu_0 \mu(i,j,k)\Delta y}\left[E_z^n(i,j,k) - E_z^n(i,j-1,k)\right] \end{aligned} \tag{4.47}$$

$$\begin{aligned} H_y^{n+1}(i,j,k) &= H_y^n(i,j,k) + \frac{\Delta t}{\mu_0 \mu(i,j,k)\Delta x}\left[E_z^n(i,j,k) - E_z^n(i-1,j,k)\right] - \\ &- \frac{\Delta t}{\mu_0 \mu(i,j,k)\Delta z}\left[E_x^n(i,j,k) - E_x^n(i,j,k-1)\right] \end{aligned} \tag{4.48}$$

$$\begin{aligned} H_z^{n+1}(i,j,k) &= H_z^n(i,j,k) + \frac{\Delta t}{\mu_0 \mu(i,j,k)\Delta y}\left[E_x^n(i,j,k) - E_x^n(i,j-1,k)\right] - \\ &- \frac{\Delta t}{\mu_0 \mu(i,j,k)\Delta x}\left[E_y^n(i,j,k) - E_y^n(i-1,j,k)\right] \end{aligned} \tag{4.49}$$

$$\begin{aligned} E_x^{n+1}(i,j,k) &= E_x^n(i,j,k) + \frac{\Delta t}{\varepsilon_0 \varepsilon(i,j,k)\Delta y}\left[H_z^n(i,j+1,k) - H_z^n(i,j,k)\right] - \\ &- \frac{\Delta t}{\varepsilon_0 \varepsilon(i,j,k)\Delta z}\left[H_y^n(i,j,k+1) - H_y^n(i,j,k)\right] \end{aligned} \tag{4.50}$$

$$\begin{aligned} \mathrm{E}_y^{n+1}(i,j,k) &= \mathrm{E}_y^n(i,j,k) + \frac{\Delta t}{\varepsilon_0 \varepsilon(i,j,k)\Delta z}\left[H_x^n(i,j,k+1) - H_x^n(i,j,k)\right] - \\ &- \frac{\Delta t}{\varepsilon_0 \varepsilon(i,j,k)\Delta z}\left[H_z^n(i+1,j,k) - H_z^n(i,j,k)\right] \end{aligned} \tag{4.51}$$

$$\begin{aligned} E_z^{n+1}(i,j,k) &= E_z^n(i,j,k) + \frac{\Delta t}{\varepsilon_0 \varepsilon(i,j,k)\Delta x}\left[H_y^n(i+1,j,k) - H_y^n(i,j,k)\right] - \\ &- \frac{\Delta t}{\varepsilon_0 \varepsilon(i,j,k)\Delta y}\left[H_x^n(i,j+1,k) - H_x^n(i,j,k)\right] \end{aligned} \tag{4.52}$$

In (4.47)-(4.52), the indices i, j, k and n are calculated from:

$$i = \frac{x}{\Delta x} \tag{4.53}$$

$$j = \frac{y}{\Delta y} \tag{4.54}$$

$$k = \frac{z}{\Delta z} \tag{4.55}$$

$$n = \frac{t}{\Delta t} \tag{4.56}$$

A brief description of the FDTD algorithm is given below. The first step, before setting up the source, is to initialize all the field components to zero. Next, the source, which can be an electromagnetic wave, electric/magnetic wave or current/voltage distribution. Then, the first part of the base equations of FDTD (4.47)-(4.49) are used to calculate the magnetic field H_x, H_y, H_z from the electric field values that have been calculated from the previous time step. Afterwards, the equations (4.50)-(4.52) update the values of electric field E_x, E_y, E_z using the magnetic field values which have been computed from the previous step and is going to be used to the next step to update the values of the magnetic field. Finally, the boundary conditions should be also checked. At this stage, the algorithm is repeated for the next time step value, creating a loop, where the source signal and the values of the magnetic field are being updated. The algorithm stops when either the number of time steps reaches the termination point or a stability criterion has been met.

The use of boundary conditions is usually compulsory. The memory in computers is limited therefore, periodic boundary conditions are applied, so the simulation space becomes smaller. In the case of the unwanted reflected waves, back to the simulation space, it is necessary to apply a set of absorbing boundary conditions (ABC) [124, 125] or perfect matched layers (PML) [126]. The most accurate and widely used approach of the above concept is the PML introduced by Berenger [126].

As it is presented above, the concept of the FDTD algorithm is simple and therefore can be simulated in a programming language such as MATLAB or C. The main

disadvantages of this algorithm are the huge computational power that is needed for execution and the numerical errors that are introduced which can lead to numerical instabilities and consequently incorrect results. These numerical instabilities are introduced due to the finite Taylor series (only first and second order) that is used to transform the partial derivatives of the Maxwell's equations (4.35)-(4.38) to finite difference approximations.

FDTD can be applied in many different areas in science. A feature that is very useful is that each grid point, can be assigned with a unique value of permittivity of permeability. That gives the opportunity to simulate many different types of geometries and structures, using complex media without any computational effort. Antennas [127], microwave circuit designs [128], carbon nanotubes [129] and liquid crystals [130] can be simulated using FDTD. Some examples of the above applications are given in this thesis.

In [129] an FDTD method is used to model thermal radiative properties of VACNTs. Each CNT is treated as a solid cylinder with an effective dielectric tensor. Results are compared with Maxwell-Garnett theory and generally confirm that VACNT arrays are highly absorptive. It is also proven that low volume fraction and long tubes are more favorable to achieve high absorbance. The effect of incident angle is also investigated which reveals an optimum incident angle at which the absorption can be maximized.

In general, when the permittivity or permeability of a material is a function of frequency, the material is said to be dispersive. In many cases, these material parameters can be assumed to be constant, therefore the results are considered to be slightly inaccurate. Such materials cannot be found in nature because they violate causality [131]. For a material behaving causally, a dispersive model has to be introduced to characterize its behaviour. The most famous frequency dispersive models are Drude [132] and Lorentz [133] model.

Moreover, the noble metals have negative permittivity values at infrared (IR), visible and ultra-violet (UV) frequencies [134] and their electromagnetic response can be accurately described with the Drude model [135]. Note that if relative permittivity

and permeability are less than one $(\varepsilon, \mu < 1)$, and are directly substituted to the conventional FDTD equations (4.47) to (4.52), then the electromagnetic energy does not anymore obey the second law of thermodynamics, the causality is violated [131], and the FDTD simulation becomes unstable and inaccurate [135].

Equations (4.47) to (4.52) must include the dispersive properties of the medium. The Lorentz dispersive model [133] was used to discretise time in (4.29) and (4.30), where the relative permittivity and permeability of the material are given by:

$$\varepsilon_r = \mu_r = 1 - \frac{\omega_p^2}{\omega^2 - j\omega\gamma - \omega_o^2} \tag{4.57}$$

where ω_p is the plasma frequency, ω_o the resonant frequency and γ the collision frequency.

Following the procedure explained in [135], the updating equations of the dispersive FDTD technique, which are otherwise known as the (E, D, H, B) scheme are given by:

$$\begin{aligned} B_x^{n+1}(i,j,k) &= B_x^n(i,j,k) + \frac{\Delta t}{\Delta z}\left[E_y^n(i,j,k) - E_y^n(i,j,k-1)\right] - \\ &- \frac{\Delta t}{\Delta y}\left[E_z^n(i,j,k) - E_z^n(i,j-1,k)\right] \end{aligned} \tag{4.58}$$

$$\begin{aligned} B_y^{n+1}(i,j,k) &= B_y^n(i,j,k) + \frac{\Delta t}{\Delta x}\left[E_z^n(i,j,k) - E_z^n(i-1,j,k)\right] - \\ &- \frac{\Delta t}{\Delta z}\left[E_x^n(i,j,k) - E_x^n(i,j,k-1)\right] \end{aligned} \tag{4.59}$$

$$\begin{aligned} B_z^{n+1}(i,j,k) &= B_z^n(i,j,k) + \frac{\Delta t}{\Delta y}\left[E_x^n(i,j,k) - E_x^n(i,j-1,k)\right] - \\ &- \frac{\Delta t}{\Delta x}\left[E_y^n(i,j,k) - E_y^n(i-1,j,k)\right] \end{aligned} \tag{4.60}$$

$$\begin{aligned} D_x^{n+1}(i,j,k) &= D_x^n(i,j,k) + \frac{\Delta t}{\Delta y}\left[H_z^n(i,j+1,k) - H_z^n(i,j,k)\right] - \\ &- \frac{\Delta t}{\Delta z}\left[H_y^n(i,j,k+1) - H_y^n(i,j,k)\right] \end{aligned} \tag{4.61}$$

$$D_y^{n+1}(i,j,k)=D_y^n(i,j,k)+\frac{\Delta t}{\Delta z}\left[H_x^n(i,j,k+1)-H_x^n(i,j,k)\right]-$$
$$-\frac{\Delta t}{\Delta x}\left[H_z^n(i+1,j,k)-H_z^n(i,j,k)\right] \tag{4.62}$$

$$D_z^{n+1}(i,j,k)=D_z^n(i,j,k)+\frac{\Delta t}{\Delta x}\left[H_y^n(i+1,j,k)-H_y^n(i,j,k)\right]-$$
$$-\frac{\Delta t}{\Delta y}\left[H_x^n(i,j+1,k)-H_x^n(i,j,k)\right] \tag{4.63}$$

$$E_{x,y,z}^{n+1}(i,j,k)=\left\{\left(\frac{1}{\varepsilon_o\Delta t^2}+\frac{\gamma_e}{2\varepsilon_o\Delta t}+\frac{\omega_{oe}^2}{4\varepsilon_o}\right)D_{x,y,z}^{n+1}(i,j,k)-\right.$$
$$-\left(\frac{2}{\varepsilon_o\Delta t^2}-\frac{\omega_{oe}^2}{2\varepsilon_o}\right)D_{x,y,z}^{n}(i,j,k)+$$
$$+\left(\frac{1}{\varepsilon_o\Delta t^2}-\frac{\gamma_e}{2\varepsilon_o\Delta t}+\frac{\omega_{oe}^2}{4\varepsilon_o}\right)D_{x,y,z}^{n-1}(i,j,k)+\left(\frac{2}{\Delta t^2}-\frac{\omega_{oe}^2+\omega_{pe}^2}{2}\right)E_{x,y,z}^{n}(i,j,k)-$$
$$\left.-\left(\frac{1}{\Delta t^2}-\frac{\gamma_e}{2\Delta t}+\frac{\omega_{oe}^2+\omega_{pe}^2}{4}\right)E_{x,y,z}^{n-1}(i,j,k)\right\}\Bigg/\left(\frac{1}{\Delta t^2}+\frac{\gamma_e}{2\Delta t}+\frac{\omega_{oe}^2+\omega_{pe}^2}{4}\right) \tag{4.64}$$

$$\mathrm{H}_{x,y,z}^{n+1}(i,j,k)=\left\{\left(\frac{1}{\mu_o\Delta t^2}+\frac{\gamma_m}{2\mu_o\Delta t}+\frac{\omega_{om}^2}{4\mu_o}\right)\mathrm{B}_{x,y,z}^{n+1}(i,j,k)-\right.$$
$$-\left(\frac{2}{\mu_o\Delta t^2}-\frac{\omega_{om}^2}{2\mu_o}\right)B_{x,y,z}^{n}(i,j,k)+$$
$$+\left(\frac{1}{\mu_o\Delta t^2}-\frac{\gamma_m}{2\mu_o\Delta t}+\frac{\omega_{om}^2}{4\mu_o}\right)B_{x,y,z}^{n-1}(i,j,k)+\left(\frac{2}{\Delta t^2}-\frac{\omega_{om}^2+\omega_{pm}^2}{2}\right)H_{x,y,z}^{n}(i,j,k)-$$
$$\left.-\left(\frac{1}{\Delta t^2}-\frac{\gamma_m}{2\Delta t}+\frac{\omega_{om}^2+\omega_{pm}^2}{4}\right)H_{x,y,z}^{n-1}(i,j,k)\right\}\Bigg/\left(\frac{1}{\Delta t^2}+\frac{\gamma_m}{2\Delta t}+\frac{\omega_{om}^2+\omega_{pm}^2}{4}\right) \tag{4.65}$$

Note that if the plasma, collision and resonant frequencies are set equal to zero: $\omega_{pe}=\omega_{pm}=\gamma_e=\gamma_m=\omega_{oe}=\omega_{om}=0$, the equations (4.64) and (4.65) are transformed to the free space FDTD updating algorithm.

4.6 Summary

We have considered the dynamic properties of single-walled carbon nanotubes from a circuit point of view and derived an effective RF circuit model for a single walled carbon nanotube, including the effects of kinetic inductance as well as the electrostatic and quantum capacitance. The nano-transmission line model is a circuit description of a 1-D plasmon, and as such is directly related to the long postulated Lüttinger liquid properties of 1-D systems. The RF circuit models we have presented here provide the foundation for further research on nanotube devices such as semiconducting nanotube transistors.

Finally, an introduction to the FDTD algorithm is given, using Maxwell's equations. Using the discretised (in both space and time) version of these equations the behaviour of electromagnetic waves in a variety of complex media can be accurately calculated. Hence, the concept of FDTD algorithm is presented and simulations of electromagnetic waves can be constructed and thoroughly studied using a programming language.

Chapter 5:

Further Investigation of Carbon Nanotube Properties

5.1 Introduction

The measurements of the VACNT films presented earlier, have shown that the uncertainties of complex permittivity and complex permeability are large, therefore it is necessary to introduce a function for both permittivity and permeability enabling the characterization of all the VACNT films. As expected, the equivalent permittivity and permeability of the CNT slabs are independent of their thickness. The thickness should affect the transmission and reflection parameters because of the change in the geometry of the slab. Therefore, it is necessary to introduce here the general permittivity and general permeability function that is independent of the thickness of the VACNT films.

The results presented in chapter 3, as well as the general permittivity and permeability functions, treat the carbon nanotube array as a homogeneous medium. However, theoretical models such as the Drude model for lossy metals applied to the VACNT films, and generally the effective medium approach, neglects phenomena such as field enhancement and multiple scattering [136]. Assuming that the S-parameter results are accurate enough, we applied optimization techniques to a unit

cell of a periodic structure, consisting of solid anisotropic cylinders with unknown complex permittivity and permeability. As a result, both complex permittivity and permeability were calculated for each frequency point.

Finally, an individual multi-walled carbon nanotube is treated as a solid anisotropic cylinder with an effective permittivity and permeability tensor. HFSS simulations were set up to calculate the behaviour (transmission, reflection and absorption) in optical frequencies (400 THz - 750 THz). The effect of some geometric parameters of the tube such as length, diameter and inter-tube distance between two consecutive tubes was also examined.

5.2 General permittivity and permeability functions in X-band and Ku-band

In this study, we validate the material parameter extraction presented in chapter 3 by using the in-house dispersive FDTD model on the effective medium of VACNT films. Measurements performed in low microwave frequencies in X-band (8-12 GHz) and Ku-band (12.4-18 GHz) are compared with the numerical results from the FDTD code. The model comprises a slab with the thickness of the sample in each case (30 μm, 95 μm, 252 μm). The complex permittivity of the slab was equivalent to the effective medium parameters extracted in chapter 3.

In general, when the permittivity or permeability of a material is a function of frequency, the material is said to be dispersive. In many cases, these material parameters can be assumed to be constant, therefore the results are considered to be slightly inaccurate. Such materials cannot be found in nature because they violate causality [131]. For a material behaving causally, a dispersive model has to be introduced to characterize its behaviour. The most famous frequency dispersive models are Drude [132] and Lorentz [133] model.

The main difference between the full wave simulations using CST and the FDTD presented here is the use of boundary conditions. The use of boundary conditions is usually compulsory. The memory in computers is limited therefore, periodic

boundary conditions are applied, so the simulation space becomes smaller. A brief description of the FDTD simulation setup, is given below. The source, which is an electromagnetic plane wave is placed on the left hand side of the simulation domain, Figure 59. The generated wave passes through a probe before it interacts with the slab with thickness d, which represents the effective medium of the VACNT films. After the slab, on the right hand side of the simulation domain, another probe is placed to monitor the transmitted wave which has been just penetrated the slab. It is interesting to note, that the air-slab interfaces make the wave to reflect back, therefore, the first probe is being able to monitor the reflected waves from the effective medium.

The use of a set of absorbing boundary conditions (ABC) [124, 125] is necessary as periodicity is crucial on x-direction, whereas, all the reflected waves touching the boundaries on y-direction are unwanted, therefore, perfect matched layers (PML) [126] are needed.

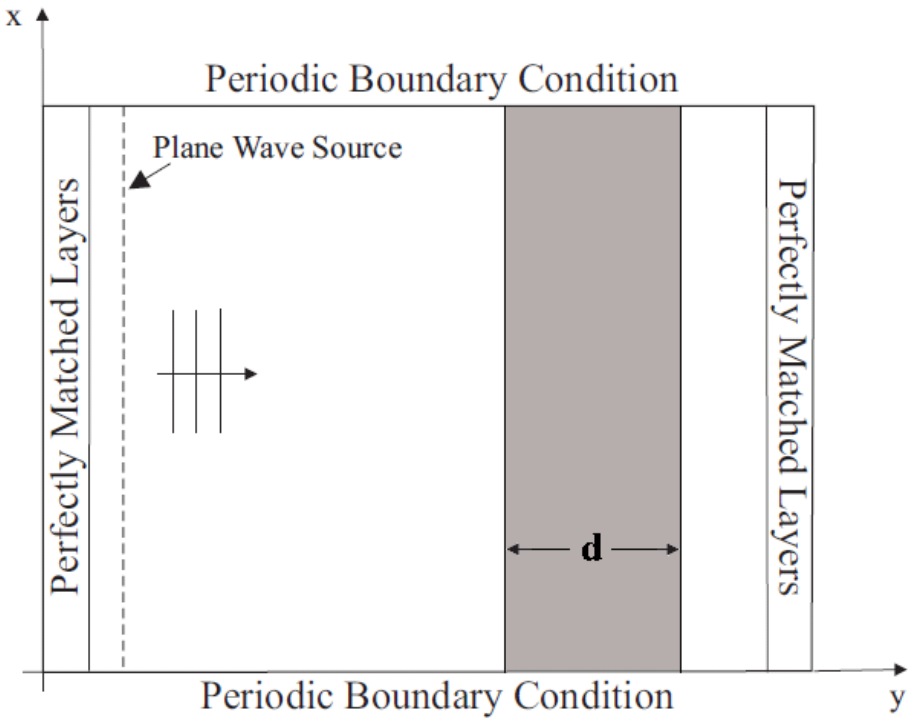

Figure 59: FDTD computation domain of the effective medium VACNT films for the case of plane wave excitation.

The S-parameters were calculated and plotted in the X-band with the measured results.

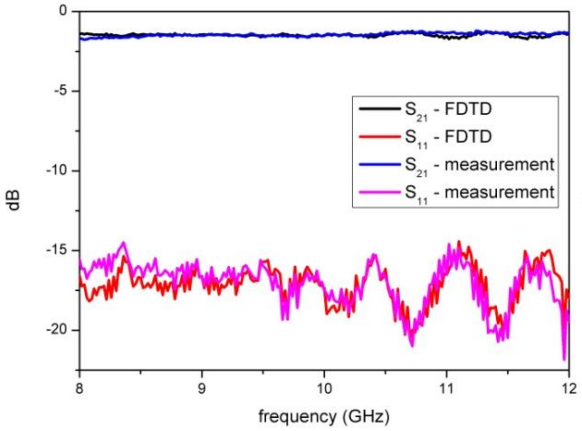

(a)

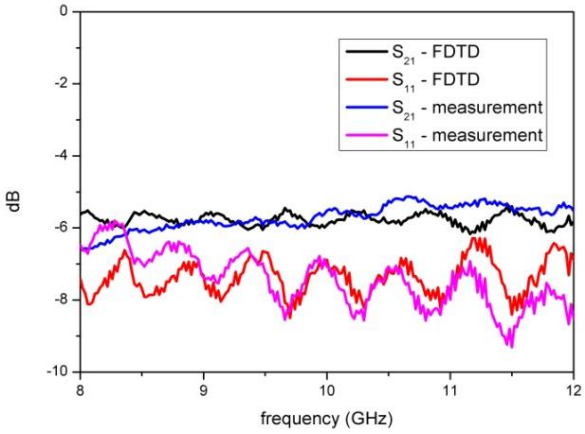

(b)

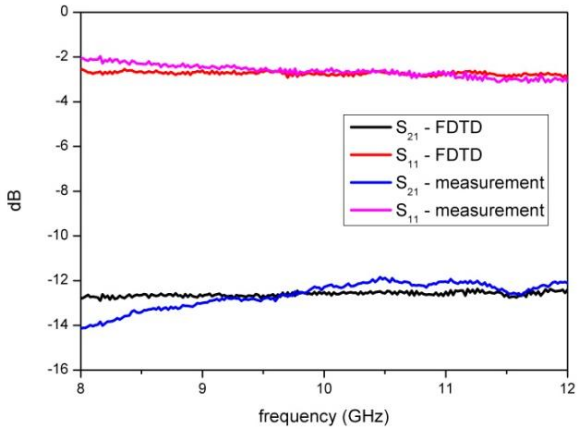

(c)

Figure 60: Comparison of FDTD results and measurements of the VACNT films (X-band). a) 30 μm b) 95 μm c) 252 μm.

Similar behaviour of the FDTD code was observed in Ku-band as well.

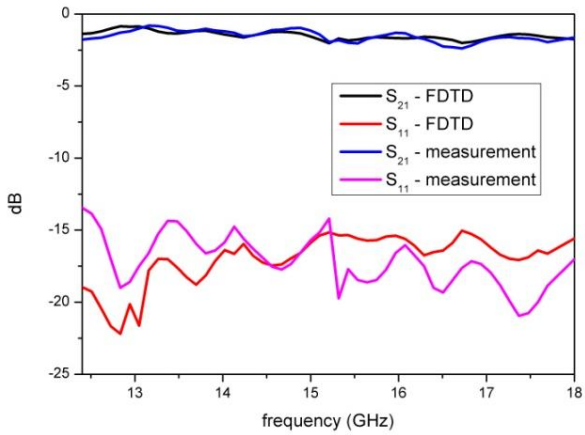

(a)

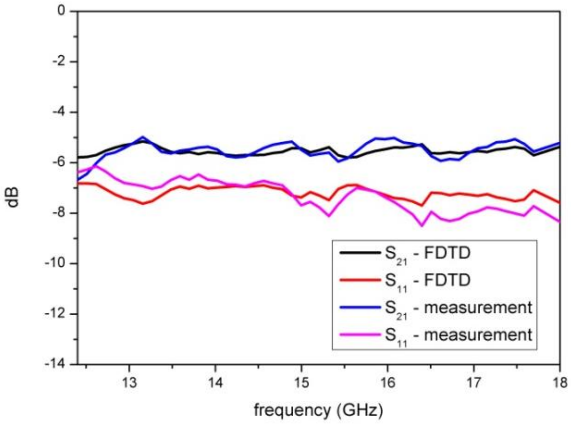

(b)

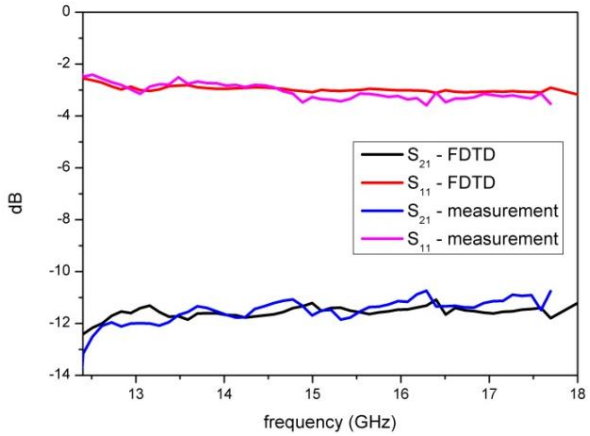

(c)

Figure 61: Comparison of FDTD results and measurements of the VACNT films (Ku-band). a) 30 μm b) 95 μm c) 252 μm.

The extracted parameters were verified by full wave simulations (CST) and numerical methods (FDTD) and very good agreement was obtained. The FDTD and CST simulation S-parameters and absorption were plotted with measurements for every different sample measured in both frequency bands. It should be noted that inserting the extracted complex permittivity and complex permeability into CST dispersive model, 1st order fitting is applied to the data automatically by the software, therefore the ripples cannot be predicted (Figure 62).

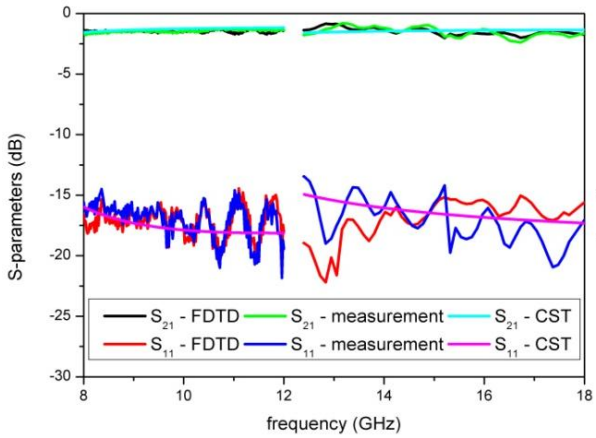

(a)

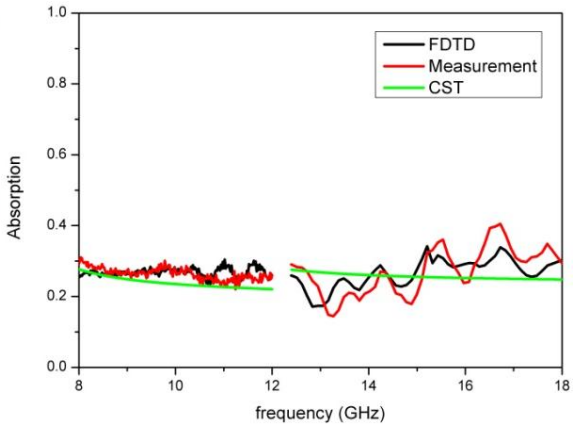

(b)

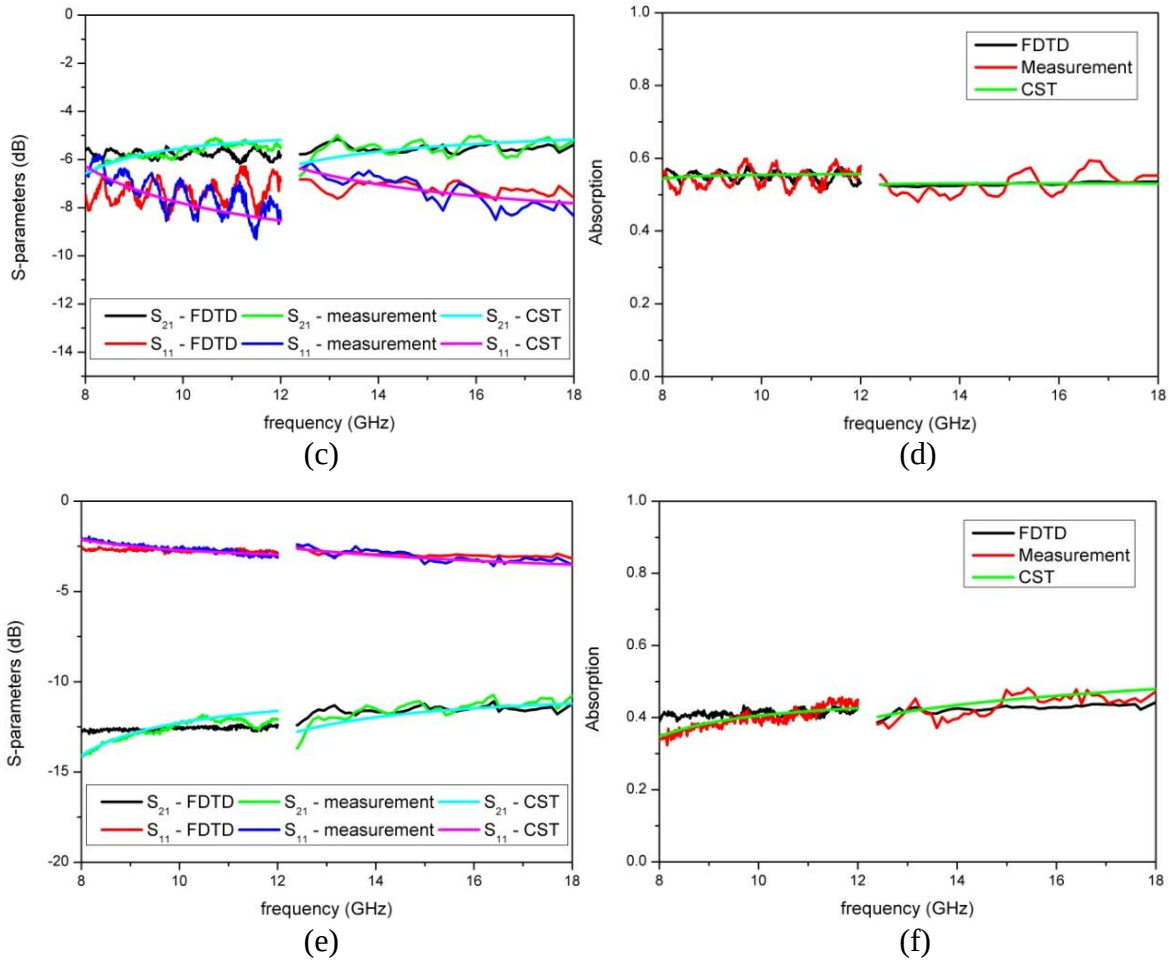

Figure 62: Comparison of numerical simulations (FDTD), full-wave simulations (CST) and measurements of the VACNT films. Magnitude of S-parameters and absorption are plotted. a-b) 30 μm c-d) 95 μm e-f) 252 μm.

As discussed above, the expected corresponding permittivity and permeability of any homogeneous medium, such as the VACNT films, is independent of the thickness. The different thickness of the three samples of VACNT films was a result of different S-parameters, but the material properties should remain unchanged. The samples have been grown similarly, however were not identical to each other. They appeared to have discrepancies arising from non-controlled, geometrical uncertainties in parameters such as air-gaps with neighboring nanotubes, concentrations of CNTs and concentrations of the Fe catalyst, resulting in moderately distinct effective media in all three samples. It is also understood that lengthening nanotubes, create entanglements with adjacent ones, directly proportional to the resulting length. The aforementioned, in addition to the measurement uncertainties of the S-parameters and

thickness, lead to a much different value of effective permittivity and permeability in each sample.

Creating an assumption that all the samples are exactly identical, and therefore none of the uncertainties explained in the above paragraph exist, it is only reasonable in attempting to find the general permittivity (GEF) and general permeability function (GMF) of the vertically aligned carbon nanotube films presented here. The mean values of the relative permittivity and permeability in each frequency point, was taken, for the three films under test and the general VACNT permittivity (Figure 63) and permeability (Figure 64) functions were calculated.

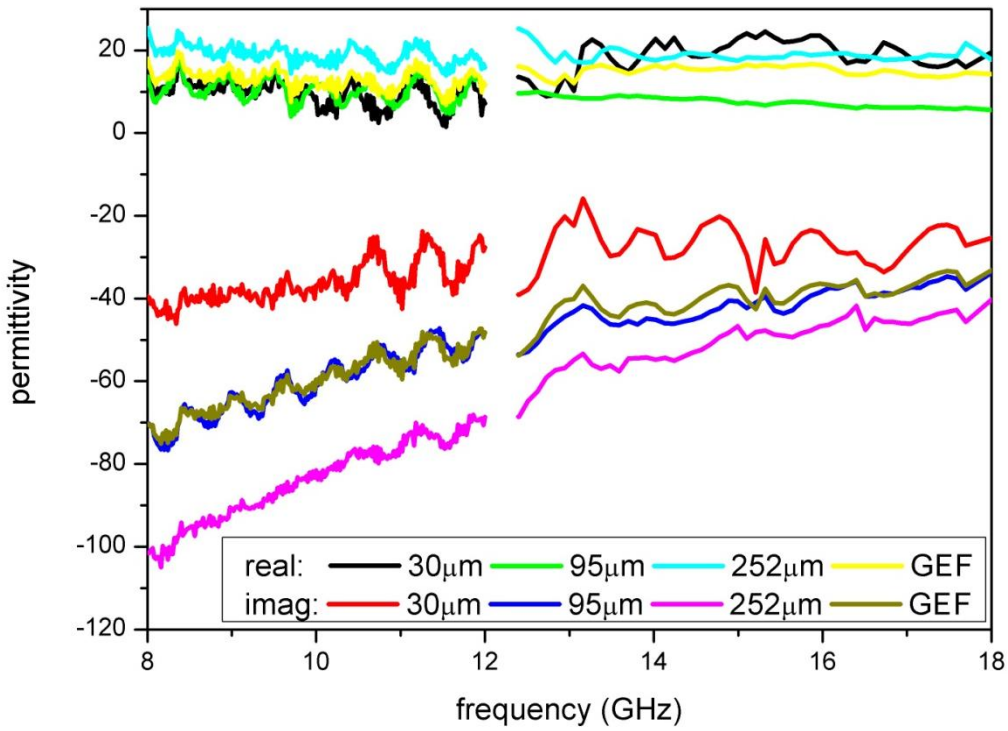

Figure 63: Relative permittivity of the three VACNT films. The general permittivity function (GEF) is calculated by taking the mean value on each frequency point.

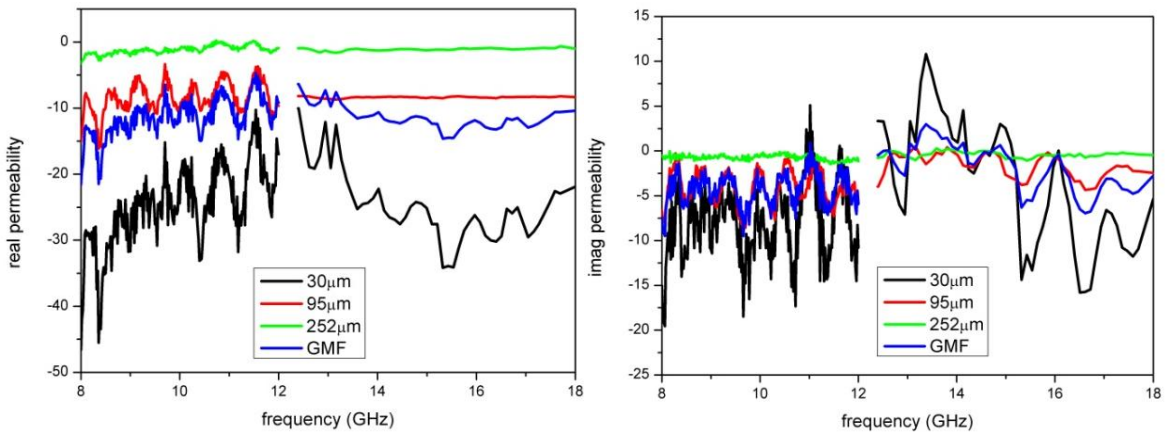

Figure 64: Relative permeability of the three VACNT films. The general permeability function (GMF) is calculated.

In the following Figure 65, the GEF of the VACNT films is plotted. The real part of the GEF shows values of 8 to 17 whereas the imaginary of -75 to -33. The complex general permittivity function ($\varepsilon = \varepsilon' - j \cdot \varepsilon''$) was approximated by fitting the real and the imaginary parts with linear and 2nd order polynomial fits according to the following equations:

$$\varepsilon' = 12.012 + 0.134 \cdot f \tag{5.1}$$

$$\varepsilon'' = 155 - 13.16 \cdot f + 0.363 \cdot f^2 \tag{5.2}$$

where f is the frequency in GHz.

Similarly, the complex general permeability function ($\mu = \mu' - j \cdot \mu''$) was approximated by linear fit of the real and the imaginary parts:

$$\mu' = -14.165 + 0.248 \cdot f \tag{5.3}$$

$$\mu'' = 6.866 - 0.278 \cdot f \tag{5.4}$$

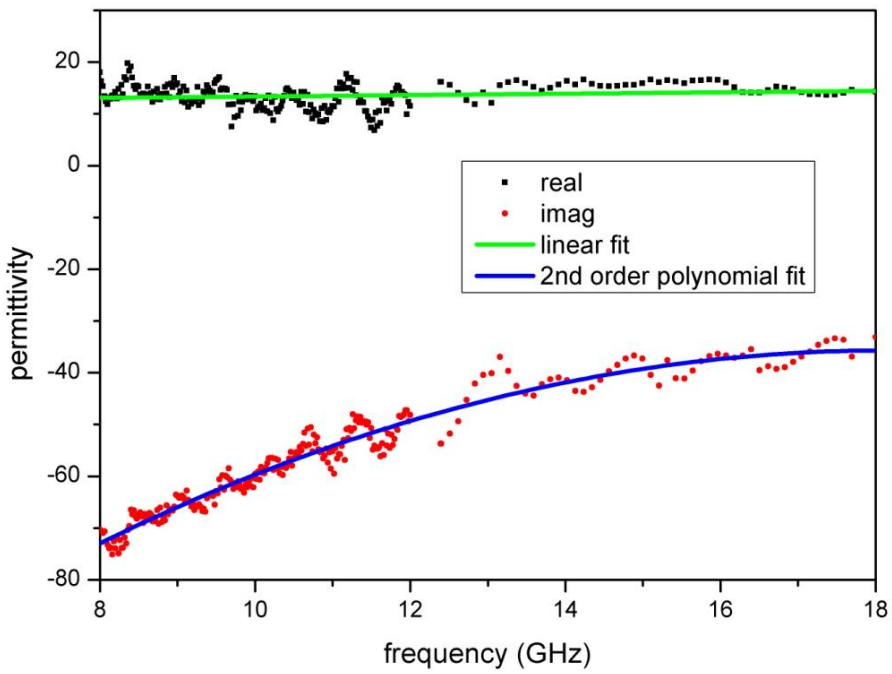

Figure 65: General permittivity function.

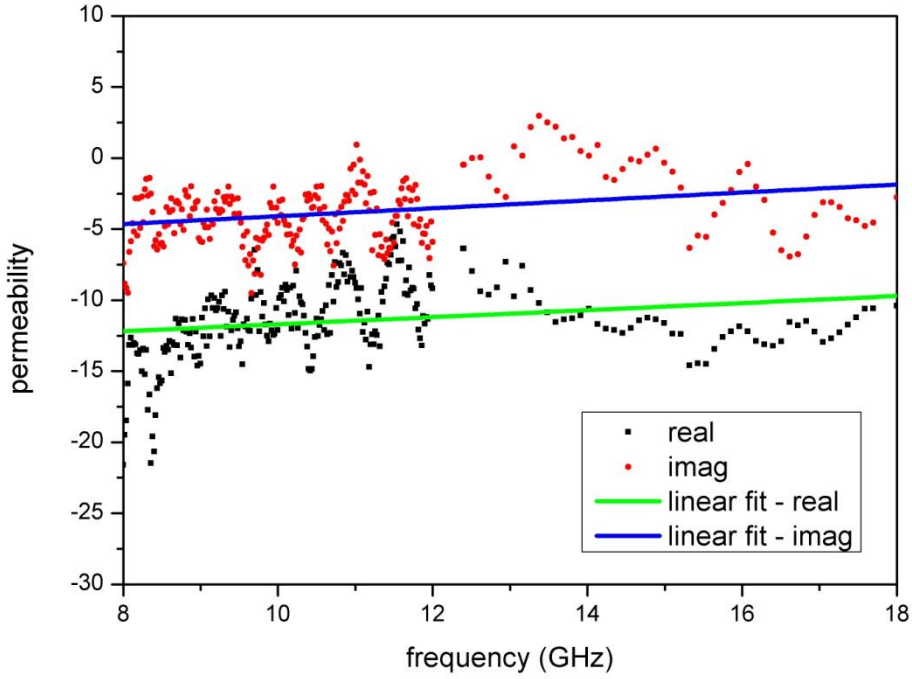

Figure 66: General permeability function

In the following Figure 67, the GEF and GMF assigned to the material parameters of a frequency dispersive material and then CST simulations were performed across the measured frequency bands. Analysis of the results shows that simulated magnitude and phase of the S-parameters follow the trend of the measured results and that they are in a very good agreement. The difference between Figure 67 and Figure 26 (X-

band) and Figure 33 (Ku-band), is negligible, therefore, the GEF and GMF were verified as an approximation of the permittivity and permeability function for VACNT films.

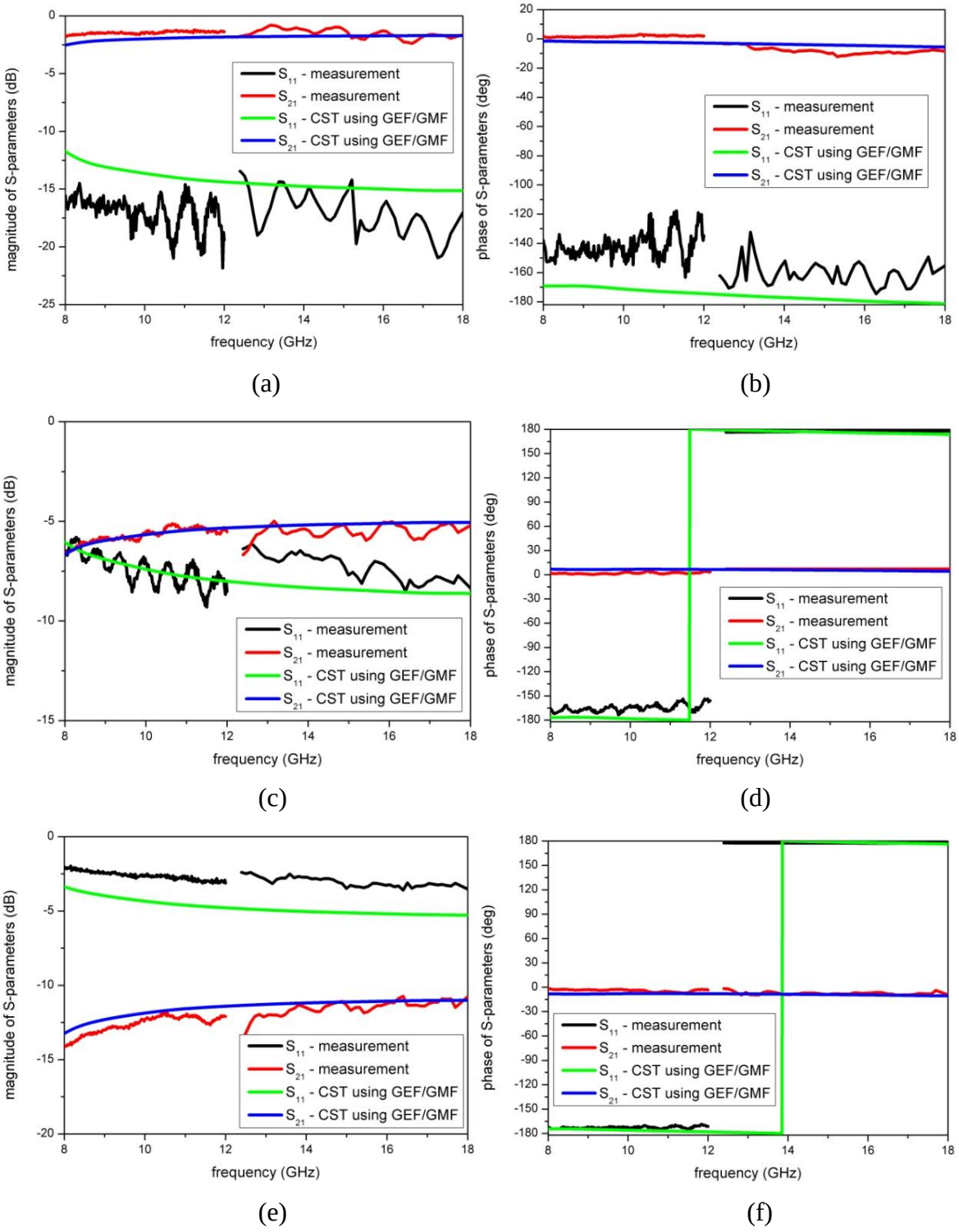

Figure 67: Measured and simulated magnitude and phase S-parameters. The simulations have been performed using the general permittivity (GEF) and permeability function (GMF). a-b) 30 µm c-d) 95 µm e-f) 252 µm.

5.3 Permittivity and permeability function for an individual carbon nanotube

The results presented treat the carbon nanotube array as a homogeneous medium. The complex permittivity and permeability were extracted, the general permittivity and permeability functions were calculated and the absorption performance of the films were examined. However, theoretical models, such as the Drude model for lossy metals applied to the VACNT films, and generally the effective medium approach, oversimplifies the problem. Some phenomena, such as field enhancement and multiple scattering [136] have therefore been neglected.

Recently individual carbon nanotubes have been numerically analyzed using the FDTD technique. Lidorikis et al. [137] simulated infinitely long multi-walled carbon nanotube arrays with irradiation incident from the one side of the array. In that study [137], it has been shown that CNT arrays are very good absorbers in the visible frequency range. Another work [129] examines the optical properties of vertical multi-walled carbon nanotubes, using the FDTD method as well, also comparing the predicted FDTD results with the effective medium Maxwell-Garnett theory.

The general permittivity (5.1)-(5.2) and permeability (5.3)-(5.4) functions show the effective medium characteristics of the VACNT films. That medium can be transformed into another, more complicated, but more realistic structure with aligned compact cylinders (Figure 68). The cylinder was placed in the center of the rectangular 3D unit cell. The cylinder which has a radius of $r = 40nm$ and length $d = 30\mu m$, whereas the periodicity is $a = 90nm$, was placed in the center of the periodic boundary conditions of the rectangular unit cell (Figure 69). This is an approximation of the geometry of the nanotubes assembled one of the VACNT film presented at the previous stage.

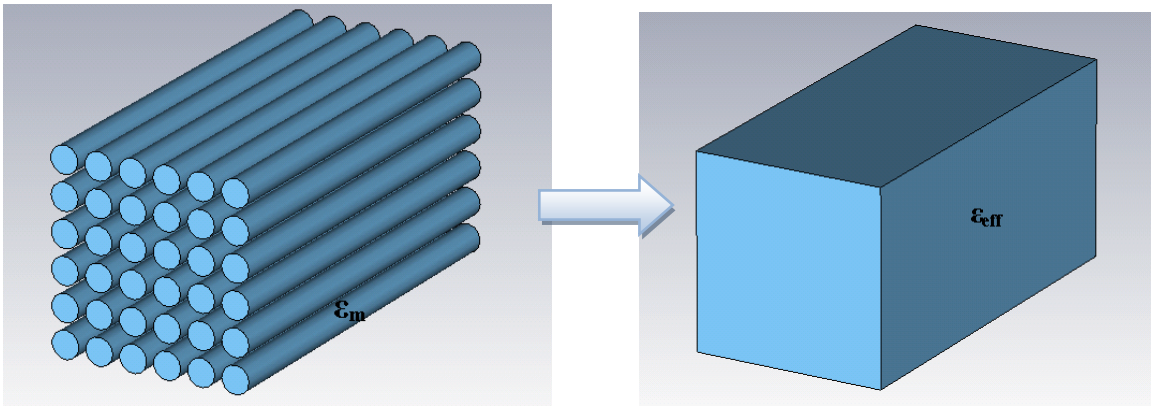

(a) (b)

Figure 68: a) Multi-walled carbon nanotubes with dielectric constant ε_m b) effective medium.

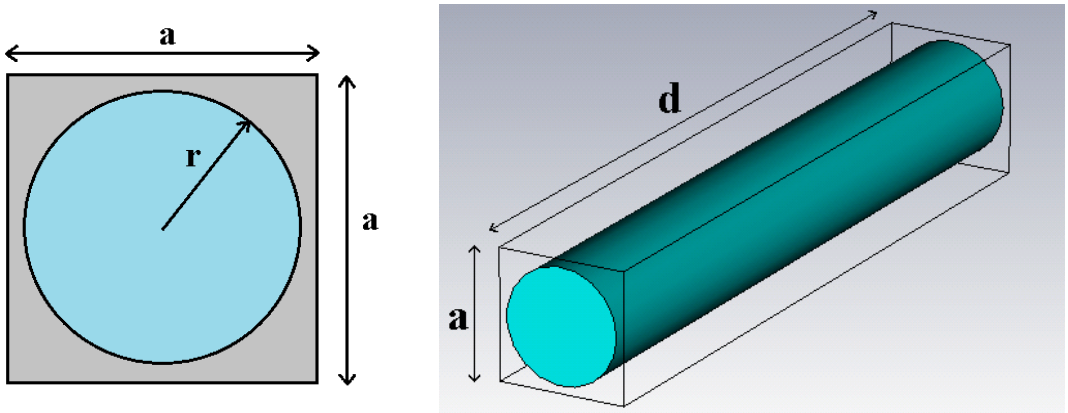

(a) (b)

Figure 69: a) cross-section of the unit cell b) 3D-view.

The S-parameters of the 30 μm effective medium sample were calculated, using the GEF and GMF. Setting these parameters as a target, optimization techniques were applied to the unit cell presented in Figure 69 with a large number of iterations, until the S-parameters of the two structures were matched (goal).

The optimization method used is that of Sequential Non-Linear Programming (SNLP). In Ansoft HFSS optimization analyses, five different methods are available including SNLP. The other four are Sequential Mixed Integer Non-Linear Programming (SMINLP), Quasi Newton, Pattern Search and Genetic Algorithm [138]. In the problem specified above, the SNLP was selected as the preferable method, as it is the only one that combines linear or non-linear relationships between

the parameters and the result, and not quantized values for the optimization parameters. Hence, the SNLP method assumes that the optimization variables span a continuous space and therefore, no minimum step size is needed to be specified. The variables may take any value within the allowable constraints and within the numerical precision limits of the simulator.

A 3D model of a unit cell in Ansoft HFSS full wave electromagnetic field simulation was set up, as illustrated in Figure 69. Eight different parameters characterizing the anisotropic compact cylinder of the unit cell, were representative of the carbon nanotube of the 30 μm film presented in chapter 3. Considering that the cylinder was placed along the z direction (propagation direction), it was therefore symmetric along the z-axis. Permittivity, permeability, dielectric and magnetic loss tangents for the x- and y- components were identical. The necessary parameters were:

ε_x, ε_x, ε_z: relative permittivity

$\tan\delta_{\varepsilon_x}$, $\tan\delta_{\varepsilon_x}$, $\tan\delta_{\varepsilon_z}$: dielectric loss tangent

μ_x, μ_x, μ_z: relative permeability

$\tan\delta_{\mu_x}$, $\tan\delta_{\mu_x}$, $\tan\delta_{\mu_z}$: magnetic loss tangent

where $\varepsilon_x = \varepsilon_\perp$ and $\varepsilon_z = \varepsilon_\parallel$.

The frequency step was set at 0.5 GHz where one simulation for each frequency point was needed. The optimized complex relative permittivity and permeability in each frequency step are presented in Figure 70-Figure 73. The relative permittivity of the individual carbon nanotube, followed the trend of the conventional lossy medium [139] and therefore Figure 70 and Figure 71 are fitted with (5.5):

$$\varepsilon = \varepsilon' + i\varepsilon'' = \varepsilon' + i\frac{\sigma}{\omega\varepsilon_o} \tag{5.5}$$

where ε' is the real part of the relative permittivity, and $\varepsilon'' = \frac{\sigma}{\omega\varepsilon_o}$ is the imaginary. The conductivity, σ, was considered to be constant and $\varepsilon_o = 8.854 \cdot 10^{-12}\, F/m$ was the permittivity of free space. Table 11 shows the fitted parameters of both components of the relative permittivity.

Table 11: Fitting parameters of the relative permittivity of a single CNT.

Parameter	Value	Standard Error
$\varepsilon'_{\perp}$	39.21	2.18
$\varepsilon'_{\parallel}$	31.87	1.44
$\sigma_{\varepsilon_{\perp}}$	69.54	2.67
$\sigma_{\varepsilon_{\parallel}}$	178.65	1.77

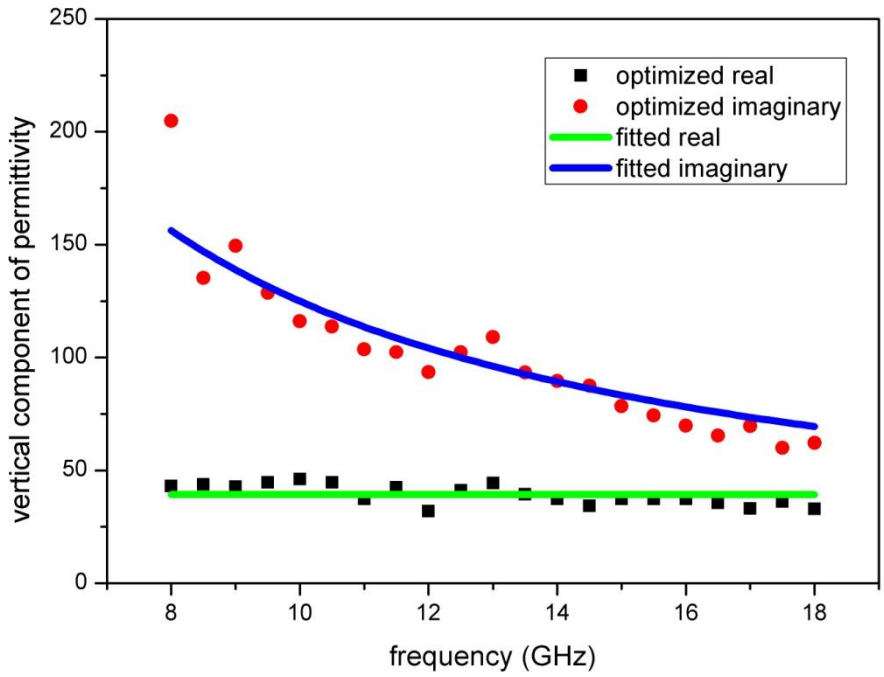

Figure 70: Vertical component of the permittivity, $\varepsilon_{\perp}$, of a single CNT. The results were fitted with the conventional lossy medium.

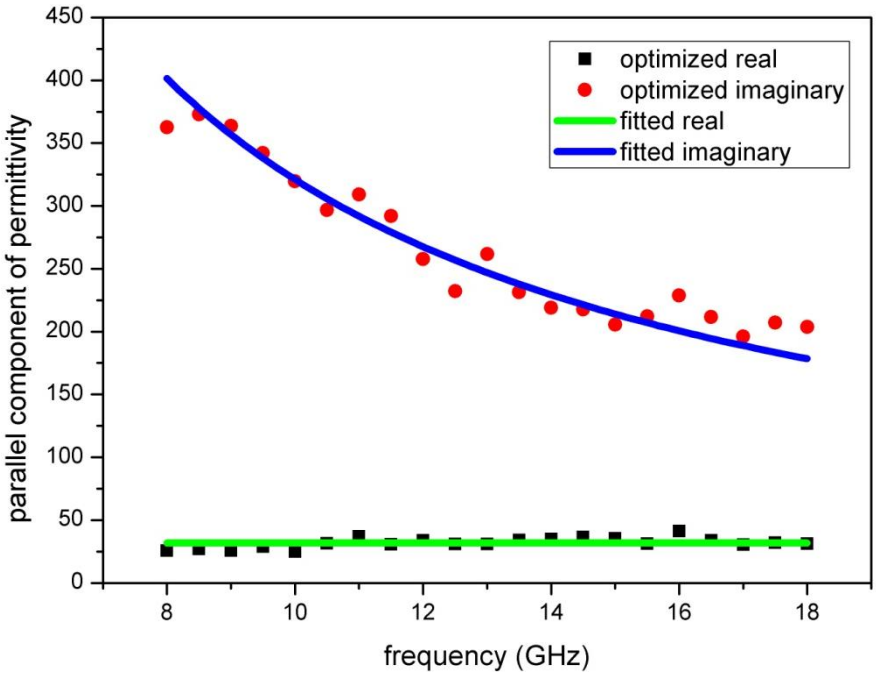

Figure 71: Parallel component of the permittivity, $\varepsilon_{\parallel}$, of a single CNT. The results were fitted with the conventional lossy medium.

It is clear from Figure 70 and Figure 71, that the conventional lossy medium explains the behaviour of the carbon nanotube when that is part of an infinite array as explained in Figure 68. Carbon, which is the base element of the nanotube, is not a Perfect Electric Conductor (PEC), thus the sample is significantly lossy across the frequency band, due to the interband exchange of electrons in Carbon atoms.

The relative permeability of the individual carbon nanotube, shows one resonance within the frequency band examined. Therefore, it was fitted with the Lorentz model (5.6) [133, 140-143]:

$$\mu = \mu_o + \frac{\mathrm{A}\omega^2}{\omega_o^2 - \omega^2 - j\omega\Gamma} \tag{5.6}$$

where A is the amplitude factor and is restricted to $0 \le A \le 1$, ω_o is the undamped angular frequency of the zeroth pole pair (the resonant frequency of the array), and Γ is the loss factor. Table 12 shows the fitted parameters of both components of the relative permeability.

Table 12: Fitting parameters of the relative permeability of a single CNT.

Parameter	Value	Standard Error
$\mu_{o,\perp}$	0.66	0.33
$A_{\perp}$	1	0.32
$\omega_{o,\perp}$	15.08	0.53
$\Gamma_{\perp}$	5.47	2.03
$\mu_{o,\parallel}$	-0.03	3.93
$A_{\parallel}$	1	1.07
$\omega_{o,\parallel}$	17.09	0.42
$\Gamma_{\parallel}$	1.02	1.37

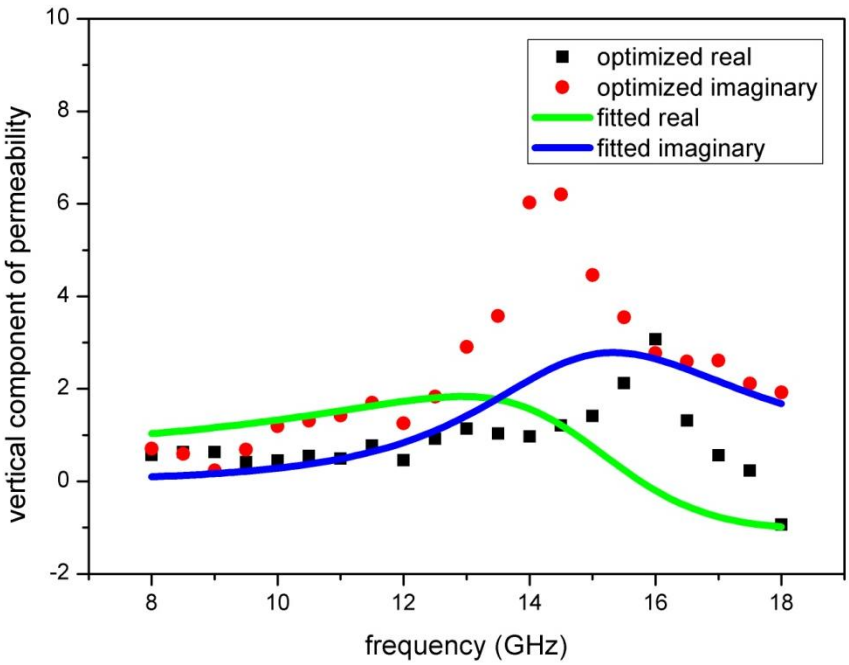

Figure 72: Vertical component of the permeability, $\mu_{\perp}$, of a single CNT. The results were fitted with the Lorentz model.

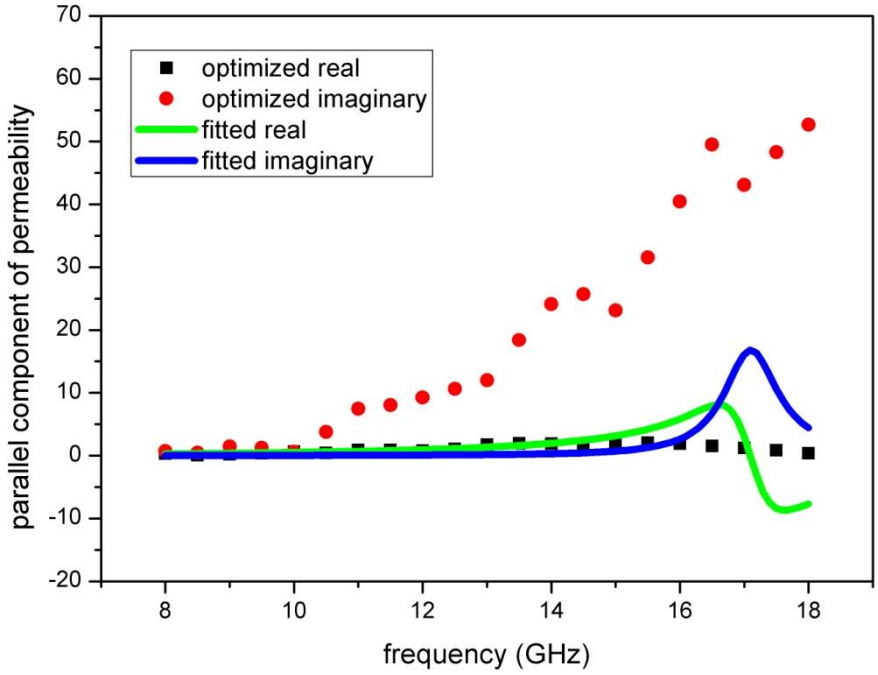

Figure 73: Vertical component of the permeability, $\mu_{\parallel}$, of a single CNT. The results were fitted with the Lorentz model.

This model, (5.6), is only applicable in the quasi-static regime since, in the limit $\omega \to \infty$, the permeability does not tend to μ_o. At extremely high frequencies, materials cannot be polarized due to the inertia of electrons, thus, this model cannot be used to describe the magnetic behaviour of the nanotube. It is interesting that both vertical and parallel components of relative permeability gave a resonance of approximately 15 GHz and 17 GHz respectively. The amplitude factor, A, was restricted to $0 \le A \le 1$, and in both cases takes the maximum possible value, $A = 1$. That restriction, mathematically, makes the fit inaccurate especially in the parallel component. Despite this inaccuracy of the fit being large, it is obvious from Figure 74 and Figure 75 that the magnetic properties of the nanotubes, are not dominant and do not cause much of a difference in the S-parameters.

It is also interesting to note, that the optimization technique used, is only accurate in the dominant parameters of the compact cylinder. A small change of the complex permittivity, affects the S-parameters more severely than the complex permeability. Therefore, multiple solutions were observed, where the permittivity is relatively constant and fluctuating around the value reported in Table 11. On the other hand,

complex permeability had large errors between these solutions and does not affect the S-parameters, therefore the inaccuracy on the actual value was large.

Finally, to verify the optimization procedure, the optimum values of the eight different parameters, were used to characterize a compact cylinder with periodic boundary conditions as it was explained in Figure 69. The complex S-parameters (magnitude and phase) of the periodic structure were compared with the S-parameters of the effective medium model extracted for the VACNT film of 30 μm.

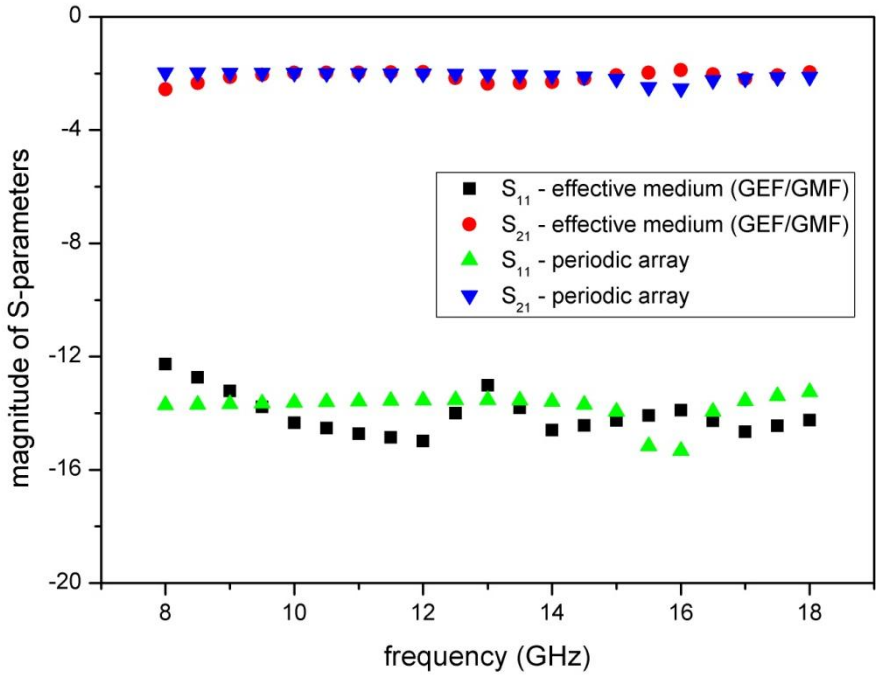

Figure 74: Comparison of the magnitude of S-parameters of the effective medium presented in section 5.2 and the periodic structure of CNTs.

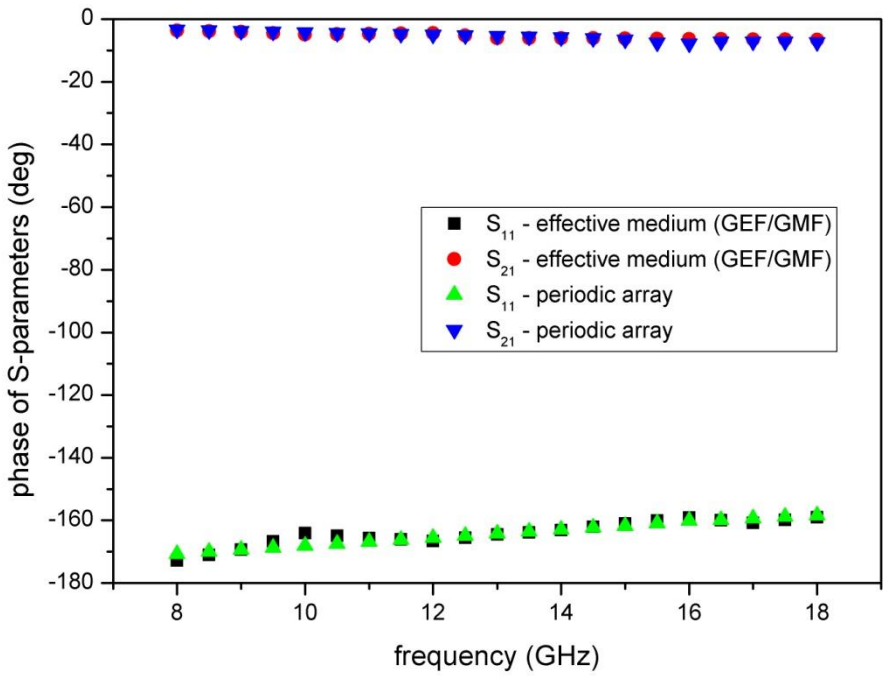

Figure 75: Comparison of the phase of S-parameters of the effective medium presented in section 5.2 and the periodic structure of CNTs.

5.4 Carbon nanotube for a dipole nano-antenna

In this section, we will compare the theoretical electrical properties of a nanotube dipole antenna described in chapter 2 with the model that proposed in the previous section. Table 1 showed the input impedance and efficiency of a solid cylindrical metal wire for radius of 375 μm, 20 nm and 2 nm. The table below presents the input impedance and efficiency of a carbon nanotube with fixed length $L = 10\mu m$ and radius $\alpha = 2.712nm$ at various frequencies such as 10 GHz, 160 GHz, 292 GHz and 460 GHz.

It is worth noting that the above radiation efficiency, and therefore gain, obtained with the carbon nanotube dipole antenna are very low compared to a typical efficiency, of a macro-sized copper made antenna.

Table 13: Normalized input impedance and efficiency of a carbon nanotube dipole antenna for several frequencies [13].

Frequency GHz	Z_{in}/R_o	$e_r = P_r/P_{in}$
10	$0.527 - j \cdot 31.24$	1.2×10^{-8}
160	$0.876 - j \cdot 0.014$	3.3×10^{-6}
292	$10.46 - j \cdot 1.48$	1.1×10^{-5}
460	$0.83 - j \cdot 0.0058$	2.6×10^{-6}

With regards of the input impedance in a macro conventional dipole antenna, the impedance is at 50Ω, whereas for the nanotube antenna, this input impedance is equivalent to the quantum resistance of the carbon nano-tube, which is around $12.6k\Omega$. This basic characteristic impedance refers to all nano-sized transmitting devices based on carbon, such as a transmission line or an antenna. That, introduces a fundamental matching problem between the nano-device with the macro-size world. Therefore, in order to make the carbon nanotube antenna a reality, perfect impedance matching must be considered, which will lead to much higher values of efficiency than Table 13.

The model proposed in (5.5) and (5.6) will be used to compare a similar size dipole antenna with efficiencies of Table 13. A CST-Microwave Studio model of a nano-sized dipole antenna with a radius of 2.5 nm and length of 10 μm was set up. The permittivity and permeability that have been used for that dipole are the ones introduced by (5.5) and (5.6). Table 14 compares the model introduced here with the theoretical work of [13] and very good agreement is observed.

Table 14: Efficiency comparison between [13] and model proposed by (5.5) and (5.6).

Frequency GHz	Theoretical efficiency	Experimental efficiency
10	1.2×10^{-8}	5.3×10^{-9}
160	3.3×10^{-6}	1.2×10^{-6}
292	1.1×10^{-5}	1.14×10^{-5}
460	2.6×10^{-6}	6.1×10^{-5}

5.5 Geometrical effect of vertically aligned carbon nanotube arrays at optical frequencies

In this part of the thesis, an individual multi-walled carbon nanotube was treated as a solid anisotropic cylinder with an effective permittivity and permeability tensor. Periodic boundary conditions were applied, creating an infinite size of VACNTs. HFSS simulations were set up to calculate the transmission, reflection as well as absorption at optical frequencies (400 THz - 750 THz). The effect of geometrical parameters of the tube such as length, diameter and the distance between two consecutive tubes was also examined.

It was observed that VACNT films have many interesting applications and properties at optical frequencies, such as photonic crystals [137, 144, 145] and high absorption [96, 146]. These optical properties of VACNT arrays strongly depend on the individual structure of each CNT, in the atomic level, as well as on their arrangement (periodicity of the array). It is well known that properties of single-walled carbon nanotubes (SWNTs) exhibit strong dependence on their chirality (atomic structure) [147-149]. It is worthy to remind here, that control of chirality, during fabrication is still impossible. On the other hand, multi-walled carbon nanotubes (MWNTs), due to their multiple layers and generally large size, have more uniform optical properties [150].

Carbon nanotube arrays, and especially vertically aligned carbon nanotube arrays have attracted much attention in photonic crystal [151], nanoantenna [152] and solar applications [153-156]. In all of these applications, the arrangement of the nanowires, including the pattern and the distance between the tubes, strongly affect their properties.

In this section, the MWNTs are treated as solid anisotropic cylinders with an effective permittivity given by [129]. It is also assumed that the nanotubes have no magnetic properties at optical frequencies. The dielectric properties of graphite from [157] were used and, therefore, it was possible to calculate the dielectric tensor of an individual CNT using:

$$\begin{aligned} \varepsilon_{\parallel} &= \varepsilon_o \\ \varepsilon_{\perp} &= \sqrt{\varepsilon_e \varepsilon_o} \end{aligned} \tag{5.7}$$

where $\varepsilon_{\parallel}$ and $\varepsilon_{\perp}$ are the components of the dielectric tensor parallel and perpendicular to the CNT axis, respectively (Figure 76). The final results for the two dielectric components with the losses are shown in Figure 77 [129].

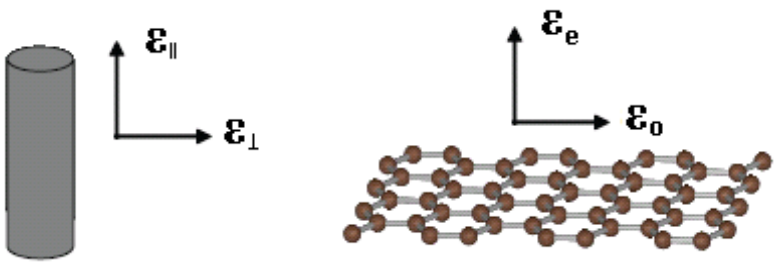

Figure 76: A sketch of a CNT with the two permittivity components and single layer graphite with the anisotropic dielectric tensor.

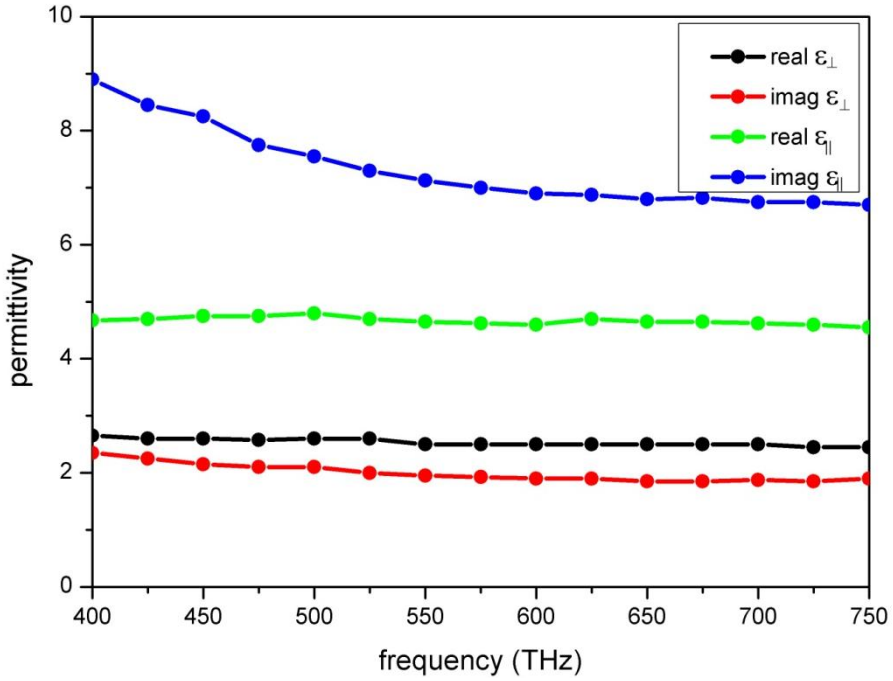

Figure 77: Effective permittivity function of an individual CNT at optical frequencies [129].

The radius of a typical multi-walled carbon nanotube, is between 30 nm and 120 nm, the intertube distance of the two-dimensional square lattice varying from 80 nm to 500 nm, and the tube lengths from 500 nm to 5 μm. It is important to note here, that when the array of nanotubes is perfectly periodic, the length of the CNTs cannot exceed 5 μm during the fabrication. On the contrary, when the array is extremely dense (forest of CNTs), the length can reach several hundreds of microns. In the following sections, the transmission, reflection and absorption properties of the CNT arrays were observed, while the above three parameters changed. As it is very difficult to track the changes when these parameters are changing simultaneously, two of them were set fixed while the third changed.

5.5.1 Volume fraction

In the case of the nanotube, the volume fraction was exactly the same as the area ratio of a cross section of the unit cell. That happened because the length of the nanotube and the length of the unit cell were identical. According to the nominal values of periodicity suggested before, when the radius is fixed at 30 nm, the maximum possible volume fraction of a typical CNT is 0.442, whereas the minimum one is

0.011. The calculated results of transmission, reflection and absorption are presented in Figure 78 and Figure 79 for an 1μm long CNT.

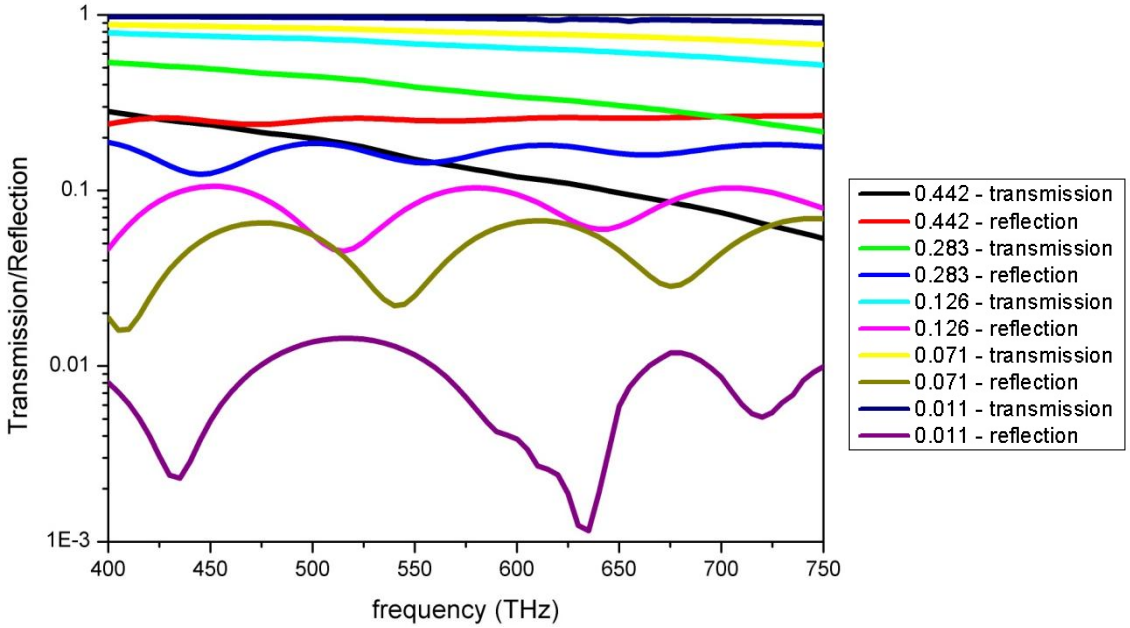

Figure 78: Transmission and reflection of the CNT array from HFSS simulations for different volume fractions.

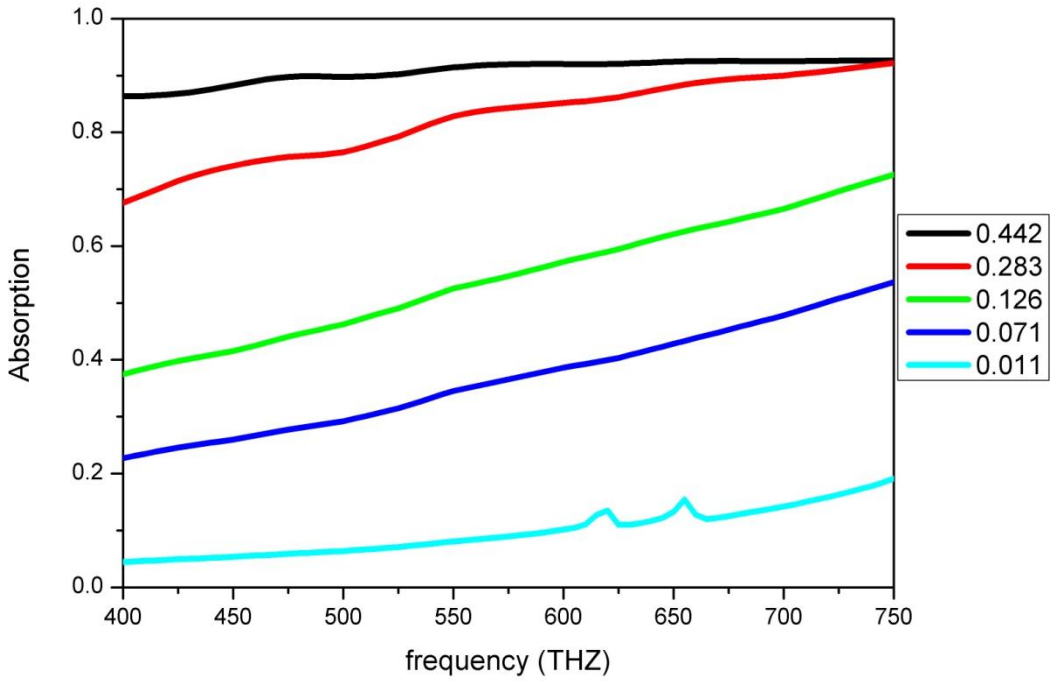

Figure 79: Absorption of the CNT array from HFSS simulations for different volume fractions.

As indicated in Figure 78, the reflection is generally small, and it is always in lower levels than transmission, apart from the dense array, when the volume fraction is 0.442 (radius is 30 nm and periodicity 80 nm). In these calculations it was shown that transmission moves higher and reflection lower, as periodicity increases, indicating that when the array is sparse, the light enters easily into the array. It was also shown that absorption increases with larger volume fractions, which is reasonable as the only absorber materials in the array are the CNTs, therefore more area in the array covered by CNTs lead to higher absorption values. Absorption also increases as frequency increases, indicating that CNT arrays absorb more violet and blue colour than red.

Generally speaking, the absorption α of an individual CNT is related with wavelength λ and the imaginary part of the refractive index κ by [158]

$$\alpha = \frac{4\pi\kappa}{\lambda} \tag{5.8}$$

where κ can be calculated from the complex dielectric function

$$\kappa = \sqrt{\frac{\sqrt{\varepsilon'^2 + \varepsilon''^2} - \varepsilon'}{2}} \tag{5.9}$$

where ε' and ε'' are the real and imaginary part of the dielectric function, respectively. That makes the observation reasonable as (5.8) shows that lower wavelengths λ, result in higher absorption levels.

5.5.2 Length effect

In this section, the changes in the properties of CNTs with different lengths were investigated. As mentioned previously, typical lengths of a CNT is 500 nm to 5 μm. To analyze the properties of these tubes, HFSS simulations were set up with compact anisotropic cylinders of 500 nm, 1 μm, 2 μm and 5 μm in length. The simulated transmission, reflection and absorption of the CNT array for different tube lengths and fixed radius and intertube distances of 40 nm and 200 nm respectively, are shown in Figure 80 and Figure 81.

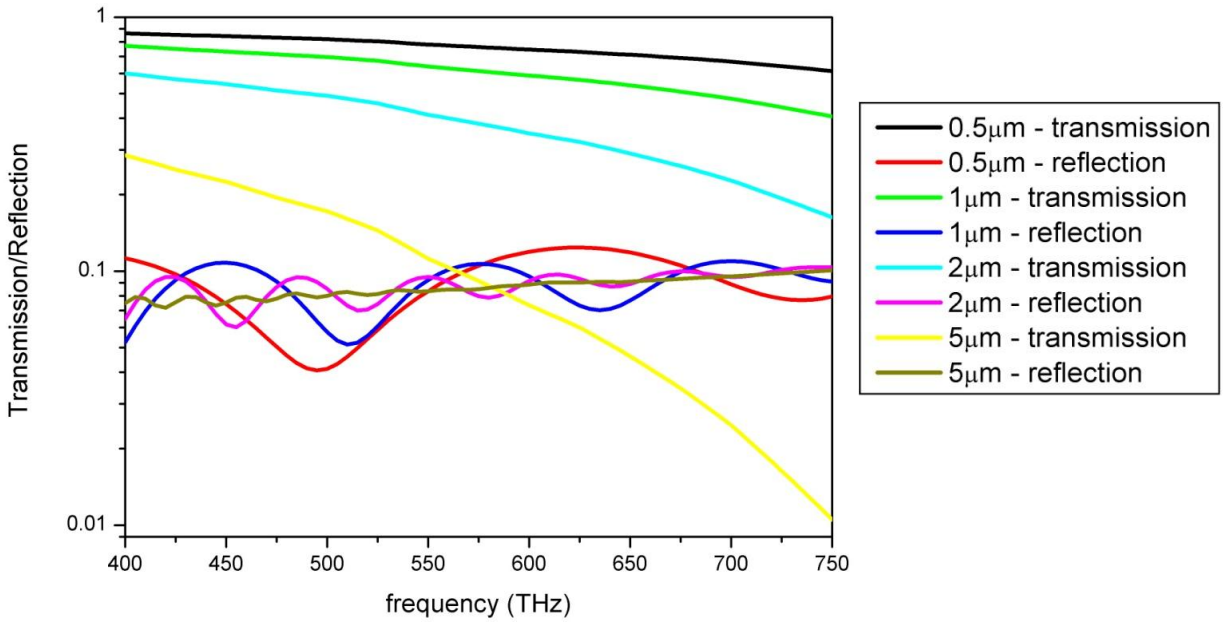

Figure 80: Transmission and reflection of the CNT array from HFSS simulations for different lengths.

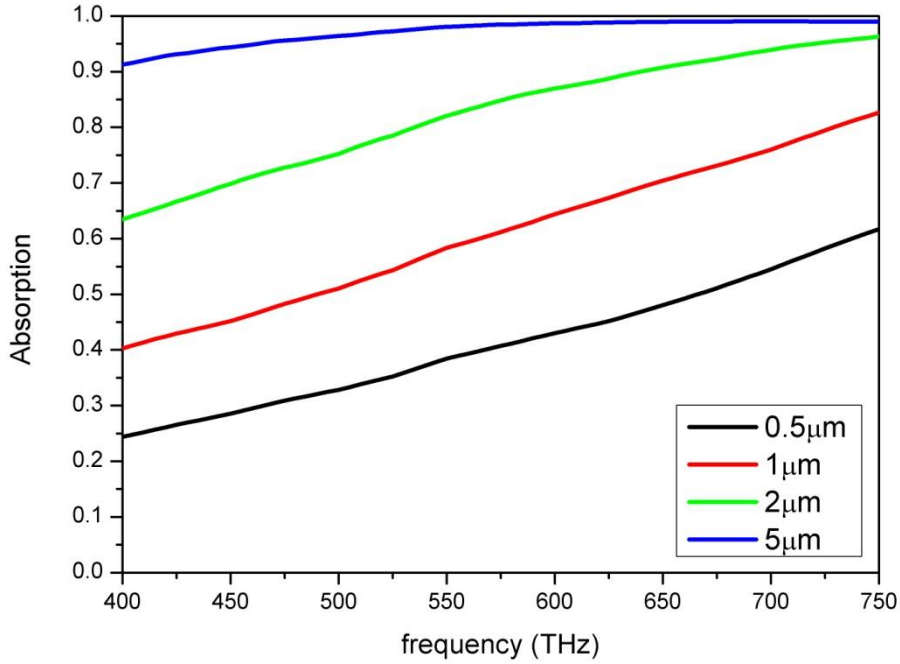

Figure 81: Absorption of the CNT array from HFSS simulations for different lengths.

The results indicate that longer tubes have less transmission which also reduces when frequency increases. For the longer CNT, 5 μm, transmission becomes 30-times less across the optical frequency band, whereas for the shortest one, 500 nm, the reduction is only 30%. The simulated reflection for all the thicknesses exhibit oscillations with

the frequency. These oscillations are smaller when the tube is long but it seems that they are approximately at same level, regardless of the length. Hence, reflection is independent of length in optical frequencies and it is around 0.08 (-22dB). Absorption data in Figure 81 indicate that there is a strong relationship between absorption and nanotube length, and more specifically, longer nanotubes absorb light better. That can explain recent reports [96, 159] that CNTs appear dark, as only the upper part of each nanotube can reflect light slightly.

5.5.3 Radius and periodicity

One could assume that regardless of radius and periodicity, if the ratio of these two is constant, then they should exhibit exactly the same properties, such as transmission, reflection and absorption. Because this is not the case, in this section the volume fraction was fixed at 0.126, and the effect of radius and periodicity was investigated. The carbon nanotube radii varied from 30 nm to 250 nm and therefore, keeping the volume fraction constant, periodicity varied from 150 nm to 600 nm. The nanotube length was fixed at 1 μm.

It is interesting to note here, as the periodicity reached 600 nm, that this value is larger than some of the incident wavelengths in optical spectrum. More specifically, in that example, the combinations of radius-periodicity used were the following: 30 nm -150 nm, 50 nm - 150 nm, 75 nm - 300 nm, 100 nm - 500 nm and 125 nm - 600 nm. In all of these combinations, the incident wavelength was outside the optical spectrum (sub-wavelength regime) apart from the last two cases where the equivalent frequencies are 600 THz and 500 THz, respectively. It is important to investigate the relationship between incident wavelength and periodicity. The results shown in Figure 82 and Figure 83 for transmission and reflection respectively, indicate that perfect CNT arrays exhibit different performance in wavelength and sub-wavelength regime.

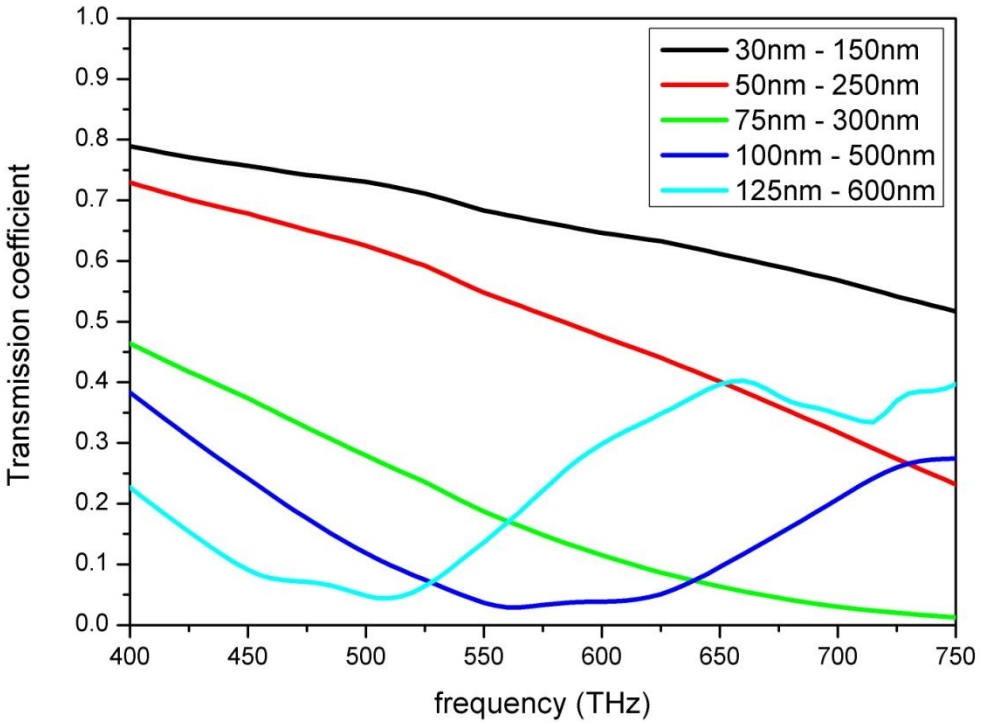

Figure 82: Transmission of the CNT array for different sets of radius - periodicity, obtained by HFSS simulations.

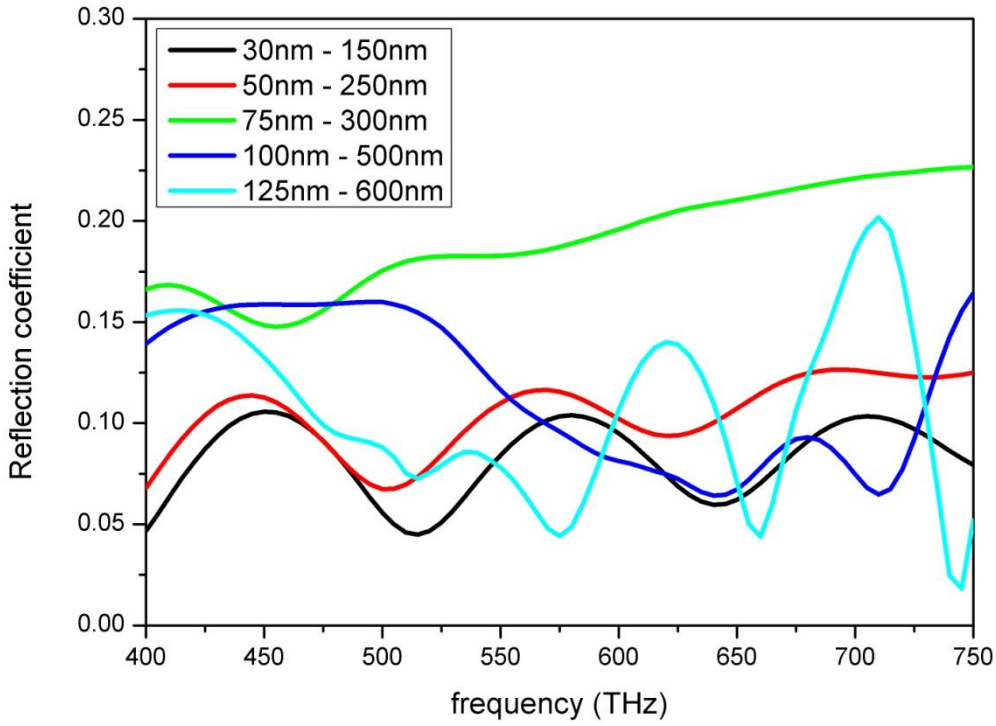

Figure 83: Reflection of the CNT array for different sets of radius - periodicity, obtained by HFSS simulations.

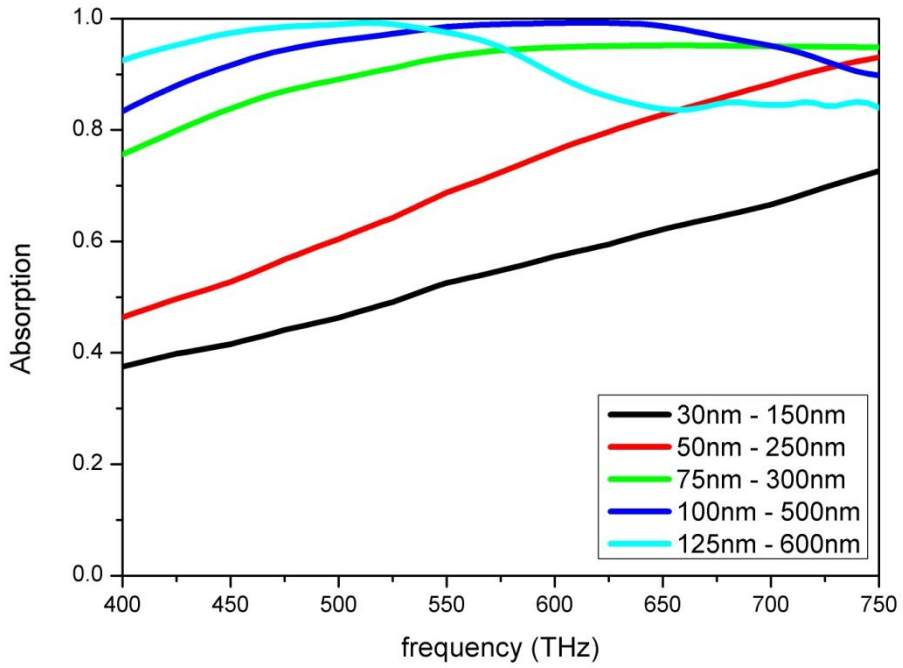

Figure 84: Absorption of the CNT array for different sets of radius - periodicity obtained by HFSS simulations.

It can be seen in Figure 82, that in the sub-wavelength regime the transmission decreases with larger periodicity and it also decreases for higher frequencies. However, this was not the case for the 100 nm - 500 nm and 125 nm - 600 nm set of radius - periodicity of the CNT array. Transmission had an abnormal behaviour around the resonant frequency, where it significantly falls below 5%. On the other hand, reflection appeared to oscillate across the frequency spectrum. Finally, absorption had an abrupt increase, at around 600 THz and 500 THz at the two different sets with periodicity values of 500 nm and 600 nm respectively. To summarize, a maximum absorption (and minimum transmission) was observed when periodicity of the CNTs was equal to the incident wavelength. Similar results have been reported for silicon nanowire arrays and nanohole arrays in [160, 161].

5.6 Summary

In this chapter, further investigation of the carbon nanotube properties, at low microwave frequencies, as an effective medium have been performed. A model,

characterized by the general permittivity (GEF) and general permeability functions (GMF) was presented. These model's functions, are independent of thickness and can be used for any similarly dense VACNT array, to predict the transmission, reflection and absorption of this array. It was also shown that the difference between these GEF and GMF and the actual measurement is within the reasonable error.

The estimation of the permittivity and permeability of an individual carbon nanotube is necessary. Effective models are usually accurate enough, but they lack flexibility. The difference in geometry of the carbon nanotubes, results in a totally different model. It was presented, using HFSS optimization techniques, that characterization of individual nanotubes is possible. A periodic structure of CNTs was therefore simulated, under periodic boundary conditions, consisting of solid anisotropic cylinders. The complex permittivity and permeability of both components were calculated. Effective medium models were also applied here, at a nanotube-level, rather than to the whole dielectric slab. Both vertical and parallel components of the complex permittivity validated the lossy medium approach. In addition, complex permeability fitted with the Lorentz-model. The introduced model fits the permittivity very well, whereas permeability had large errors, due to the large number of solutions of the optimization technique.

Finally, the optical properties of VACNT arrays, when the periodicity is within the sub-wavelength regime, were calculated. The effect of some geometrical parameters of the tube such as length, diameter and inter-tube distance between two consecutive tubes was also examined. All the results show that VACNT films in the optical range are highly absorptive. Longer nanotubes, result in higher levels of absorption, usually close to 100%. Higher volume fraction, also result in higher absorption as well as higher reflection and lower transmission. Finally, keeping the volume fraction constant but changing the radius and periodicity accordingly, will also result in higher absorption when the radius is increased. The absorption performance of the VACNT arrays was also investigated, when the periodicity is equal to the incident wavelength. A very interesting phenomenon was observed similar to silicon nanowire arrays with finite length [160] where the transmission is heavily depressed, resulting in absorption level close to unity.

Chapter 6: Optically Transparent and Liquid Crystal Substrate Based Antennas

6.1 Introduction

Liquid crystals are characterized by a type of molecular ordering which either exhibits positional or orientational order. It is known that electric or magnetic field, make liquid crystal's molecules to change its orientational order towards the direction of the field, thus, changing the permittivity. Modern mobile devices require reconfigurable antennas operating at many frequency bands, therefore, the development of tunable antennas is essential. The two main advantages over existing tunable materials, are that liquid crystals need comparatively low applied fields for switching the orientation of the molecules, and they demonstrate low dielectric losses.

The possibility of realizing a tunable patch antenna using liquid crystal as a substrate is investigated in that chapter. It is also desirable to increase the tunability of such a structure, therefore, liquid crystal with higher dielectric anisotropy at microwave frequencies is needed. This can be achieved by doping the liquid crystal with carbon nanotubes with as low concentrations as 0.01%wt.

Optically transparent antennas (such as monopoles, patches and PIFAs) are becoming more popular as several applications are possible, when exploiting their transparency which is their main advantage. Their use for communication systems with frequencies

of the order of a few gigahertz have been proposed. Transparent antennas can be mounted on video displays for efficient integration in communication systems such as tablet computers, mobile phones, and flat-panel television displays. Additionally, antennas could provide seamless GPS navigation when integrated to automobile windshields or building windows Figure 85. Furthermore, such antennas are suitable for structures where lack of space provide an impairment. In addition, optically transparent antennas are low profile, light weight and more flexible compared to conventional antennas.

Figure 85: Optically transparent antenna for automobile applications.

It is well known that liquid crystals are transparent in optical frequencies. Adding a very small amount of carbon nanotubes, does not affect the optical properties of the liquid crystals, however, the tuning is strongly affected as explained earlier. It is now clear, that optically transparent tunable antenna based on CNT-doped liquid crystal substrate can be achieved.

6.2 Optically transparent Ultra Wide-Band antenna

The first optically transparent microstrip antenna was reported in NASA's technical memorandum by Simons et al. [162] operating at 2.3 GHz and 19.5 GHz. They used an AgHT-8 optically transparent conductive coating on a clear polyester substrate. Later, Mias et. al [163] compared dipole antennas with different conductive materials, while more recently Guan et al. [164] focused on PIFA and monopole transparent antennas. In the meanwhile, in 2002, the Federal Communication Commission (FCC) authorized the unlicensed use of UWB in 3.1 GHz - 10.6 GHz [165].

6.2.1 Introduction to Ultra Wide-Band Technology

Ultra Wideband (UWB) technology is a wireless technology which can transmit digital data in short range communications. It uses extremely wide frequency spectrum and the transmission is accomplished with very low power and very high data rates. Usually, with UWB systems we can transmit signals through obstacles, an area where technologies with narrower bandwidths and higher power would have failed [166].

In April 2002, the Federal Communications Commission (FCC) issued a 'report on part 15 commission's rules regarding ultra wide-band transmission systems [165] which specifies frequencies and power limitations in order to control interference between other technologies that are using the same frequency spectrum. UWB signals may be transmitted in frequencies between $3.1\ GHz$ to $10.6\ GHz$ with maximum power spectral density limit of $75\ nW/MHz$ which corresponds to $-41\ dBm/MHz$. Also, the average effective isotropic radiated power (EIRP) should always be less than $0.56\ mW$ across the entire bandwidth. Efforts to achieve similar status about this novel radio technology in Europe [167] and Asia are underway.

The bandwidth of UWB systems is either more than 25% of the centre resonant frequency or more than 1.5GHz [165]. The percentage bandwidth is expressed as

$$BW_{-10dB} = \frac{2(f_H - f_L)}{f_H + f_L} \times 100\% \tag{6.1}$$

where f_H is the upper frequency and f_L the lower frequency at the $-10dB$ emission point. Centre frequency is the average between the higher and the lower frequency points and it can be calculated using the equation: $f_C = \frac{(f_H + f_L)}{2}$. This bandwidth is much larger than any other known communication technology.

UWB technology will play a central role in the future scenarios of interactive communications, involving both human and device communications with all its combinations, human - human, human - device, device - human and device - device.

Apart from the first communication link between humans, all the other links exchange data, i.e. for navigation. Currently, transfer of information between humans is still by voice, however, we will very soon have a rapid increase in data transfers involving video transfer capabilities within home or office environments.

A number of practical usage scenarios which are well suited to UWB technology are shown in Figure 86. In these scenarios system implementations based on UWB radio technology could be beneficial and potentially welcome by industry and service providers alike [166]:

- High-data-rate wireless personal area network (HDR-WPAN)
- Wireless Body Area Network (WBAN)
- Intelligent wireless area network (IWAN)
- Outdoor peer-to-peer network (OPPN)
- Sensor, positioning, and identification network (SPIN)

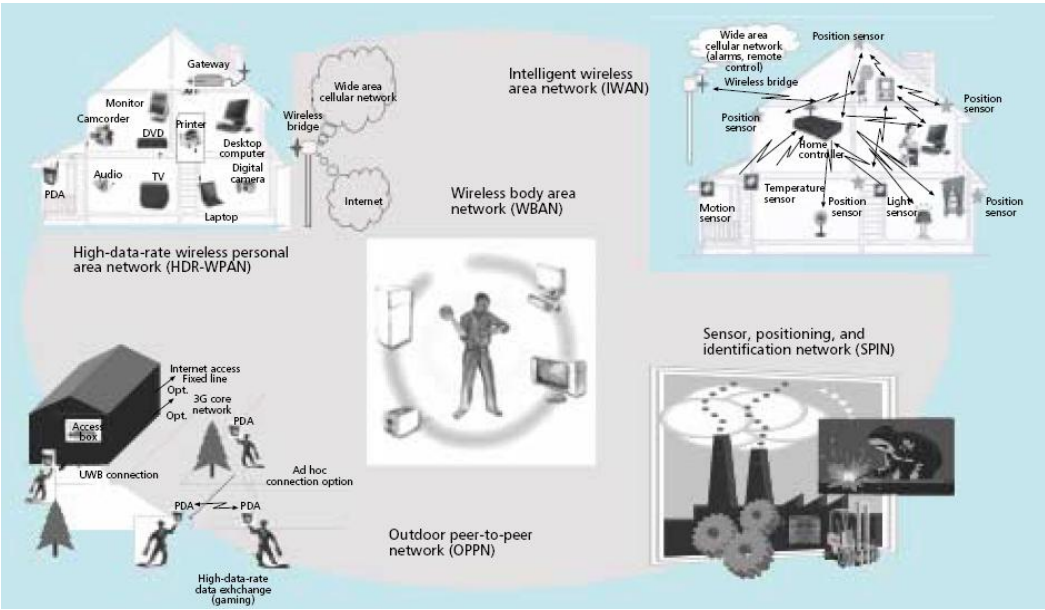

Figure 86: Potential applications for UWB radio communications: the first three scenarios (HDR-WPAN, WBAN, IWAN) assume a network of UWB devices deployed in a residential or office environment, mainly to enable wireless video/audio distribution for entertainment, control signals or high-rate data transfers. The fourth scenario (OPPN) presents a deployment in outdoor peer-to-peer situations, while the fifth (WBAN) takes industry and commercial environments into account [166].

6.2.2 Optically transparent and conductive films

The ideal scenario of constructing antennas would be the use of certain types of transparent films. These antennas could be used on vehicle windows or windscreens, on building windows, on the surface of the display of an electronic device or mobile phones and many more. To fabricate these antennas, the optically transparent conductor would provide ideal conductivity comparable to that of copper and even comparable to glass in terms of transparency.

Optically transparent conductive films, such as indium tin oxide (ITO) and fluorine-doped tin oxide (FTO) films, allow the transmission of electric currents while retaining optical transparency [164]. These two films are widely used as a transparent electrode in optoelectronics devices including liquid crystal displays (LCDs), photovoltaic solar cells and plasma display panels.

At room temperature, ITO films show high transparency and electrical conductivity. At higher temperatures, such as $300^{o}C$ or higher, the electrical resistance increases more than threefold. An explanation for this behaviour is given through the electron suppliers of these films which are in the oxygen vacancies. When the material is heated, oxygen from the atmosphere is trying to bond to the oxygen-vacant structures within the ITO thin film and as a result a reduction of these vacancies leads to an increase in the electrical resistance.

A solution to this problem for ITO is proposed by Kawashima [168] using novel transparent conductive films formed by ITO covered FTO films (FTO/ITO films). The reason of developing that film is that FTO has less electrical resistance in higher temperatures than ITO films.

Another optically transparent film used for electronic applications where EMI shielding is crucial, is the highly conductive AgHT film. As demonstrated in Figure 87, this film is outstanding in its ability to transmit visible light and reject infrared heat. The table below, shows the main characteristics of this film, where for the

surface resistance for AgHT-4 is $4.5 Ohms/sq$ which corresponds to a conductivity around 30 times less than copper's.

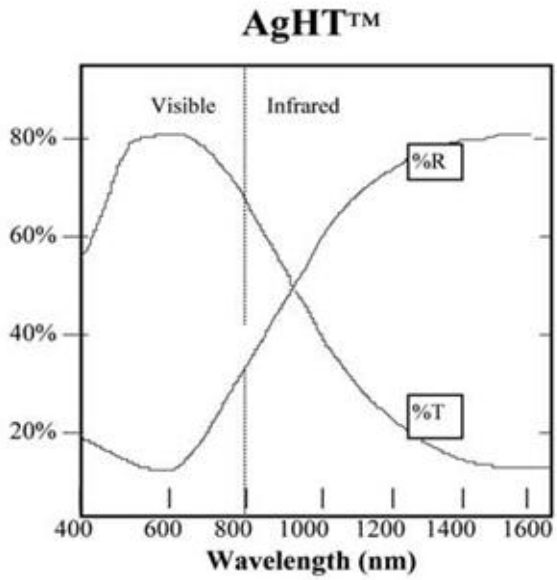

Figure 87: Transmission and reflection response of the optically transparent conductive AgHT film in the visible and infrared spectrum [169].

Table 15: Properties of AgHT and ITO optically transparent conductive films.

	AgHT-4	**AgHT-8**	**ITO**
Visible Transmittance	75%	82%	75%
Infrared Reflectance	80%	75%	75%
Surface Resistance $(Ohms/sq)$	4.5±1.0	8.0±2.0	5-1000
Shielding Effectiveness (1 GHz - 10 GHz)	24-44dB	20-40dB	

6.2.3 Proposed Antenna

In the following section an optically transparent Ultra Wide Band (UWB) disc monopole antenna is presented [170, 171] as well as gain and radiation patterns. The antenna is fed by a 50Ω coplanar waveguide and its operational measured bandwidth is from 1GHz up to 8.5GHz. The antenna shows omni-directional and monopole-like radiation patterns in low frequencies for H-plane and E-plane respectively. The

proposed antenna uses the highly conductive AgHT-4 transparent film, rendering it more suitable for inter-vehicle communication.

6.2.3.1 Antenna Design

An optically transparent UWB monopole antenna is fabricated on a perspex substrate, the geometry of which, is shown in Figure 88. The size of the substrate is exactly the size of an A4 page $(W = 210mm, L = 297mm)$. An identical A4 sized perspex superstrate is used, exactly above the monopole antenna. These two layers of perspex are $2mm$ thick and they have a relative permittivity of 3.3.

Figure 88: UWB transparent antenna. The University logo is placed underneath the antenna to show the transparency. A penny is placed on the left down corner, for scale purposes [170, 171].

The antenna is a circular disc monopole (Figure 89) with a radius of $r = 40mm$, which corresponds to the $\lambda_g/4$ of the lower desired frequency. This monopole is fed by a $50\Omega - CPW$ (co-planar waveguide) which is composed by a metal strip of $W_s = 4mm$ width and a gap of $g = 0.25mm$ between the strip and the ground plane. The dimensions of the ground plane are $37 \times 25mm^2$ ($W_g \times L_g$). The feed gap between the disc and the ground is again $h = 0.25mm$. Several studies suggest that this gap between the disc and the ground plane is very close to the CPW line gap. This is due to the feed gap will have a smooth transition to the CPW fed line.

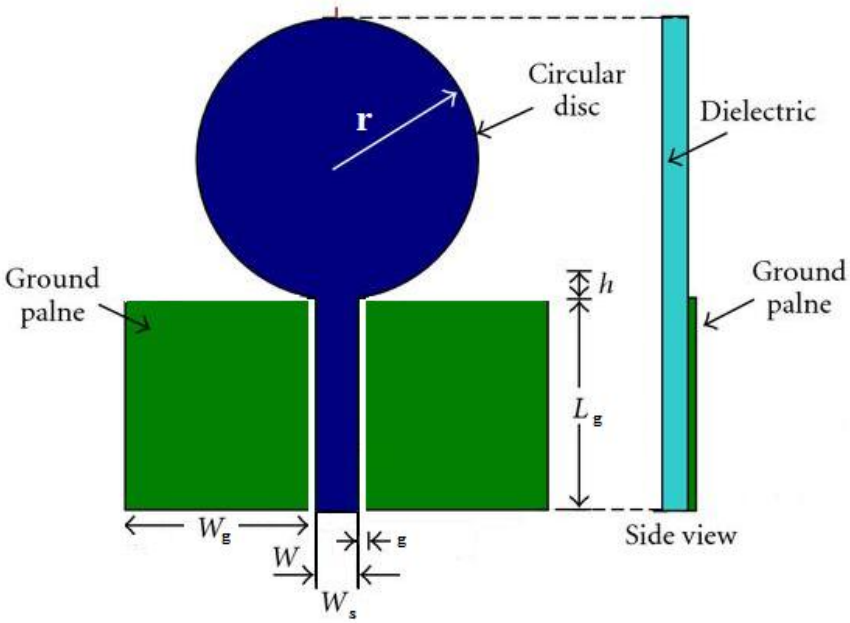

Figure 89: Schematic Diagram of the proposed antenna.

6.2.3.2 Simulated and measured results

The performance of this CPW-fed disc monopole is very sensitive to several parameters which would affect the performance of the antenna, such as the size of radiation element, the size of the ground plane and the gap between the disc and the ground. A comparison between simulated (CST Microwave Studio) and measured return loss is presented in Figure 90.

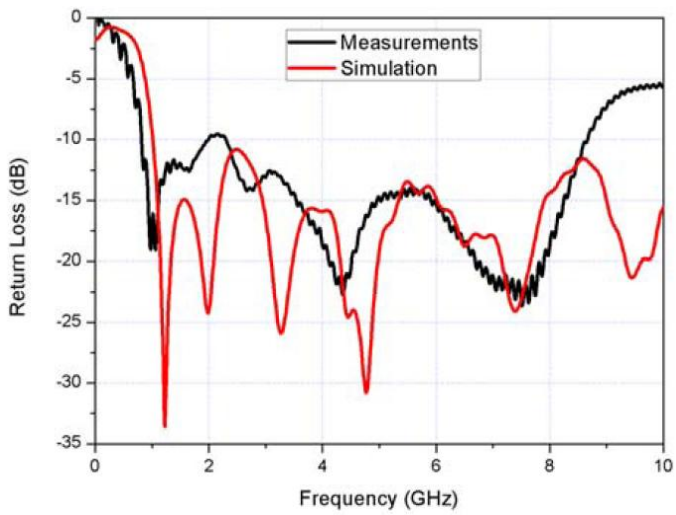

Figure 90: Measurement and simulated return loss of the transparent UWB antenna.

Simulated antenna bandwidth (BW_{-10dB}) is extended to an extremely wide frequency range, from 1GHz up to 11GHz. This characteristic of the proposed optically transparent UWB antenna is confirmed by measurements and good agreement with simulated results.

Figure 91 shows the measured antenna gain using coaxial cable and optical fibre for the optically transparent antenna. At 1 GHz the measured antenna gain is around $-2dB$. For the optical fibre gain measurements, we used the Opto-Electric Field Sensor System (OEFS system); the measurement performed in National Physical Laboratory (NPL). An OEFS controller supplies with optical power the transducer, and then it converts the returned detected optical signal into an RF electric signal [172].

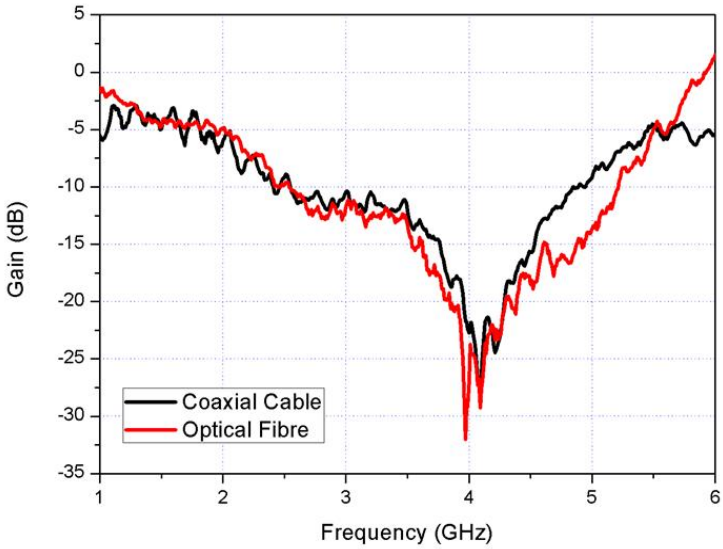

Figure 91: Gain sweep for the optically transparent UWB antenna using both coaxial cable and optical fibre.

Next, we fabricated an identical to the UWB transparent antenna, using conventional conductive material, instead of the transparent conductor proposed above. Figure 92 shows the measured antenna gain for the new aluminum antenna (non-transparent), using both coaxial cable and optical fibre.

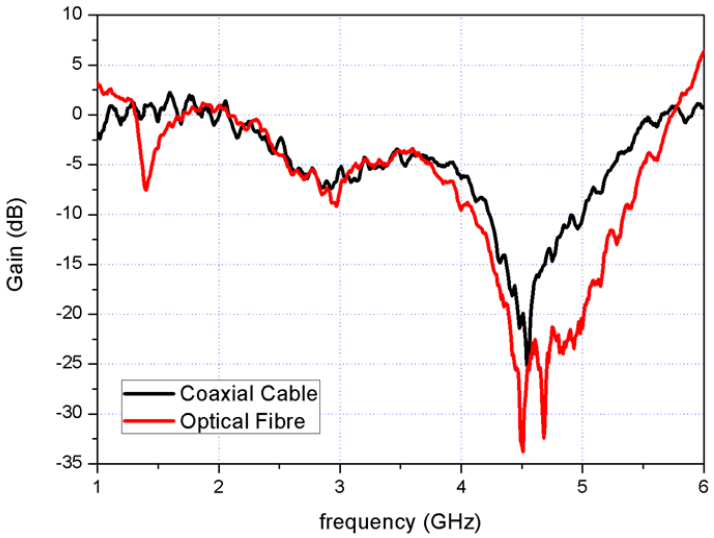

Figure 92: Gain sweep for the aluminum UWB antenna using both coaxial cable and optical fibre.

Figure 93 below illustrates that the transparent antenna gain is always 5 dB lower compared with the aluminium one. This is reasonable, as aluminum is around 30 times more conductive than the AgHT-4 film.

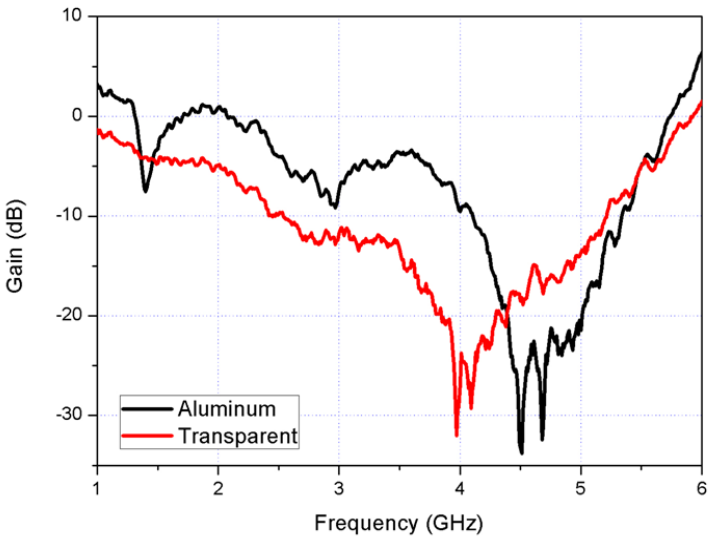

Figure 93: Antenna gain comparison between optically transparent antenna and aluminum antenna using the OEFS system. We can easily realize that the optically transparent antenna has 5dB less gain, constantly in all frequency.

The radiation patterns of the transparent and aluminium UWB antenna have been measured inside an anechoic chamber. The measured co-polar and cross-polar radiation patterns (H-plane) at 1, 2, and 6GHz are plotted in Figure 94 and Figure 95. As shown in this figure, the H-plane patterns are omni-directional at low frequencies. As the frequency increases, the omni-directionality is distorted by a perturbing effect in high frequencies, caused by the feeding structure.

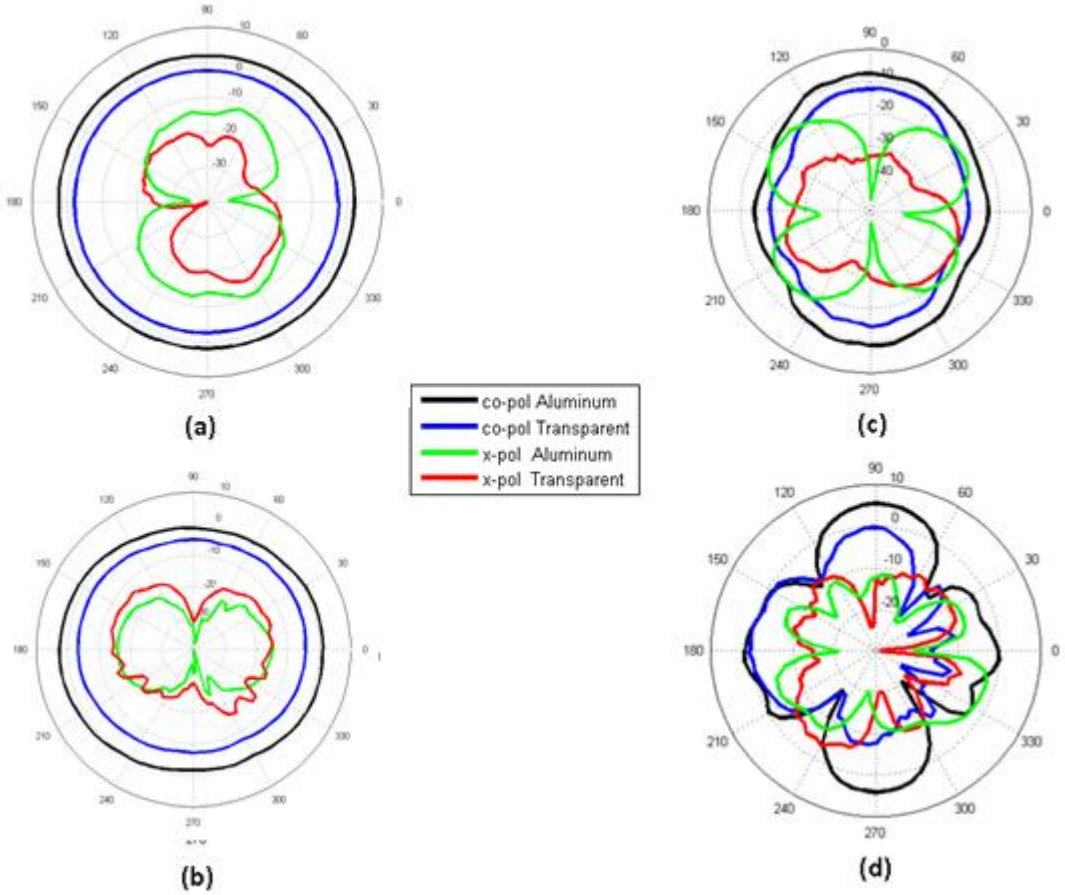

Figure 94: Measured radiation patterns at 1GHz, 2GHz, 3GHz and 6GHz of the optically transparent and aluminum antenna. H-plane co-polarization and cross-polarization are shown.

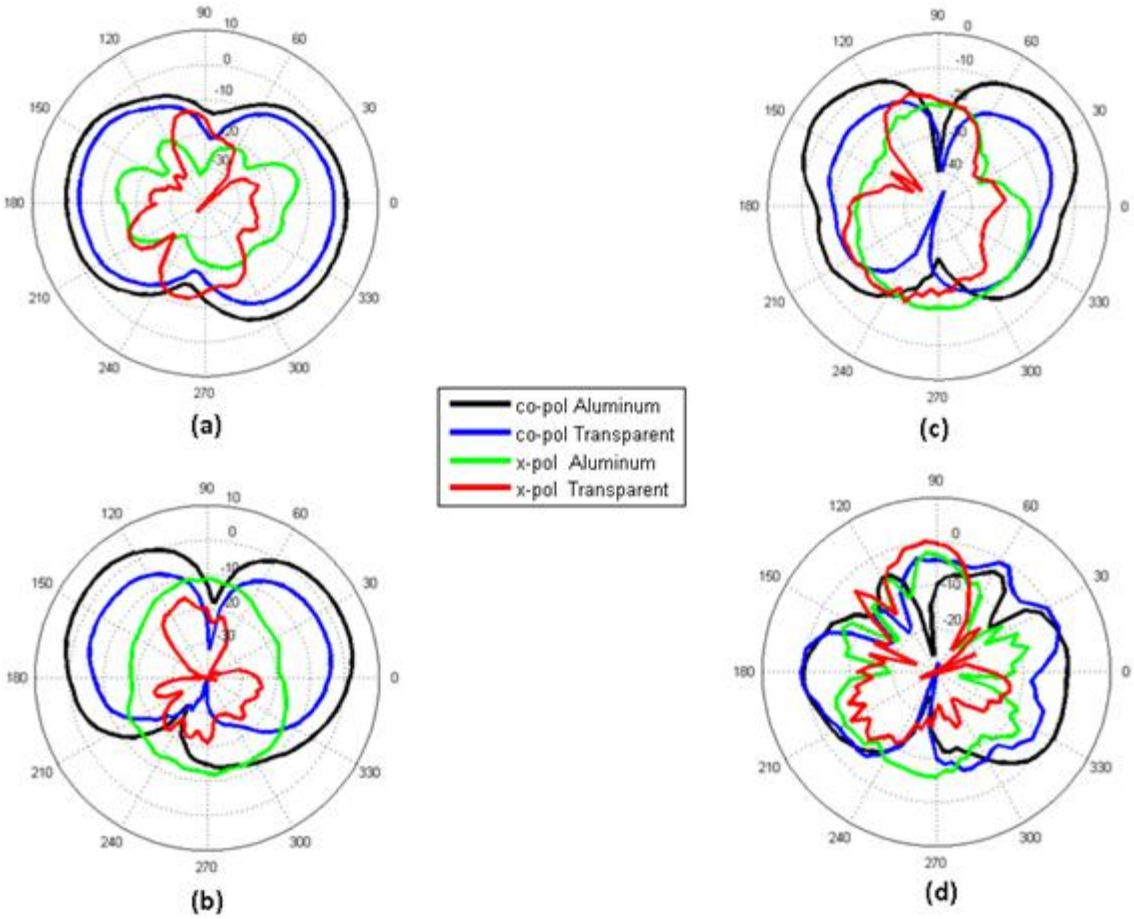

Figure 95: Measured radiation patterns at 1GHz, 2GHz, 3GHz and 6GHz of the optically transparent and aluminum antenna. E-plane co-polarization and cross-polarization are shown.

6.3 Liquid Crystals

Liquid crystals are mesophases between crystalline solids and isotropic liquids [173-176] and each various phases also called mesophases. They are characterized by a type of molecular ordering, which exhibits a positional order, with molecules arranged in multitude of ordered lattices, and orientational order with molecules mostly pointing in the same direction. The molecules resemble elongated rod-like structures typically few nanometers in length. The ratio between the length and the diameter of the molecules or the ratio between the diameter and the thickness of the disk-like molecules is about 5 or larger [173].

In a nematic liquid crystal phase, molecules have no positional order but they have orientational order.

Figure 96: Schematic of molecule alignment in a nematic phase [63].

Liquid crystals in Figure 96 belong to anisotropic materials, of which the physical properties, and especially their dielectric constant, varies with the alignment of the director, a dimensionless unit vector representing the direction of the preferred orientation of molecules in the neighbourhood of a point.

The permittivity of LC can be altered by simply applying an electrostatic or magnetostatic field, i.e. DC bias voltage ranging usually from 0 to 20V, and then the dielectric constant may vary up to 25-30% [177, 178]. This happens because by applying this field we rotate the director of LC molecules with respect to that field (Figure 97). Dielectric anisotropy is given by:

$$\Delta\varepsilon_r = \varepsilon_{r\|} - \varepsilon_{r\perp} \tag{6.2}$$

where $\varepsilon_{r\|}$ and $\varepsilon_{r\perp}$ are the parallel and perpendicular (to the director) permittivity values for the LC, respectively.

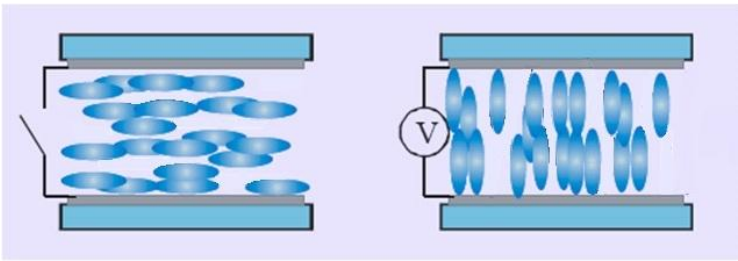

Figure 97: Liquid crystal cell. Orientation of the liquid crystal occurs above a threshold voltage.

There are several other LC phases but they will not be analysed here, as nematic LC is the most common substrate used for substrate construction. Smectic phases can be found at lower temperatures than the nematic phase LC. The main difference with the nematic LC is that they form well-defined layers (positional order along one direction) that can slide over one another like soap. In Smectic A phase, the molecules are oriented along the layer normal, while in the Smectic C phase they are tilted away from the layer normal. Leading from this there is an extremely large number of different smectic phases, characterized by different degrees of orientational order (Figure 98).

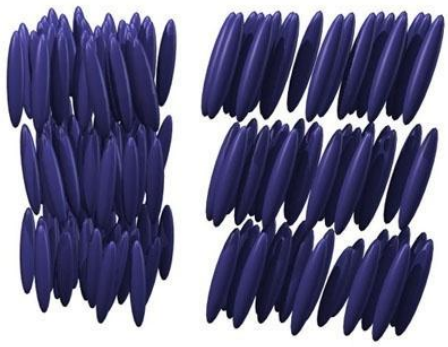

Figure 98: Schematic of molecules alignment in smectic A phase and smectic C phase, respectively [63].

As we know from antenna theory, by changing the substrate properties, such as the permittivity, the resonance frequency of our antenna can be easily altered because the resonance frequency is inversely proportional to the square root of the effective permittivity: $f \propto \frac{1}{\sqrt{\varepsilon_r}}$.

6.4 Carbon Nanotube doped liquid crystal

As it was described in the previous section, liquid crystals have attracted attention in recent years in the antenna and propagation community, due to the low losses at microwave frequencies and generally high anisotropy [179-181]. Low loss materials, with high tunability of dielectric constant are required. Liquid crystals are advantageous over other tunable materials, such as ferroelectric ceramics because of their high anisotropy [181].

Liquid Crystals can be loaded with various types of nanoparticles, such as metallic micro tubules for enhanced performance. For instance, 0.2%wt metallic micro tubules increase the birefringence by 54% at 30GHz when they are inserted in liquid crystal [182].

The extraordinary properties of carbon nanotubes, including their large mechanical and electrical anisotropy [58], have been previously detailed in that thesis. The growth process generally leads to a random orientation of the nanotubes [2, 16, 183]. Moreover, the flexibility, the high aspect ratio of the tubes and the strong van der Waals forces between individual nanotubes, usually lead to the formation of bundles and entanglements with neighbour nanotubes. In many applications, the uniform alignment of carbon nanotubes is essential and is desirable to be able to manipulate the direction of alignment, in order to exploit their extraordinary properties.

There are several reports on fabricating aligned nanotubes. CNT composites inside an epoxy matrix [184, 185], nanotubes as polymer composite systems [186] array of parallel bundles synthesized by arc discharge [187], multiwalled nanotubes on a patterned substrate by pyrolisis [188] have been presented. Liquid crystals can also be used as a host of the carbon nanotubes (Figure 99). The advantage of this is that liquid crystals exhibit orientational order themselves while they are maintaining flow properties in nematic phase. Therefore, these properties of liquid crystals will be used to impose alignment on disperse CNTs [189-191]. CNTs can be aligned applying electric [192] or magnetic [193] fields with high-order parameter, up to 0.9 [192].

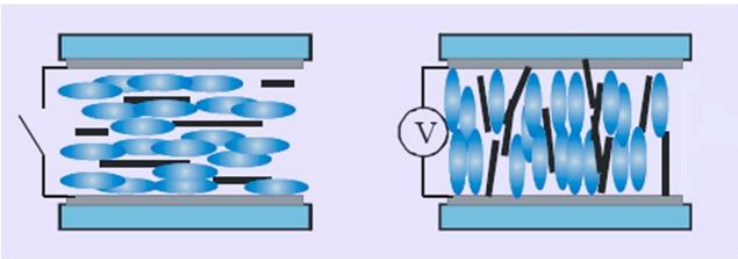

Figure 99: Alignment of the CNT-doped liquid crystal when a field is applied.

The dielectric properties of these mixtures in low-frequencies have been studied [190] by measuring the reflection coefficient of a capacitor at the end of a transmission line [181]. A liquid crystal sample cell with a thickness of $20\mu m$ is sandwiched between two parallel metal electrodes for the $\varepsilon_{\perp}$ measurement. An electric field of up to $40V$ AC with low frequency $(1\ kHz)$ is applied for the other direction of the doped liquid crystal, $\varepsilon_{\parallel}$. CNT-doped liquid crystals appear to have different electrical properties compared to the unloaded ones [194, 195]. An increase of the anisotropy at microwave frequencies is also observed [190].

Measurements have been performed in both low, $1-4GHz$, and high frequencies at $30GHz$. The parallel component of the dielectric permittivity, $\varepsilon_{\parallel}$, of CNT-doped liquid crystals increases, compared to that of pure ones Figure 100. In contrast, the perpendicular component, $\varepsilon_{\perp}$, does not fluctuate [190]. Figure 100 and Figure 101 show the dielectric anisotropy, $\Delta\varepsilon$, at $1-4GHz$ and $30GHz$ respectively [190]. 0.01%wt CNT-doped liquid crystals increases the dielectric anisotropy by 120% compared with the unloaded one, across the whole frequency band $1-4GHz$, and around 165% at $30GHz$ [190]. The 0.005%wt shows intermediate properties between the 0.01%wt CNT-doped and the pure liquid crystal. According to these results compared to the metallic microtubules [182], more tunability with less concentration of dopants has been achieved.

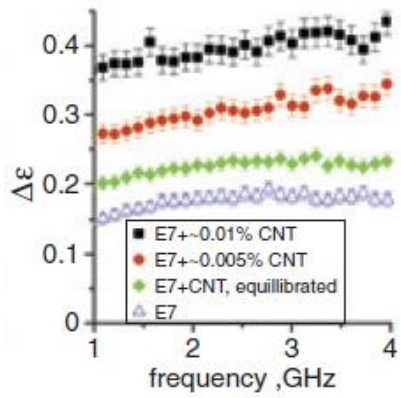

Figure 100: Comparison of Δε in 1-4 GHz range, switching with 0.5V/μm for pure and CNT doped E7 liquid crystal [190].

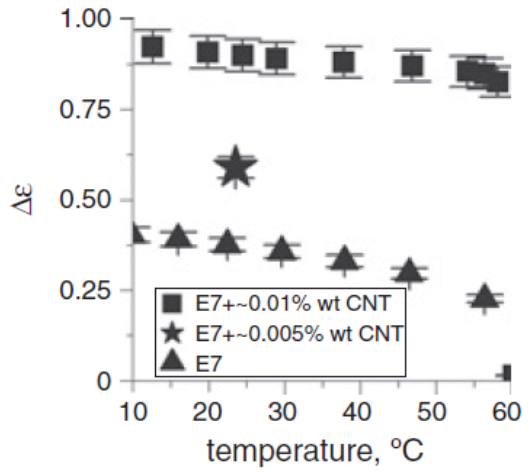

Figure 101: Δε of pure and CNT doped E7 liquid crystal, at 30 GHz, against temperature [190].

In Figure 102 the actual values of the dielectric permittivity and loss tangent at $3GHz$ is shown when the applied field is increased. According to [190] the loss is correlated with the percentage of CNT concentration. The perpendicular loss component, $\tan\delta_{\perp}$, has been increased by 10-30% after the insertion of the CNT, where the increase of the parallel loss component, $\tan\delta_{\parallel}$, was increased by 26% in the 0.005%wt CNT-doped liquid crystal and two to five times more in the 0.01%wt one.

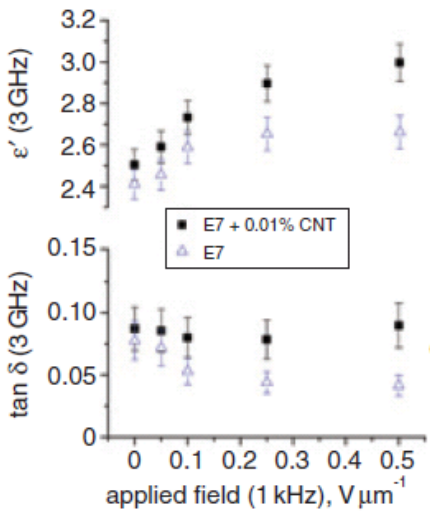

Figure 102: Sweeping from $\varepsilon_{\perp}$ to $\varepsilon_{\parallel}$ and from $\tan\delta_{\perp}$ to $\tan\delta_{\parallel}$, at 3 GHz for both pure and CNT doped E7 liquid crystal [190].

6.5 Frequency tunable antennas

In this section, we will present a simple microstrip patch antenna placed on a liquid crystal substrate. Patch antennas are generally very simple to design and construct, inexpensive, low profile, conformal and light weight. Printed antennas, such as microstrip patch antennas, are mechanically robust when mounted on rigid surfaces [127]. Microstrip patch antennas are inherently resonant antennas characterized by extremely low bandwidths. Some applications of patch antennas are mobile-phones, access points, satellites and aircrafts.

Lately, improved patch antennas have been proposed and the current state of substrates used leaves room for further improvement. For several communications it is desirable to have miniaturized and frequency tunable antennas. Several ways to tune an antenna are known from the literature such as the use of pin diodes, varactor diodes and MEMs switches [196, 197] as well as varying substrate properties as with ferrites and ferroelectrics [198]. A modern technique has been reported where a microstrip patch antenna was made based on nematic liquid crystals (LCs) substrates [199-201]. Our goal in the following structures is to find a way to control these resonances and improve the tunability of the antennas using CNT doped liquid crystals.

6.5.1 Proposed Antenna

In the following section a frequency tunable antenna operating at $3GHz$ is presented. The antenna is a simple patch antenna which is fed by a 50Ω microstrip line. The operational bandwidth is around 3.6%, due to the small thickness of the substrate, and a satisfying tunability of 4.94% is achieved. The substrate is composed of the highly anisotropic E7 liquid crystal [202], where the permittivity changes from $\varepsilon_{\perp} = 2.41$ to $\varepsilon_{\parallel} = 2.66$ at $3GHz$ when maximum voltage is applied to the cell. Radiation patterns of the microstrip patch antenna are also presented.

6.5.2 Antenna Design

A microstrip patch antenna operating at $3GHz$ was designed with CST Microwave Studio software. The E7 liquid crystal was used as a substrate and placed exactly beneath the radiating patch. The following Figure 103 shows a top and side-view of the antenna and substrate geometry. The substrate was mylar with 0.5 mm thickness except for the area underneath the patch, where the liquid crystal cell was placed. The permittivity of the mylar was 2.23. The microstrip patch, with dimensions of $31\times31.5mm^2$ was directly fed by a 50Ω microstrip line.

The liquid crystal cell had a thickness of 0.5 mm and extended by 2 mm beyond the area of the patch. The liquid crystal was used, is the high anisotropic E7 liquid crystal (Merck) [202]. The values of the relative permittivity and loss tangent of the E7 liquid crystal was taken from Figure 102 and presented in Table 16 [190]. The different values of the dielectric constant are achieved by applying a low frequency (1 kHz) AC voltage up to 20V across the liquid crystal cell.

Table 16: Real and imaginary dielectric permittivity with losses of the E7 liquid crystal at 3GHz [190].

Applied Voltage (V)	ε'	ε''	$\tan\delta$
0	2.41	0.19	0.079
2	2.47	0.17	0.07
4	2.6	0.13	0.05
10	2.66	0.11	0.042
20	2.66	0.11	0.041

The patch antenna was placed directly in contact with the LC to gain maximum tuning range. The antenna has a superstrate of 1 mm thick glass with relative permittivity of 6 to make the creation of a cavity feasible, where the liquid crystal was inserted.

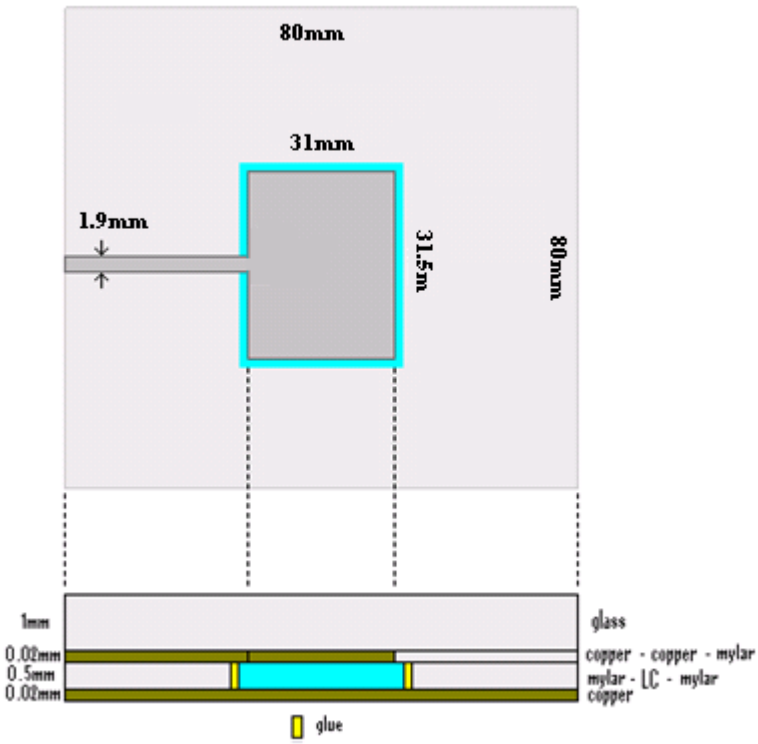

Figure 103: Schematic diagram of the proposed microstrip patch antenna. Top view and side view respectively.

6.5.3 Simulated Results

Figure 104 shows the simulated results of the return loss of the patch antenna presented. The five states of liquid crystal bias, 0, 2, 4, 10 and 20V correspond to five different permittivity values, from $\varepsilon_{\perp} = 2.41$ to $\varepsilon_{\parallel} = 2.66$ and loss tangent from $\tan\delta_{\perp} = 0.079$ to $\tan\delta_{\parallel} = 0.042$. For the simulated results the matched frequency ranged from 3.07GHz at 0V to 2.922GHz at 20V, giving a tuning range of 4.94% (148MHz). The bandwidth was between 3.46% and 3.83%.

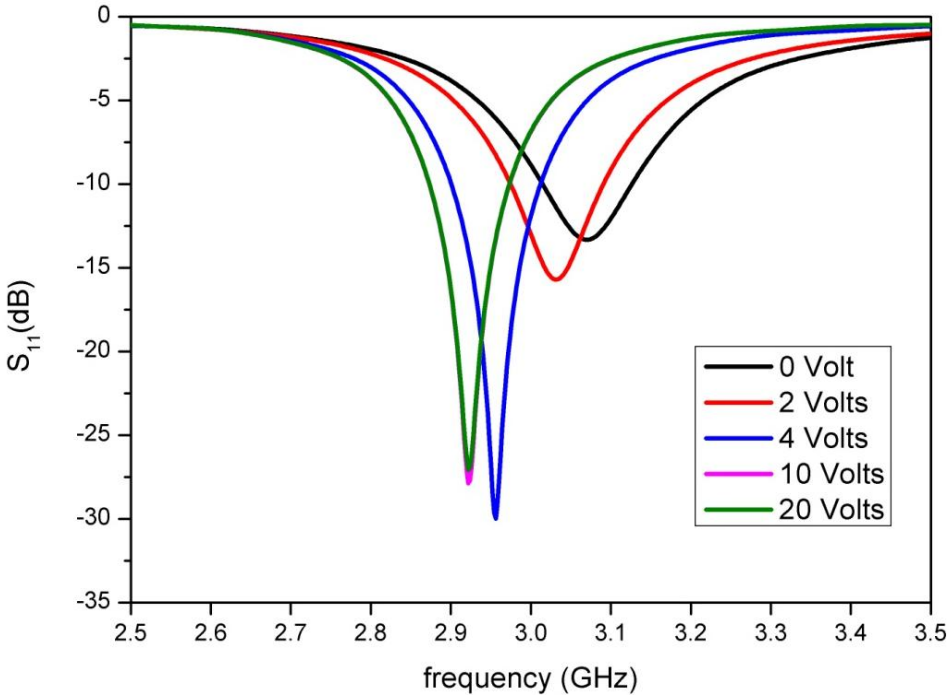

Figure 104: Reflection parameter changing the relative permittivity of the liquid crystal substrate. The values of permittivity correspond to a change of bias voltage from 0V up to 20V.

However, a key issue is the radiation efficiency of LC antennas at the frequencies where the loss tangent ranges from 0.042 to 0.079. Radiation patterns were plotted for the biased microstrip patch and the patterns were the expected patterns of a conventional microstrip patch antenna. Figure 105a shows the 3D radiation pattern of the tunable antenna when the applied voltage is at 0V, and Figure 105(b-f) show the E-plane cuts for the five different frequencies when the voltage gradually increased up to 20V. The efficiency was relatively low; 20%, due to substrate losses and the directivity was around 7.4dB. Table 17 shows frequency versus directivity and efficiency for all the different states.

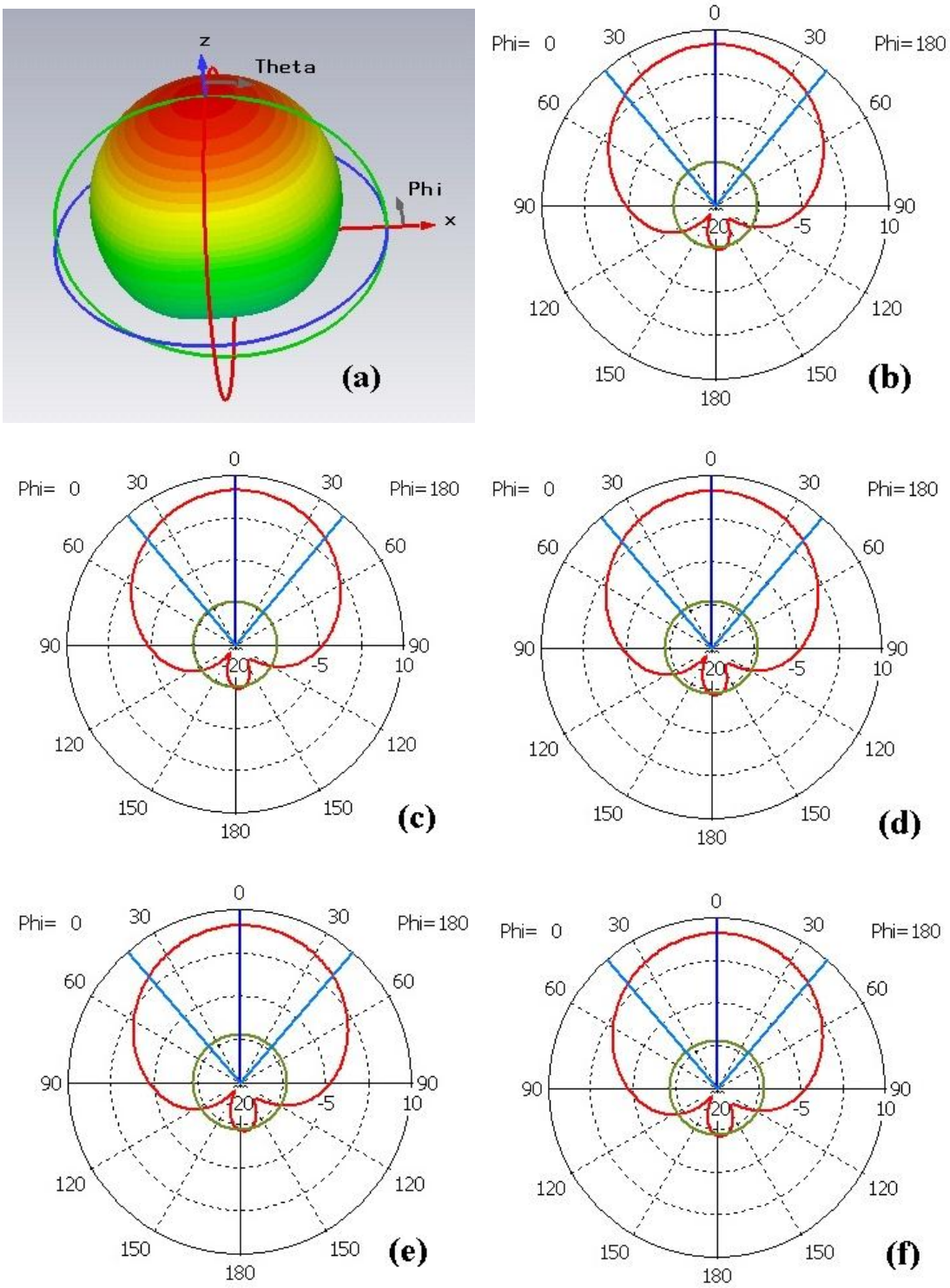

Figure 105: a) 3D radiation pattern of the tunable patch antenna, when the voltage is set at 0V $(\varepsilon = 2.41)$. E-plane cuts for b) 0V, c) 2V, d) 4V, e) 10V and f) 20V . All figures are at 3 GHz.

Table 17: Resonance frequencies versus directivity and efficiency for the different states.

Voltage (V)	epsilon	Frequency (GHz)	BW (%)	Directivity (dB)	Efficiency (%)
0	2.41	3.07	3.65	7.533	16.6
2	2.47	3.032	3.83	7.501	18.3
4	2.6	2.956	3.79	7.404	21.2
10	2.66	2.922	3.49	7.36	22.8
20	2.66	2.922	3.46	7.36	22.9

As observed, the shape of the radiation patterns remained unchanged for every different state. However, the efficiency of the antenna increased as the bias voltage increased and the loss tangent has reduced. The simulated radiation efficiencies taken from CST Microwave Studio software for the five states were between 16.6% and 22.9%.

6.5.4 CNT-doped liquid crystal antenna

A similar microstrip patch antenna operating at 3 GHz was designed again with CST-MS software. The E7 liquid crystal from the previous design was replaced with the CNT-doped liquid crystal previously presented. The new substrate was placed, as before, exactly beneath the area that covered by the radiating patch. The dimensions of the microstrip patch were $29.8 \times 30 mm^2$.

The liquid crystal (E7+0.01%wt CNT) cell had the characteristics reported in Figure 102 and the thickness is 0.5 mm. The values of relative permittivity and loss tangent of the doped liquid crystal when a field was applied as presented in Table 18 [190].

Table 18: Real and imaginary dielectric permittivity with losses of the E7+0.01%wt CNT liquid crystal at 3 GHz [190].

Applied Voltage (V)	ε'	ε''	$\tan\delta$
0	2.51	0.22	0.088
2	2.6	0.22	0.085
4	2.73	0.22	0.08
10	2.9	0.23	0.078
20	2.98	0.27	0.092

6.5.5 Simulated Results

Figure 106 shows the simulated results of the reflection parameter of the patch antenna presented. The five states of liquid crystal bias, 0, 2, 4, 10 and 20V correspond to five different permittivity values, from $\varepsilon_{\perp} = 2.51$ to $\varepsilon_{\parallel} = 2.98$ and loss tangent from $\tan\delta_{\perp} = 0.088$ to $\tan\delta_{\perp} = 0.092$. For the simulated results the frequency can be tuned from 3.132GHz at 0V to 2.868GHz at 20V, a tuning range of 8.8% (264MHz), almost double of that been achieved using the pure liquid crystal. The bandwidth was between 2.02% and 3.56%.

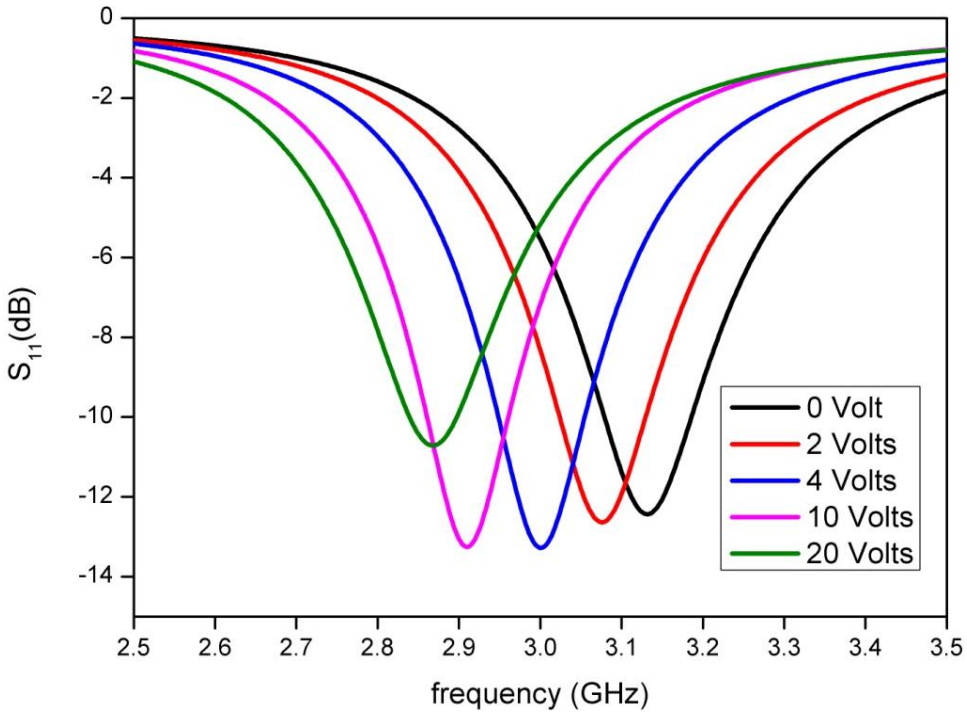

Figure 106: Reflection parameter changing the relative permittivity of the CNT-doped liquid crystal substrate. The values of permittivity correspond to a change of bias voltage from 0V up to 20V.

It was observed that when the new CNT-doped liquid crystal was used for antenna design, the tunability of the antenna was almost doubled, as expected, due to the very high anisotropy. However, the losses of the CNT-doped liquid crystal are much higher than the pure one, therefore, the efficiency was negatively affected, and it was as low as 15.44%. Radiation patterns are plotted again in Figure 107. Finally, Table 19 shows frequency versus directivity and efficiency for all the different states.

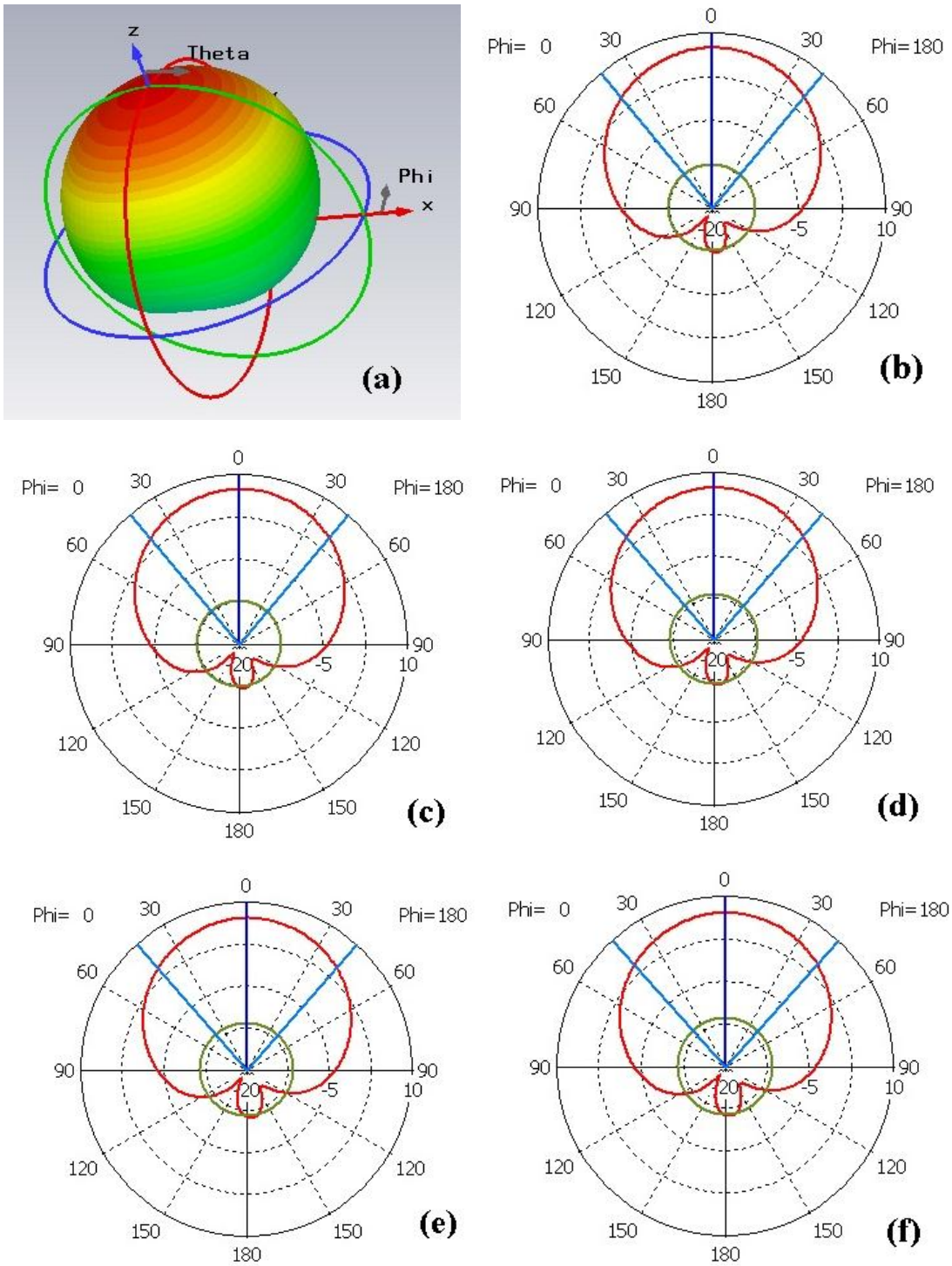

Figure 107: a) 3D radiation pattern of the new tunable patch antenna, when the voltage is set at 0V $(\varepsilon = 2.51)$. E-plane cuts for b) 0V, c) 2V, d) 4V, e) 10V and f) 20V . All figures are at 3 GHz.

Table 19: Resonance frequencies versus directivity and efficiency for the different states.

Voltage (V)	epsilon	Frequency (GHz)	BW (%)	Directivity (dB)	Efficiency (%)
0	2.51	3.132	3.38	7.533	16.7
2	2.6	3.076	3.45	7.46	16.7
4	2.73	3	3.56	7.36	16.9
10	2.9	2.91	3.44	7.239	16.7
20	2.98	2.868	2.02	7.176	15.4

As it was expected, the shape of the radiation patterns were very similar for different bias voltage applied on the CNT-doped liquid crystal substrate. However, the efficiency of the antenna fluctuated around 16% and it strongly depended on the losses on each state.

6.5.6 Measurement Results

A tunable microstrip patch antenna operating at low frequencies, i.e. 3 GHz is not feasible to be manufactured at present. That limitation exists because of the total volume that the liquid crystal can occupy, in order to keep the high anisotropy that has been analyzed in a previous section. According to the alignment techniques currently applied, the limit of the maximum volume of the cell is at 100 mm^3. The patch antenna presented in the previous section, operating at 3 GHz, needs a volume of 488 mm^3.

Therefore, a microstrip patch antenna operating at 11 GHz was designed and fabricated on an E7 liquid crystal substrate. The liquid crystal cell was 100 μm in thickness and was directly placed between the ground plane and the conductive patch, to achieve the maximum tuning range. The liquid crystal filled the volume of the cell, 10mm x 13mm x 0.1mm, which was slightly larger than the patch (8mm x 11mm) to avoid any edge effects while applying the external field. The geometry is shown in Figure 108. On the top of this 3-layer structure, a 1mm thick glass layer was placed.

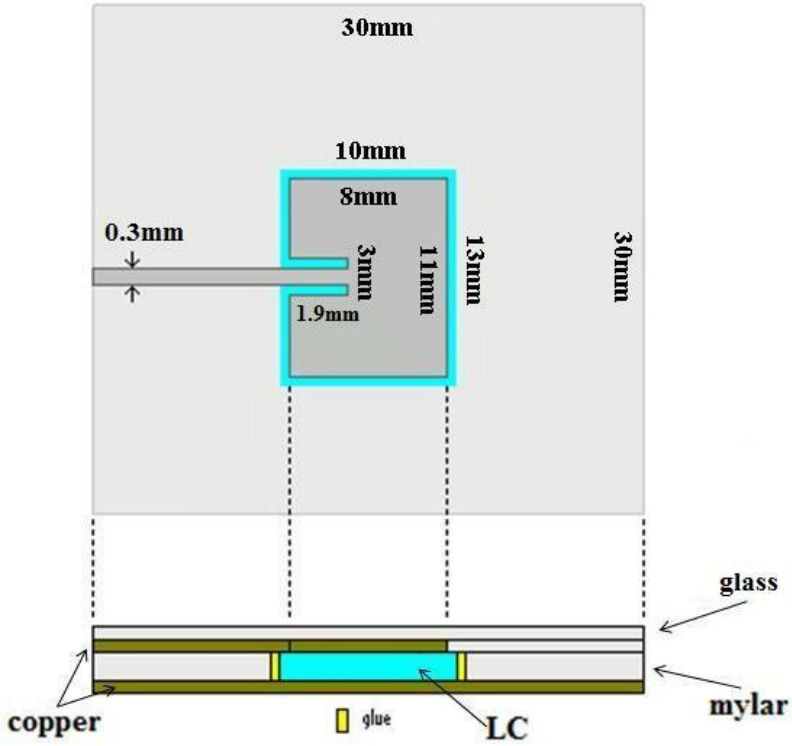

Figure 108: Schematic diagram of the fabricated microstrip patch antenna operating at 11 GHz. Top view and side view respectively.

A DC bias voltage was then applied between the patch and the ground plane, across the liquid crystal using a bias tee at the feed input. Calibration was not accurate in the above configuration as the system is fragile and unstable. That explain the behaviour of the system, where the reflection coefficient attains values above 0dB (Figure 109).

It is interesting to note that the behaviour of the antenna is more like a "switch", rather than that of tuning as observed in the simulation results. The resonant frequency switches in lower values for about 230 MHz (2.14%), when a DC is applied. It appears that there is a threshold of around 2 V, allowing the molecules to gradually rotate with respect to the field. When the voltage past the threshold, the resonant frequency moves slightly towards lower values.

Table 20 shows the tunability of the microstrip patch antenna.

Table 20: Antenna performance over the tuning range from no-field to 25 V.

	0 V	**5 V**	**10 V**	**15 V**	**25 V**
Res. freq (GHz)	11.0875	10.875	10.875	10.8625	10.85
S_{11} (dB)	-22.9	-21.7	-23.1	-22.3	-20.5
BW (%)	4.06	1.5	1.6	1.5	1.61

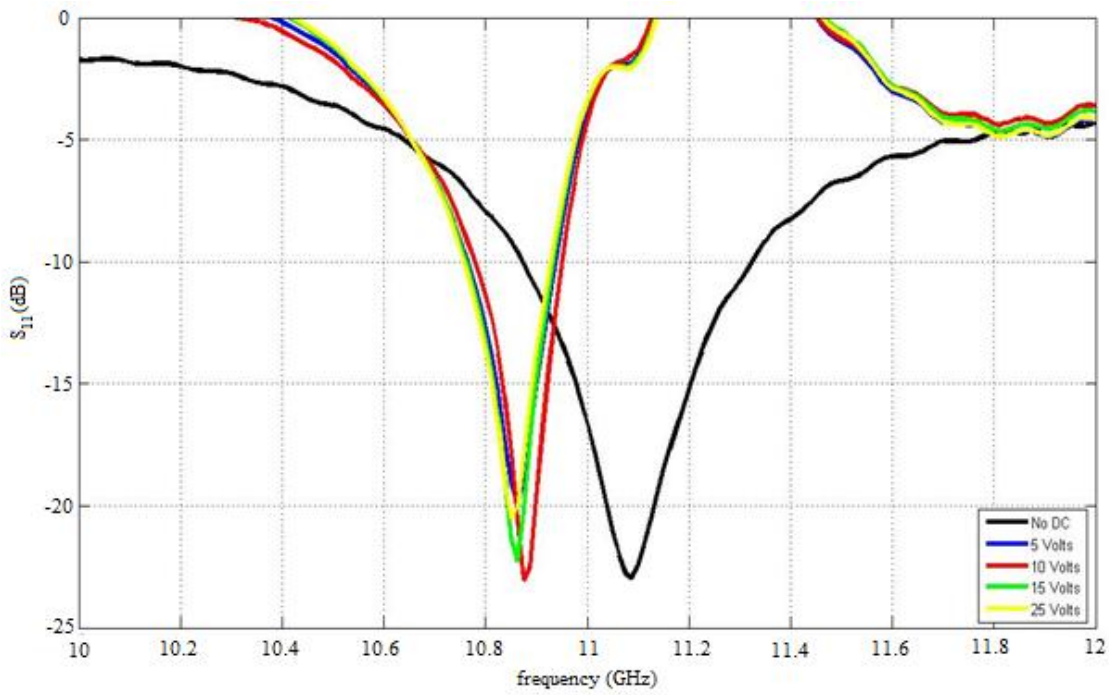

Figure 109: Frequency tuning of the fabricated microstrip patch antenna applying DC bias voltage.

Simulations have also been performed for the design of Figure 108. The values of the relative permittivity, $\varepsilon_{\perp}$ and $\varepsilon_{\parallel}$, and loss tangent, $\tan\delta_{\perp}$ and $\tan\delta_{\parallel}$, of the E7 liquid crystal used for the measurement were taken from [177] and presented in Table 21.

Table 21: Permittivity values of E7-liquid crystal at 11 GHz [177].

$\varepsilon_{\perp}$	$\varepsilon_{\parallel}$	$\tan\delta_{\perp}$	$\tan\delta_{\parallel}$
2.6	2.76	0.045	0.025

Figure 110 shows the simulated versus measurement results of the microstrip patch antenna. Good agreement is observed. Only two states of the E7-liquid crystal were simulated as these were the only known permittivity and loss tangent values at 11GHz given in [177]. At the simulated results, the matched frequency switches from 11.1 GHz to 10.78 GHz, a tuning range of 2.88% (320 MHz). The bandwidth is around 2.6%.

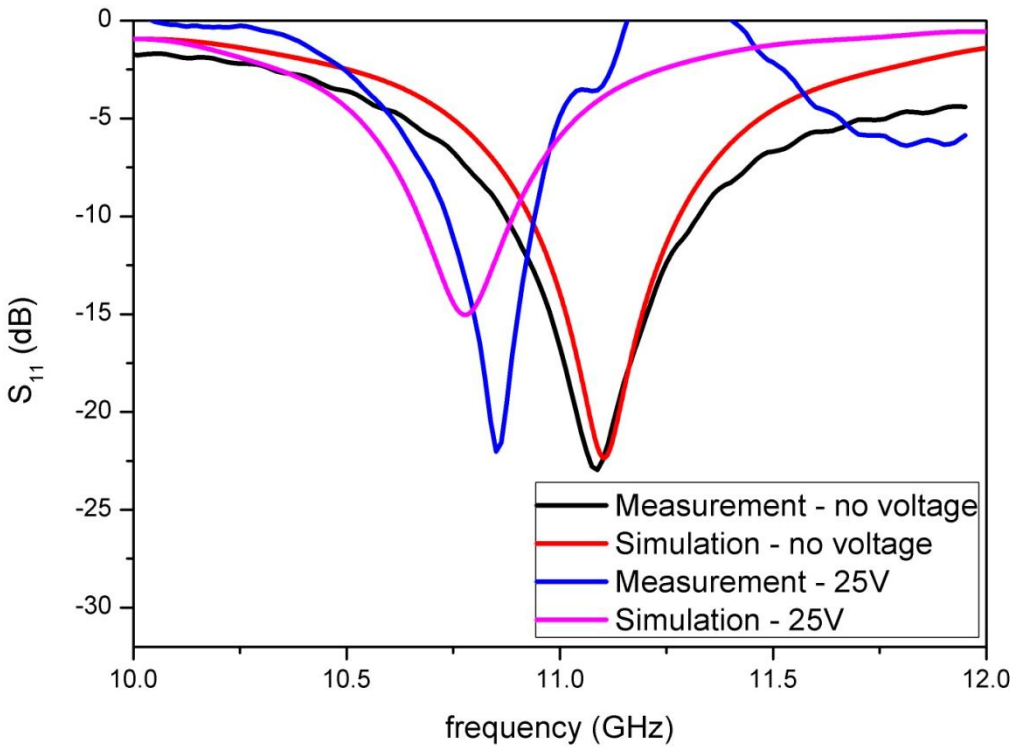

Figure 110: Comparison between simulation and measurement of the tunable microstrip patch antenna.

6.6 Summary

An Ultra Wide-Band (UWB) circular disc monopole antenna has been designed using a thin and optically transparent conductive film. The simulation results obtained by CST show good agreement with the measured ones. The measured radiation patterns of the proposed UWB antenna are omnidirectional and monopole-like at low frequencies in the H-plane and E-plane, respectively. A comparison between the performance of the antenna using the transparent conductor and aluminium is also presented. In the final part of this chapter, liquid crystals and tunable antennas were introduced. A method for electrical characterization of different liquid crystals was presented. Simulated and measured results of the use of liquid crystals revealed the advantages of using them for antenna design purposes.

Chapter 7: Conclusion and future work

7.1 Conclusions

Carbon nanotubes have attracted increased research interest and public attention recently. Many applications, using carbon nanotubes have become very popular. These include field emission sources, transistors, nano-transmission lines and nano-antennas because of their outstanding metallic conductivity and mobility along the entire length. Focusing on the possibility of a structure performing as a nano-antenna, many laboratories around the world, are trying to create longer nanotubes from nanometer to few centimeters. This would potentially lead to a new subject area to study, which is the use of CNTs for sub-millimeter, millimiter wave and microwave applications.

This thesis started with an overview of the history and the basic concepts of the carbon nanotubes. Some structural as well as electrical properties were also presented. Fundamental properties of a dipole transmitting carbon nanotube antenna were reviewed, via a Hallen's-type integral equation. The equation is based on a semiclassical conductivity, equivalent to a more rigorous quantum mechanical conductivity at the frequencies of interest here. Interesting properties such as the input impedance, current distribution, and radiation pattern were discussed. A comparison was made between the prototype CNT antenna and a conventional dipole antenna made of copper with exactly the same dimensions. It was observed that, due to some significant properties of the CNT conductivity function, alongside the relationship to plasmon effects, some properties of carbon nanotube antennas are

quite different from the case of an infinitely thin copper antenna of the same size and shape. Finally, carbon nanotube antennas were found to exhibit plasmon resonances above a limited frequency have high input impedances (which is probably beneficial for connecting to nanoelectronic circuits, but not the best for antenna applications), and exhibit very low efficiencies.

In the third chapter, vertically aligned multi-walled carbon nanotube (VACNT) films were characterized by rectangular waveguide measurement in X- and Ku- bands as well as low terahertz frequencies, performing transmission terahertz time-domain spectroscopy (THz-TDS) measurements. The carbon nanotube arrays were placed on the top surface of a rectangular silicon substrate. All the samples were fabricated at the Center for Advanced Photonics and Electronics at Cambridge University (CAPE). The effective complex permittivity of the VACNT films were extracted in a frequency band, starting from 8 GHz to 2.5 THz, with some few interruptions. The effective complex permeability could only be extracted in the microwave region (8 GHz to 18GHz) because both reflection and transmission of the slab could only be measured at these frequencies. All the extracted parameters were verified by full wave simulations and very good agreement was obtained. In the microwave region, a systematic error analysis was presented and the errors calculated were within the acceptable range of errors. The absorbing performance of VACNT films was also examined, in both X- and Ku- bands, and was compared to conventional materials, proving that a 90% reduction in size is possible without losing in absorption.

In low terahertz frequencies, the transmission THz-TDS technique was applied. From this measurement, a time domain signal was obtained which was then transformed to the frequency domain. The frequency dependent complex permittivity was found, applying a fast Fourier transform on each time-domain signal. These transmission spectra were used to investigate the complex permittivity of the films versus frequency (on the assumption that permeability μ=1), and conductivity of the samples. By introducing the Drude model for lossy metals the behaviour of the VACNT samples was explained by fitting to the measured complex permittivity. The material properties of this film provided useful information for potential microwave and terahertz applications.

In the following chapter, the dynamic properties of single-walled carbon nanotubes from a circuit point of view were considered and an effective RF equivalent circuit was presented. An introduction to modelling techniques, such as the FDTD algorithm, was also given, using Maxwell's equations. The procedure of constructing simulations of electromagnetic waves was explained and thoroughly studied using a programming language.

In order to understand material properties of carbon nanotubes in microwaves, detailed measurements need to be conducted. For antenna and microwave designs based on carbon nanotubes, it is very important to understand their properties at a single tube level. Furthermore, an efficient modelling tool is needed for proposing new antenna designs for further industrial applications.

In chapter five, further investigation of the carbon nanotube properties, at low microwave frequencies, as an effective medium was performed. A model, characterized by the general permittivity (GEF) and general permeability functions (GMF) was presented, both independent of thickness and can be used for any similarly dense VACNT array, to predict the absorption properties of the array. The estimation of the permittivity and permeability of an individual carbon nanotube was presented. A periodic structure was therefore simulated, under periodic boundary conditions, consisting of solid anisotropic cylinders. The complex permittivity and permeability of both vertical and parallel components were calculated and fitted with the lossy medium approach for the effective permittivity, and the Lorentz-model for the effective permeability. The number of solutions of the optimization was very large, even though thousands of iterations were performed, leading to huge errors in the permeability, compared to the fitted model.

Optical properties of VACNT arrays, when the periodicity is within the sub-wavelength regime were calculated. The effect of geometrical parameters of the tube such as length, diameter and inter-tube distance between two consecutive tubes were also examined. All the results show that VACNT films in optical range are highly absorptive. Longer nanotubes, result in higher levels of absorption, usually close to 1. Higher volume fraction, will also result in higher absorption as well as higher reflection and lower transmission. Finally, keeping the volume fraction constant but

changing the radius and periodicity accordingly, will also result in higher absorption when the radius is increased. The absorption performance of the VACNT arrays has also investigated, when periodicity is equal to the incident wavelength. A very interesting phenomenon was observed similar to the one in silicon nanowire arrays with finite length [160], where the transmission is heavily depressed, resulting to absorption level close to unity.

In the last chapter, a planar circular disc monopole antenna for ultra-wideband applications was designed using thin conductive films such as AgHT-4. The simulation results obtained by CST show good agreement with the measured ones. The measured radiation patterns of the proposed UWB antenna are omni-directional and monopole-like in low frequencies in H-plane and E-plane respectively. A comparison between the performance of the antenna using the transparent conductor and aluminium is also proposed.

Fundamental ideas on frequency tunable rectangular printed patch antenna using liquid crystal such as were presented. Simulation and measurement results showed that frequency tuning is possible, using a liquid crystal cell in the substrate (in the area which is underneath the radiating patch). Additionally, we have ascertained that we can achieve greater tuning using liquid crystals with higher dielectric anisotropy at microwave frequencies doping them with carbon nanotubes. For instance, 0.2%wt metallic micro tubules increase the birefringence by 54% at 30GHz when inserted in liquid crystals. Carbon nanotubes, inserted in a host medium such as a liquid crystal, can easily be aligned, applying electric or magnetic field across the liquid crystal cell. Frequency tunable antennas, using carbon nanotubes doped liquid crystals, were simulated in 3 GHz. Different values of dielectric constant were achieved by applying a low frequency (1 kHz) AC voltage across the cell. The real permittivity changed from 2.51 for 0 V to 2.98 for 20 V of applied field, resulting in a frequency tuning of the proposed antenna of 8.8%. Radiation patterns were plotted, and radiation parameters such as directivity and efficiency were calculated. This tuning performance is almost two times better, than a patch antenna having as a substrate pure E7-liquid crystal. The tuning range was as low as 4.94% in the same frequency range (around 3 GHz). Finally, a measurement was performed with pure E7-liquid crystal at 11 GHz. The behaviour of the antenna was more like a "switch", with two

on and off state, rather than a tuning function as observed in the simulations. Although good agreement with the simulations was observed for the two opposing states, the measurement system was very fragile and unstable. The fabrication was not ideal, as air bubbles were inserted in the liquid crystal cell, not allowing the molecules to be aligned along the applied field.

7.2 Future work

Arising from the research carried out during this work, areas of potential further research could include the following:

- Further properties investigation of carbon nanotubes in microwave and terahertz frequencies. This would involve the measurement of different samples made by CAPE, Cambridge University. The samples would be both transmission lines and simple patch antennas, where an array of carbon nanotubes would be placed very close to the design. By coupling, we would expect to excite these nanotubes at frequencies corresponding to their length. Comparison between structures with and without carbon nanotubes would be made and through transmission and reflection coefficients (amplitudes and phase) further properties of the CNTs would be extracted. Simulations on these designs would be made in the initial stage, and it is expected that the appearance of a bandgap in a frequency would be strongly related to the length and the spacing between the carbon nanotubes in the array.

- The electrical properties of an individual carbon nanotube could be investigated. This, would lead to the fabrication of a dipole or monopole-like nano-antenna which operating in THz frequencies. This nanotube would either be vertical or parallel to the substrate. In the case of a vertical standing carbon nanotube, which preferably should be multi-walled as it is highly conductive, there are some fabrication constraints. At the moment, with plasma-enhanced chemical vapour deposition (PECVD), it is only possible to have a 5 μm long carbon nanotube. That would result in an operation frequency of few terahertz, making measurement very difficult. The

horizontal case, seems to be more realistic, where 10 μm long carbon nanotubes can be grown and then attaching in both ends a metallic electrode. DC measurements can be easily performed, whereas in low GHz would be impossible, being well below from the sub-wavelength regime. Co-planar probe stations, operating in few hundreds of GHz would make this measurement feasible, but for much longer nanotubes.

- More complex optically transparent antenna designs, apart from the UWB disc monopole, would be implemented. To begin with, a simple patch antenna on a flexible substrate would be necessary. Then, a planar series fed microstrip patch array could be fabricated, using metamaterial transmission lines to manipulate the beam. Similar cylindrical antennas could be designed for base-station applications. Partially Reflected Surfaces (PRS) would be placed in all the designs, planar and cylindrical, to achieve improved gain and reduced side lobe levels (SLL).

- As discussed above, liquid crystals developed by CAPE have advantages on tunability and flexibility. The structures using the mixtures of either single wall carbon nanotubes (SWNTs) or multi-wall carbon nanotubes (MWNTs) with liquid crystals can be fabricated and measured. Several techniques would have to be employed to prevent the nanotubes to make clusters. From the measurements, the simulated results regarding the gain and efficiency of tunable microstrip patch would have to be verified.

- Other designs could also be implemented here, using the combination of technology proposed in previous chapters, with regards to transparent substrates, transparent conductors and carbon nanotubes in the same structure. The final design would compromise on all these technologies resulting in a highly bendable and frequency tunable optically transparent antenna based on carbon nanotube enhanced liquid crystals.

- The main purpose of THz investigation of Carbon Nanotube films is the extraction of the dielectric properties of these films which would be very useful for designing antennas, using vertically aligned Carbon Nanotubes. The

main drawback of these films is their high resistance. One way of increasing the sheet resistivity of a CNT film is to increase the density of the CNT array (grow CNTs with smaller spacing distance). However, current fabrication techniques cannot achieve highly dense arrays. At the moment, the minimum spacing distance between CNTs can be approximately 80 nm. Another approach to increase the entanglement of CNTs is to squash the CNT array [105] thus possibly achieving 82% reduction in sheet resistance. Finally, as shown in Figure 53 and Figure 54, DC resistance is proportional to the CNT line length (L) and inversely proportional to the thickness (t) of the film. A combination of the above methods would allow the fabrication of a very-low resistant CNT film (below $1\Omega/sq$ - 90% reduction) so that we can use CNT for antenna and RF systems.

- Further investigation of the anisotropic properties of the effective medium of the VACNT slabs is needed. Ellipsometry, is an optical technique for the investigation of the complex refractive index of thin films. As carbon nanotube films can be considered to be biaxial anisotropic materials, there are several methods to investigate the characteristics of this anisotropy. The most basic one, require measuring a wide range of incident angles changing the path length, where light is travelling through the film. In this case, the light experiences different optical properties in different directions, and therefore the anisotropy can be characterized. A more complicated technique, is the so called, generalized ellipsometry. That is an advanced ellipsometry measurement that involves the complete 2x2 Jones matrix description of the sample. The difference with normal ellipsometry is that the later ignores the off-diagonal elements of this matrix, as they are zero for isotropic materials. With this advanced method the CNT films can be fully characterized, as anisotropic thin films.

- Among the wide range of available nanofillers, CNTs have attracted particular interest as reinforcing fillers because of their superb mechanical properties - Young's modulus 1 TPa, but they are also considered as fillers for creating electrically conductive or semi-conductive polymer composites. These composite are expected to have high absorption rate and the investigation of

this property can be done. Different concentrations of CNTs would lead to different levels of absorption.

- One of the very interesting properties of carbon nanotubes at optical frequencies that has been observed is the dramatic optical absorption enhancement that occurs when the lattice constant is increased and it is much higher than any other combination of radius - periodicity sets. These arrays could be fabricated and measured. They could either stand alone on a silicon based substrate or be embedded in polymers. Performance over different angle of incidence could be investigated and therefore, CNT arrays could be used for next generation solar cells with higher energy conversion efficiencies and lower costs.

References

[1] H. W. Kroto, J. R. Heath, S. C. Obrien, R. F. Curl, and R. E. Smalley, "C-60 - Buckminsterfullerene," *Nature,* vol. 318, pp. 162-163, 1985.

[2] S. Iijima, "Helical Microtubules of Graphitic Carbon," *Nature,* vol. 354, pp. 56-58, Nov 7 1991.

[3] Y. Y. G. Huang, D. Y. Khang, J. L. Xiao, C. Kocabas, S. MacLaren, T. Banks, H. Q. Jiang, and J. A. Rogers, "Molecular scale buckling mechanics on individual aligned single-wall carbon nanotubes on elastomeric substrates," *Nano Letters,* vol. 8, pp. 124-130, Jan 2008.

[4] T. Cagin, G. H. Gao, and W. A. Goddard, "Energetics, structure, mechanical and vibrational properties of single-walled carbon nanotubes," *Nanotechnology,* vol. 9, pp. 184-191, Sep 1998.

[5] X. J. Zhou, J. Y. Park, S. M. Huang, J. Liu, and P. L. McEuen, "Band structure, phonon scattering, and the performance limit of single-walled carbon nanotube transistors," *Physical Review Letters,* vol. 95, Sep 30 2005.

[6] Z. Yao, C. L. Kane, and C. Dekker, "High-field electrical transport in single-wall carbon nanotubes," *Physical Review Letters,* vol. 84, pp. 2941-2944, Mar 27 2000.

[7] S. Berber, Y. K. Kwon, and D. Tomanek, "Unusually high thermal conductivity of carbon nanotubes," *Physical Review Letters,* vol. 84, pp. 4613-4616, May 15 2000.

[8] J. P. Salvetat, A. J. Kulik, J. M. Bonard, G. A. D. Briggs, T. Stockli, K. Metenier, S. Bonnamy, F. Beguin, N. A. Burnham, and L. Forro, "Elastic modulus of ordered and disordered multiwalled carbon nanotubes," *Advanced Materials,* vol. 11, pp. 161-165, Jan 22 1999.

[9] C. M. Lieber, T. W. Odom, J. L. Huang, and P. Kim, "Atomic structure and electronic properties of single-walled carbon nanotubes," *Nature,* vol. 391, pp. 62-64, Jan 1 1998.

[10] J. M. Bonard, J. P. Salvetat, T. Stockli, L. Forro, and A. Chatelain, "Field emission from carbon nanotubes: perspectives for applications and clues to the emission mechanism," *Applied Physics a-Materials Science & Processing,* vol. 69, pp. 245-254, Sep 1999.

[11] M. S. Dresselhaus, G. Dresselhaus, and P. Avouris, *Carbon nanotubes : synthesis, structure, properties, and applications.* Berlin ; London: Springer, 2001.

[12] P. Avouris, J. Appenzeller, R. Martel, and S. J. Wind, "Carbon nanotube electronics," *Proceedings of the IEEE,* vol. 91, pp. 1772-1784, Nov 2003.

[13] G. W. Hanson, "Fundamental transmitting properties of carbon nanotube antennas," *IEEE Transactions on Antennas and Propagation,* vol. 53, pp. 3426-3435, Nov 2005.

[14] P. J. Burke, S. D. Li, and Z. Yu, "Quantitative theory of nanowire and nanotube antenna performance," *IEEE Transactions on Nanotechnology,* vol. 5, pp. 314-334, Jul 2006.

[15] C. Dekker, J. W. G. Wildoer, L. C. Venema, A. G. Rinzler, and R. E. Smalley, "Electronic structure of atomically resolved carbon nanotubes," *Nature,* vol. 391, pp. 59-62, Jan 1 1998.

[16] A. Thess, R. Lee, P. Nikolaev, H. Dai, P. Petit, J. Robert, C. Xu, Y. H. Lee, S. G. Kim, A. G. Rinzler, D. T. Colbert, G. E. Scuseria, D. Tománek, J. E. Fischer, and R. E. Smalley, "Crystalline Ropes of Metallic Carbon Nanotubes," *Science,* vol. 273, pp. 483-487, 1996.

[17] K. L. Jiang, Q. Q. Li, and S. S. Fan, "Nanotechnology: Spinning continuous carbon nanotube yarns - Carbon nanotubes weave their way into a range of imaginative macroscopic applications.," *Nature,* vol. 419, pp. 801-801, Oct 24 2002.

[18] F. Wei, Q. Zhang, M. Q. Zhao, J. Q. Huang, Y. Liu, Y. Wang, and W. Z. Qian, "Vertically aligned carbon nanotube arrays grown on a lamellar catalyst by fluidized bed catalytic chemical vapor deposition," *Carbon,* vol. 47, pp. 2600-2610, Sep 2009.

[19] F. Wei, Q. Zhang, W. P. Zhou, W. Z. Qian, R. Xiang, J. Q. Huang, and D. Z. Wang, "Synchronous growth of vertically aligned carbon nanotubes with pristine stress in the heterogeneous catalysis process," *Journal of Physical Chemistry C,* vol. 111, pp. 14638-14643, Oct 11 2007.

[20] W. Feng, X. D. Bai, Y. Q. Lian, J. Liang, X. G. Wang, and K. Yoshino, "Well-aligned polyaniline/carbon-nanotube composite films grown by in-situ aniline polymerization," *Carbon,* vol. 41, pp. 1551-1557, 2003.

[21] Z. W. Pan, H. G. Zhu, Z. T. Zhang, H. J. Im, S. Dai, D. B. Beach, and D. H. Lowndes, "Patterned growth of vertically aligned carbon nanotubes on pre-patterned iron/silica substrates prepared by sol-gel and shadow masking," *Journal of Physical Chemistry B,* vol. 107, pp. 1338-1344, Feb 13 2003.

[22] Y. J. Jung, B. Q. Wei, R. Vajtai, and P. M. Ajayan, "Mechanism of selective growth of carbon nanotubes on SiO2/Si patterns," *Nano Letters,* vol. 3, pp. 561-564, Apr 2003.

[23] Q. M. Gong, Z. Li, D. Li, X. D. Bai, and J. Liang, "Fabrication and structure: a study of aligned carbon nanotube/carbon nanocomposites," *Solid State Communications,* vol. 131, pp. 399-404, Aug 2004.

[24] R. H. Hauge, C. L. Pint, S. T. Pheasant, M. Pasquali, K. E. Coulter, and H. K. Schmidt, "Synthesis of high aspect-ratio carbon nanotube "Flying Carpets" from nanostructured flake substrates," *Nano Letters,* vol. 8, pp. 1879-1883, Jul 2008.

[25] P. G. He, L. Z. Yang, Y. Xu, X. H. Wang, J. Zhu, R. Y. Zhang, and Y. Z. Fang, "The application of beta-cyclodextrin derivative functionalized aligned carbon nanotubes for electrochemically DNA sensing via host-guest recognition," *Analytica Chimica Acta,* vol. 689, pp. 39-46, Mar 9 2011.

[26] Y. Z. Fang, J. Yang, R. Y. Zhang, Y. Xu, and P. G. He, "Direct electrochemistry study of glucose oxidase on Pt nanoparticle-modified aligned carbon nanotubes electrode by the assistance of chitosan-CdS and its biosensoring for glucose," *Electrochemistry Communications,* vol. 10, pp. 1889-1892, Dec 2008.

[27] W. D. Zhang and B. Xu, "A solid-state pH sensor based on WO(3)-modified vertically aligned multiwalled carbon nanotubes," *Electrochemistry Communications,* vol. 11, pp. 1038-1041, May 2009.

[28] M. Penza, R. Rossi, M. Alvisi, M. A. Signore, G. Cassano, D. Dimaio, R. Pentassuglia, E. Piscopiello, E. Serra, and M. Falconieri, "Characterization of metal-modified and vertically-aligned carbon nanotube films for functionally

enhanced gas sensor applications," *Thin Solid Films*, vol. 517, pp. 6211-6216, Sep 30 2009.

[29] R. P. H. Chang, Q. H. Wang, A. A. Setlur, J. M. Lauerhaas, J. Y. Dai, and E. W. Seelig, "A nanotube-based field-emission flat panel display," *Applied Physics Letters*, vol. 72, pp. 2912-2913, Jun 1 1998.

[30] K. A. Dean and B. R. Chalamala, "Field emission microscopy of carbon nanotube caps," *Journal of Applied Physics*, vol. 85, pp. 3832-3836, Apr 1 1999.

[31] C. Dekker, S. J. Tans, and A. R. M. Verschueren, "Room-temperature transistor based on a single carbon nanotube," *Nature*, vol. 393, pp. 49-52, May 7 1998.

[32] R. Martel, T. Schmidt, H. R. Shea, T. Hertel, and P. Avouris, "Single- and multi-wall carbon nanotube field-effect transistors," *Applied Physics Letters*, vol. 73, pp. 2447-2449, Oct 26 1998.

[33] H. T. Soh, C. F. Quate, A. F. Morpurgo, C. M. Marcus, J. Kong, and H. J. Dai, "Integrated nanotube circuits: Controlled growth and ohmic contacting of single-walled carbon nanotubes," *Applied Physics Letters*, vol. 75, pp. 627-629, Aug 2 1999.

[34] A. C. Dillon, K. M. Jones, T. A. Bekkedahl, C. H. Kiang, D. S. Bethune, and M. J. Heben, "Storage of hydrogen in single-walled carbon nanotubes," *Nature*, vol. 386, pp. 377-379, Mar 27 1997.

[35] R. H. Baughman, A. E. Aliev, J. Y. Oh, M. E. Kozlov, A. A. Kuznetsov, S. L. Fang, A. F. Fonseca, R. Ovalle, M. D. Lima, M. H. Haque, Y. N. Gartstein, M. Zhang, and A. A. Zakhidov, "Giant-Stroke, Superelastic Carbon Nanotube Aerogel Muscles," *Science*, vol. 323, pp. 1575-1578, Mar 20 2009.

[36] Y. Nakayama, "Scanning probe microscopy installed with nanotube probes and nanotube tweezers," *Ultramicroscopy*, vol. 91, pp. 49-56, May 2002.

[37] C. V. Nguyen, K. J. Chao, R. M. D. Stevens, L. Delzeit, A. Cassell, J. Han, and M. Meyyappan, "Carbon nanotube tip probes: stability and lateral resolution in scanning probe microscopy and application to surface science in semiconductors," *Nanotechnology*, vol. 12, pp. 363-367, Sep 2001.

[38] T. A. Edison, "Manufacture of filaments for incandescent electric lamps," USA Patent, 1892.

[39] P. Schützenberger and L. Schützenberger, "Sur quelques faits relatifs a l'histoire du carbone," *Les Comptes rendus de l'Académie des sciences*, vol. 111, p. 774, 1890.

[40] L. C. F. Blackman and A. R. Ubbelhode, "Stress Recrystallization of Graphite," *Proceedings of the Royal Society of London. Series A, Mathematical and Physical Sciences*, vol. 266, pp. 20-32, 1962.

[41] A. P. Levitt, *Whisker Technology*. New York: Wiley-Interscience, 1970.

[42] M. Endo, T. Koyama, and Y. Hishiyama, "Structural Improvement of Carbon-Fibers Prepared from Benzene," *Japanese Journal of Applied Physics*, vol. 15, pp. 2073-2076, 1976.

[43] G. G. Tibbetts, "Carbon-Fibers Produced by Pyrolysis of Natural-Gas in Stainless-Steel Tubes," *Applied Physics Letters*, vol. 42, pp. 666-668, 1983.

[44] M. S. Dresselhaus and G. Dresselhaus, *Graphite Fibers and Filaments* vol. 5. Berlin: Springer-Verlag, 1988.

[45] A. Oberlin, M. Endo, and T. Koyama, "High-Resolution Electron-Microscope Observations of Graphitized Carbon-Fibers," *Carbon*, vol. 14, pp. 133-135, 1976.

[46] M. Endo, *The growth mechanism of vapor-grown carbon fibers*. Orleans, France: University of Orleans, 1975.
[47] R. E. Smalley, in *Department of Defence Workshop in Washington*, Washington, DC, Dec. 1990.
[48] D. R. Huffman, in *Department of Defence Workshop in Washington*, Washington, DC, Dec. 1990.
[49] M. S. Dresselhaus, in *Department of Defence Workshop in Washington*, Washington, DC, Dec. 1990.
[50] M. S. Dresselhaus, G. Dresselhaus, and P. C. Eklund, in *University of Pennsylvania Workshop*, University of Pennsylvania, 1991.
[51] Z. Y. Kosakovskaya, L. A. Chernozatonskii, and E. A. Fedorov, "Nanofilament Carbon Structure," *Jetp Letters*, vol. 56, pp. 26-30, Jul 10 1992.
[52] A. Oberlin, M. Endo, and T. Koyama, "Filamentous Growth of Carbon through Benzene Decomposition," *Journal of Crystal Growth*, vol. 32, pp. 335-349, 1976.
[53] T. W. Ebbesen and P. M. Ajayan, "Large-Scale Synthesis of Carbon Nanotubes," *Nature*, vol. 358, pp. 220-222, Jul 16 1992.
[54] S. M. Huang, X. Y. Cai, and J. Liu, "Growth of millimeter-long and horizontally aligned single-walled carbon nanotubes on flat substrates," *Journal of the American Chemical Society*, vol. 125, pp. 5636-5637, May 14 2003.
[55] J. Tersoff and R. S. Ruoff, "Structural-Properties of a Carbon-Nanotube Crystal," *Physical Review Letters*, vol. 73, pp. 676-679, Aug 1 1994.
[56] T. W. Odom, J. L. Huang, P. Kim, and C. M. Lieber, "Structure and electronic properties of carbon nanotubes," *Journal of Physical Chemistry B*, vol. 104, pp. 2794-2809, Apr 6 2000.
[57] K. Sattler, "Scanning-Tunneling-Microscopy of Carbon Nanotubes and Nanocones," *Carbon*, vol. 33, pp. 915-920, 1995.
[58] R. Saito, M. S. Dresselhaus, and G. Dresselhaus, *Physical Properties of Carbon Nanotubes*. London, UK: Imperial College Press, 2003.
[59] T. Guo, P. Nikolaev, A. G. Rinzler, D. Tomanek, D. T. Colbert, and R. E. Smalley, "Self-Assembly of Tubular Fullerenes," *Journal of Physical Chemistry*, vol. 99, pp. 10694-10697, Jul 6 1995.
[60] J. Kong, H. T. Soh, A. M. Cassell, C. F. Quate, and H. J. Dai, "Synthesis of individual single-walled carbon nanotubes on patterned silicon wafers," *Nature*, vol. 395, pp. 878-881, Oct 29 1998.
[61] J. Hao and G. W. Hanson, "Infrared and optical properties of carbon nanotube dipole antennas," *IEEE Transactions on Nanotechnology*, vol. 5, pp. 766-775, Nov 2006.
[62] G. L. Sewell, *Quantum mechanics and its emergent macrophysics*. Princeton ; Oxford: Princeton University Press, 2002.
[63] Available: http://www2.rohde-schwarz.com/file_3463/RAC-0607-0019.pdf
[64] C. T. White and J. W. Mintmire, "Fundamental properties of single-wall carbon nanotubes," *Journal of Physical Chemistry B*, vol. 109, pp. 52-65, Jan 13 2005.
[65] C. T. White, D. H. Robertson, and J. W. Mintmire, "Helical and Rotational Symmetries of Nanoscale Graphitic Tubules," *Physical Review B*, vol. 47, pp. 5485-5488, Mar 1 1993.
[66] E. D. Graugnard, "The electronic properties of multi-walled carbon nanotubes," Ph.D., Purdue University, December 2000.

[67] M. S. Dresselhaus, G. Dresselhaus, and P. C. Eklund, *Science of fullerenes and carbon nanotubes*. San Diego ; London: Academic Press, 1996.
[68] P. R. Wallace, "The Band Theory of Graphite," *Physical Review,* vol. 71, p. 622, 1947.
[69] M. P. Anantram and F. Leonard, "Physics of carbon nanotube electronic devices," *Reports on Progress in Physics,* vol. 69, pp. 507-561, Mar 2006.
[70] J. W. Mintmire, B. I. Dunlap, and C. T. White, "Are Fullerene Tubules Metallic," *Physical Review Letters,* vol. 68, pp. 631-634, Feb 3 1992.
[71] C. T. White and T. N. Todorov, "Carbon nanotubes as long ballistic conductors," *Nature,* vol. 393, pp. 240-242, May 21 1998.
[72] C. Kittel, *Introduction to solid state physics,* 6th ed. ed. New York ; Chichester: Wiley, 1986.
[73] O. N. Singh and A. Lakhtakia, *Electromagnetic fields in unconventional materials and structures*. New York ; Chichester: John Wiley, 2000.
[74] G. Y. Slepyan, S. A. Maksimenko, A. Lakhtakia, O. Yevtushenko, and A. V. Gusakov, "Electrodynamics of carbon nanotubes: Dynamic conductivity, impedance boundary conditions, and surface wave propagation," *Physical Review B,* vol. 60, pp. 17136-17149, Dec 15 1999.
[75] G. W. Hanson, *Fundamentals of nanoelectronics*: Pearson/Prentice Hall, 2008.
[76] R. S. Elliott, *Antenna theory and design*. Englewood Cliffs ; London: Prentice-Hall, 1981.
[77] G. Fikioris and T. T. Wu, "On the application of numerical methods to Hallen's equation," *IEEE Transactions on Antennas and Propagation,* vol. 49, pp. 383-392, Mar 2001.
[78] S. D. Li, Z. Yu, C. Rutherglen, and P. J. Burke, "Electrical properties of 0.4 cm long single-walled carbon nanotubes," *Nano Letters,* vol. 4, pp. 2003-2007, Oct 2004.
[79] Y. S. Chen, Y. F. Ma, B. Wang, Y. P. Wu, and Y. Huang, "The production of horizontally aligned single-walled carbon nanotubes," *Carbon,* vol. 49, pp. 4098-4110, Nov 2011.
[80] Z. F. Ren, Z. P. Huang, J. W. Xu, J. H. Wang, P. Bush, M. P. Siegal, and P. N. Provencio, "Synthesis of large arrays of well-aligned carbon nanotubes on glass," *Science,* vol. 282, pp. 1105-1107, Nov 6 1998.
[81] H. J. Dai, S. S. Fan, M. G. Chapline, N. R. Franklin, T. W. Tombler, and A. M. Cassell, "Self-oriented regular arrays of carbon nanotubes and their field emission properties," *Science,* vol. 283, pp. 512-514, Jan 22 1999.
[82] K. Hata, D. N. Futaba, K. Mizuno, T. Namai, M. Yumura, and S. Iijima, "Water-assisted highly efficient synthesis of impurity-free single-waited carbon nanotubes," *Science,* vol. 306, pp. 1362-1364, Nov 19 2004.
[83] M. D. Lima, X. Lepro, and R. H. Baughman, "Spinnable carbon nanotube forests grown on thin, flexible metallic substrates," *Carbon,* vol. 48, pp. 3621-3627, Oct 2010.
[84] D. N. Futaba, B. Zhao, S. Yasuda, M. Akoshima, T. Yamada, and K. Hata, "Exploring Advantages of Diverse Carbon Nanotube Forests With Tailored Structures Synthesized by Supergrowth from Engineered Catalysts," *Acs Nano,* vol. 3, pp. 108-114, Jan 2009.
[85] B. Q. Wei, R. Vajtai, Y. Jung, J. Ward, R. Zhang, G. Ramanath, and P. M. Ajayan, "Organized assembly of carbon nanotubes - Cunning refinements help to customize the architecture of nanotube structures.," *Nature,* vol. 416, pp. 495-496, Apr 4 2002.

[86] C. V. Thompson, G. D. Nessim, M. Seita, K. P. O'Brien, A. J. Hart, R. K. Bonaparte, and R. R. Mitchell, "Low Temperature Synthesis of Vertically Aligned Carbon Nanotubes with Electrical Contact to Metallic Substrates Enabled by Thermal Decomposition of the Carbon Feedstock," *Nano Letters,* vol. 9, pp. 3398-3405, Oct 2009.

[87] A. J. Hart, E. R. Meshot, D. L. Plata, S. Tawfick, Y. Y. Zhang, and E. A. Verploegen, "Engineering Vertically Aligned Carbon Nanotube Growth by Decoupled Thermal Treatment of Precursor and Catalyst," *Acs Nano,* vol. 3, pp. 2477-2486, Sep 2009.

[88] K. Hata, S. Yasuda, D. N. Futaba, T. Yamada, J. Satou, A. Shibuya, H. Takai, K. Arakawa, and M. Yumura, "Improved and Large Area Single-Walled Carbon Nanotube Forest Growth by Controlling the Gas Flow Direction," *Acs Nano,* vol. 3, pp. 4164-4170, Dec 2009.

[89] A. Katsounaros, K. Z. Rajab, Y. Hao, M. Mann, and W. I. Milne, "Microwave characterization of vertically aligned multiwalled carbon nanotube arrays," *Applied Physics Letters,* vol. 98, May 16 2011.

[90] A. Katsounaros, M. Mann, M. Naftaly, K. Z. Rajab, Y. Hao, and W. I. Milne, "THz Characterisation of Vertically Aligned Carbon Nanotube Films " *Carbon,* vol. 50, pp. 939-942, 2012.

[91] A. M. Nicolson and G. F. Ross, "Measurement of Intrinsic Properties of Materials by Time-Domain Techniques," *IEEE Transactions on Instrumentation and Measurement,* vol. Im19, pp. 377-&, 1970.

[92] W. B. Weir, "Automatic Measurement of Complex Dielectric-Constant and Permeability at Microwave-Frequencies," *Proceedings of the IEEE,* vol. 62, pp. 33-36, 1974.

[93] R. W. Ziolkowski, "Design, fabrication, and testing of double negative metamaterials," *IEEE Transactions on Antennas and Propagation,* vol. 51, pp. 1516-1529, Jul 2003.

[94] D. M. Pozar, *Microwave engineering*, 3rd ed. ed. New York ; Chichester: Wiley, 2004.

[95] A. Katsounaros, K. Z. Rajab, Y. Hao, M. Mann, and W. I. Milne, "Microwave Characterization of Multi-Walled Carbon Nanotube Arrays," in *European Microwave Week*, Manchester, UK, 2011.

[96] S. Y. Lin, Z. P. Yang, L. J. Ci, J. A. Bur, and P. M. Ajayan, "Experimental observation of an extremely dark material made by a low-density nanotube array," *Nano Letters,* vol. 8, pp. 446-451, Feb 2008.

[97] F. J. Garcia-Vidal, "Metamaterials - Towards the dark side," *Nature Photonics,* vol. 2, pp. 215-216, Apr 2008.

[98] K. N. Rozanov, "Ultimate thickness to bandwidth ratio of radar absorbers," *Antennas and Propagation, IEEE Transactions on,* vol. 48, pp. 1230-1234, 2000.

[99] D. Grischkowsky, S. Keiding, M. Vanexter, and C. Fattinger, "Far-Infrared Time-Domain Spectroscopy with Terahertz Beams of Dielectrics and Semiconductors," *Journal of the Optical Society of America B-Optical Physics,* vol. 7, pp. 2006-2015, Oct 1990.

[100] G. Gruner, *Millimeter and submillimeter wave spectroscopy of solids*. Berlin ; London: Springer, 1998.

[101] Z. R. Wu, L. Wang, Y. T. Peng, A. Young, S. Seraphin, and H. Xin, "Terahertz characterization of multi-walled carbon nanotube films," *Journal of Applied Physics,* vol. 103, May 1 2008.

[102] G. Mourou, C. V. Stancampiano, A. Antonetti, and A. Orszag, "Picosecond Microwave Pulses Generated with a Subpicosecond Laser-Driven Semiconductor Switch," *Applied Physics Letters,* vol. 39, pp. 295-296, 1981.
[103] D. A. Wharam, M. Pepper, H. Ahmed, J. E. F. Frost, D. G. Hasko, D. C. Peacock, D. A. Ritchie, and G. A. C. Jones, "Addition of the One-Dimensional Quantized Ballistic Resistance," *Journal of Physics C-Solid State Physics,* vol. 21, pp. L887-L891, Aug 30 1988.
[104] D. A. Wharam, T. J. Thornton, R. Newbury, M. Pepper, H. Ahmed, J. E. F. Frost, D. G. Hasko, D. C. Peacock, D. A. Ritchie, and G. A. C. Jones, "One-Dimensional Transport and the Quantization of the Ballistic Resistance," *Journal of Physics C-Solid State Physics,* vol. 21, pp. L209-L214, Mar 20 1988.
[105] Y. Zhou, "Polymer-Ceramic composites for conformal multilayer antenna and RF systems," Ph.D., The Ohio State University, Ohio, USA, 2009.
[106] M. P. A. Fisher and L. I. Glazman, "Transport in a one-dimensional Luttinger liquid," *Mesoscopic Electron Transport,* vol. 345, pp. 331-373, 1997.
[107] T. S., "Remarks on Bloch's Method of Sound Waves applied to Many-Fermion Problems," *Progress of Theoretical Physics,* vol. 5, pp. 544-569, 1950.
[108] J. M. Luttinger, "An exact solvable model of a many-Fermion system," *Journal of Mathematical Physics,* vol. 4, p. 1154, 1963.
[109] A. O. Gogolin, A. A. Nersesyan, and A. M. Tsvelik, *Bosonization and strongly correlated systems*. Cambridge, U.K. ; New York, NY: Cambridge University Press, 1998.
[110] F. D. M. Haldane, "Effective Harmonic-Fluid Approach to Low-Energy Properties of One-Dimensional Quantum Fluids," *Physical Review Letters,* vol. 47, pp. 1840-1843, 1981.
[111] P. J. Burke, I. B. Spielman, J. P. Eisenstein, L. N. Pfeiffer, and K. W. West, "High frequency conductivity of the high-mobility two-dimensional electron gas," *Applied Physics Letters,* vol. 76, pp. 745-747, Feb 7 2000.
[112] X. G. Peralta, S. J. Allen, M. C. Wanke, N. E. Harff, J. A. Simmons, M. P. Lilly, J. L. Reno, P. J. Burke, and J. P. Eisenstein, "Terahertz photoconductivity and plasmon modes in double-quantum-well field-effect transistors," *Applied Physics Letters,* vol. 81, pp. 1627-1629, Aug 26 2002.
[113] M. W. Bockrath, *Carbon Nanotubes: electrons in one dimension*. Berkeley: University of California, 1999.
[114] E. B. Sonin, "Tunneling into 1D and quasi-1D conductors and Luttinger-liquid behavior," *Journal of Low Temperature Physics,* vol. 124, pp. 321-334, Jul 2001.
[115] Y. Kane, "Numerical solution of initial boundary value problems involving maxwell's equations in isotropic media," *Antennas and Propagation, IEEE Transactions on,* vol. 14, pp. 302-307, 1966.
[116] P. J. Burke, "Luttinger liquid theory as a model of the gigahertz electrical properties of carbon nanotubes," *IEEE Transactions on Nanotechnology,* vol. 1, pp. 129-144, Sep 2002.
[117] P. J. Burke, "An RF circuit model for carbon nanotubes," *IEEE Transactions on Nanotechnology,* vol. 2, pp. 55-58, Mar 2003.
[118] S. Ramo, J. R. Whinnery, and T. Van Duzer, *Fields and waves in communication electronics,* 3rd ed. ed. New York ; Chichester: Wiley, 1994.

[119] Y. M. Blanter, F. W. J. Hekking, and M. Buttiker, "Interaction constants and dynamic conductance of a gated wire," *Physical Review Letters,* vol. 81, pp. 1925-1928, Aug 31 1998.
[120] R. Tarkiainen, M. Ahlskog, J. Penttila, L. Roschier, P. Hakonen, M. Paalanen, and E. Sonin, "Multiwalled carbon nanotube: Luttinger versus Fermi liquid," *Physical Review B,* vol. 64, pp. -, Nov 15 2001.
[121] L. F. Richardson, "The Approximate Arithmetical Solution by Finite Differences of Physical Problems Involving Differential Equations, with an Application to the Stresses in a Masonry Dam," *Philosophical Transactions of the Royal Society of London. Series A, Containing Papers of a Mathematical or Physical Character,* vol. 210, pp. 307-357, 1911.
[122] L. F. Richardson, *Weather prediction by numerical process*: Cambridge : University Press, 1922.
[123] A. Thom and C. J. Apelt, *Field computations in engineering and physics*. London: D. Van Nostrand Co, 1961.
[124] G. Mur, "Absorbing Boundary-Conditions for the Finite-Difference Approximation of the Time-Domain Electromagnetic-Field Equations," *IEEE Transactions on Electromagnetic Compatibility,* vol. 23, pp. 377-382, 1981.
[125] Z. P. Liao, H. L. Wong, B. Yang, and Y. Yuan, "A Transmitting Boundary for Transient Wave Analyses," *Scientia Sinica Series a-Mathematical Physical Astronomical & Technical Sciences,* vol. 27, pp. 1063-1076, 1984.
[126] J. P. Berenger, "A Perfectly Matched Layer for the Absorption of Electromagnetic-Waves," *Journal of Computational Physics,* vol. 114, pp. 185-200, Oct 1994.
[127] C. A. Balanis, *Antenna theory : analysis and design*, 3rd ed. ed. Hoboken, N.J.: [Great Britain] : Wiley-Interscience, 2005.
[128] D. M. Pozar, *Microwave engineering*, 3rd ed., International ed. ed. New York ; [Chichester]: Wiley, 2005.
[129] H. Bao, X. L. Ruan, and T. S. Fisher, "Optical properties of ordered vertical arrays of multi-walled carbon nanotubes from FDTD simulations," *Optics Express,* vol. 18, pp. 6347-6359, Mar 15 2010.
[130] E. E. Kriezis and S. J. Elston, "Finite-difference time domain method for light wave propagation within liquid crystal devices," *Optics Communications,* vol. 165, pp. 99-105, Jul 1 1999.
[131] L. D. Landau, E. M. Lifshits, and L. P. Pitaevskii, *Electrodynamics of continuous media*, 2nd ed. rev. and enl. / by E.M. Lifshitz and L.P. Pitaevskii. ed. Oxford: Pergamon, 1984.
[132] J. B. Pendry, A. J. Holden, W. J. Stewart, and I. Youngs, "Extremely low frequency plasmons in metallic mesostructures," *Physical Review Letters,* vol. 76, pp. 4773-4776, Jun 17 1996.
[133] J. B. Pendry, A. J. Holden, D. J. Robbins, and W. J. Stewart, "Magnetism from conductors and enhanced nonlinear phenomena," *IEEE Transactions on Microwave Theory and Techniques,* vol. 47, pp. 2075-2084, Nov 1999.
[134] S. A. Maier, *Plasmonics : fundamentals and applications*. Bath ; New York: Springer, 2006.
[135] C. Argyropoulos, "FDTD Modelling of Electromagnetic Transformation Based Devices," Ph.D., Queen Mary, University of London, London, 2010.
[136] O. L. Muskens, J. G. Rivas, R. E. Algra, E. P. A. M. Bakkers, and A. Lagendijk, "Design of light scattering in nanowire materials for photovoltaic applications," *Nano Letters,* vol. 8, pp. 2638-2642, Sep 2008.

[137] E. Lidorikis and A. C. Ferrari, "Photonics with Multiwall Carbon Nanotube Arrays," *Acs Nano,* vol. 3, pp. 1238-1248, May 2009.
[138] *HFSS v.12, Simulation Software, ANSYS*.
[139] J. S. Seybold, *Introduction to RF propagation*. Hoboken, N.J.: Wiley ; Chichester : John Wiley [distributor], 2005.
[140] M. V. Kostin and V. V. Shevchenko, "Artificial Magnetics on the Base of Circular Currents," *Radiotekhnika I Elektronika,* vol. 33, pp. 1526-1531, Jul 1988.
[141] M. Gorkunov, M. Lapine, E. Shamonina, and K. H. Ringhofer, "Effective magnetic properties of a composite material with circular conductive elements," *European Physical Journal B,* vol. 28, pp. 263-269, Aug 2002.
[142] S. Maslovski, P. Ikonen, I. Kolmakov, S. Tretyakov, and M. Kaunisto, "Artificial magnetic materials based on the new magnetic particle: Metasolenoid," *Progress in Electromagnetics Research-Pier,* vol. 54, pp. 61-81, 2005.
[143] P. M. T. Ikonen and S. A. Tretyakov, "Determination of generalized permeability function and field energy density in artificial magnetics using the equivalent-circuit method," *IEEE Transactions on Microwave Theory and Techniques,* vol. 55, pp. 92-99, Jan 2007.
[144] Z. F. Ren, K. Kempa, B. Kimball, J. Rybczynski, Z. P. Huang, P. F. Wu, D. Steeves, M. Sennett, M. Giersig, D. V. G. L. N. Rao, D. L. Carnahan, D. Z. Wang, J. Y. Lao, and W. Z. Li, "Photonic crystals based on periodic arrays of aligned carbon nanotubes," *Nano Letters,* vol. 3, pp. 13-18, Jan 2003.
[145] G. L. Zhao, D. Bagayoko, and L. Yang, "Optical properties of aligned carbon nanotube mats for photonic applications," *Journal of Applied Physics,* vol. 99, Jun 1 2006.
[146] K. Hata, K. Mizuno, J. Ishii, H. Kishida, Y. Hayamizu, S. Yasuda, D. N. Futaba, and M. Yumura, "A black body absorber from vertically aligned single-walled carbon nanotubes," *Proceedings of the National Academy of Sciences of the United States of America,* vol. 106, pp. 6044-6047, Apr 14 2009.
[147] M. F. Lin and K. W. K. Shung, "Plasmons and Optical-Properties of Carbon Nanotubes," *Physical Review B,* vol. 50, pp. 17744-17747, Dec 15 1994.
[148] S. M. Bachilo, M. S. Strano, C. Kittrell, R. H. Hauge, R. E. Smalley, and R. B. Weisman, "Structure-assigned optical spectra of single-walled carbon nanotubes," *Science,* vol. 298, pp. 2361-2366, Dec 20 2002.
[149] G. Y. Guo, K. C. Chu, D. S. Wang, and C. G. Duan, "Linear and nonlinear optical properties of carbon nanotubes from first-principles calculations," *Physical Review B,* vol. 69, May 2004.
[150] M. F. Lin, "Optical spectra of single-wall carbon nanotube bundles," *Physical Review B,* vol. 62, pp. 13153-13159, Nov 15 2000.
[151] T. Xu, S. X. Yang, S. V. Nair, and H. E. Ruda, "Nanowire-array-based photonic crystal cavity by finite-difference time-domain calculations," *Physical Review B,* vol. 75, Mar 2007.
[152] P. C. Eklund, G. Chen, J. Wu, Q. J. Lu, H. R. H. Gutierrez, Q. Xiong, M. E. Pellen, J. S. Petko, and D. H. Werner, "Optical antenna effect in semiconducting nanowires," *Nano Letters,* vol. 8, pp. 1341-1346, May 2008.
[153] R. E. Camacho, A. R. Morgan, M. C. Flores, T. A. McLeod, V. S. Kumsomboone, B. J. Mordecai, R. Bhattacharjea, W. Tong, B. K. Wagner, J. D. Flicker, S. P. Turano, and W. J. Ready, "Carbon nanotube arrays for photovoltaic applications," *Jom,* vol. 59, pp. 39-42, Mar 2007.

[154] R. A. Street, P. Qi, R. Lujan, and W. S. Wong, "Reflectivity of disordered silicon nanowires," *Applied Physics Letters,* vol. 93, Oct 20 2008.
[155] L. Tsakalakos, J. Balch, J. Fronheiser, B. A. Korevaar, O. Sulima, and J. Rand, "Silicon nanowire solar cells," *Applied Physics Letters,* vol. 91, Dec 3 2007.
[156] A. Javey, Z. Y. Fan, H. Razavi, J. W. Do, A. Moriwaki, O. Ergen, Y. L. Chueh, P. W. Leu, J. C. Ho, T. Takahashi, L. A. Reichertz, S. Neale, K. Yu, M. Wu, and J. W. Ager, "Three-dimensional nanopillar-array photovoltaics on low-cost and flexible substrates," *Nature Materials,* vol. 8, pp. 648-653, Aug 2009.
[157] L. G. Johnson and Dresselh.G, "Optical Properties of Graphite," *Physical Review B,* vol. 7, pp. 2275-2284, 1973.
[158] F. L. Pedrotti, L. M. Pedrotti, and L. S. Pedrotti, *Introduction to optics,* 3rd ed. / Frank L. Pedrotti, Leno M. Pedrotti, Leno S. Pedrotti. ed. Upper Saddle River, N.J.: Pearson/Addison Wesley, 2007.
[159] Z. M. Zhang, X. J. Wang, J. D. Flicker, B. J. Lee, and W. J. Ready, "Visible and near-infrared radiative properties of vertically aligned multi-walled carbon nanotubes," *Nanotechnology,* vol. 20, May 27 2009.
[160] C. X. Lin and M. L. Povinelli, "Optical absorption enhancement in silicon nanowire arrays with a large lattice constant for photovoltaic applications," *Optics Express,* vol. 17, pp. 19371-19381, Oct 26 2009.
[161] T. W. Ebbesen, H. J. Lezec, H. F. Ghaemi, T. Thio, and P. A. Wolff, "Extraordinary optical transmission through sub-wavelength hole arrays," *Nature,* vol. 391, pp. 667-669, Feb 12 1998.
[162] R. N. Simons and R. Q. Lee, "Feasibility study of optically transparent microstrip patch antenna," *IEEE Antennas and Propagation Society International Symposium 1997, Vols 1-4,* pp. 2100-2103, 1997.
[163] C. Tsakonas, S. C. Liew, C. Mias, D. C. Koutsogeorgis, R. M. Ranson, W. M. Cranton, and M. Dudhia, "Optically transparent frequency selective window for microwave applications," *Electronics Letters,* vol. 37, pp. 1464-1466, Nov 22 2001.
[164] N. Guan, H. Furuya, K. Himeno, K. Goto, and K. Ito, "Basic study on an antenna made of a transparent conductive film," *Ieice Transactions on Communications,* vol. E90b, pp. 2219-2224, Sep 2007.
[165] "FCC first report and order, revision of the part 15 commission's rules regarding ultra-wideband transmission systems," ET-Docket 2002.
[166] D. Porcino and W. Hirt, "Ultra-wideband radio technology: Potential and challenges ahead," *IEEE Communications Magazine,* vol. 41, pp. 66-74, Jul 2003.
[167] (20 March 2001). *European Communications Office*. Available: http://www.ero.dk
[168] T. Kawashima, H. Matsui, and N. Tanabe, "New transparent conductive films: FTO coated ITO," *Thin Solid Films,* vol. 445, pp. 241-244, Dec 15 2003.
[169] CPFilms, "AgHT product datasheet ", ed: Solutia, UK Ltd.
.
[170] A. Katsounaros, Y. Hao, N. Collings, and W. A. Crossland, "Optically transparent ultra-wideband antenna," *Electronics Letters,* vol. 45, pp. 722-723, Jul 2 2009.
[171] A. Katsounaros, Y. Hao, N. Collings, and W. A. Crossland, "Optically Transparent Antenna for Ultra Wide-Band Applications," *2009 3rd European Conference on Antennas and Propagation, Vols 1-6,* pp. 1838-1841, 2009.

[172] L. Tian Hong and M. Alexander, "New facility for minimally invasive measurements of electrically small antennas," in *Antennas and Propagation Conference, 2008. LAPC 2008. Loughborough*, 2008, pp. 313-316.
[173] D.-K. Yang and S.-T. Wu, *Fundamentals of liquid crystal devices*. Chichester: John Wiley, 2006.
[174] L. M. l. Blinov and V. G. Chigrinov, *Electrooptic effects in liquid crystal materials*. New York ; London: Springer-Verlag, 1994.
[175] S. Chandrasekhar, *Liquid crystals*, 2nd ed. ed. Cambridge: Cambridge University Press, 1992.
[176] P.-G. d. Gennes and J. Prost, *The physics of liquid crystals*, 2nd ed. ed. Oxford: Clarendon Press, 1993.
[177] S. Mueller, A. Penirschke, C. Damm, P. Scheele, M. Wittek, C. Weil, and R. Jakoby, "Broad-band microwave characterization of liquid crystals using a temperature-controlled, coaxial transmission line," *IEEE Transactions on Microwave Theory and Techniques*, vol. 53, pp. 1937-1945, Jun 2005.
[178] F. Z. Yang and J. R. Sambles, "Determination of the permittivity of nematic liquid crystals in the microwave region," *Liquid Crystals*, vol. 30, pp. 599-602, May 2003.
[179] K. C. Lim, J. D. Margerum, A. M. Lackner, L. J. Miller, E. Sherman, and W. H. Smith, "Liquid-Crystal Birefrigence for Millimeter-Wave Radar," *Liquid Crystals*, vol. 14, pp. 327-337, 1993.
[180] C. Weil, S. Muller, R. Scheele, P. Best, G. Lussem, and R. Jakoby, "Highly-anisotropic liquid-crystal mixtures for tunable microwave devices," *Electronics Letters*, vol. 39, pp. 1732-1734, Nov 27 2003.
[181] H. Xu, O. Trushkevych, N. Collings, and W. A. Crossland, "Measurement of Dielectric Anisotropy of Some Liquid Crystals for Microwave Applications," *Molecular Crystals and Liquid Crystals*, vol. 502, pp. 235-244, 2009.
[182] A. M. Lackner, K. C. Lim, J. D. Margerum, and E. Sherman, "Microtubule Particle Dispersion in Liquid-Crystal Hosts," *Liquid Crystals*, vol. 14, pp. 351-359, 1993.
[183] M. Endo, K. Takeuchi, S. Igarashi, K. Kobori, M. Shiraishi, and H. W. Kroto, "The production and structure of pyrolytic carbon nanotubes (PCNTs)," *Journal of Physics and Chemistry of Solids*, vol. 54, pp. 1841-1848, 1993.
[184] L. S. Schadler, S. C. Giannaris, and P. M. Ajayan, "Load transfer in carbon nanotube epoxy composites," *Applied Physics Letters*, vol. 73, pp. 3842-3844, Dec 28 1998.
[185] P. M. Ajayan, O. Stephan, C. Colliex, and D. Trauth, "Aligned Carbon Nanotube Arrays Formed by Cutting a Polymer Resin-Nanotube Composite," *Science*, vol. 265, pp. 1212-1214, Aug 26 1994.
[186] O. Zhou, L. Jin, and C. Bower, "Alignment of carbon nanotubes in a polymer matrix by mechanical stretching," *Applied Physics Letters*, vol. 73, pp. 1197-1199, Aug 1998.
[187] X. K. Wang, X. W. Lin, V. P. Dravid, J. B. Ketterson, and R. P. H. Chang, "Growth and Characterization of Buckybundles," *Applied Physics Letters*, vol. 62, pp. 1881-1883, Apr 19 1993.
[188] M. Terrones, N. Grobert, J. Olivares, J. P. Zhang, H. Terrones, K. Kordatos, W. K. Hsu, J. P. Hare, P. D. Townsend, K. Prassides, A. K. Cheetham, H. W. Kroto, and D. R. M. Walton, "Controlled production of aligned-nanotube bundles," *Nature*, vol. 388, pp. 52-55, Jul 3 1997.
[189] M. D. Lynch and D. L. Patrick, "Organizing Carbon Nanotubes with Liquid Crystals," *Nano Letters*, vol. 2, pp. 1197-1201, 2002.

[190] O. Trushkevych, F. Golden, M. Pivnenko, H. Xu, N. Collings, W. A. Crossland, S. Muller, and R. Jakoby, "Dielectric anisotropy of nematic liquid crystals loaded with carbon nanotubes in microwave range," *Electronics Letters,* vol. 46, pp. 693-694, May 13 2010.

[191] O. Trushkevych, N. Collings, T. Hasan, V. Scardaci, A. C. Ferrari, T. D. Wilkinson, W. A. Crossland, W. I. Milne, J. Geng, B. F. G. Johnson, and S. Macaulay, "Characterization of carbon nanotube-thermotropic nematic liquid crystal composites," *Journal of Physics D-Applied Physics,* vol. 41, Jun 21 2008.

[192] I. Dierking, G. Scalia, and P. Morales, "Liquid crystal-carbon nanotube dispersions," *Journal of Applied Physics,* vol. 97, Feb 15 2005.

[193] I. Dierking and S. E. San, "Magnetically steered liquid crystal-nanotube switch," *Applied Physics Letters,* vol. 87, Dec 5 2005.

[194] W. Lee, C. Y. Wang, and Y. C. Shih, "Effects of carbon nanosolids on the electro-optical properties of a twisted nematic liquid-crystal host," *Applied Physics Letters,* vol. 85, pp. 513-515, Jul 26 2004.

[195] I. Dierking, K. Casson, and R. Hampson, "Reorientation Dynamics of Liquid Crystal-Nanotube Dispersions," *Japanese Journal of Applied Physics,* vol. 47, pp. 6390-6393, Aug 2008.

[196] K. R. Boyle, M. Udink, A. de Graauw, and L. P. Ligthart, "A dual-fed, self-diplexing PIFA and RF front-end," *IEEE Transactions on Antennas and Propagation,* vol. 55, pp. 373-382, Feb 2007.

[197] A. C. K. Mak, C. R. Rowell, R. D. Murch, and C. L. Mak, "Reconfigurable multiband antenna designs for wireless communication devices," *IEEE Transactions on Antennas and Propagation,* vol. 55, pp. 1919-1928, Jul 2007.

[198] K. K. Tsang and R. J. Langley, "Design of circular patch antennas on ferrite substrates," *Iee Proceedings-Microwaves Antennas and Propagation,* vol. 145, pp. 49-55, Feb 1998.

[199] W. Hu, M. Y. Ismail, R. Cahill, H. S. Gamble, R. Dickie, V. F. Fusco, D. Linton, S. P. Rea, and N. Grant, "Tunable liquid crystal reflectarray patch element," *Electronics Letters,* vol. 42, pp. 509-511, Apr 27 2006.

[200] W. F. Hu, R. Dickie, R. Cahill, H. Gamble, Y. Ismail, V. Fusco, D. Linton, N. Grant, and S. Rea, "Liquid crystal tunable mm wave frequency selective surface," *IEEE Microwave and Wireless Components Letters,* vol. 17, pp. 667-669, Sep 2007.

[201] N. Martin, P. Laurent, C. Person, P. Gelin, and F. Huret, "Patch antenna adjustable in frequency using liquid crystal," *33rd European Microwave Conference, Vols 1-3, Conference Proceedings,* pp. 699-702, 2003.

[202] *Data Sheet Licristal E7, Merck KGaA.* Germany, 2001.